Thermoelectric Properties of Alkaline Earth Metal Substituted Europium Titanates

Xingxing Xiao

Dissertation submitted as a requirement for the degree of Doctor of Natural Science

August 2019 – Technical University of Darmstadt (TUD)- D17

TECHNISCHE UNIVERSITÄT DARMSTADT

This page intentionally left blank

Thermoelectric Properties of Alkaline Earth Metal Substituted Europium Titanates

Dissertation submitted to the Department of Materials and Earth Sciences at Technische Universität Darmstadt

in Fulfillment of the Requirements for the Degree of
Doctor of Natural Science (Dr. rer. nat.)

by
Xingxing Xiao

Technische Universität Darmstadt, Hochschulkennziffer D17

Date of Submission: 20.01.2020
Date of Oral Examination: 12.03.2020

Referee: Prof. Dr. Anke Weidenkaff
Co-referee: Prof. Dr. Rainer Niewa

Darmstadt 2020

Xiao, Xingxing: Thermoelectric Properties of Alkaline Earth Metal Substituted Europium Titanates

Darmstadt, Technische Universität Darmstadt

Publication Year of Dissertation at TUprints: 2021
URN: urn:nbn:de:tuda-tuprints-145931
Date of Oral Examination: 12.03.2020

THESIS SUPERVISORS

Prof. Dr. Anke Weidenkaff

Materials Science / Department of Materials and Earth Sciences / Technische Universität Darmstadt

Materials Recycling and Resource Strategies / Fraunhofer IWKS

Prof. Dr. Rainer Niewa

Institute of Inorganic Chemistry / University of Stuttgart

THESIS COMMITTEE

Referee:

Prof. Dr. Anke Weidenkaff

Materials Science / Department of Materials and Earth Sciences / Technische Universität Darmstadt
Materials Recycling and Resource Strategies / Fraunhofer IWKS

Co-referee:

Prof. Dr. Rainer Niewa

Institute of Inorganic Chemistry / University of Stuttgart

Examiner:

Prof. Dr. Lambert Alff

Materials Science / Department of Materials and Earth Sciences / Technische Universität Darmstadt

Examiner:

Jun. Prof. Dr. Hongbin Zhang

Materials Science / Department of Materials and Earth Sciences / Technische Universität Darmstadt

This page intentionally left blank

Acknowledgments

This dissertation would not have been possible without the help, support, and encouragement of supervisors, colleagues, friends, and family.

First of all, I would like to express my sincere gratitude to my supervisor, Prof. Dr. Anke Weidenkaff, for giving me the opportunity to complete my Ph.D. study in her group. She constantly provided me with valuable support since 2012 when I was an internship in her group. She is my good mentor in my career and a great friend in my life. I deeply thank my secondary supervisor, Prof. Dr. Rainer Niewa, for his unconditional support on my work, and I do appreciate his trust towards me. Special thanks go to Prof. Dr. Lambert Alff and Prof. Dr. Hongbin Zhang for being my thesis examiners.

I especially thank my daily supervisor Dr. Marc Widenmeyer. He is always very patient in providing guidance and assistance whenever I need his help in my work. His careful and serious scientific attitude has affected me a lot, which will definitely benefit my whole life. I am also grateful to my officemate Dr. Songhak Yoon. He always tried his best to help me to solve problems as soon as possible and gave me encouraging support. I truly cherish the moments when we had lots of unfettered discussion on scientific work.

Very special gratitude has to be extended to my collaborators. I am grateful to Prof. Dr. Marco Scavini for his help on high-resolution XRD Rietveld refinements. He is an approachable and friendly person and opened a window for me to see the world of crystallography. Thanks to his introduction and recommendation, Prof. Dr. Carlo Castellano did the EXAFS analysis and Dr. Stefano Checchia performed the PDF analysis for me. Although we communicated via email and never had face-to-face conversations, they trusted me and provided me with constructive suggestions and valuable contributions to my research. I am also grateful to the European Synchrotron Radiation Facility for the provision of beam time and sincerely indebted to Dr. Mauro Coduri for his assistance in using the ID22 beam-line. Many thanks must also go to Dr. Kathrin Müller and Prof. Dr. Ulrich Starke for the XPS measurements. Kathrin took lots of time to carry out the experiments and analyse the results for me. I would also like to thank one of my office-mates, Dr. Stefan Kilper. He is always very friendly and helpful during the work. I would also like to express my gratitude to Dr. Dongxia Ma, Dr. Zhicheng Zhong, and Dr. Philipp Hansmann for the DFT calculations. Dongxia helped me a lot to understand some fundamental knowledge of theoretical calculations. I admire her very much for her kindness, optimism, enthusiasm and wisdom. I am also grateful to Dr. Andrei Kovalevsky and his Ph.D. student Kiryl Zakharchuk. In addition to helping me fabricate desired bulk samples in his laboratory, Andrei also gave me wise advice for the publications. I thank Dr. Kai Philippi from the group of Prof. Dr. Hidenori Takagi for his PPMS measurements and scientific discussions. I thank Dr. Konstantin Skokov who did the low-temperature specific heat measurements for me. Many thanks also go to Prof. Dr. Jian He from Clemson University. He guides me to feel the charm of solid-state physics. His willingness to answer all of my questions on physics encouraged me to be more confident and braver to continue studying. They all gave me great help and professional support, thus I could complete this work and broaden my knowledge.

I would like to express my thanks to all colleagues of Chair 3 in the Institute for Materials Science at the University of Stuttgart for their professional support and enjoyable working

atmosphere. I often discussed various topics with Cora Bubeck, including work, study, and personal life. My thanks also go to our kind and helpful secretary, Mrs. Juliane Kränzl. She helped me a lot to do the countless administrative paperwork. I want to thank our technicians, Mr. Traugott Worner, Mr. Martin Schweizer, and Mr. Frank Hack for their professional and efficient assistance. I would like to thank my Chinese colleagues Ruijuan Yan, Tianhua Zou, Guoxing Chen, Wenmei Liu, Pingjun Ying, Bingjie Tang, Jingjing Jiang. We always had our lunch with fun chatting at canteen, which was the most relaxing time during the working days. It was a great pleasure to work together with all of you.

Last but not least, the deepest gratitude belongs to my family. I would like to thank my husband and my lovely son for accompanying me to walk along the path of life. I would like to thank my parents, sisters, and brother for giving me unconditional love always. With you, my life is much more meaningful!

Xingxing Xiao

Darmstadt. August. 2019

Biographical note

EDUCATION

Ph.D.	Materials Science	*Supervised by* Prof. Dr. Anke Weidenkaff & Prof. Dr. Rainer Niewa
	04 / 2019 ~	Technische Universität Darmstadt *Department of Materials and Earth Sciences*
	12 / 2013 ~ 04 / 2014 06 / 2015 ~ 03 / 2019	University of Stuttgart *Institut für Materialwissenschaft*
	05 / 2014 ~ 05 / 2015	maternity leave
M.Sc.	Materials Science	*Supervised by* Prof. Dr. Xinfeng Tang & Prof. Dr. Qingjie Zhang
	09 / 2008 ~ 06 / 2011	Wuhan University of Technology (WUT) *State Key Laboratory of Advanced Technology for Materials Synthesis and Processing*
B.Eng.	Materials Science and Engineering	*Supervised by* Prof. Dr. Xiaohong Xu
	09 / 2004 ~ 06 / 2008	Wuhan University of Technology

WORK EXPERIENCE

12 / 2013 ~ 04 / 2014 06 / 2015 ~ 03 / 2019	*Research Assistant*	University of Stuttgart, Germany
09 / 2012 ~ 12 / 2013	*Internship*	Swiss Federal Laboratories for Materials Science and Technology (Empa), Switzerland
03 / 2011 ~ 02 / 2012	*Teaching Assistant*	Wuhan Huaxia University of Technology, China
09 / 2008 ~ 06 / 2011	*Laboratory Assistant*	Wuhan University of Technology, China
09 / 2006 ~ 06 / 2008	*Student Assistant*	Wuhan University of Technology, China

PUBLICATIONS

1. **X. Xiao**, M. Widenmeyer, K. Mueller, M. Scavini, S. Checchia, C. Castellano, D. Ma, S. Yoon, W. Xie, U. Starke, K. Zakharchuk, A. Kovalevsky, A. Weidenkaff, "A squeeze on the perovskite structure improves the thermoelectric performance of Europium Calcium Titanates", *Materials Today Physics*, 2018, 7: 96-105.
2. **X. Xiao**, M. Widenmeyer, W. Xie, T. Zou, S. Yoon, M. Scavini, S. Checchia, Z. Zhong, P. Hansmann, S. Kilper, A. Kovalevsky, A. Weidenkaff, "Tailoring the structure and thermoelectric properties of $BaTiO_3$ via Eu^{2+} substitution", *Physical Chemistry Chemical Physics,* 2017, 19(21): 13469-13480.

3. K. V. Zakharchuk, D. M. Tobaldi, **X. Xiao**, W. Xie, S. M. Mikhalev, J. F. Martins, J. R. Frade, A. Weidenkaff, A. V. Kovalevsky, "Synergistic effects of zirconium- and aluminum co-doping on the thermoelectric performance of zinc oxide", *Journal of the European Ceramic Society*, 2019, 39(4): 1222-1229.
4. T. Zou, W. Xie, M. Widenmeyer, **X. Xiao**, A. Weidenkaff, "Enhancing point defect scattering in copper antimony selenides via Sm and S Co-doping", *Rare Metals*, 2018, 37(4): 290-299.
5. T. Zou, T. Jia, W. Xie, Y. Zhang, M. Widenmeyer, **X. Xiao**, A. Weidenkaff, "Band structure modification in thermoelectric Heusler-phase $TiFe_2Sn$ via Mn substitution", *Physical Chemistry Chemical Physics*, 2017, 19(28): 18273-18278.
6. W. Xie, S. Populoh, K. Galazka, **X. Xiao**, L. Sagarna, Y. Liu, M. Trottmann, J. He, A. Weidenkaff, "Thermoelectric Study of Crossroads Material MnTe via Sulfur Doping", *Journal of Applied Physics*, 2014, 115(10): 103707.
7. **X. Xiao**, W. Xie, X. Tang, Q. Zhang, "Phase Transition and High Temperature Thermoelectric Transport Properties of Copper Selenide $Cu_{2-x}Se$ ($0 \leq x \leq 0.25$)", *Chinese Physics B*, 2011, 20(8): 087201.

CONFERENCE CONTRIBUTIONS

1. **X. Xiao**, M. Widenmeyer, S. Yoon, W. Xie, A. Weidenkaff, "Interplay between chemical pressure effects and thermoelectric performance in perovskite-type titanates: the case of $EuTiO_3$", *2019 E-MRS Spring Meeting*, Nice, France, (oral presentation)
2. **X.Xiao**, M. Widenmeyer, T. Zou, W. Xie, and A. Weidenkaff, "Tuning thermo electric properties of $BaTiO_{3-\delta}$ via Eu^{2+} substitution", *2016 ICT*, Wuhan, China, (Poster)
3. M. Widenmeyer, **X. Xiao**, J. Häcker, C. M. Bubeck, W. Xie, A. Weidenkaff, "Modified Novel Perovskite-type Oxides and Oxynitride Fluorides for Thermolelectric and Solar Water Splitting Applications", *2016 DGK*, Stuttgart, Germany, (Poster)
4. **X. Xiao**, S. Yoon, L. Sagarna, A. Shkabko, S. Populoh, A. Maegli, A. Weidenkaff, Microstructure and thermoelectric properties of $SrTiO_{3-\delta}$–TiO_2 composites, *MRS 2013 Spring meeting*, San Francisco, USA. (Poster)
5. Symposium assistant, The 29th international conference on thermoelectrics, *2010 ICT*, China.

HONORS &AWARDS

- 2013 Manep Internship supported by MANEP program, Switzerland
- 2011 "Excellent thesis for Master Degree" awarded by WUT, Top 5%;
- 2007-2008 Outstanding Graduate awarded by WUT
- 2006-2007 National Scholarship awarded by Ministry of Education of the People's Republic of China, and Outstanding Student awarded by WUT
- 2005-2006 Second-class Scholarship, Outstanding Student awarded by WUT
- 2004-2005 National Scholarship awarded by Ministry of Education of the People's Republic of China, and Outstanding Student awarded by WUT

Contents

Abstract

$EuTiO_3$ (ETO) is a perovskite-type oxide consisting of divalent Eu and tetravalent Ti. Due to Eu^{2+} possessing a half-filled 4*f* shell with a large spin magnetic moment (7 μ_B), ETO is a magnetic material with localized Eu 4*f* electrons, which are related to its giant Seebeck coefficient and considerable thermoelectric performance. Crystalline ETO is isostructural with $SrTiO_3$ (cubic, $Pm\bar{3}m$) on the long-range scale at ambient temperature, but its local structure has a high degree of disorder. In this dissertation, the magnetic Eu^{2+} was partly substituted by isovalent nonmagnetic alkaline-earth metal cations *A* (*A* = Ba^{2+}, Sr^{2+}, Ca^{2+}, and Mg^{2+}). The aims were to synthesize perovskite-type $Eu_{1-x}A_xTiO_{3-\delta}$ solid solutions and investigate their crystal structures, local structures, electronic band structures, thermoelectric properties, and interrelations among them.

All samples were synthesized by using a two-step process including the Pechini method for precursor synthesis and subsequent high-temperature annealing under reducing atmosphere. The combination of crystal structure and transport properties analysis revealed that polycrystalline $Eu_{1-x}A_xTiO_{3-\delta}$ (*A* = Ba^{2+}, Sr^{2+}, Ca^{2+}) solid solutions were successfully synthesized in the full compositional range of $0 \leq x \leq 1$. An exception was the (partial) Mg^{2+} substitution. It was impossible within the used experimental parameters to obtain a single-phase $Eu_{1-x}Mg_xTiO_3$ solid solution, resulting from that the ionic radius of Mg^{2+} is too small to be bonded in an AO_{12} cuboctahedron. In the case of Sr^{2+} substitution, the long-range cubic symmetry was maintained in the entire compositional range due to the virtually equal ionic radii of Sr^{2+} and Eu^{2+}. A minor effect on the electrical conductivity and the *ZT* values had been achieved by the Sr^{2+} substitution in a wide compositional range. Promising thermoelectric results were observed for the Ba^{2+} and Ca^{2+} substituted samples. The partial substitution of Eu^{2+} with Ba^{2+}/Ca^{2+} led to an expansion/contraction of cubic sub-cell volume, resulting in different kinds of lattice defects and local structural distortions. Both Ba^{2+} and Ca^{2+} substitutions increased electrical conductivity, decreased lattice thermal conductivity, and hence improved the *ZT* values. In comparison with Ba^{2+} substitution, the enhanced thermoelectric performance by Ca^{2+} substitution was more pronounced at lower temperatures. Since the ionic radius of Ca^{2+} is smaller than that of Eu^{2+}, the given smaller unit cell induced chemical pressure which facilitated lattice deformations and defect formations (e.g. Eu^{3+}). The resulting impurity levels in the electronic band structure played an important role in the electronic conduction at low temperatures. The pristine ETO sample displayed a glass-like thermal conductivity (κ) at low temperatures, while the Ca^{2+}-rich samples displayed ordinary crystalline κ behavior. The glass-feature of κ was one solid evidence for verifying the local structure disorder of ETO. Due to a large spin moment of Eu^{2+}, magnons as additional heat carriers contributed with a large magnitude to the heat conduction in all Eu^{2+} containing samples at intermediate temperatures. The temperature-independent large Seebeck coefficient below ambient temperature was ascribed to the magnon-drag effect together with the influence of Eu 4*f* hybridization and the local structural disorder.

The influence of Eu^{2+} 4*f* electrons on transport properties was strongly related to crystal structure variations, which was verified through isovalent chemical substitution by *A*-site cations with different ionic radii. The obtained results demonstrated how by invoking "lattice deformation and local disorder" one can manipulate the electronic transport properties and in parallel reduce intrinsic lattice κ of the perovskite-type ETO oxides. The substitution of Eu^{2+} with naturally abundant Ca^{2+} is a promising approach for improving thermoelectric performance and simultaneously reducing the usage of valuable europium.

Zusammenfassung

$EuTiO_3$ (ETO) ist ein perowskitisches Oxid und enthält zweiwertiges Europium und vierwertiges Titan. Die halb gefüllte 4*f*-Schale der Eu^{2+}-Kationen bewirkt ein großes magnetisches Spinmoment (7 μ_B). Die lokalisierten Eu 4*f*-Elektronen begünstigen das Auftreten eines sehr großen Seebeck-Koeffizienten und damit eine nennenswerte thermoelektrische Energieumwandlung. Zudem machen sie ETO zu einem magnetischen Material. Kristallines ETO ist bei Umgebungstemperatur isostrukturell zu $SrTiO_3$ (kubisch, $Pm\bar{3}m$), aber die lokalen Strukturen unterscheiden sich deutlich, wobei ETO ein höheres Maß an Unordnung zeigt. Im Rahmen dieser Dissertation wurden magnetische Eu^{2+}-Kationen teilweise durch nicht-magnetische Erdalkalimetallkationen *A* (*A* = Ba^{2+}, Sr^{2+}, Ca^{2+}, and Mg^{2+}) ersetzt. Perowskitische Mischkristalle $Eu_{1-x}A_xTiO_{3-\delta}$ wurden hergestellt und ihre Kristallstrukturen, lokale Strukturen, elektronischen Bandstrukturen, thermoelektrischen Eigenschaften sowie die Zusammenhänge zwischen diesen untersucht.

Alle Materialien wurden mittels eines zweistufigen Verfahrens synthetisiert. Zunächst wurden Präkursoren per Pechini-Methode hergestellt. Diese wurden anschließend in reduzierender Atmosphäre zu $Eu_{1-x}A_xTiO_{3-\delta}$ umgesetzt. Die gemeinsame Analyse von Kristallstruktur und Transporteigenschaften bestätigte die erfolgreiche Synthese der Mischkristallreihen $Eu_{1-x}A_xTiO_{3-\delta}$ (*A* = Ba^{2+}, Sr^{2+}, Ca^{2+}) im gesamten Zusammensetzungsbereich $0 \leq x \leq 1$. Für Mg^{2+} war dies im getesteten Parameterfenster nicht möglich, da es für eine Platzierung in einem AO_{12} Kuboktaeder zu klein ist. Im Falle der Sr^{2+}-Substitution bleibt aufgrund der nahezu identischen Ionenradien von Sr^{2+} und Eu^{2+} die kubische Kristallstruktur über den gesamten Zusammensetzungsbereich erhalten. Deshalb konnte auch in einem weiten Substitutionsbereich nur ein kleiner Einfluss auf die elektrische Leitfähigkeit und die *ZT*-Werte festgestellt werden. Im Gegensatz hierzu wurden für Ba^{2+}- und Ca^{2+}-substituierte Proben vielversprechende thermoelektrische Ergebnisse beobachtet. Die teilweise Substitution von Eu^{2+} mit Ba^{2+}/Ca^{2+} führte zu einer Ausdehnung/Schrumpfung des Volumens der kubischen Unterzelle. Dies begünstigte das Entstehen von verschiedenen Gitterdefekten und lokalen Strukturverzerrungen. Beide Substitutionen, sowohl mit Ba^{2+} als auch mit Ca^{2+}, erhöhten die elektrische Leitfähigkeit und reduzierten gleichzeitig die thermische Leitfähigkeit des Kristallgitters. Dies führte final zu deutlich verbesserten thermoelektrischen Eigenschaften. Die erzielten Verbesserungen der thermoelektrischen Umwandlung im Vergleich zu ETO war für die Ca^{2+}-Substitution bei niedrigen Temperaturen besonders ausgeprägt, während die Ba^{2+}-Substitution im höheren Temperaturbereich hilfreich war. Der kleinere Ionenradius von Ca^{2+} verglichen mit Eu^{2+} führt zum Vorhandensein von chemischem Druck und gekoppelt zur Entstehung von Gitterverzerrungen und Defekten (z.B. Eu^{3+}). Dadurch entstehen zusätzliche Zustände in der elektronischen Bandstruktur. Diese spielten eine entscheidende Rolle für die gemessene elektrische Leitfähigkeit bei niedrigen und sehr niedrigen Temperaturen. Unsubstituiertes ETO zeigte bei niedrigen Temperaturen eine glasartige thermische Leitfähigkeit (κ), während die calciumreichen Zusammensetzungen ein für kristalline Proben normales Verhalten von κ zeigten. Daher ist die Analyse von κ bei niedriger Temperatur ein starker Nachweis der diskutierten lokalen Unordnung in ETO. Aufgrund des großen magnetischen Spinmoments von Eu^{2+} zeigten alle Eu^{2+}-haltigen Materialien einen zusätzlichen Beitrag zur thermischen Leitfähigkeit durch Magnonen. Dieser war im Bereich der Umgebungstemperatur sogar dominierend. Der unterhalb der Umgebungstemperatur beobachtete nahezu temperaturunabhängige Seebeck-Koeffizient wurde auf den Magnon-Drag-

Effekt und den Einfluss des Eu 4*f*-Hybridisierungszustandes sowie Änderungen der lokalen Unordnung zurückgeführt.

Der Einfluss der Eu 4*f*-Elektronen auf die resultierenden Transporteigenschaften sind stark mit den beobachteten Kristallstrukturänderungen korreliert. Dies konnte durch die angewandte isovalente chemische Substitution des *A*-Seiten-Kations Eu^{2+} mit Kationen verschiedener Größe verifiziert werden. Die erhaltenen Ergebnisse demonstrieren wie Gitterverzerrungen und lokale Unordnung gezielt genutzt werden können um die elektronischen Transporteigenschaften zu beeinflussen und parallel die intrinsische thermische Leitfähigkeit des Kristallgitters in perowskitischem ETO zu reduzieren. Darüber hinaus ist die Substitution von Eu^{2+} durch Ca^{2+} ein erfolgversprechender Ansatz um verbesserte thermoelektrische Umwandlung mit einer nachhaltigeren Verwendung von Europium zu koppeln.

Abbreviations & Symbols

AFM	Antiferromagnetic
adp	Atomic mean square displacement parameter
CB	Conduction band
CIP	Cold isostatic pressing
DFT	Density functional theory
DOS	Electronic density of state
ETO	$EuTiO_3$
ESRF	European Synchrotron Radiation Facility
EDS	Energy dispersive X-ray spectroscopy
EXAFS	Extended X-ray absorption fine structure
ESDs	Estimated standard deviations
ICP-OES	Inductively coupled plasma-optical emission spectrometry
LFA	Laser Flash Analyzer
PDF	Pair distribution function
PPMS	Physical property measurement system
PXRD	Powder X-ray diffraction
PGEC	Phonon glass electron crystal
PF	Power factor
RT	Room temperature
SEM	Scanning electron microscope
SR-PXRD	Synchrotron radiation diffraction
TE	Thermoelectric
UP	Uniaxial pressing
VB	Valence band
XRD	X-ray diffraction
XPS	X-ray photoelectron spectroscopy
ZT	Dimensionless thermoelectric figure of merit
α	Seebeck coefficient
c_V	Isochoric specific heat capacity
c_p	Isobaric specific heat capacity

d	Density of bulk samples
e	Elemental electronic charge
ΔE	Energy gap
η	Thermoelectric conversion efficiency of a TE material
κ	Thermal conductivity
k	Boltzmann constant
L	Lorenz number
Λ	Thermal diffusivity
l	Phonon mean free path
l_e	Mean free path of charge carrier
λ	Wavelength of the incident X-ray beam
m^*	Effective mass of carrier
μ	Mobility of charge carrier
n	Charge carrier concentration
ν	Sound velocity
v_e	Average speed of charge carriers
θ_D	Debye temperature
ρ	Electrical resistivity
σ	Electrical conductivity
T	Absolute temperature
T_c	Critical temperature
T_N	Neél temperature
τ	Phonon relaxation time

Chapter 1 Introduction

Thermoelectricity is an energy conversion technology that directly converts heat into electricity and vice versa. It has numerous advantages, such as noiseless, gas-free emissions, excellent scalability and reliability, and self-sufficiency to enable mobile or remote applications [1–4]. The application of thermoelectric (TE) devices for power generation can be extensive because TE devices can make use of all kinds of heat, e.g. from the sun, radioisotopes, automobiles, industrial sectors, or even the human body, and convert it to electricity [5,6]. For example, TE generators have been used reliably for powering long maintenance-free operation in space missions of NASA for half a century [7,8]. Although the development of thermoelectricity has attracted much attention for decades, it is still on the way to develop superior TE materials. Developing non-toxic and earth-abundant materials with superior TE performance is the first critical step for practical TE application.

1.1 Thermoelectricity background

Thermoelectricity involves three effects: Seebeck effect, Peltier effect, and Thomson effect. The Seebeck effect, which was discovered by Thomas Johann Seebeck in 1821, is the basic principle for TE power generation. It describes that an electric voltage is produced by applying a temperature gradient through a material. When an applied current flows through two different conductors, heat is released at one junction and absorbed at the other junction, thus generating different temperatures at the junctions on each side. This is known as the Peltier effect, which was discovered in 1834 by French physicist Jean Charles Athanase Peltier. It can be used for heating or cooling without combustion or moving parts. The Thomson effect, which was observed by William Thomson Lord Kelvin in 1851, explains the heating or cooling of a current-carrying conductor with a temperature gradient. It is a supplementary description of the Seebeck effect and the Peltier effect. These three effects are different manifestations of one principal physical effect because they essentially relate to the transportation of charge and heat carriers in a material. In this dissertation, the study focuses on the Seebeck effect and related parameters for TE energy generation. The Peltier effect and the Thomson effect will not be further addressed.

1.1.1 State-of-the-art Thermoelectric materials

The TE performance of materials is described by the dimensionless figure of merit value *ZT*, which is defined by the following equation:

$$ZT = \frac{\alpha^2 T}{\rho \kappa} = \frac{\alpha^2 \sigma T}{k} = \frac{PF}{k} T \tag{1-1}$$

where α is the Seebeck coefficient, ρ the electrical resistivity, κ the thermal conductivity, T the absolute temperature, σ the electrical conductivity ($\sigma = \frac{1}{\rho}$), and PF the power factor ($PF = \alpha^2\sigma$). Good TE performance needs high *ZT* values. Although there is no theoretical upper limit for the *ZT*

values, most state-of-the-art TE materials have their maximum *ZT* values between 1 and 2.5, and they mainly include the critical elements such as Te, Pb, Sb, etc., as shown in Fig. 1.1. In the TE community, a *ZT* = 1 is regarded as a performance benchmark for viable TE materials.

The first generation TE materials developed since the 1950s are the classic Bi_2Te_3 [9–11], PbTe [12–14] and Si–Ge alloys [15]. They are recognized as low temperature (T < 500 K), middle temperature, and high temperature (T > 900 K) TE materials, respectively. However, the Bi_2Te_3 and PbTe are unfavorable materials due to the critical elements bismuth, tellurium, and lead. As time goes on, more and more materials are discovered as potential TE materials and have been studied extensively, such as lead-free chalcogenides (e.g., $Cu_2CdSnSe_4$ [16], Cu_2Se [17,18], and SnSe [19,20]), clathrates (e.g., $Sr_8Ga_{16}Ge_{30}$ [21], $Ba_8Ga_{16}Ge_{30}$ [22]), silicides (e.g., Mg_2Si [23], MnSi [24]), zintl phases (e.g., $YbZn_2Sb_2$ [25], $Yb_{14}MnSb_{11}$ [26]), half-heusler (e.g., (Ti,Zr,Hf)NiSn [27,28]), skutterudites (e.g., $CoSb_3$ [29]), and oxides (e.g., $CaMnO_3$ [30], $Ca_3Co_4O_9$ [31], ZnO [32], $SrTiO_3$ [33], Na_xCoO_2 [34] or $Na_xCo_2Co_4$ [35]). Though the discovered *ZT* values of these oxides are smaller than 1, the oxide TE materials are still favored for their potential superiorities such as availability, chemical tunability, regeneratively, and low toxicity [1,36,37].

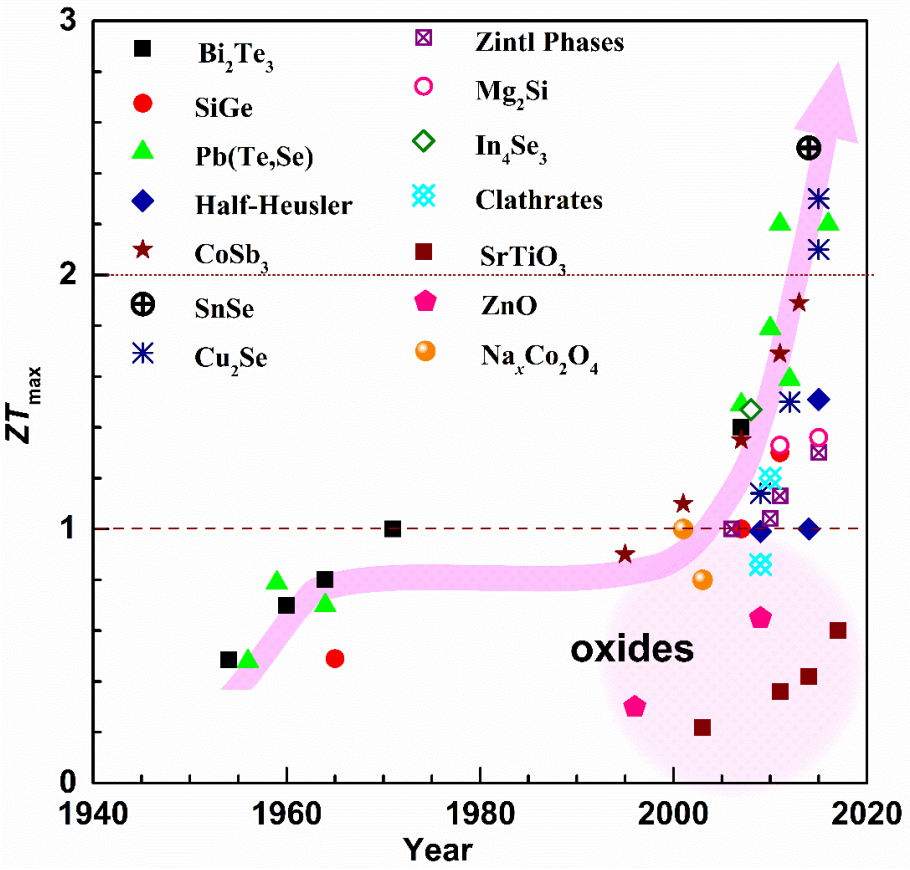

Fig. 1.1 Timeline of the maximum *ZT* value for some representative families of TE materials. Figure modified from references [5,38]. The *ZT* values of $SrTiO_3$ from Ref. [33,39–41], ZnO from Ref. [42,43], and $Na_xCo_2O_4$ from Ref. [34,44].

The *ZT* values mentioned above are the peak values. The average *ZT* value, generally denoted by ZT_{ave} or ZT_m, covers a wide temperature range and is more practical than a peak *ZT* value as to

the thermoelectric conversion efficiency [45]. The conversion efficiency of a TE device is determined by Carnot efficiency and the ZT_m values of the TE materials. Assuming in the condition of negligible contact resistance and an optimized load, the maximum thermoelectric conversion efficiency of a TE material η is expressed as [46]

$$\eta = \left(\frac{T_{hot}-T_{cold}}{T_{hot}}\right)\left[\frac{\sqrt{1+ZT_m}-1}{\sqrt{1+ZT_m}+\left(\frac{T_{cold}}{T_{hot}}\right)}\right], \quad (1\text{-}2)$$

where $\frac{T_{hot}-T_{cold}}{T_{hot}}$ is the Carnot efficiency, the ratio of the temperature difference between the hot and the cold end to the temperature of the hot end.

From the standpoint of efficiency, a ZT_m value (at least) larger than 2 is comparable with other energy generation technologies as shown in Fig. 1.2. As so far, the highest device efficiency was recorded up to 12 % for bismuth telluride/skutterudite segmented modules [47]. Currently, although the *ZT* value of oxides is far smaller than 2 and far from commercial applications, oxide ceramics possess an inherent advantage of high-temperature applicability, which is unreachable for bismuth telluride based materials. An available large temperature gradient between T_{hot} and T_{cold} thereby leads to a high Carnot efficiency, which to a certain extent compensates the low *ZT* value [5,48]. For example, the melting point of $SrTiO_3$ is 2353 K and the reported *ZT* values still show an increasing trend at 1200 K [33]. The melting point of Bi_2Te_3 is 853 K and the peak *ZT* was generally observed at 300 K [140]. Assuming in the condiction of T_{cold} at 273 K and the T_{hot} at 1200 K for $SrTiO_3$ and 300 K for Bi_2Te_3, the Carnot efficiencies of $SrTiO_3$ and Bi_2Te_3 are 77.25 % and 9 %, respectively.

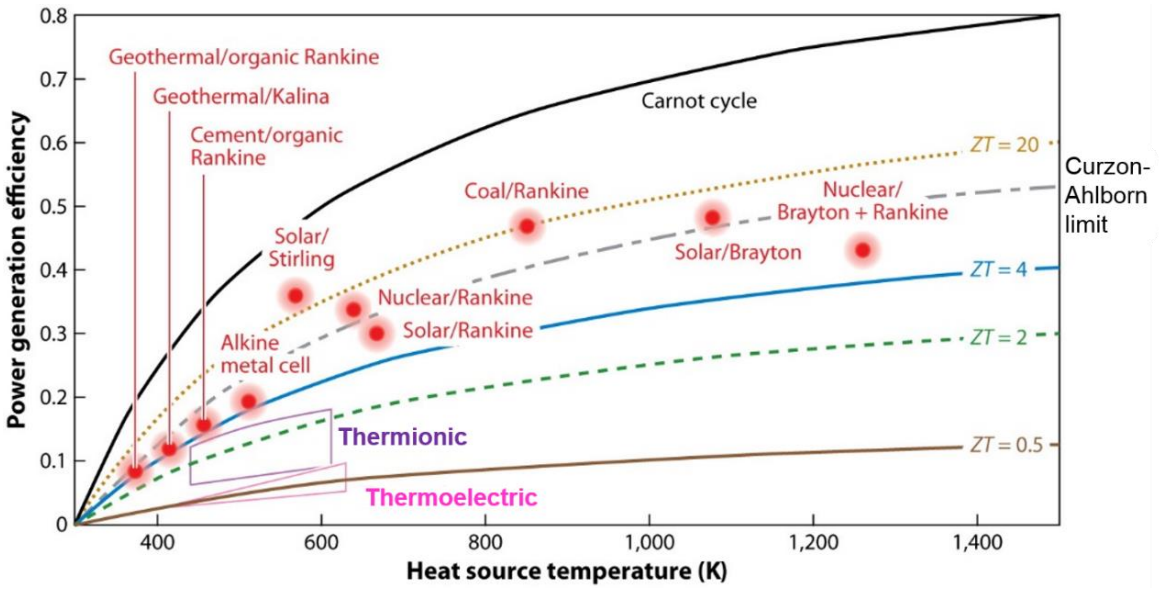

Fig. 1.2 Power generation efficiency as a function of heat source temperature for various representative energy-conversion technologies in the global landscape. The heat sink temperature is set at 300 K. The power generation efficiency of thermoelectric with different *ZT* values is in comparison with the other energy-conversion technologies. Figure adapted from Ref. [49].

The *ZT* value is dictated by three macroscopically measurable transport parameters α, σ, and κ. A simultaneously high σ, large α, and low κ values are required for a high *ZT* value. The ideal TE

material is a so-called "phonon glass electron crystal" (PGEC) material which was coined first by Slack [50]. PGEC materials possess electric properties normally associated with good semiconductor single crystals but the thermal conductivities are similar to that of amorphous materials, which requires independence of electrical and thermal transport. However, the three parameters, α, σ, and κ are strongly intercorrelated in a way that an adjustment to any of the three properties often adversely influences the other properties. For instance, an increase of σ is generally accompanied by a decrease of α and simultaneously an enhancement of κ. The α and σ typically yield an opposite variation tendency as to a function of charge carrier concentration n [51]. Consequently, it is not straightforward to achieve simultaneously a large α and σ. For non-magnetic materials, the κ consists of two main contributions, i.e., $\kappa = \kappa_e + \kappa_l$, where κ_e is electronic thermal conductivity resulting from the contribution of charge carriers and κ_l is lattice thermal conductivity originating from the lattice vibrations (phonons). The κ_e can be estimated via the Wiedemann-Franz relation, $\kappa_e = L\sigma T$, where L is the Lorenz number and whose values depend on the materials. Thus, the increase of σ inevitably causes an increase in κ_e. For magnetic materials, magnons are also heat carriers for thermal conduction and hence an additional magnons contribution κ_m to the total κ has to be considered [52]. Altogether, this is the reason why only a few semiconductors with high ZT values were found until now among a huge number of available semiconductors. In the following sections, the underlying fundamental principles and the interplay of the three parameters are further introduced in detail.

1.2.2 Electronic Transport Properties

1.2.2.1 Electrical Conductivity σ

The electrical conductivity (σ) of a material is given by

$$\sigma = ne\mu \tag{1-3}$$

where n is the charge carrier concentration contributing to the electric current, μ is the mobility of the charge carriers, and e is the elemental electronic charge. Both n and μ are temperature dependent in semiconductors. In a certain case, n follows the Boltzmann distribution $e^{-\frac{\Delta E}{2kT}}$, where ΔE is the energy gap and k is the Boltzmann constant. Thus, n increases exponentially with increasing temperature T [53]. The charge carriers mentioned above mainly involve electrons and holes in semiconductors. A p-type semiconductor is defined when the majority charge carriers are holes and minority charge carriers are electrons. On the contrary, it is an n-type semiconductor.

In view of band theory, the magnitude of n strongly relies on the energy gap ΔE of materials. If the ΔE is so large that only a few electrons or holes can be thermally excited across the gap, it results in a small charge carrier concentration n. The materials are insulators when ΔE is too large for thermal excitation of charge carriers. In contrast, a large n can be obtained when ΔE is small and the thermal excitation is much easier. In a semiconductor, a small band gap (e.g., $\Delta E < 0.5$ eV) [54] can easily arouse the bipolar effect (i.e., the minority carriers begin to counteract the majority carriers and both holes and electrons are responsible for transporting energy), which is detrimental for the TE performance because the bipolar contribution generally decreases α and increases κ. Therefore, an appropriate band gap is very important for obtaining a practicable n value. One guideline stated

that semiconductors with a band gap in the range of $10kT$, where T accounts for the intended operating temperature, can have a good TE performance [55]. Such a band gap size ensures a reasonable value for μ and minimizes the detrimental contributions from the minority carriers to α.

Most of the state-of-the-art TE materials are typically heavily doped degenerate semiconductors with n values in the range of 10^{19} cm^{-3} < n < 10^{21} cm^{-3} as shown in Fig. 1.3 [51]. Experimentally, in general, there are two different ways for adjusting n, extrinsic doping and tuning intrinsic defects [38]. Extrinsic doping, including chemical substitutions to form solid solutions, is a conventional method to adjust n. The intrinsic defects involve a variety of lattice defects, such as vacancies, interstitials, antisites, lattice disorder, and so on. They generally can be manipulated by extrinsic doping or specified experimental conditions. The intrinsic defects play an important role in the adjustment of n in a given material. For instance, a slight oxygen deficiency or excess can result in significantly different $\sigma(T)$ behaviors in perovskite-type oxides such as $SrTiO_{3-\delta}$ [56,57], $CaMnO_{3-\delta}$ [58,59], $LaMnO_{3\pm\delta}$ [60], and $LaCoO_{3\pm\delta}$ [61].

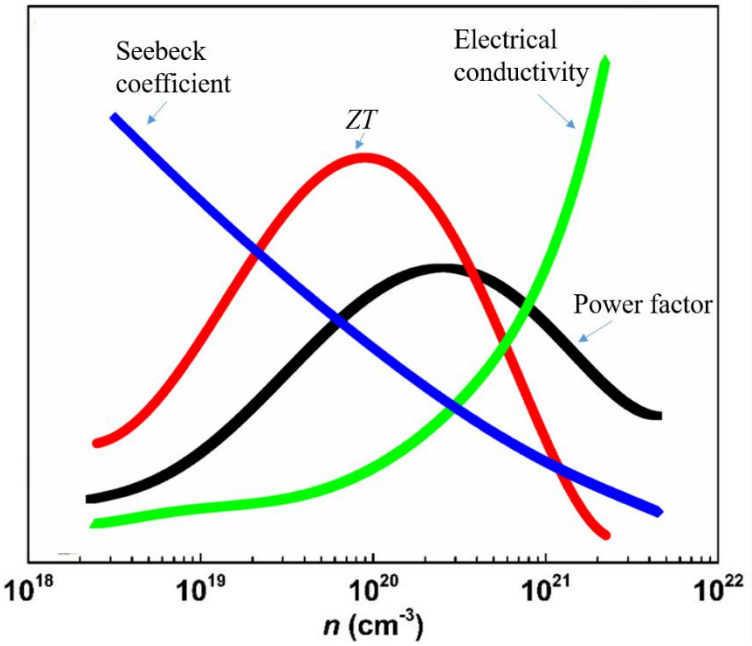

Fig. 1.3 Optimum carrier concentration for *ZT* and *PF*. Good TE materials are typically heavily doped semiconductors with carrier concentrations in the range of $10^{19} < n < 10^{21}$ cm^{-3}. Figure modified from Ref. [51].

The charge carrier mobility μ is determined by the effective carrier mass m^* and relaxation time τ_e (or the mean free path l_e) [53],

$$\mu = \frac{e\tau_e}{m^*} = \frac{el_e}{v_e m^*} \tag{1-4}$$

where l_e and v_e are the mean free path and average speed of the carriers. The μ refers to the average drift velocity of carriers under a constant electric field. The moving carriers are continuously collided or disturbed by lattice vibrations, impurities, defects, etc., and thus change their motion directions irregularly during their movement. This is the reason for carrier scattering. In a solid semiconductor, the associated factors to affect μ are very complex to describe. Many different scattering mechanisms

could affect μ in a semiconductor, for instance, lattice vibrations. The lattice vibrations include acoustical mode and optical mode vibrations. Especially, the nonpolar acoustic vibrational scattering is the dominant scattering mechanism above room temperature in most known good TE materials. The polar optical vibrational scattering plays an important role in charge carrier mobility when the crystal shows ionicity which is usually characterized by the large electronegativity difference among the constituent elements [38]. This is the reason why some oxides have a low μ [5]. The lattice vibrations increase with increasing temperature and consequently result in a stronger scattering effect. Another important scattering effect originates from ionized impurities in extrinsic semiconductors. On the one hand, the impurities provide charge carriers. On the other hand, they act as scattering centers arousing the ionized impurity scattering. The ionized impurities scattering, in contrast, follows the relationship that it decreases with increasing temperature. Therefore, different scattering mechanisms will dominate the charge transfer at different temperature ranges. In a given compositional material, the polycrystalline samples generally possess much lower μ compared with their single-crystal counterparts, which is mainly due to grain boundary scattering. It is evident in nanostructured materials when the grain size becomes comparable to the electron mean free path.

Although both *n* and μ are temperature-dependent parameters, the temperature dependence of *n* is more sensitive and significant compared with μ in a given semiconductor. The *n* increases exponentially with temperature as mentioned above, while many semiconductors follow the $\mu \propto T^{w}$ relationship (e.g., $w = -\frac{3}{2}$ for acoustic vibrational scattering and $w = \frac{3}{2}$ for ionized impurities scattering). The adjustment of *n* is more pronounced than μ utilizing experimental approaches such as doping or chemical substitution. Experimentally, it is more achievable and manageable to improve *ZT* by adjusting *n* through chemical compositional adjustment.

1.2.2.2 Seebeck Coefficient α

The main principle of the Seebeck effect is that a temperature gradient in a conducting material results in charge carrier diffusion, as illustrated in Fig. 1.4. The absolute value of the average velocity of charge carriers is higher on the hot side, leading to effective diffusion towards the cold side. As a result, there is a voltage difference between hot and cold sides, and electricity can be produced in the condition of a closed circuit. The Seebeck effect is described by the Seebeck coefficient (α), also known as thermopower, as the following relation,

$$\alpha = \frac{\Delta U}{\Delta T} \tag{1-5}$$

As the Seebeck effect originates from the charge carrier diffusion, the sign of α indicates the dominant charge carriers in the material. If the α is positive, it means that the major carriers are holes. On the contrary, a negative value of α indicates the electrons as the major carriers. The SI unit of α is Volts per Kelvin (V/K), though it is more often given in microvolts per Kelvin (μV/K). The typical absolute value of $|\alpha|$ ranges from around several mV/K for non-degenerate semiconductors to ~100 μV/K for degenerate semiconductors, and a few μV/K for metals [62].

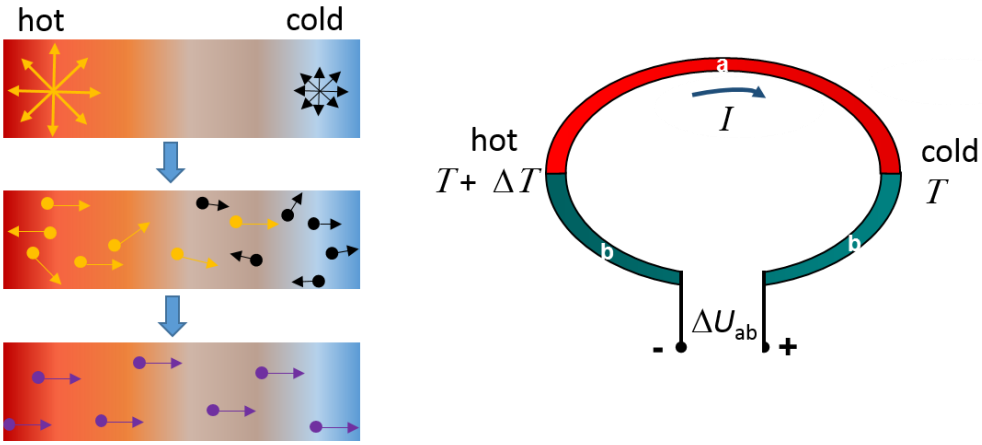

Fig. 1.4 Schematic diagrams of charge carriers diffusion (left) and basic thermocouple consisting of two dissimilar conductors and / or semiconductors *a* and *b* (right).

A high *ZT* requires a high *PF*. As the exponent of α for determining *ZT* in equation (1-1) is two, the improvement of α is generally more important than enhancing the σ. To ensure a large $|\alpha|$, materials should have only a single type of carriers taking part in conduction [51]. Otherwise, mixed electron and hole conduction will lead to both charge carriers moving to the cold end, canceling out the induced Seebeck voltages and resulting in a small $|\alpha|$. For degenerate semiconductors with a single parabolic band (energy-independent scattering approximation), the α is given by [51]:

$$\alpha = \frac{8\pi^2 k^2}{3eh^2} m^* T \left(\frac{\pi}{3n}\right)^{\frac{2}{3}} \tag{1-6}$$

It shows that the α is inversely proportional to *n* and proportional to *m**. The *m** is almost a constant and independent with the variation of *n* in a given material with a parabolic energy band structure. When the energy bands are non-parabolic, the *m** changes with *n* and is more complicated to define [62]. By using a single parabolic band model, the Pisarenko plot can well describe the relationship between α and *n* in some typical TE materials [38,63]. For instance, Fig. 1.5 illustrates the Pisarenko relation of doped *p*-type Bi_2Te_3 at 300 K in the case of $m^* = 0.35\ m_e$.

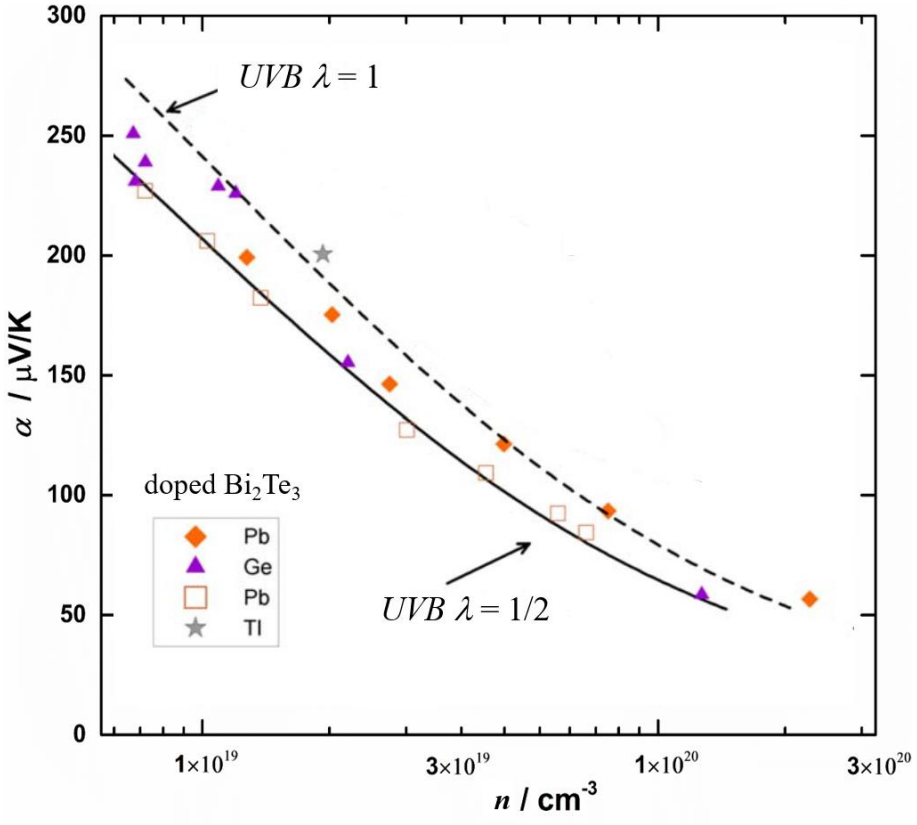

Fig. 1.5 Pisarenko relation (Seebeck coefficient α as a function of carrier concentration n) at 300 K for doped p-type Bi_2Te_3. The lines were calculated using a classical parabolic band with the effective mass for the upper valence bands (*UVB*) and $m^* = 0.35\ m_e$. The scattering exponent λ was assuming to be a polar optical scattering ($\lambda = 0.5$) and ionized impurity scattering ($\lambda = 1$). The figure was extracted and modified from Ref. [64]

The description of α in equation (1-6) is only applicable to a solid in which the Fermi surface consists of a single parabolic band. Actually, the deep understanding of α is still incomplete. Owing to the elusiveness of α, it is often described non-quantitatively as being dependent on the symmetry/asymmetry of the electronic band, or the energy dependence of electronic density of state (DOS) in the range of the Fermi level, or that ‘‘high and steep’’ DOS is required for large $|\alpha|$ [62]. Since the α of materials is rooted in charge carrier entropy of the TE process, the magnitude of α manifests the average entropy of a charge carrier divided by its charge in the limit of thermal equilibrium. To more generally describe the α, an approximate formula derived from the Bethe-Sommerfeld expansion of the Mott relation valid for degenerate statistics and the single band conduction is given in Ref. [5]:

$$\alpha = \frac{\pi^2}{3}\frac{k^2 T}{e}\left[\frac{DOS(E)}{n(E)} + \frac{1}{\mu(E)}\frac{d_\mu(E)}{dE}\right]_{E=E_F} \quad (1\text{-}7)$$

where DOS(E) is the energy-dependent electronic density of states, $n(E)$ is the energy-dependent charge carrier concentration of states, $\mu(E)$ is the energy-dependent carrier mobility, and E_F is the Fermi energy. According to this equation, a larger DOS (E_F) and a stronger $\mu(E)$ can offer a larger $|\alpha|$. Thus, tuning the DOS in the vicinity of the Fermi level is an effective way to adjust α. Recently,

band structure engineering as a popular strategy for improving *ZT* has been implemented in many TE materials, such as band flattening achieved by doping or alloying (e.g., hole-doped PbSe [65,66]) and band convergence in many studied systems (e.g., $PbTe_{1-x}Se_x$ [67], $Mg_2Si_{1-x}Sn_x$ [68], $Bi_{2-x}Sb_xSe_3$ [69]). There are also several other potentially paradigm-changing mechanisms identified for $|\alpha|$ enhancement in the past two decades, e.g., resonant levels [63], energy–filtering effect [75,76], rashba effect [77,78], a large-band degeneracy with an unchanged energy pocket (energy structure valley) [72–74], etc.

It would be more complicated to describe α in a magnetic system because spin adds a new degree of freedom and in principle can be used to improve α. For example, a large $|\alpha|$ discovered in the system of La_xCoO_4 was ascribed to the contribution of spin entropy [70]. The thermal fluctuation of spin moments organizes into spin waves or magnons. Like phonons that can enhance α by phonon-drag effect at low temperatures, magnons also can boost the α by the magnon-electron drag effect [52]. The total α is then the sum of the two contributions electronic α_e and magnonic α_m:

$$\alpha = \alpha_e + \alpha_m \tag{1-8}$$

For the sake of simplicity, the magnons are treated essentially like an ideal gas. Under steady-state conditions of zero electric current, by invoking the conservation law of linear momentum during electron-magnon collisions, the α_m is given by [52,71]

$$\alpha_m = \frac{2}{3}\frac{c_m}{ne}\frac{1}{1+\frac{\tau_{em}}{\tau_m}} \quad , \tag{1-9}$$

where c_m is a magnonic specific heat, *n* is the number density of electrons, τ_{em} is a scattering time of magnon-electron collisions, and τ_m is a total scattering time for magnons representing collisions with defects, electrons, phonons or other magnons. Equation (1-9) shows an inverse relationship between *n* and α_m. An increase of *n* results in a decrease in α_m. Therefore, the density of itinerant electrons *n* is still a key parameter for determining the magnitude of α. Although the role of spin for α has not been widely studied and the mechanisms are not fully understood, the large contribution of spin entropy to α discovered in some systems has attracted much attention [70,79,80]. The spin Seebeck effect has been introduced in the TE community as a new guideline for discovering the next generation of good TE materials [5].

1.2.3 Thermal Transport Properties

Heat energy can be transmitted through solids via various excitations, e.g., lattice waves (phonons), electrical carriers (electrons or holes), spin waves (magnons), electromagnetic waves, and so on [81]. Depending on a simple kinetic theory of thermal conduction in solids, the thermal conductivity is expressed as

$$\kappa = \frac{1}{3}\sum_i c_{Vi} v_i l_i = \frac{1}{3}\sum_i c_{Vi} v_i^2 \tau_i, \tag{1-10}$$

where *i* denotes an excitation, c_V is specific heat capacity, *v* is average velocity, *l* is mean free path, and τ is relaxation time. The lattice thermal conductivity (κ_l), aroused via phonon propagation, is more or less independent of the electrical parameters α and σ. Improving *ZT* by reducing κ_l has been one of the main strategies in recent decades. The c_V is proportional to T^3 at extremely low

temperatures according to Debye T^3 law and saturates at high temperatures (i.e., $T > \theta_D$, where θ_D is the Debye temperature) according to the Dulong–Petit law. The l saturates at extremely low temperatures and follows a T^{-1} rule at high temperatures. As a result, κ_l exhibits strong temperature-dependent behaviors. Experimentally, for ordinary crystalline materials, κ_l increases rapidly following the T^3 tendency at very low temperatures (typically $T < 10$ K) and reaches a maximum value roughly at $T = \frac{\theta_D}{10}$ and then decreases as T^{-1} at high temperatures [81], as illustrated in Fig. 1.6. The relation of $k_l \propto T^{-1}$ is also described as Umklapp processes (U-process), where the dominant thermal conduction mechanism is the phonon-phonon scattering. The κ_l of amorphous materials (i.e., glasses) is obviously different from typical crystalline materials. Amorphous materials display a universal temperature dependence that the κ_l varies as T^2 below 1 K and shows a plateau in the region from 1 K to 10 K and is approximately temperature independent above 100 K [82-84]. The $\kappa(T)$ performance of amorphous materials is apparently distinct from ordinary crystalline materials, apart from the very small κ values.

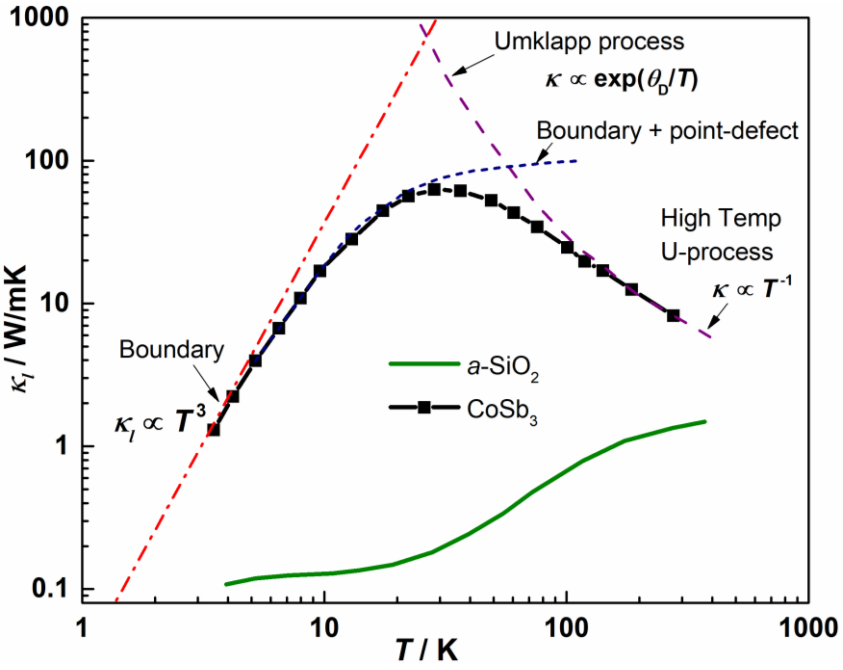

Fig. 1.6 The κ_l as a function of T of a polycrystalline $CoSb_3$ sample from Ref. [85] and an amorphous a-SiO_2 sample from Ref. [86]. The dashed curves refer to the theoretical limits applied on the phonon heat transport by boundary scatterings, a combination of boundary plus point-defect scatterings, and Umklapp scatterings, as arrows pointed, respectively. Figure modified from Ref. [81].

The reduction of κ_l can be achieved by decreasing any of the parameters c_V, v, and l (or τ). The c_V is determined by the crystal structure and the mass of the constituent elements. The v is chiefly determined by the strength of chemical bonds [87]. Consequently, c_V and v are more or less fixed and very difficult to tune in a given material. In contrast, reducing the l (or enhancing τ) is a more effective and manipulable approach to minimize the κ_l. The τ is strongly frequency dependent. The phonon scattering rate can be significantly altered by changing the frequency of phonons as well as the scattering mechanisms as illustrated in Fig. 1.7 The scattering processes involve grain boundary scattering (τ_B), point defect scattering (τ_{PD}), phonon-phonon scattering (U-processes, τ_U), electron-

phonon scattering interaction (τ_{e-p}), and so on [28,73]. The overall scattering processes can be described by taking into account the individual scattering processes by using Matthiessen's rule [34]:

$$\frac{1}{\tau} = \frac{1}{\tau_B} + \frac{1}{\tau_{PD}} + \frac{1}{\tau_U} + \frac{1}{\tau_{e-p}} + \cdots \tag{1-11}$$

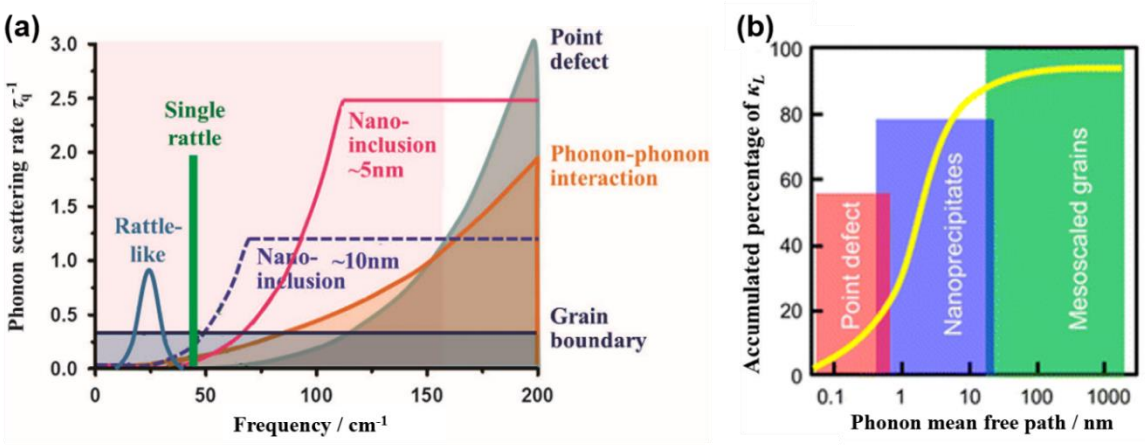

Fig. 1.7 Schematic diagram of the phonon scattering rates as a function of frequency for various mechanisms (a) and the accumulated percentage of κ_l as a function of the phonon mean free path *l* in solid materials (b). Figures adapted from Ref. [73] and [88], respectively.

Applying multiscale phonon scattering can remarkably lower the κ_l. Nanostructuring is one of the most popular and useful approaches to reduce κ_l in TE materials research. Other concepts such as point defects, precipitates, rattling fillers, dislocations, and electron-phonon interactions, etc., are also widely studied for reducing κ_l as schematically shown in Fig. 1.8(a).

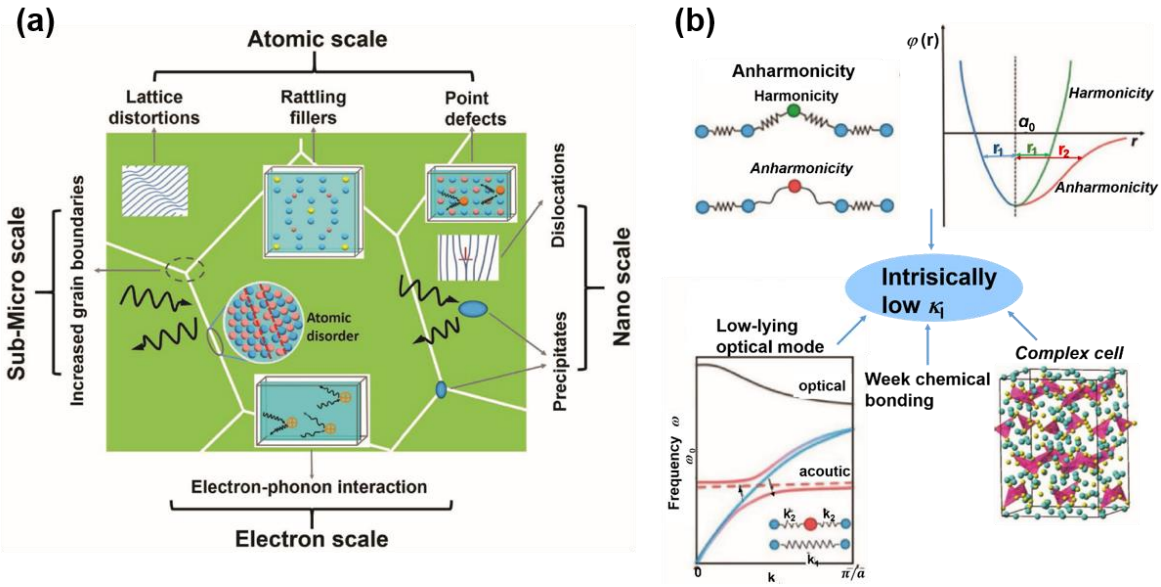

Fig. 1.8 Schematic illustration showing the multiple scattering centers introduced into given materials for reducing the κ_l (a) and several typical strategies for obtaining intrinsically low κ_l. Figures adapted from Ref. [38].

Ideally, the scattering centers should be carefully introduced in a matrix to suppress phonon propagation maximally and concurrently not detriment the electrical transport. However, the introduced multiscale scattering centers more or less affect the electronic transport, e.g., reducing μ and thus σ. The introduction of multiscale scattering centers is relatively coarse engineering compared with manipulation on the atomic level, where the modification of lattice is delicate and the resulting influences are remarkable. It is found that the materials with characteristics of strong anharmonicity [89,90], complex unit cells like Zintl phases [91], and heavy constituent elements like PbTe [92], etc., have intrinsically low κ_l, as shown in Fig. 1.8(b).

1.3 Thermoelectric oxides and $EuTiO_3$

Conventionally, oxides were considered to be poor TE materials because of the low *ZT* values, resulting from the low σ and relatively high κ_l. Yet, the discovery of high TE performance in single-crystal Na_xCoO_2 [34], ZnO [32], and Ruddlesden-Popper homologous series $A_{m+1}B_mO_{3m+1}$ [93–95] is pioneering and enlightening for new TE oxides. Fig. 1.9 illustrates the temperature dependence of *ZT* for some state-of-the-art oxides as thermoelectrics. The high-temperature applicability makes oxides superior due to their broad application temperature range, which leads to a high Carnot efficiency and somewhat compensates the low *ZT*. Perovskite-type titanates with a chemical formula of $ATiO_3$ is one of the most widespread ternary phases of transition metal oxides displaying rich of physical properties, which chiefly result from the partially filled *d* shell of Ti and the highly symmetric crystal structure. Donor-substituted $SrTiO_3$ (STO) is one of the most thoroughly investigated materials in the perovskite family [39–41,96,97]. The record-peak $ZT > 0.6$ at 1000–1100 K was obtained in La-Nb-substituted STO bulk materials [41]. $ATiO_3$ as an important family of thermoelectric oxides is seen as a promising alternative to intermetallic and alloys-based thermoelectrics due to their high-temperature ($T > 1000$ *K*) applicability and considerable TE performance.

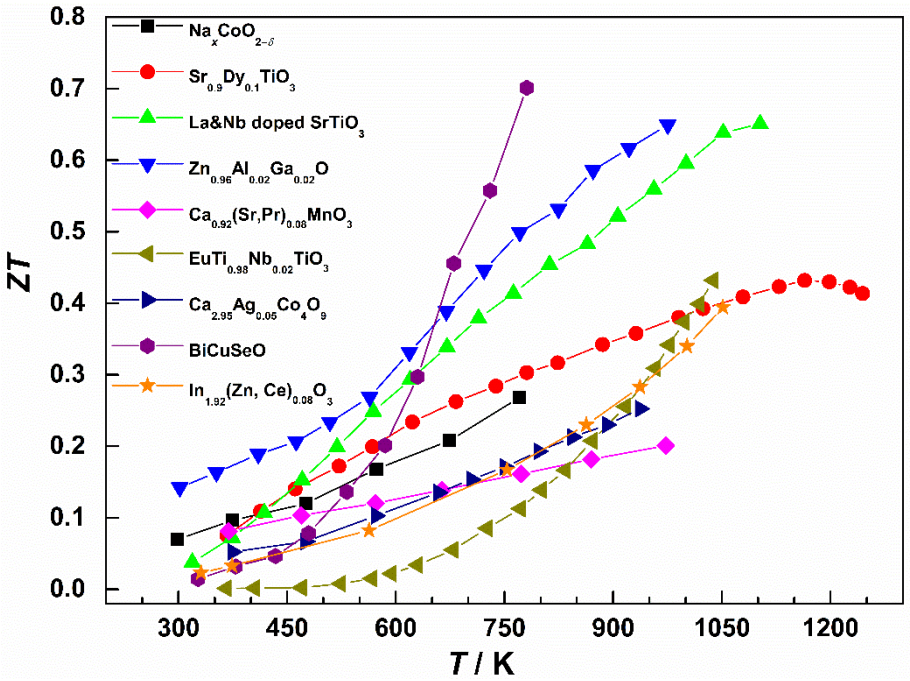

Fig. 1.9 Temperature dependence of *ZT* for several representative state-of-the-art thermoelectric polycrystalline oxides: $Na_xCoO_{2-\delta}$ [34], $Sr_{0.9}Dy_{0.1}TiO_3$ [33], La & Nb doped $SrTiO_3$ [41], $Zn_{0.96}Al_{0.02}Ga_{0.02}O$ [42], $Ca_{0.92}(Sr,Pr)_{0.08}MnO_3$ [98], $EuTi_{0.98}Nb_{0.02}O_3$ [99], $Ca_{2.95}Ag_{0.05}Co_4O_9$ [100], BiCuSeO [101], $In_{1.92}(Zn, Ce)_{0.08}O_3$ [102].

Europium (Eu), being a member of the lanthanide series with atomic number 63, can have the oxidation states +2 and +3. The commonly used europium oxide is trivalent Eu_2O_3 rather than EuO in laboratories due to its relatively higher stability in air. As one of the rarest rare earth elements, Eu is used as fluorescent and phosphor in color cathode-ray tubes and liquid-crystal displays, wildly employed in lamps, television, computer, lasers, and optical-electronics [103,104]. The relatively low abundance and high demand are making Eu extremely valuable. For instance, the prices of Eu_2O_3 (*REacton*®, 99.9%)[1] and $SrCO_3$ (99.99%)[2] per 100 grams are 1074 €and 291 €, respectively.

Perovskite-type $EuTiO_3$ (ETO) is seen as a sister compound with STO because they have almost identical crystal structure at ambient temperature and many physical properties in common. ETO has received much less attention for TE investigations compared to STO. One reason could be owing to its expensive resource of Eu and another reason could be critical conditions required for ETO synthesis. STO-based compounds can be obtained under an air atmosphere with different synthesis methods such as solid-state reaction [105], many different soft-chemistry methods [1,106,107], etc. While, the ETO has to be synthesized under a strongly reducing atmosphere, otherwise the pyrochlore-type phase of $Eu_2Ti_2O_7$ will be obtained. Owing to its relative stability and cost-efficiency, Eu_2O_3 as one of the starting chemical resources is generally used for ETO synthesis. While Eu_2O_3 is insoluble in water and thus solid-state reaction is the most common method for the ETO compound synthesis [99,108,109]. In this dissertation, ETO is chosen as a pristine compound

[1] *https://www.alfa.com/en/catalog/011300/*

[2] *https://www.alfa.com/en/catalog/035793/*

and substituted with alkaline-earth elements. The crystal structure, phase transitions, electronic band structure, and related physical properties of ETO will be introduced in what follows.

The ETO possesses a perovskite-type structure with Eu^{2+} cation in 12-fold cuboctahedral coordination and Ti^{4+} cation in 6-fold octahedral coordination surrounded by O^{2-} as shown in Fig. 1.10. The infinite corner-sharing octahedral network resulting in a high symmetry of the perovskite-type structure. ETO and STO are isostructural (cubic, space group $Pm\bar{3}m$) at room temperature [111] because Eu^{2+} and Sr^{2+} have identical ionic radii (ionic radii $r(Eu^{2+})$ = 1.58 Å and $r(Sr^{2+})$ = 1.58 Å) [114] in a 12-fold coordination leading to nearly identical unit cell parameters.

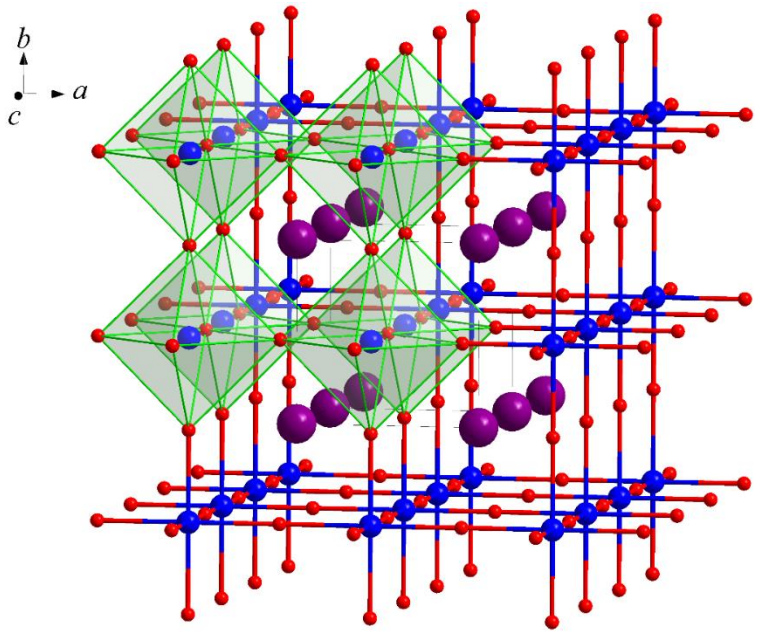

Fig. 1.10 Section of the crystal structure of cubic perovskite-type $EuTiO_3$. The purple spheres are Eu^{2+}, the blue spheres are Ti^{4+}, and the red spheres are O^{2-}. The TiO_6 octahedra are filled in light green.

The well-known perovskite-type STO is usually introduced when addressing about ETO [110–113]. Unlike the well-recognized phase transition of STO from cubic $Pm\bar{3}m$ to tetragonal $I4/mcm$ at around 110 K [115], however, the phase transitions of ETO are still controversial. The reported critical temperature T_c of ETO varied from 160 K to 300 K depending on the applied experimental techniques. Most reports located T_c at 282 ± 5 K using specific heat [110,116], thermal expansion [117], inelastic X-ray scattering [118], and resonant ultrasound spectroscopy measurements [119]. By synchrotron powder X-ray diffraction lower values of $T_c \approx 235$ K [120] and 160 K [121] were found. Bessas et al. [122] did not even detect a direct phase transition but the phenomenon of Eu delocalization was observed on thorough structural studies using complementary techniques. Regarding such a large variation of the observed T_c, many different interpretations were given for this phenomenon. The impurities such as Eu^{3+} and oxygen vacancies were associated with T_c variation [122,123]. ETO was proposed to be an intrinsically disordered system in which the structure itself is willing to form nanodomains in the order of ~ 20 Å and a disorder-order transition takes place at ~ 235 K [120]. Bessas et al. [122] stated that the bulk ETO has the characteristic of lattice dynamical instabilities mainly originating from the Eu atomic delocalization. According to these different characterizations, it suggests that the description of the structural phase-transition

mechanism might be incomplete. The crystal structure of ETO seems to be in a special case of "long-range order but local disorder".

Both ETO and STO have a similar fundamental band gap with similar magnitude [111]. The filled oxygen 2*p* states contribute mainly to the valence band and the conduction band consists predominantly of empty Ti 3*d* states. However, the major difference is the presence of narrow localized Eu 4*f* levels in ETO, as shown in Fig. 1.11. Owing to the presence of Eu 4*f* states located above the O 2*p* states, the Fermi level shifts resulting in some reduction of the band gap. The band gaps are roughly determined at 0.96 eV and 3.25 eV for ETO [124] and STO [125], respectively.

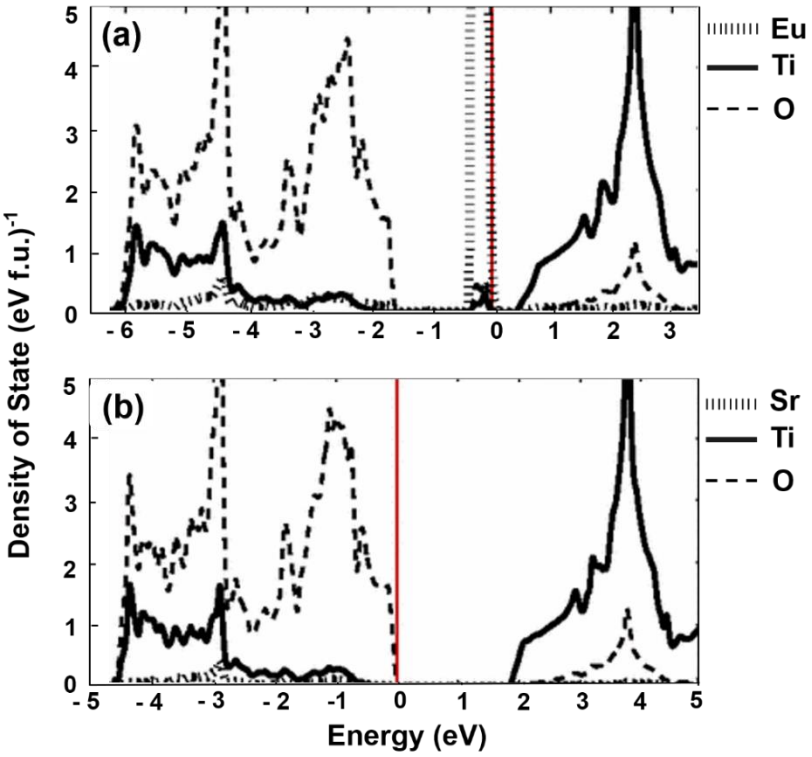

Fig. 1.11 Approximated DOS of (a) $EuTiO_3$ and (b) $SrTiO_3$. The red lines represent the position of the Fermi level. Figures modified from Ref. [111].

ETO contains divalent europium and tetravalent titanium and Eu^{2+} possesses a half-filled 4*f* shell with large magnetic spin moments (7 μ_B) [111,124]. It is a well-known G-type antiferromagnetic magnetic material below Neél temperature (T_N = 5.3 K) [126]. The interest in this material is ever increasing since ETO has displayed a number of fascinating physical properties, such as anomalous Hall effect [127,128], a crossover from negative to positive magnetostriction [129], weak dynamical magnetism at high temperatures [130], giant spin-lattice coupling [111], the magnetodielectric effect [131], the giant magnetocaloric effect [116]. Some substituted or doped ETO compounds, e.g. $Eu_{0.5}Ba_{0.5}TiO_3$ as a multiferroic material with a permanent electric dipole moment [132], could be promising candidates for novel functionalities [133,134]. Although ETO is always famous for its magnetic properties, it also could be a potential promising thermoelectric material due to its enormous Seebeck coefficient and considerable electrical conductivity [99].

1. 4 Research Motivations, Aims, and Objectives

ETO has some superiorities originating from Eu^{2+} compared with STO. ETO has a half-filled Eu 4*f* shell and seven electrons in a high-spin state ($S = 7/2$). Though the contribution of spin to TE is not yet well studied in the ETO system, it was proven that the spin entropy of Co ions induces large $|\alpha|$ in $Na_xCo_2O_4$ [51,70]. Spin acts like discrete magnetic moments carried either by delocalized conduction electrons or by the core electrons on fixed atoms [52]. Unlike the electron charge, spin is not conserved. The net total spin of a system can increase or decrease. Spin adds a new degree of freedom to the TE materials and the effect of spin to TE properties is unpredictable. In principle, spin can be used to improve *ZT* values. Thus, a new paradigm for seeking good TE materials is that thermoelectrics needs a "spin", and the emerging roles of spin and orbital states were proposed for developing next-generation TE materials [5]. On the other hand, the localized Eu^{2+} 4*f* electrons near the Fermi level form a large and steep DOS, which was believed to be responsible for the large $|\alpha|$ of ETO [99,108,113]. Besides, as mentioned before, semiconductors with a band gap in the range of $10kT$ can provide good TE performance. According to the discovered band gap of ETO (0.96 eV), it is implying that ETO could display good TE performance when T is in the range of 1000 K < T < 1200 K, where $10kT$ is 0.86 ~ 1 eV. The high-spin state, large and steep DOS, and suitable band gap of ETO suggest that ETO-based materials can be promising potential TE candidate materials.

Crystalline ETO is isostructural with $SrTiO_3$ (cubic, $Pm\bar{3}m$) on the long-range scale at ambient temperature, but its local structure has a high degree of disorder. The intrinsic structural disorder is expected to profoundly influence the low-temperature electric properties and thermal conductivity. This dissertation aims to expose the alteration of the crystal structure, local structural disorder, and TE properties through chemical substitutions and uncover the interrelation between the crystal structure and transport properties of ETO. Chemical substitution with the alkaline-earth metal cations (Ba^{2+}, Sr^{2+}, Ca^{2+}, and Mg^{2+}) at Eu-site is considered to be an ideal model system to implement this research. At first, the alkaline-earth cations are divalent which is isovalent to Eu^{2+} in the perovskite structure. Isovalent chemical substitution is expected to only modify the crystal structure but not introduce additional charge carries. Secondly, the chosen substituted cations, expect for Sr^{2+}, have different ionic radii compared with Eu^{2+} in the perovskite-type structure. A gradual change of unit cell volume and Eu-Eu distance in the lattice is expected to verify the theoretical prediction that the localized Eu 4*f* levels can be broadened or narrowed during alteration of the orbital overlap. The corresponding DOS and electric properties will be modified. Besides, alkaline-earth metal cations are nonmagnetic. Magnetic effects to TE properties might be exposed by means of Eu^{2+} dilution during substitution. Last but not the least, the chosen alkaline-earth elements are naturally abundant as listed in Table 1.1 [135, 139]. In particular, Ca^{2+} and Mg^{2+} are nontoxic. Seeking environmentally friendly and sustainable thermoelectric materials has always been one of the research targets.

Goldschmidt's empirical substitution rule is a very useful standard for the prediction of perovskite structures and stability through Goldschmidt's tolerance factor *t* calculation. Perovskite-type compounds generally have *t* values in the range of $0.7 < t < 1.1$ [136,137]. In an ideal cubic perovskite structure, *t* equals 1. Real structures coming closest to 1 are STO and ETO ($t = 1.002$). However, this *t* range is only a prerequisite for the formation of perovskites, but not a sufficient condition. For example, the *t* values of $Eu_{1-x}A_xTiO_3$ (A = Mg^{2+}, Ca^{2+}, Sr^{2+}, Ba^{2+}) are calculated as shown in Fig. 1. 12. The formation of perovskite-type $Eu_{1-x}A_xTiO_3$ (A = Ca^{2+}, Sr^{2+}, Ba^{2+}) solid solutions anticipated for the entire range of compositions $0 \le x \le 1$ is reasonable due to the fact that the end compositions $ATiO_3$ (A = Ca^{2+}, Sr^{2+}, Ba^{2+}) are perovskite-type structures. The $MgTiO_3$

compound possesses ilmenite-type structure but not perovskite-type structure [138]. The ionic radius of Mg^{2+} is considerably smaller than the ionic radii of Ca^{2+}, Sr^{2+}, and Ba^{2+}, and much closer to the ionic radius of Ti^{4+}. Supposing the ionic radius of Mg^{2+} in perovskite structure is 1.03 Å which is the ionic radius with 8-fold coordination, then the calculated *t* value is 0.81 which is in the *t* range of perovskite-type structure. However, in fact, it is not as demonstrated by the ilmenite-type structure of $MgTiO_3$. A question is whether it is possible to synthesize single-phase $Eu_{1-x}Mg_xTiO_3$ solid solutions with partial Mg^{2+} substitution. If yes, how much amount of the Mg^{2+} can be substituted in $EuTiO_3$ matrix? Based on all considerations mentioned above, the alkaline-earth metal substituted ETO was subjected to this research.

Table 1.1 The basic parameters of the elements of perovskite-type $Eu_{1-x}A_xTiO_{3-\delta}$ solid solutions: oxidation state (*OS*), electron configuration of the outermost shell of the ions (*EC*), coordination number (*CN*), ionic radius (*R*), relative atomic mass (M_{atomic}) [139] , and abundance of the element in the earth (*Abun.*). (* the value was extrapolated from the data given in literature [114])

Element	Eu		Mg	Ca	Sr	Ba	Ti	O
OS	+2	+3	+2	+2	+2	+2	+4	-2
EC	$4f^7$	$4f^6$	$2p^6$	$3p^6$	$4p^6$	$5p^6$	$3p^6$	$2p^6$
CN	12	12	12	12	12	12	6	2
R (Å)	1.58*	1.43*	1.35*	1.48	1.58	1.75	0.745	1.21
M_{atomic} (g/mol)	151.964		24.305	40.078	87.62	137.327	47.867	15.9994
Abun. (%)	10^{-5}		1.94	3.39	0.01	0.03	0.41	49.4

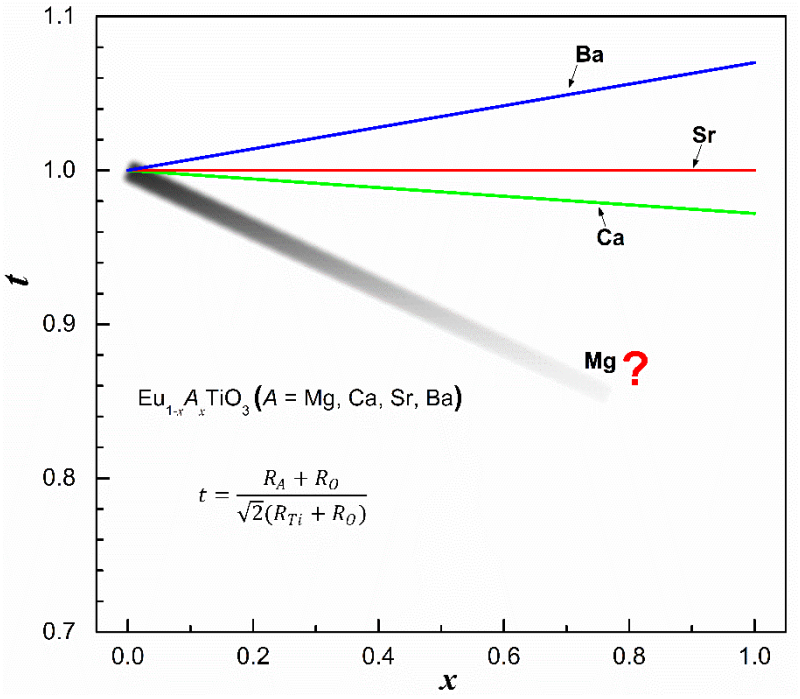

Fig. 1.12 Goldschmidt tolerance factor *t* as a function of substitution fraction *x*. R_A, R_{Ti}, and R_O are ionic radii of *A*-site cations, Ti^{4+} cation, and O^{2-} anion, respectively. Inset table is crystal ionic radii of *A*-site ions in $Eu_{1-x}A_xTiO_3$. EC and CN denote the electron configuration and coordination number, respectively.

References

[1] A.V. Kovalevsky, M.H. Aguirre, S. Populoh, S.G. Patrício, N.M. Ferreira, S.M. Mikhalev, D.P. Fagg, A. Weidenkaff, J.R. Frade, Designing strontium titanate-based thermoelectrics: insight into defect chemistry mechanisms, *Journal of Materials Chemistry A* 5 (2017) 3909–3922.

[2] D.M. Rowe, Thermoelectrics handbook: macro to nano, *CRC press*, 2005.

[3] D.M. Rowe, Modules, systems, and applications in thermoelectrics, *CRC press*, 2012.

[4] W. He, G. Zhang, X. Zhang, J. Ji, G. Li, X. Zhao, Recent development and application of thermoelectric generator and cooler, *Applied Energy* 143 (2015) 1–25.

[5] J. He, T.M. Tritt, Advances in thermoelectric materials research: Looking back and moving forward, *Science* 357 (2017) eaak9997

[6] L.C. Ding, A. Akbarzadeh, L. Tan, A review of power generation with thermoelectric system and its alternative with solar ponds, *Renewable and Sustainable Energy Reviews* 81 (2018) 799–812.

[7] D.M. Rowe, Applications of nuclear-powered thermoelectric generators in space, *Applied Energy* 40 (1991) 241–271

[8] L.A. Fisk, Journey into the unknown beyond, *Science* 309 (2005) 2016–2017.

[9] S. Shigetomi, S. Mori, Electrical properties of Bi_2Te_3, *Journal of the Physical Society of Japan* 11 (1956) 915–919.

[10] N.E. Lindenblad, Thermoelectric elements and materials, *United States Patents*, (1956) 2758146.

[11] H.J. Goldsmid, R.W. Douglas, The use of semiconductors in thermoelectric refrigeration, *British Journal of Applied Physics* 5 (1954) 386.

[12] T.C. Harman, D.L. Spears, M.J. Manfra, High thermoelectric figures of merit in PbTe quantum wells, *Journal of Electronic Materials* 25 (1996) 1121–1127.

[13] A.L. Eiss, Thermoelectric bonding study, *phase II SUMMARY report* (1966).

[14] R.R. Heikes, R.W. Ure, Thermoelectricity: science and engineering, *Interscience Publishers*, 1961.

[15] J.P. Dismukes, L. Ekstrom, E.F. Steigmeier, I. Kudman, D.S. Beers, Thermal and electrical properties of heavily doped Ge-Si alloys up to 1300 K, *Journal of Applied Physics* 35 (1964) 2899–2907.

[16] M.-L. Liu, I.-W. Chen, F.-Q. Huang, L.-D. Chen, Improved thermoelectric properties of Cu-doped quaternary chalcogenides of $Cu_2CdSnSe_4$, *Advanced Materials* 21 (2009) 3808–3812.

[17] H. Liu, X. Yuan, P. Lu, X. Shi, F. Xu, Y. He, Y. Tang, S. Bai, W. Zhang, L. Chen, Y. Lin, L. Shi, H. Lin, X. Gao, X. Zhang, H. Chi, C. Uher, Ultrahigh Thermoelectric Performance by Electron and Phonon Critical Scattering in $Cu_2Se_{1-x}I_x$, *Advanced Materials* 25 (2013) 6607–6612.

[18] L. Yang, Z.-G. Chen, G. Han, M. Hong, Y. Zou, J. Zou, High-performance thermoelectric Cu_2Se nanoplates through nanostructure engineering, *Nano Energy* 16 (2015) 367–374.

[19] L.-D. Zhao, S.-H. Lo, Y. Zhang, H. Sun, G. Tan, C. Uher, C. Wolverton et al., Ultralow thermal conductivity and high thermoelectric figure of merit in SnSe crystals, *Nature* 508 (2014) 373.

[20] L.D. Zhao, G. Tan, S. Hao, J. He, Y. Pei, H. Chi, H. Wang, S. Gong, H. Xu, V.P. Dravid, C. Uher. G.J. Snyder, C. Wolverton, M.G. Kanatzidis, Ultrahigh power factor and thermoelectric performance in hole-doped single-crystal SnSe, *Science* (2015) aad3749.

[21] G.S. Nolas, T.J.R. Weakley, J.L. Cohn, R. Sharma, Structural properties and thermal conductivity of crystalline Ge clathrates, *Physical Review B* 61 (2000) 3845.

[22] A. Saramat, G. Svensson, A.E.C. Palmqvist, C. Stiewe, E. Mueller, D. Platzek, S.G.K. Williams, D.M. Rowe, J.D. Bryan, G.D. Stucky, Large thermoelectric figure of merit at high temperature in Czochralski-grown clathrate $Ba_8Ga_{16}Ge_{30}$, *Journal of Applied Physics* 99 (2006) 23708.

[23] S.K. Bux, M.T. Yeung, E.S. Toberer, G.J. Snyder, R.B. Kaner, J.-P. Fleurial, Mechanochemical synthesis and thermoelectric properties of high quality magnesium silicide, *Journal of Materials Chemistry* 21 (2011) 12259–12266.

[24] W. Luo, H. Li, Y. Yan, Z. Lin, X. Tang, Q. Zhang, C. Uher, Rapid synthesis of high thermoelectric performance higher manganese silicide with in-situ formed nano-phase of MnSi, *Intermetallics* 19 (2011) 404–408.

[25] F. Gascoin, S. Ottensmann, D. Stark, S.M. Haïle, G.J. Snyder, Zintl phases as thermoelectric materials: tuned transport properties of the compounds $Ca_xYb_{1-x}Zn_2Sb_2$, *Advanced functional materials* 15 (2005) 1860–1864.

[26] E.S. Toberer, C.A. Cox, S.R. Brown, T. Ikeda, A.F. May, S.M. Kauzlarich, G.J. Snyder, Traversing the metal-insulator transition in a Zintl phase: rational enhancement of thermoelectric efficiency in $Yb_{14}Mn_{1-x}Al_xSb_{11}$, *Advanced Functional Materials* 18 (2008) 2795–2800.

[27] S. Populoh, M.H. Aguirre, O.C. Brunko, K. Galazka, Y. Lu, A. Weidenkaff, High figure of merit in (Ti, Zr, Hf)NiSn half-Heusler alloys, *Scripta Materialia* 66 (2012) 1073–1076.

[28] W. Xie, A. Weidenkaff, X. Tang, Q. Zhang, J. Poon, T.M. Tritt, Recent advances in nanostructured thermoelectric half-Heusler compounds, *Nanomaterials* 2 (2012) 379–412.

[29] Y. Tang, Z.M. Gibbs, L.A. Agapito, G. Li, H.-S. Kim, M.B. Nardelli, S. Curtarolo, G.J. Snyder, Convergence of multi-valley bands as the electronic origin of high thermoelectric performance in $CoSb_3$ skutterudites, *Nature Materials* 14 (2015) 1223.

[30] L. Bocher, M.H. Aguirre, D. Logvinovich, A. Shkabko, R. Robert, M. Trottmann, A. Weidenkaff, $CaMn_{1-x}Nb_xO_3$ ($x \leq 0.08$) Perovskite-Type Phases As Promising New High-Temperature n-Type Thermoelectric Materials, *Inorganic Chemistry* 47 (2008) 8077–8085.

[31] K. Koumoto, R. Funahashi, E. Guilmeau, Y. Miyazaki, A. Weidenkaff, Y. Wang, C. Wan, Thermoelectric ceramics for energy harvesting, *Journal of the American Ceramic Society* 96 (2013) 1–23.

[32] N. Vogel-Schäuble, Y.E. Romanyuk, S. Yoon, K.J. Saji, S. Populoh, S. Pokrant, M.H. Aguirre, A. Weidenkaff, Thermoelectric properties of nanostructured Al-substituted ZnO thin films, *Thin Solid Films* 520 (2012) 6869–6875.

[33] A.V. Kovalevsky, A.A. Yaremchenko, S. Populoh, P. Thiel, D.P. Fagg, A. Weidenkaff, J.R. Frade, Towards a high thermoelectric performance in rare-earth substituted $SrTiO_3$: effects provided by strongly-reducing sintering conditions, *Physical Chemistry Chemical Physics* 16 (2014) 26946–26954.

[34] K. Fujita, T. Mochida, K. Nakamura, High-temperature thermoelectric properties of $Na_xCoO_{2-\delta}$ single crystals, *Japanese Journal of Applied Physics* 40 (2001) 4644.

[35] X. Tang, T.M. Tritt, Overview of thermoelectric sodium cobaltite: $Na_xCo_2O_4$, *Journal of the South Carolina Academy of Science* 6 (2008) 2.

[36] K. Koumoto, I. Terasaki, R. Funahashi, Complex oxide materials for potential thermoelectric applications, *MRS Bulletin* 31 (2006) 206–210.

[37] J.W. Fergus, Oxide materials for high temperature thermoelectric energy conversion, *Journal of the European Ceramic Society* 32 (2012) 525–540.

[38] T. Zhu, Y. Liu, C. Fu, J.P. Heremans, J.G. Snyder, X. Zhao, Compromise and synergy in high-efficiency thermoelectric materials, *Advanced Materials* 29 (2017) 1605884.
[39] H.C. Wang, C.L. Wang, W.B. Su, J. Liu, Y. Sun, H. Peng, L.M. Mei, Doping effect of La and Dy on the thermoelectric properties of $SrTiO_3$, *Journal of the American Ceramic Society* 94 (2011) 838–842.
[40] H. Muta, K. Kurosaki, S. Yamanaka, Thermoelectric properties of rare earth doped $SrTiO_3$, *Journal of Alloys and Compounds* 350 (2003) 292–295.
[41] J. Wang, B.-Y. Zhang, H.-J. Kang, Y. Li, X. Yaer, J.-F. Li, Q. Tan, Sh. Zhang, G. Fan, Ch. Liu, L. Miao, D. Nan, T. Wang, L.D. Zhao, Record high thermoelectric performance in bulk $SrTiO_3$ via nano-scale modulation doping, *Nano Energy* 35 (2017) 387–395.
[42] M. Ohtaki, K. Araki, K. Yamamoto, High thermoelectric performance of dually doped ZnO ceramics, *Journal of Electronic Materials* 38 (2009) 1234–1238.
[43] M. Ohtaki, T. Tsubota, K. Eguchi, H. Arai, High-temperature thermoelectric properties of $(Zn_{1-x}Al_x)O$, *Journal of Applied Physics* 79 (1996) 1816–1818.
[44] M. Ito, T. Nagira, D. Furumoto, S. Katsuyama, H. Nagai, Synthesis of $Na_xCo_2O_4$ thermoelectric oxides by the polymerized complex method, *Scripta Materialia* 48 (2003) 403–408.
[45] G.S. Nolas, J. Sharp, J. Goldsmid, Thermoelectrics: basic principles and new materials developments, *Springer Science & Business Media*, 2013.
[46] X.F. Zheng, C.X. Liu, Y.Y. Yan, Q. Wang, A review of thermoelectrics research–Recent developments and potentials for sustainable and renewable energy applications, *Renewable and Sustainable Energy Reviews* 32 (2014) 486–503.
[47] Q. Zhang, J. Liao, Y. Tang, M. Gu, C. Ming, P. Qiu, S. Bai, X. Shi, C. Uher, L. Chen, Realizing a thermoelectric conversion efficiency of 12 % in bismuth telluride/skutterudite segmented modules through full-parameter optimization and energy-loss minimized integration, *Energy & Environmental Science* 10 (2017) 956–963.
[48] J. He, Y. Liu, R. Funahashi, Oxide thermoelectrics: The challenges, progress, and outlook, *Journal of Materials Research* 26 (2011) 1762–1772.
[49] A. Shakouri, Recent developments in semiconductor thermoelectric physics and materials, *Annual Review of Materials Research* 41 (2011) 399–431.
[50] G.A. Slack, New materials and performance limits for thermoelectric cooling, *CRC handbook of thermoelectrics* (1995) 407–440.
[51] G.J. Snyder, E.S. Toberer, Complex thermoelectric materials, in: Materials For Sustainable Energy: A Collection of Peer-Reviewed Research and Review Articles from Nature Publishing Group, *World Scientific*, 2011, pp. 101–110.
[52] K. Vandaele, S.J. Watzman, B. Flebus, A. Prakash, Y. Zheng, S.R. Boona, J.P. Heremans, Thermal spin transport and energy conversion, *Materials Today Physics* 1 (2017) 39–49.
[53] P.F. Weller, Solid state chemistry and physics, *M. Dekker*, 1973.
[54] J.J. Gong, A.J. Hong, J. Shuai, L. Li, Z.B. Yan, Z.F. Ren, J.-M. Liu, Investigation of the bipolar effect in the thermoelectric material $CaMg_2Bi_2$ using a first-principles study, *Physical Chemistry Chemical Physics* 18 (2016) 16566–16574.
[55] G.D. Mahan, Figure of merit for thermoelectrics, *Journal of Applied Physics* 65 (1989) 1578–1583.
[56] C. Yu, M.L. Scullin, M. Huijben, R. Ramesh, A. Majumdar, The influence of oxygen deficiency on the thermoelectric properties of strontium titanates, *Applied Physics Letters* 92 (2008) 92118.

[57] N.-H. Chan, R.K. Sharma, D.M. Smyth, Nonstoichiometry in $SrTiO_3$, *Journal of The Electrochemical Society* 128 (1981) 1762–1769.

[58] P. Thiel, J. Eilertsen, S. Populoh, G. Saucke, M. Döbeli, A. Shkabko, L. Sagarna, L. Karvonen, A. Weidenkaff, Influence of tungsten substitution and oxygen deficiency on the thermoelectric properties of $CaMnO_{3-\delta}$, *Journal of Applied Physics* 114 (2013) 243707.

[59] L. Bocher, M.H. Aguirre, R. Robert, D. Logvinovich, S. Bakardjieva, J. Hejtmanek, A. Weidenkaff, High-temperature stability, structure and thermoelectric properties of $CaMn_{1-x}Nb_xO_3$ phases, *Acta Materialia* 57 (2009) 5667–5680.

[60] A.Y. Zuev, D.S. Tsvetkov, Oxygen nonstoichiometry, defect structure and defect-induced expansion of undoped perovskite $LaMnO_{3\pm\delta}$, *Solid State Ionics* 181 (2010) 557–563.

[61] K. Berggold, M. Kriener, C. Zobel, A. Reichl, M. Reuther, R. Müller, A. Freimuth, T. Lorenz, Thermal conductivity, thermopower, and figure of merit of $La_{1-x}Sr_xCoO_3$, *Physical Review* B 72 (2005) 155116.

[62] P. Pichanusakorn, P. Bandaru, Nanostructured thermoelectrics, *Materials Science and Engineering: R: Reports* 67 (2010) 19–63.

[63] J.P. Heremans, B. Wiendlocha, A.M. Chamoire, Resonant levels in bulk thermoelectric semiconductors, *Energy & Environmental Science* 5 (2012) 5510–5530.

[64] C.M. Jaworski, V. Kulbachinskii, J.P. Heremans, Resonant level formed by tin in Bi_2Te_3 and the enhancement of room-temperature thermoelectric power, *Physical Review B* 80 (2009) 233201.

[65] D. Parker, D.J. Singh, High-temperature thermoelectric performance of heavily doped PbSe, *Physical Review B* 82 (2010) 35204.

[66] H. Wang, Y. Pei, A.D. LaLonde, G.J. Snyder, Heavily Doped p-Type PbSe with High Thermoelectric Performance: An Alternative for PbTe, *Advanced Materials* 23 (2011) 1366–1370.

[67] Y. Pei, X. Shi, A. LaLonde, H. Wang, L. Chen, G.J. Snyder, Convergence of electronic bands for high performance bulk thermoelectrics, *Nature* 473 (2011) 66.

[68] W. Liu, X. Tan, K. Yin, H. Liu, X. Tang, J. Shi, Q. Zhang, C. Uher, Convergence of conduction bands as a means of enhancing thermoelectric performance of n-type $Mg_2Si_{1-x}Sn_x$ solid solutions, *Physical Review Letters*108 (2012) 166601.

[69] S. Wang, Y. Sun, J. Yang, B. Duan, L. Wu, W. Zhang, J. Yang, High thermoelectric performance in Te-free $(Bi, Sb)_2Se_3$ via structural transition induced band convergence and chemical bond softening, *Energy & Environmental Science* 9 (2016) 3436–3447.

[70] Y. Wang, N.S. Rogado, R.J. Cava, N.P. Ong, Spin entropy as the likely source of enhanced thermopower in $Na_xCo_2O_4$, *Nature* 423 (2003) 425.

[71] S.J. Watzman, R.A. Duine, Y. Tserkovnyak, S.R. Boona, H. Jin, A. Prakash, Y. Zheng, J. P. Heremans, Magnon-drag thermopower and Nernst coefficient in Fe, Co, and Ni, *Physical Review B* 94 (2016) 144407.

[72] C. Fu, T. Zhu, Y. Pei, H. Xie, H. Wang, G.J. Snyder, Y. Liu, Y. Liu, X. Zhao, High band degeneracy contributes to high thermoelectric performance in p-type half-Heusler compounds, *Advanced Energy Materials* 4 (2014) 1400600.

[73] J. Yang, L. Xi, W. Qiu, L. Wu, X. Shi, L. Chen, J. Yang, W. Zhang, C. Uher, D.J. Singh, On the tuning of electrical and thermal transport in thermoelectrics: an integrated theory–experiment perspective, *npj Computational Materials* 2 (2016) 15015.

[74] W.G. Zeier, H. Zhu, Z.M. Gibbs, G. Ceder, W. Tremel, G.J. Snyder, Band convergence in the non-cubic chalcopyrite compounds Cu_2MGeSe_4, *Journal of Materials Chemistry* C 2 (2014) 10189–10194.
[75] S.V. Faleev, F. Léonard, Theory of enhancement of thermoelectric properties of materials with nanoinclusions, *Physical Review B* 77 (2008) 214304.
[76] B. Paul, P. Banerji, Embedded Ag-rich nanodots in PbTe: Enhancement of thermoelectric properties through energy filtering of the carriers, *Journal of Applied Physics* 108 (2010) 64322.
[77] L. Wu, J. Yang, S. Wang, P. Wei, J. Yang, W. Zhang, L. Chen, Thermopower enhancement in quantum wells with the Rashba effect, Applied Physics Letters 105 (2014) 202115.
[78] L. Wu, J. Yang, T. Zhang, S. Wang, P. Wei, W. Zhang, L. Chen, J. Yang, Enhanced thermoelectric performance in the Rashba semiconductor BiTeI through band gap engineering, *Journal of Physics: Condensed Matter* 28 (2016) 85801.
[79] S. Butt, W. Xu, W.Q. He, Q. Tan, G.K. Ren, Y. Lin, C.-W. Nan, Enhancement of thermoelectric performance in Cd-doped $Ca_3Co_4O_9$ via spin entropy, defect chemistry and phonon scattering, *Journal of Materials Chemistry A* 2 (2014) 19479–19487.
[80] G.D. Tang, Z.H. Wang, X.N. Xu, L. Qiu, Y.W. Du, Evidence of spin-density-wave transition and enhanced thermoelectric properties in $Ca_{3-x}Ce_xCo_4O_{9+\delta}$, *Journal of Applied Physics* 107 (2010) 53715.
[81] T.M. Tritt, Thermal conductivity: theory, properties, and applications, *Springer Science & Business Media*, 2005.
[82] R.C. Zeller, R.O. Pohl, Thermal conductivity and specific heat of noncrystalline solids, *Physical Review B* 4 (1971) 2029.
[83] W.A. Phillips, A.C. Anderson, Amorphous solids: low-temperature properties, *Springer*, 1981.
[84] J.L. Cohn, G.S. Nolas, V. Fessatidis, T.H. Metcalf, G.A. Slack, Glasslike heat conduction in high-mobility crystalline semiconductors, *Physical Review Letters* 82 (1999) 779.
[85] J. Yang, D.T. Morelli, G.P. Meisner, W. Chen, J.S. Dyck, C. Uher, Influence of electron-phonon interaction on the lattice thermal conductivity of $Co_{1-x}Ni_xSb_3$, *Physical Review B* 65 (2002) 94115.
[86] D.G. Cahill, H.E. Fischer, T. Klitsner, E.T. Swartz, R.O. Pohl, Thermal conductivity of thin films: Measurements and understanding, *Journal of Vacuum Science & Technology A: Vacuum, Surfaces, and Films* 7 (1989) 1259–1266.
[87] X. Shi, L. Chen, C. Uher, Recent advances in high-performance bulk thermoelectric materials, *International Materials Reviews* 61 (2016) 379–415.
[88 G. Tan, L.-D. Zhao, M.G. Kanatzidis, Rationally designing high-performance bulk thermoelectric materials, *Chemical Reviews* 116 (2016) 12123–12149.
[89] T. Matsunaga, N. Yamada, R. Kojima, S. Shamoto, M. Sato, H. Tanida, T. Uruga, S. Kohara, M. Takata, P. Zalden, G. Bruns, I. Sergueev, H. C. Wille, R. P. Hermann, M. Wuttig, Phase-change materials: vibrational softening upon crystallization and its impact on thermal properties, *Advanced Functional Materials* 21 (2011) 2232–2239.
[90] F. Zhou, W. Nielson, Y. Xia, V. Ozoliņš, Lattice anharmonicity and thermal conductivity from compressive sensing of first-principles calculations, *Physical Review Letters* 113 (2014) 185501.
[91] S.M. Kauzlarich, S.R. Brown, G.J. Snyder, Zintl phases for thermoelectric devices, *Dalton Transactions* (2007) 2099–2107.

[92] K. Biswas, J. He, I.D. Blum, C.-I. Wu, T.P. Hogan, D.N. Seidman, V.P. Dravid, M.G. Kanatzidis, High-performance bulk thermoelectrics with all-scale hierarchical architectures, *Nature* 489 (2012) 414.

[93] K.H. Lee, S.W. Kim, H. Ohta, K. Koumoto, Ruddlesden-Popper phases as thermoelectric oxides: Nb-doped $SrO(SrTiO_3)_n$ (n = 1, 2), *Journal of Applied Physics* 100 (2006) 63717.

[94] K. Koumoto, Y. Wang, R. Zhang, A. Kosuga, R. Funahashi, Oxide thermoelectric materials: a nanostructuring approach, *Annual Review of Materials Research* 40 (2010) 363–394.

[95] Y. Wang, K.H. Lee, H. Ohta, K. Koumoto, Thermoelectric properties of electron doped $SrO(SrTiO_3)_n$ (n = 1, 2) ceramics, *Journal of Applied Physics* 105 (2009) 103701.

[96] A.V. Kovalevsky, S. Populoh, S.G. Patrício, P. Thiel, M.C. Ferro, D.P. Fagg, J.R. Frade, A. Weidenkaff, Design of $SrTiO_3$-based thermoelectrics by tungsten substitution, *The Journal of Physical Chemistry C* 119 (2015) 4466–4478.

[97] A. Mehdizadeh Dehkordi, S. Bhattacharya, T. Darroudi, J.W. Graff, U. Schwingenschlögl, H.N. Alshareef, T.M. Tritt, Large thermoelectric power factor in Pr-doped $SrTiO_{3-\delta}$ ceramics via grain-boundary-induced mobility enhancement, *Chemistry of Materials* 26 (2014) 2478–2485.

[98] K.K. Liu, Z.Y. Liu, F.P. Zhang, J.X. Zhang, X.Y. Yang, J.W. Zhang, J.L. Shi, G. Ren, T.W. He, J.J. Duan, Improved thermoelectric performance in Pr and Sr Co-doped $CaMnO_3$ materials, *Journal of Alloys and Compounds* 808 (2019) 151476.

[99] L. Sagarna, A. Shkabko, S. Populoh, L. Karvonen, A. Weidenkaff, Electronic structure and thermoelectric properties of nanostructured $EuTi_{1-x}Nb_xO_{3-\delta}$ (x = 0.00; 0.02), *Applied Physics Letters* 101 (2012) 33908.

[100] M.-E. Song, H. Lee, M.-G. Kang, W. Li, D. Maurya, B. Poudel, J. Wang, M.A. Meeker, G.A. Khodaparast, S.T. Huxtable, S. Priya, Nanoscale texturing and interfaces in compositionally modified $Ca_3Co_4O_9$ with enhanced thermoelectric performance, *ACS Omega* 3 (2018) 10798–10810.

[101] F. Li, J.-F. Li, L.-D. Zhao, K. Xiang, Y. Liu, B.-P. Zhang, Y.-H. Lin, C.W. Nan, H.M. Zhu, Polycrystalline BiCuSeO oxide as a potential thermoelectric material, *Energy & Environmental Science* 5 (2012) 7188–7195.

[102] J. Lan, Y.-H. Lin, Y. Liu, S. Xu, C.-W. Nan, High Thermoelectric Performance of Nanostructured In_2O_3-Based Ceramics, *Journal of the American Ceramic Society* 95 (2012) 2465–2469.

[103] N. Haque, A. Hughes, S. Lim, C. Vernon, Rare earth elements: Overview of mining, mineralogy, uses, sustainability and environmental impact, *Resources* 3 (2014) 614–635.

[104] K.M. Goodenough, F. Wall, D. Merriman, The rare earth elements: demand, global resources, and challenges for resourcing future generations, *Natural Resources Research* 27 (2018) 201–216.

[105] S. Yoon, A.E. Maegli, L. Karvonen, S.K. Matam, A. Shkabko, S. Riegg, T. Großmann, S.G. Ebbinghaus, S. Pokrant, A. Weidenkaff, Bandgap tuning in $SrTi(N, O, F)_3$ by anionic-lattice variation, *Journal of Solid State Chemistry* 206 (2013) 226–232.

[106] Y. Liu, L. Xie, Y. Li, R. Yang, J. Qu, Y. Li, X. Li, Synthesis and high photocatalytic hydrogen production of $SrTiO_3$ nanoparticles from water splitting under UV irradiation, *Journal of Power Sources* 183 (2008) 701–707.

[107] R. Ashiri, R. Ajami, A. Moghtada, Sonochemical Synthesis of $SrTiO_3$ Nanocrystals at Low Temperature, *International Journal of Applied Ceramic Technology* 12 (2015) E202-E206.

[108] L. Sagarna, K.Z. Rushchanskii, A. Maegli, S. Yoon, S. Populoh, A. Shkabko, S. Pokrant, M. Ležaić, R. Waser, A. Weidenkaff, Structure and thermoelectric properties of $EuTi(O, N)_{3\pm\delta}$, *Journal of Applied Physics* 114 (2013) 33701.

[109] V. Scagnoli, M. Allieta, H. Walker, M. Scavini, T. Katsufuji, L. Sagarna, O. Zaharko, C. Mazzoli, $EuTiO_3$ magnetic structure studied by neutron powder diffraction and resonant X-ray scattering, *Physical Review B* 86 (2012) 94432.

[110] A. Bussmann-Holder, J. Köhler, R.K. Kremer, J.M. Law, Relation between structural instabilities in $EuTiO_3$ and $SrTiO_3$, *Physical Review B* 83 (2011) 212102.

[111] T. Birol, C.J. Fennie, Origin of giant spin-lattice coupling and the suppression of ferroelectricity in $EuTiO_3$ from first principles, *Physical Review B* 88 (2013) 94103.

[112] J.L. Bettis, M.-H. Whangbo, J. Köhler, A. Bussmann-Holder, A.R. Bishop, Lattice dynamical analogies and differences between $SrTiO_3$ and $EuTiO_3$ revealed by phonon-dispersion relations and double-well potentials, *Physical Review B* 84 (2011) 184114.

[113] L. Sagarna, S. Populoh, A. Shkabko, J. Eilertsen, A.E. Maegli, R. Hauert, M. Schrade, L. Karvonen, A. Weidenkaff, Influence of the Oxygen Content on the Electronic Transport Properties of $Sr_xEu_{1-x}TiO_{3-\delta}$, *The Journal of Physical Chemistry C* 118 (2014) 7821–7831.

[114] R.D. Shannon, Revised effective ionic radii and systematic studies of interatomic distances in halides and chalcogenides, *Acta crystallographica section A: crystal physics, diffraction, theoretical and general crystallography* 32 (1976) 751–767.

[115] G. Shirane, Y. Yamada, Lattice-Dynamical Study of the 110 K Phase Transition in $SrTiO_3$, *Physical Review* 177 (1969) 858.

[116] A. Midya, P. Mandal, K. Rubi, R. Chen, J.-S. Wang, R. Mahendiran, G. Lorusso, M.Evangelisti, Large adiabatic temperature and magnetic entropy changes in $EuTiO_3$, *Physical Review B* 93 (2016) 94422.

[117] P.G. Reuvekamp, R.K. Kremer, J. Köhler, A. Bussmann-Holder, Evidence for the first-order nature of the structural instability in $EuTiO_3$ from thermal expansion measurements, *Physical Review B* 90 (2014) 104105.

[118] D.S. Ellis, H. Uchiyama, S. Tsutsui, K. Sugimoto, K. Kato, D. Ishikawa, A.Q.R. Baron, Phonon softening and dispersion in $EuTiO_3$, *Physical Review B* 86 (2012) 220301.

[119] L.J. Spalek, S.S. Saxena, C. Panagopoulos, T. Katsufuji, J.A. Schiemer, M.A. Carpenter, Elastic and anelastic relaxations associated with phase transitions in $EuTiO_3$, *Physical Review B* 90 (2014) 54119.

[120] M. Allieta, M. Scavini, L.J. Spalek, V. Scagnoli, H.C. Walker, C. Panagopoulos, S.S. Saxena, T. Katsufuji, C. Mazzoli, Role of intrinsic disorder in the structural phase transition of magnetoelectric $EuTiO_3$, *Physical Review B* 85 (2012) 184107.

[121] J.W. Kim, P. Thompson, S. Brown, P.S. Normile, J.A. Schlueter, A. Shkabko, A. Weidenkaff, P.J. Ryan, Emergent superstructural dynamic order due to competing antiferroelectric and antiferrodistortive instabilities in bulk $EuTiO_3$, *Physical Review Letters* 110 (2013) 27201.

[122] D. Bessas, K.Z. Rushchanskii, M. Kachlik, S. Disch, O. Gourdon, J. Bednarcik, K. Maca, I. Sergueev, S. Kamba, M. Ležaić, R. P. Hermann, Lattice instabilities in bulk $EuTiO_3$, *Physical Review B* 88 (2013) 144308.

[123] V. Goian, S. Kamba, O. Pacherová, J. Drahokoupil, L. Palatinus, M. Dušek, J. Rohlíček, M. Savinov, F. Laufek, W. Schranz, A. Fuith, M. Kachlík, K. Maca, A. Shkabko, L. Sagarna, A. Weidenkaff, A. A. Belik, Antiferrodistortive phase transition in $EuTiO_3$, *Physical Review B* 86 (2012) 54112.

[124] T. Kolodiazhnyi, M. Valant, J.R. Williams, M. Bugnet, G.A. Botton, N. Ohashi, Y. Sakka, Evidence of Eu^{2+} 4*f* electrons in the valence band spectra of $EuTiO_3$ and $EuZrO_3$, *Journal of Applied Physics* 112 (2012) 83719.

[125] K. van Benthem, C. Elsässer, R.H. French, Bulk electronic structure of $SrTiO_3$: experiment and theory, *Journal of Applied Physics* 90 (2001) 6156–6164.

[126] T.R. McGuire, M.W. Shafer, R.J. Joenk, H.A. Alperin, S.J. Pickart, Magnetic structure of $EuTiO_3$, *Journal of Applied Physics* 37 (1966) 981–982.

[127] K.S. Takahashi, H. Ishizuka, T. Murata, Q.Y. Wang, Y. Tokura, N. Nagaosa, M. Kawasaki, Anomalous Hall effect derived from multiple Weyl nodes in high-mobility $EuTiO_3$ films, *Science Advances* 4 (2018) eaar7880.

[128] K.S. Takahashi, M. Onoda, M. Kawasaki, N. Nagaosa, Y. Tokura, Control of the anomalous Hall effect by doping in $Eu_{1-x}La_xTiO_3$ thin films, *Physical Review Letters* 103 (2009) 57204.

[129] P.G. Reuvekamp, R.K. Kremer, J. Köhler, A. Bussmann-Holder, Spin-lattice coupling induced crossover from negative to positive magnetostriction in $EuTiO_3$, *Physical Review B* 90 (2014) 94420.

[130] Z. Guguchia, H. Keller, R.K. Kremer, J. Köhler, H. Luetkens, T. Goko, A. Amato, A. Bussmann-Holder, Spin-lattice coupling induced weak dynamical magnetism in $EuTiO_3$ at high temperatures, *Physical Review B* 90 (2014) 64413.

[131] T. Katsufuji, H. Takagi, Coupling between magnetism and dielectric properties in quantum paraelectric $EuTiO_3$, *Physical Review B* 64 (2001) 54415.

[132] K.Z. Rushchanskii, S. Kamba, V. Goian, P. Vaněk, M. Savinov, J. Prokleška, D. Nuzhnyy, K. Knížek, F. Laufek, S. Eckel, S. K. Lamoreaux, A. O. Sushkov, M. Ležaić, N. A. Spaldin, A multiferroic material to search for the permanent electric dipole moment of the electron, *Nature Materials* 9 (2010) 649.

[133] S. Eckel, A.O. Sushkov, S.K. Lamoreaux, Limit on the Electron Electric Dipole Moment Using Paramagnetic Ferroelectric $Eu_{0.5}Ba_{0.5}TiO_3$, *Physical Review Letters* 109 (2012) 193003.

[134] T. Wei, Q.J. Zhou, X. Yang, Q.G. Song, Z.P. Li, X.L. Qi, J.-M. Liu, Competition between quantum fluctuation and ferroelectric order in $Eu_{1-x}Ba_xTiO_3$, *Applied Surface Science* 258 (2012) 4601–4606.

[135] D.R. Lide, CRC Handbook of Chemistry and Physics, *89th Edition*.

[136] Z. Li, M. Yang, J.-S. Park, S.-H. Wei, J.J. Berry, K. Zhu, Stabilizing perovskite structures by tuning tolerance factor: formation of formamidinium and cesium lead iodide solid-state alloys, *Chemistry of Materials* 28 (2015) 284–292.

[137] H. Zhang, N. Li, K. Li, D. Xue, Structural stability and formability of ABO_3-type perovskite compounds, *Acta Crystallographica Section B*: *Structural Science* 63 (2007) 812–818.

[138] Y. Kawada, M. Fujimoto, Phase Separation and Solid Solution in Nonstoichiometric and Stoichiometric (Sr, Mg)TiO_3 Ceramics, *Japanese Journal of Applied Physics* 29 (1990) L126-L128.

[139] E. Fluck, K. G. Heumann, Periodic Table of the Elements (2nd Edition), *Wiley-Vch* (2000)

[140] W. Xie, X. Tang, Y. Yan, Q. Zhang, T.M. Tritt, Unique nanostructures and enhanced thermoelectric performance of melt-spun BiSbTe alloys, *Applied Physics Letters* 94 (2009) 102111.

This page intentionally left blank

Chapter 2 Experimental methods

2.1 Material synthesis and preparation

2.1.1 Pechini Method

The Pechini method was patented by M. Pechini in the United States as early as 1967. He invented this method for preparing high purity lead and alkaline earth titanates, zirconates and niobates as dielectric materials and thin films of the same, and any selected combinations and proportions thereof via resin intermediates [1]. Citric acid and ethylene glycol are indispensable chemicals for this process. The principle of this technique is first utilizing the ability of citric acid to form polybasic acid chelates with metal cations. Then the chelates are subjected to polyesterification forming resin intermediates when heated with ethylene glycol. Afterwards the resin is calcined to remove the organic components leaving behind the desired ceramic composition as product [2,3]. The advantages of this synthesis technique are numerous compared to the conventional solid-state reaction for synthesizing perovskite-type oxides. For example, highly homogeneous and finely dispersed nanocrystal materials can be obtained at a relatively low temperature in air.

2.1.2 Precursor Synthesis

Seen from the point of view of the economy, Eu_2O_3 is the cheapest source compared to other Eu containing chemicals. Thus, Eu_2O_3 was chosen as one of the starting materials. Eu_2O_3 is insoluble in water at RT, similar to most of the other metal oxides (e.g., TiO_2). The ETO-based ceramic compounds were generally synthesized by means of solid-state reaction [4,5]. Due to the fact that Eu_2O_3 is soluble in acidic aqueous solutions, the studied polycrystalline $Eu_{1-x}A_xTiO_{3-\delta}$ (A = Mg^{2+}, Ca^{2+}, Sr^{2+}, Ba^{2+}) samples were aimed to be synthesized via a soft chemistry route. To the best of my knowledge, there is only one reference that reported the synthesis of $Eu_{1-x}Ca_xTiO_3$ polycrystalline compounds via a modified sol-gel method by using HNO_3 solution [6]. In this thesis, a modified Pechini method is applied for the synthesis of precursors of the studied samples without additional consumption of HNO_3.

The starting chemicals used for the material synthesis were europium(III) oxide (Eu_2O_3, Alfa Aesar, 99.9 %), magnesium acetate tetrahydrate ($Mg(OOCCH_3)_2{\cdot}4H_2O$, Alfa Aesar, 99 %), calcium nitrate tetrahydrate ($Ca(NO_3)_2 \cdot 4H_2O$, Merck, 99.95 %), strontium acetate hemihydrate ($Sr(OOCCH_3)_2{\cdot}0.5H_2O$, Alfa Aesar, 98 %), barium acetate ($(CH_3COO)_2Ba$, Sigma-Aldrich, 99 %), titanium(IV) bis (ammonium lactato) dihydroxide solution ($[CH_3CH(O-)CO_2NH_4]_2Ti(OH)_2$, Sigma-Aldrich, 50 wt. % in H_2O), citric acid ($HOC(COOH)(CH_2COOH)_2$, Sigma-Aldrich, 99 %), and ethylene glycol ($HOCH_2CH_2OH$, Sigma-Aldrich, ≥ 99 %). The molar ratio of citric acid, ethylene glycol, and the expected final product were set at 6:30:1. First, a stoichiometric amount of Eu_2O_3, one of the alkaline earth chemicals mentioned above and citric acid were weighted separately and

placed all into a round-bottom flask. Then an appropriate amount of demineralized water (roughly 200 ml in the case of 0.02 mol final product) was added into the flask. Subsequently, the flask containing the mixture was heated to 373 K in an oil bath under vigorous magnetic stirring. Due to the fact that Eu_2O_3 is soluble in citric acid containing aqueous solution, the white suspension in the flask slowly changed to a clear transparent solution within a few minutes. When the solution was completely clear and transparent, the flask was moved to a lower temperature environment (e.g., RT) and the vigorous stirring was stopped. After that, the titanium(IV) bis (ammonium lactato) dihydroxide solution and ethylene glycol were added into the solution. Then, the flask was placed in an oil bath of 338 K, and the solution was vigorously stirred for another 2 hours. Finally, the transparent solution was transferred to a Pyrex crystallizing dish and heated in a muffle furnace at 473 K for 12 h followed by calcination at 753 K for 6 h, leaving a white powdery residue as oxide precursors for further preparation.

2.1.3 Material Synthesis and Bulk Samples Preparation

The white precursors are amorphous oxides, which were annealed at 1273 K for 12 h under a reducing condition in a tube furnace for crystallization. The reducing condition was given by a forming gas (5 vol.% H_2 in Ar) with a flow rate of 100 ml/min. The colors of the obtained materials were dark black or light black depending on the europium concentration, i.e., the higher europium concentration, the deeper black color. The powder materials were densified to bulk samples for the physical properties measurement and characterization afterwards.

The pores and microstructures of the bulk samples have a major influence on the transport properties [7–9], so the highly compacted dense bulk samples were selected for the evaluation of the materials intrinsic properties. The powder samples were subjected to cold pressing followed by conventional sintering to achieve the dense bulk samples. The cold pressing included an uniaxial pressing (UP) and a cold isostatic pressing (CIP) step. First, an appropriate amount of powder sample was placed in a metal pressing die with 20 mm diameter. Subsequently, the die was loaded in a uniaxial press under 20 kN for a few minutes. Afterwards, the compacted samples were gently removed from the die and a disc-shaped pellet was obtained. The main purpose of this UP step is forming a disc-shaped green body. Due to the frictions among the powder particles and the frictions between the powder and the metal die, the uniaxial pressure applied on the metal die leads to a large density gradient in the green body. If the density gradient is too large, it will eventually form a bent disc with inhomogeneous contraction after the following high-temperature sintering. This risk can be greatly reduced or avoided by using CIP for further compression after the UP process. The obtained disc-shape green body was sealed in a rubber bag and immersed in the oil chamber of the press. Then a pressure of ~ 0.64 GPa was loaded for 5 min resulting in a highly compacted green body. Compared to UP, the CIP applies isostatic pressure uniformly over the entire surface of the rubber bag, yielding a product with a uniform density and homogeneity.

The conventional sintering was carried out on green body samples for further increasing the strength and density. The sintering temperature of the $Eu_{1-x}A_xTiO_{3-\delta}$ (A = Mg^{2+}, Ca^{2+}, Sr^{2+}, Ba^{2+}, $0 \leq x \leq 1$) samples was varied from 1300 K to 1420 K for 10 h depending on the chemical composition. The atmospheric conditions were a forming gas (10 vol.% H_2 in Ar) with a flow rate of 100 ml/min. The heating rate was 5 K/min. During the sintering, an appropriate cooling rate was required. For ceramic bulk materials too fast cooling at very high temperatures could cause cracks through the bulk due to the stress variation. Therefore, the cooling rate was varied from 2 K/ min to

5 K/min, i.e., the cooling rate is 2 K/ min at the maximum temperature and then gradually changed to 5 K/min at lower temperatures.

Finally, the sintered bulk samples were cut and polished to desired shapes and sizes for property measurements and characterizations, i.e., rectangular bars (~ 10 × 3 × 2 mm^3) for the electrical transport property measurements, square pellets (~ 8 × 8 × 2 mm^3) for the thermal diffusivity measurements, and very thin square pellets (~ 8 × 8 × 0.5 mm^3 or 5 × 5 × 0.5 mm^3) for the high temperature Hall measurements, small pieces with a highly polished and flat surface for heat capacity measurements. A small part of bulk samples was ground to fine powder for XRD and ICP-OES measurements. A scheme of the material synthesis and bulk samples preparation is illustrated in Fig. 2.1.

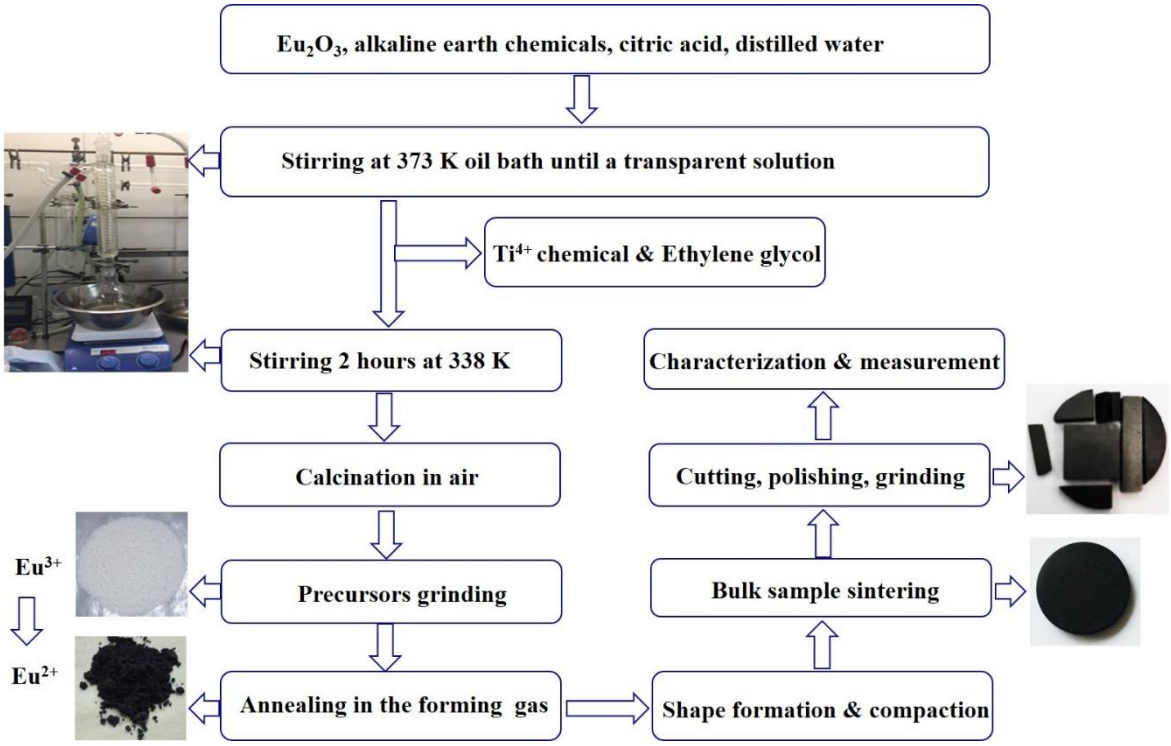

Fig. 2.1 Scheme of material synthesis and bulk samples preparation.

2.2 Sample characterization

2.2.1 Bulk Density Determination

There are several methods for density determination [10]. An appropriate measurement method is essential for getting a precise density result. For a bulk sample with measurable dimensions and simple regular shape, the method of measuring the mass and dimension can be used for a fast estimation, but the results are generally not precise. In the laboratory, the Archimedes balance is often used for the density evaluation of a highly densified bulk sample without open pores. In contrast, for a porous sample with open pores, a large deviation of measured density would be observed by using the Archimedes balance. Open or closed pores are defined by whether the pores

are isolated within a material. They can be easily distinguished by measuring the mass of bulk samples in liquids via the Archimedes balance. When the bulk sample is completely submerged in the liquid, a constant mass value should be observed for the closed-porous sample and various values will be observed for the open-porous sample. In this thesis, most of the sintered samples were evidenced to have closed pores and were highly densified. The Archimedes balance filled with demineralized water was utilized for the density measurement.

When a bulk sample is completely immersed in water, there is an apparent weight loss due to the buoyancy. The Archimedes' principle equates the buoyancy to the weight of the water displaced by the sample. Accordingly, the density of the sample can be calculated by the formula:

$$d = \frac{m_{air}}{m_{air} - m_{water}} * d_{water}(T) \tag{2-1}$$

where d is the sample's density, m_{air} the mass measured in air, m_{water} the mass in water, $d_{water}(T)$ the temperature dependent water density. Every sample was measured at least three times and the average value was recorded for the density evaluation.

2.2.2 Crystal Structure Analysis

The physical properties of materials are closely related to their crystal structure. In this thesis, different diffraction techniques and analysis methods were used to collect the crystal structural information in different length scales, i.e., long-range and local scales.

2.2.2.1 Laboratory X-Ray Diffraction

X-ray diffraction (XRD) is a widely used instrumental technique for structural characterization of crystalline materials with a periodic array, not for amorphous materials [11]. When a X-ray beam hits a sample, diffraction occurs producing constructive interference at specific angles and providing a unique "fingerprint" of this material. The observed diffraction pattern can be used to determine the phase composition, unit cell parameters, crystal structure, average crystallite size of polycrystalline samples, crystallite microstrain, residual stress, etc. For instance, the interplanar distance d_{hkl} (distances between adjacent planes of atoms) can be calculated by applying Bragg's Law:

$$2d_{hkl}\sin\theta_{hkl} = n\lambda \tag{2-2}$$

where n is a positive integer, θ_{hkl} is the angle of incidence of the X-ray beam, and λ is the wavelength of the incident X-ray beam. The forms of materials for a measurement can be powder, sintered bulk samples, metal foils, coatings, films, and so on. The laboratory XRD was applied to identify the phase purity for every sample before and after sintering.

The XRD data were collected by a Rigaku Smartlab X-ray diffractometer using Cu-$K_{\alpha 1,2}$ radiation. Cu-K_{β} radiation was suppressed by a thin nickel foil with approximately 90 % efficiency. The diffraction patterns were recorded from 10° to 90° (2 theta) using continuous scanning at a step size of 0.01°. Once the purity of the samples was confirmed, Rietveld refinements [12,13] were carried out using *FullProf* 2.k [14] for determining the correct space group and unit cell parameters. A pseudo-Voigt function was selected to describe the reflection profile. The background was treated by a 4th order polynomial function. Diffraction patterns were collected as 2 theta vs absolute intensity but were presented as 2 theta vs relative intensity for the sake of clarity. It is because the absolute

intensity can vary due to instrumental and/or experimental parameters. The relative intensity is calculated by dividing the absolute intensity of every data point by the absolute intensity of the most intense reflection. The Rietveld refinements were performed by Dr. Marc Widenmeyer at the University of Stuttgart.

2.2.2.2 Synchrotron Radiation Powder Diffraction

Electrons traveling at a speed close to the speed of light are forced to change the direction of their motion under the effect of magnetic fields (perpendicular to the direction of their motion). This leads to the emission of light with peculiar characteristics, known as synchrotron radiation [15]. Compared to the conventional laboratory XRD, one of the advantages of the synchrotron powder radiation is its superior resolution. The synchrotron produces more intense reflections due to the high beam intensity and stability. The ultra-high vacuum environment significantly lowers the effect of noise leading to better reflection profiles. Additionally, the background fluorescence, which can be a problem for iron-rich samples in a Cu-K_α beam if conventional laboratory X-ray sources are used with only a pre-sample monochromator, can be eliminated by applying a different wavelength.

In this thesis, the high-resolution XRD data were obtained by using the synchrotron radiation powder diffraction, which was carried out at European Synchrotron Radiation Facility (ESRF) in Grenoble, France. The detailed technical information of data analysis is presented in the following individual chapters. The Rietveld refinements of high-resolution XRD data were carried out by Prof. Dr. Marco Scavini at the University of Milan.

2.2.2.3 Pair Distribution Function

Both the laboratory XRD and high-resolution XRD give the long-range average structural information. In some materials, a slight variation of structure can significantly vary physical properties. Therefore, a local structure probe is requested to characterize such influences. The pair distribution function (PDF) reveals local scale structural information [16]. It is a mathematical method for describing the distribution of distances between pairs of atoms contained within a given volume. The raw data for PDF analysis were collected during the synchrotron radiation process at ESRF. The detailed technical and analysis parameters are presented in the following individual chapters. The PDF data analysis was conducted by Dr. Stefano Checchia at ESRF.

2.2.2.4 Extended X-ray absorption fine structure

Extended X-ray absorption fine structure (EXAFS) is another appealing local structural technique, which describes the information on the local geometrical structure surrounding a given atomic species. Since the mean free path of photoelectrons is short, the observed structure information is usually limited to about 10 Å. Owing to this feature of focusing on the local scale, EXAFS can be used in many atomic noncrystalline systems, like amorphous alloys or oxide glasses. The atomic selectivity, which is achieved by tuning the X-ray energy at the corresponding absorption edge, allows one to separately investigate the surroundings of each component species. In this thesis, the EXAFS measurements were carried out in transmission geometry at the Eu *K*-edge (48519 eV) for studying the surroundings of Eu atoms at ESRF. The detailed technical and analysis parameters are presented in chapter 4. The EXAFS measurements and data analysis were conducted by Prof. Dr. Carlo Castellano, at the University of Milan.

2.2.3 Thermoelectric Properties Measurement

2.2.3.1 High-Temperature Transport Properties Measurement

The electrical resistivity (ρ) and the Seebeck coefficient (α) were measured simultaneously by a Seebeck coefficient / electric resistance measurement system (ZEM-3, Ulvac Riko). A bar shape (~ 2×2×10 mm^3) sample was vertically positioned and subjected to be in good contact between the upper and lower electrode blocks of the furnace. Then two thermocouples were contacted with the sample. The dc 4-point probe method ensures the highest measurement accuracy. The thermal diffusivity (Λ) was measured using a Netzsch LFA 457 laser flash analyzer. The LFA technique is a fast, non-destructive and non-contact method for determining Λ. The plane-parallel square shaped (~ 8×8×2 mm^3) samples were placed in the sample holder. During the measurement, the front surface of the sample was heated via an energy pulse (i.e., laser flash). Subsequently, the resulting time-dependent temperature rise of the back surface was tracked by an infrared detector. In the adiabatic case the thermal diffusivity can be calculated by the flowing equation:

$$\Lambda = \frac{1.38\,H^2}{\pi^2 t_{1/2}}, \tag{2-3}$$

where H is the thickness of the samples and $t_{1/2}$ is the time to the half maximum. The cowan-plus model was used for the data analysis.

The thermal conductivity (κ) was derived from experimental density d, thermal diffusivity Λ and specific heat capacity c_p values using the relationship:

$$\kappa = d\Lambda c_p \tag{2-4}$$

The d of the bulk samples were determined by the Archimedes balance as described above. The specific heat capacity c_p was calculated by the Dulong-Petit law $3NR/M$, where N is the number of moles including all atoms, R the gas constant (8.314 J/mol K) and M the molar mass of the compound (g/mol).

The Hall coefficient measurement provides many intrinsic physical characteristics of semiconductor materials [17]. For instance, the sign of Hall constant R_H discovers the dominant charge carriers, i.e., positive indicating the holes and negative indicating the electrons. The relations of R_H, n, μ, and σ are the following:

$$n = \frac{1}{R_H|e|} \tag{2-5}$$

$$\mu = \sigma R_H \tag{2-6}$$

In this thesis, the Hall coefficient measurements were carried out by a HT-Hall 1100 K (Fraunhofer, IPM) measurement system from ambient temperature to 673 K. The values of R_H, n, μ, and σ were simultaneously obtained during the measurement. This system applies a 4-point probe van der Pauw method. The obtained σ matched very well with the results of the ZEM-3 measurements, indicating that the data obtained from Hall measurement are reliable.

2.2.3.2 Low-Temperature Transport Properties Measurement

All the low temperature (i.e., below 300 K) transport properties (σ, α, and κ) were determined by using the thermal transport option kit of Quantum Design and the corresponding equipment provided

with their physical property measurement system (PPMS) cryostat. The measurements were carried out in the temperature range of 2 K < T < 350 K by continuously changing the temperature with a sweep rate of 0.5 K/min and applying a temperature gradient of approximately 3 %. The heating and cooling cycle measurements were carried out for recognizing a possible mismatch and obtaining reproducible data. The low-temperature transport property measurements were carried out by Kai Philippi using PPMS at Max Planck Institute for Solid State Research in Stuttgart. Yamei Liu repeated the low-temperature transport property by PPMS at Clemson University, United States of America for data verification.

The low temperature heat capacity of some selected samples was measured on a Quantum Design® PPMS from 1.8 K to 300 K. These measurements were carried out by Dr. Konstantin Skokovat from the research group of Functional Materials of Technische Universität Darmstadt. The Quantum Design PPMS is a powerful tool in a laboratory for low temperature physical properties measurement, such as heat capacity, thermal and electro-transport, Hall effect, magnetic measurements, and so on. More detailed information can be found elsewhere [18].

2.2.4 X-ray Photoelectron Spectroscopy

X-ray photoelectron spectroscopy (XPS) is a surface-sensitive quantitative spectroscopic technique [19], which can be used to determine the elemental composition and oxidation states of the surface (top 0 ~ 10 nm usually). The bulk samples with flat surfaces were prepared for the XPS measurement. Because the surfaces of the samples were exposed in the ambient environment, the surfaces were polluted with contamination and/or oxidation. The samples have to be treated by Ar^+ sputtering in order to remove the contaminated surface layer and get a clean and fresh surface for the measurement. The XPS was performed with a Kratos Axis Ultra system using monochromatized Al K_α X-ray radiation (1486.6 eV). The detailed technique and analysis parameters are presented in chapter 4. The XPS measurements and data analysis were performed by Dr. Kathrin Müller at Max Planck Institute for Solid State Research in Stuttgart.

2.2.5 Chemical Analysis

The metal element composition of the materials was determined by using an inductively coupled plasma-optical emission spectrometry (ICP-OES, Spectro Ciros CCD) instrument. The ICP-OES, which takes advantage of the unique emission spectra of elements, is a commonly used elemental analysis technique for determining the chemical elements. It has numerous advantages compared with other elemental analysis methods [20]. For example, it offers excellent accuracy and precision results, excellent detection limits for most elements (0.1 ~ 100 mg/L), cost-effective analysis, etc.

The oxygen content was determined by carbothermal fusion using carrier hot gas extraction technique (Eltra ONH-2000 analyzer). The carrier gas hot gas extraction is a widely used method for the identification and quantitation of the non-metals element O, N, C, S, and H in inorganic materials. It offers much higher precision compared with other methods for oxygen content determination.

Each measurement of ICP-OES and carrier gas hot extraction was repeated at least three times and the average values were recorded. The chemical analysis measurements and analysis were carried out by Samir Hammoud at Max Planck Institute for Intelligent Systems in Stuttgart.

2.2.6 Scanning Electron Microscopy

Scanning electron microscopy (SEM) is one of the most versatile techniques for the microstructural characterization of solid objects [21]. SEM utilizes a focused beam of high-energy electrons to hit on the surface of solid specimens, resulting in the generation of a variety of signals that derive from electron-sample interactions. The signals unveil the information of the electron impact area, mainly including external morphology (texture), chemical composition, and crystalline orientation. In this thesis, SEM was performed for the characterization of the morphology for different specimens, i.e., the morphologies of the powder samples before sintering and the cross sections of the sintered bulk samples, and the grain boundaries of the polished and thermally etched bulk samples. The SEM images presented in chapter 3 were taken by Dr. Stefan Kilper via SEM (Zeiss Merlin) at Max Planck Institute for Intelligent Systems in Stuttgart and the SEM images presented in other chapters were taken by Marvin Sauter via SEM (Zeiss Gemini SEM 500 instrument) at the University of Stuttgart. The elemental distribution information was collected by energy dispersive X-ray spectroscopy (EDS Bruker XFlash 6|60 detector), which was equipped together with the instrument of Gemini SEM 500.

2.2.7 Density Functional Theory

The density functional theory (DFT) is a computational quantum mechanical modeling method based on the electron density distribution [22]. It is one of the most frequently used computational tools and has been widely used for decades by physicists and chemists to study the structural, magnetic and electronic properties of molecules, materials, defects, and so on. More detailed information can be found elsewhere [23,24]. In this thesis, the DFT calculations were performed to obtain the electronic density of states (DOS) in the vicinity of the Fermi level. The DOS of $Eu_{1-x}Ba_xTiO_3$ and $Eu_{1-x}Ca_xTiO_3$ (x = 0, 0.25, 0.5, 0.75, 1) were calculated by Dr. Zhicheng Zhong and Dr. Dongxia Ma at Max Planck Institute for Solid State Research in Stuttgart, respectively. The detailed technical parameters are presented in chapters 3 and 4, respectively.

References

[1] M.P. Pechini, Method of preparing lead and alkaline earth titanates and niobates and coating method using the same to form a capacitor, *U.S. Patent*, (1967) 3330697.

[2] L.-W. Tai, P.A. Lessing, Modified resin–intermediate processing of perovskite powders: Part I. Optimization of polymeric precursors, *Journal of Materials Research* 7 (1992) 502–510.

[3] L.-W. Tai, P.A. Lessing, Modified resin-intermediate processing of perovskite powders. II: Processing for fine, nonagglomerated Sr-doped lanthanum chromite powders, *Journal of Materials Research* 7 (1992) 511–519.

[4] D. Bessas, K.Z. Rushchanskii, M. Kachlik, S. Disch, O. Gourdon, J. Bednarcik, K. Maca, I. Sergueev, S. Kamba, M. Ležaić, R. P. Hermann, Lattice instabilities in bulk $EuTiO_3$, *Physical review B* 88 (2013) 144308.

[5] K.Z. Rushchanskii, S. Kamba, V. Goian, P. Vaněk, M. Savinov, J. Prokleška, D. Nuzhnyy, K. Knížek, F. Laufek, S. Eckel, S. K. Lamoreaux, A. O. Sushkov, M. Ležaić, N. A. Spaldine, A multiferroic material to search for the permanent electric dipole moment of the electron, *Nature Materials* 9 (2010) 649-654.

[6] N.L. Henderson, X. Ke, P. Schiffer, R.E. Schaak, Solution precursor synthesis and magnetic properties of $Eu_{1-x}Ca_xTiO_3$, *Journal of Solid State Chemistry* 183 (2010) 631–635.

[7] P. Kumar, F. Topin, Thermal conductivity correlations of open-cell foams: Extension of Hashin–Shtrikman model and introduction of effective solid phase tortuosity, *International Journal of Heat and Mass Transfer* 92 (2016) 539–549.

[8] J.N. Roberts, L.M. Schwartz, Grain consolidation and electrical conductivity in porous media, *Physical Review B* 31 (1985) 5990-5997.

[9] K.W. Schlichting, N.P. Padture, P.G. Klemens, Thermal conductivity of dense and porous yttria-stabilized zirconia, *Journal of Materials Science* 36 (2001) 3003–3010.

[10] F. Rabier, M. Temmerman, T. Böhm, H. Hartmann, P.D. Jensen, J. Rathbauer, J. Carrasco, M. Fernández, Particle density determination of pellets and briquettes, *Biomass and Bioenergy* 30 (2006) 954–963.

[11] B.D. Cullity, S.R. Stock, Elements of X-ray Diffraction, *Pearson Education*, 2014.

[12] H.M. Rietveld, Line profiles of neutron powder-diffraction peaks for structure refinement, *Acta Crystallographica* 22 (1967) 151–152.

[13] H. Rietveld, A profile refinement method for nuclear and magnetic structures, *Journal of Applied Crystallography* 2 (1969) 65–71.

[14] J. Rodriguez-Carvajal, FullProf. 2k, version 5.30, March 2012, ILL.

[15] S. Mobilio, F. Boscherini, C. Meneghini, Synchrotron Radiation, *Springer*, 2016.

[16] S.J.L. Billinge, M.G. Kanatzidis, Beyond crystallography: the study of disorder, nanocrystallinity and crystallographically challenged materials with pair distribution functions, *Chemical Communications* (2004) 749–760.

[17] S. Kasap, Hall effect in semiconductors, *Electronic Booklet* (2001).

[18] Quantum Design, Physical Property Measurement System: Hardware Manual, February, 2000.

[19] J.F. Watts, X-ray photoelectron spectroscopy, *Surface Science Techniques* (1994) 5–23.

[20] X. Hou, B.T. Jones, Inductively coupled plasma/optical emission spectrometry, *Encyclopedia of Analytical Chemistry* (2000).

[21] J. Goldstein, Practical scanning electron microscopy: electron and ion microprobe analysis, *Springer Science & Business Media*, 2012.

[22] W. Kohn, A.D. Becke, R.G. Parr, Density functional theory of electronic structure, *The Journal of Physical Chemistry* 100 (1996) 12974–12980.
[23] R.M. Dreizler, E.K.U. Gross, Density functional theory: an approach to the quantum many-body problem, *Springer Science & Business Media*, 2012.
[24] D. Sholl, J.A. Steckel, Density functional theory: a practical introduction, *John Wiley & Sons*, 2011.

Chapter 3 Thermoelectric properties of Ba^{2+} substituted $EuTiO_3$

This chapter is based on the publication:

"Tailoring the structure and thermoelectric properties of $BaTiO_3$ via Eu^{2+} substitution", Xingxing Xiao, Marc Widenmeyer, Wenjie Xie, Tianhua Zou, Songhak Yoon, Marco Scavini, Stefano Checchia, Zhicheng Zhong, Philipp Hansmann, Stefan Kilper, Andrei Kovalevsky and Anke Weidenkaff, *Physical Chemistry Chemical Physics* 19 (2017) 13469–13480.

Abstract

A series of $Eu_{1-x}Ba_xTiO_{3-\delta}$ ($0 \leq x \leq 1$) compounds with ~ 40 nm particle size was synthesized via a Pechini method followed by annealing and sintering under a reducing atmosphere. The effects of Ba^{2+} substitution on the $EuTiO_3$ crystal structure and thermoelectric transport properties were systematically investigated. According to synchrotron XRD data only cubic perovskite structures were observed for all powder samples. On the local scale below about 20 Å (equal to ~ 5 unit cells) deviations from the cubic structure model ($Pm\bar{3}m$) were detected by evaluation of the PDF. These deviations cannot be explained by a simple symmetry breaking model like in $EuTiO_{3-\delta}$. The best fit was achieved in space group *Amm*2 allowing for a movement of Ti and Ba/Eu along <110> of the parent unit cell as observed for $BaTiO_3$. The electronic transport properties revealed that europium barium titanates exhibit n-type semiconducting behavior and that at high temperature the electrical conductivity is strongly depended on the Eu^{2+} content. Activation energies calculated from the electrical conductivity and Seebeck coefficient data indicate that at high temperature (800 K < T < 1123 K) the conduction mechanism of $Eu_{1-x}Ba_xTiO_{3-\delta}$ ($0 \leq x \leq 0.9$) is a polaron hopping when $0.4 \leq x \leq 1$ and a thermally activated process when $0 \leq x < 0.4$. Besides, the thermal conductivity decreases with increasing Ba^{2+} concentration. A maximum ZT value of 0.24 at 1123 K was obtained for $Eu_{0.9}Ba_{0.1}TiO_{3-\delta}$.

3.1 Introduction

Both Ba and Eu are sixth-period elements in the periodic table. Ba is the fifth element of alkaline earth metals in group 2 and Eu is the seventh rare earth element of the lanthanides. Although their perovskite-type titanates ($ATiO_3$) have many things in common, they display in a variety of very

different physical properties. $BaTiO_3$ is one of the most intensively investigated perovskite-type oxide materials due to its rich physical properties, such as ferroelectricity [1], piezoelectricity [2], high dielectric constant [3] and so on, allowing for a wide range of application. While $EuTiO_3$ is a well-known magnetic material especially renowned for its G-type antiferromagnetic (AFM) configuration below Néel temperature (T_N = 5.3 K) [4,5], it is a promising candidate as ferromagnetic and ferroelectric material [6].

Based on the combination of these inherent properties from the original system $BaTiO_3$ (ferroelectric-nonmagnetic) [1] and $EuTiO_3$ (paraelectric-antiferromagnetic) [7], the partial substituted solid solutions $Eu_{1-x}Ba_xTiO_3$ ($0 < x < 1$) are highly possible to give rise to some exceptional phenomena, such as multiferroicity, magnetocaloric effects, thermoelectricity, and so on. For instance, $Eu_{0.5}Ba_{0.5}TiO_3$ exhibits simultaneously fairly large ferroelectricity and a magnetic moment [8]. It was confirmed to be a multiferroic material used to search for the permanent electric dipole moment of the electron [9]. The compounds of the $Eu_{1-x}Ba_xTiO_{3-\delta}$ family exhibit a giant magnetocaloric effect, indicating that these compounds could be potential candidates for cryogenic magnetic refrigeration [10]. Accordingly, $Eu_{1-x}Ba_xTiO_{3-\delta}$ is a very interesting multifunctional oxide ceramic material, which has been extensively studied for various applications [11,12]. However, to the best of my knowledge, there are hardly any systematic studies about the thermoelectric properties of this material. Hence, in this chapter, the synthesized $Eu_{1-x}Ba_xTiO_{3-\delta}$ ($0 \leq x \leq 1$) compounds were systematically studied on the effect of the Ba^{2+} substitution to the crystal structure and thermoelectric properties. The possible relationships between the crystal structure and thermoelectric properties were evaluated. A possible electron conduction mechanism for $Eu_{1-x}Ba_xTiO_{3-\delta}$ is also discussed.

3.2 Experimental

3.2.1 Samples synthesis and preparation

A series of polycrystalline $Eu_{1-x}Ba_xTiO_{3-\delta}$ ($0 \leq x \leq 1$) samples were synthesized using a Pechini method followed by annealing under reducing conditions. The chemicals used for the experiment were Eu_2O_3 (Alfa Aesar, 99.9 %), barium acetate (Sigma-Aldrich, ≥ 99 %), citric acid (Sigma-Aldrich, 99 %), titanium(IV) bis (ammonium lactato) dihydroxide solution (Sigma-Aldrich, 50 wt. % in H_2O) and ethylene glycol (Sigma-Aldrich, ≥ 99 %). The detailed experimental parameters and procedures can be found in chapter 2. The colors of the obtained samples gradually changed from dark gray to black with increasing europium concentration.

The disc-shaped bulk samples were prepared by cold isostatic pressing at ~ 0.64 GPa to get the green compacted pellets followed by conventional ceramic sintering at 1473 K ≤ T ≤ ~1673 K for 12 h under the identical conditions to the annealing process. The sintering behavior becomes worse or more difficult depending on the Ba^{2+} substitution content. It is very difficult to obtain the dense bulk samples of x = 0.7 and 0.9. During several sintering experiments with or without intermediate grinding, lots of obvious cracks were always observed in these two samples. Hence, the thermoelectric transport properties of the two compositions were not taken into account in this study. The other sintered disc samples were cut into rectangular bars (~ 10 × 3 × 2 mm^3) for electrical transport property measurements and square pellets (~ 8 × 8 × 2 mm^3) for the thermal diffusivity measurements.

3.2.2 Samples characterization

Powder XRD data of all powder samples before and after sintering were collected by a Rigaku Smartlab X-ray diffractometer using Cu-$K\alpha_{1,2}$ radiation. Cu-K_β radiation was suppressed by a thin nickel foil with approximately 90 % efficiency. The diffraction patterns were recorded from 10° to 90° (2 theta) using continuous scanning at a step size of 0.01°. Rietveld refinements [13,14] were carried out using *FullProf* 2.k [15]. A pseudo-Voigt function was selected to describe the reflection profile. The background was treated by a 4th order polynomial function.

Synchrotron radiation powder diffraction was executed on the synthesized powders $Eu_{1-x}Ba_xTiO_{3-\delta}$ (x = 0.3, 0.5, 0.7) at 300 K at the ID22 beamline of the ESRF in Grenoble, France. The powder samples were loaded into 0.7 mm diameter Kapton® capillaries and mounted parallel to the axis of the diffractometer. Data were collected using both the high-resolution setup (λ = 0.32634(1) Å) for Rietveld refinements and a 2D CCD detector (Perkin Elmer XRD 1611CP3) for PDF analysis (λ = 0.17712(1) Å). In the latter case, wavelength, sample-detector distance (379.3 mm), and azimuthal integration parameters were calibrated on a CeO_2 reference that was sintered for 4 h at 1673 K. The detector mask was created with the program FIT2D [16]; calibration and azimuthal integration were all done using the program pyFAI [17].

The average crystallographic structure was determined by employing the Rietveld method [14], using the software GSAS [18]. The background was fitted by Chebyshev polynomials; absorption was corrected through the Lobanov empirical formula for the Debye-Scherrer geometry; line profiles were reproduced using a modified pseudo-Voigt function (function 3 in GSAS) accounting for asymmetry correction. In the last refinement cycles, scale factor, cell parameters, positional coordinates and atomic mean square displacements (*adp*) were allowed to vary as well as background and line profile parameters.

Deviations from the long-range structure were studied by means of the PDF method. Analysis of the interatomic distances made use of the reduced PDF, G(r), which is the product of the sine Fourier transform of the experimental total scattering function, *S(Q)*, defined as [19]:

$$G(r) = 4\pi r[\rho(r) - \rho_0] = \frac{2}{\pi}\int_{Q_{min}}^{Q_{max}} Q[S(Q) - 1]\, sin(Qr)\, dQ \qquad (3\text{-}1)$$

where $\rho(r)$ is the atomic pair density function and indicates the probability of finding an atom at a distance r from another atom, while ρ_0 is the atom number density. The G(r) function measures deviations from the average atomic density: a positive (negative) peak in the G(r) pattern indicates a range of r values whereby the probability of finding interatomic vectors is greater (lower) than that determined by the number density. G(r) curves were computed using the PDFgetX3 program [20] using data up to Q_{max} = 28.0 Å (where $Q = 4\pi\cdot\sin\theta/\lambda$ is the scattering vector). After background subtraction, the data were corrected for sample self-absorption, multiple scattering, and Compton scattering before Fourier transform finally yields the G(r) function. Structure refinements against the $G(r)$ curves were carried out using the PDF GUI program [21]. The program assesses the accuracy of the refinements by the agreement factor (R_w) defined as follows [21]:

$$R_w = \left[\frac{\sum wi(G_i^{exp} - G_i^{calc})^2}{\sum wi(G_i^{exp})^2}\right]^{\frac{1}{2}} \qquad (3\text{-}2)$$

DFT calculations were performed with the VASP (Vienna ab initio simulation package) code [22] using the Heyd-Scuseria-Ernzerhof (HSE) hybrid functional [23] for the electronic exchange and correlation and an 8 × 8 × 6 *k*-point grid. Therefore, a $\sqrt{2} \times \sqrt{2} \times 2$ supercell of the cubic perovskite structure of $Eu_{1-x}Ba_xTiO_3$ was modeled. The supercell contains four formula unit cells and hence allows to tune *x* from 0, 0.25, 0.50, 0.75 to 1. The lattice parameters and internal atomic positions were fully relaxed.

The content of metal ions (Eu, Ba, Ti) was determined by ICP-OES, the oxygen content was analyzed by carbothermal fusion using carrier gas hot gas extraction technique. Each measurement was repeated at least three times. The morphology of the annealed powders and the cross sections of the sintered samples were characterized by scanning electron microscopy (SEM, Zeiss Merlin). Samples were sputtered with 1.5 nm iridium to enhance the conductivity on the surface.

The electrical resistivity (ρ) and the Seebeck coefficient (α) were measured simultaneously by a Seebeck coefficient / electric resistance measurement system (ZEM-3, Ulvac Riko) from ambient temperature to 1123 K in a forming gas atmosphere (5 vol.% H_2 in Ar). The uncertainty of the electrical resistivity and the Seebeck coefficient measurements is 3 %. The thermal conductivity (κ) was derived from experimental density (d), thermal diffusivity (Λ) and specific heat capacity (c_p) values using the relationship:

$$\kappa = d \cdot \Lambda \cdot c_p \tag{3-3}$$

Experimental densities (d) of the bulk samples were determined by the Archimedes method. The thermal diffusivity (Λ) was measured using a Netzsch LFA 457 laser flash analyzer in the temperature range of 300 K to 1173 K under a forming gas atmosphere (5 vol.% H_2 in Ar). The c_p was calculated by the Dulong-Petit law $3NR/M$, where N is the number of moles including all atoms, R the gas constant (8.314 J/mol K) and M the molar mass of the compound (g/mol). The uncertainties of the k, c_p and d are 5 %, 5 %, and 2 %, respectively. Accordingly, the uncertainty of the calculated ZT value results in 20 % by combining all those uncertainties.

3.3 Results and discussion

3.3.1 Crystal structure and microstructure

All synthesized powder samples were single phase, according to the collected PXRD data. The obtained reflections can be indexed in a cubic perovskite structure with space group $Pm\bar{3}m$, as shown in Fig. 1(a). A weak reflection was observed for all samples at around 2θ = 28.8°, which results from the residual K_β radiation. Ba^{2+} substitution in $EuTiO_3$ results in unit cell expansion because the radius of Ba^{2+} ($r(Ba^{2+})$ = 1.75 Å [24]) is larger than that of Eu^{2+} ($r(Eu^{2+})$ = 1.59 Å, the value is extrapolated from the data given in literature [24]). Therefore, the PXRD reflections regularly shift to smaller diffraction angles, as shown in Fig. 1(b). All as-prepared Ba^{2+}-substituted $EuTiO_3$ based compounds show a cubic perovskite structure at ambient temperature. The cubic perovskite structure was confirmed by synchrotron radiation diffraction measurements (s. below).

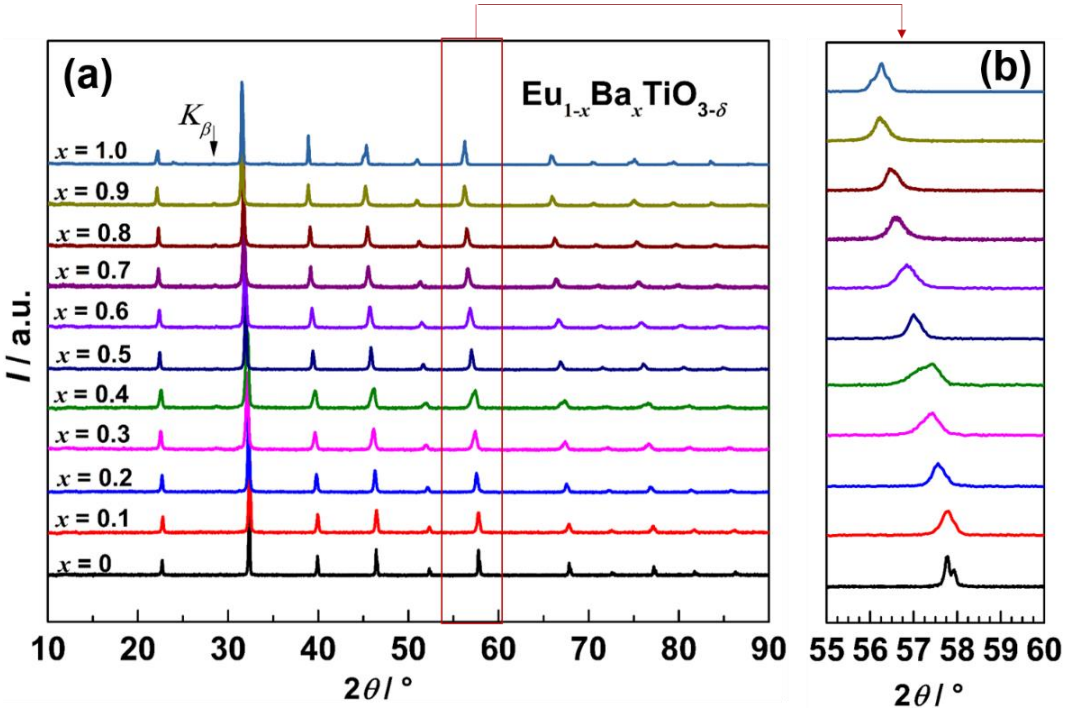

Fig. 3.1 Powder X-ray diffraction patterns for synthesized $Eu_{1-x}Ba_xTiO_{3-\delta}$ ($0 \leq x \leq 1$) samples (a) and zoom in XRD patterns (b) (all collected XRD data contain a contribution of Cu-$K\alpha_2$).

The crystal structures of the samples have been refined by using the obtained PXRD raw data at ambient conditions. All refinement results are highly consistent with the proposed cubic structure model of perovskite-type $Eu_{1-x}Ba_xTiO_{3-\delta}$. Fig. 2 (a) and (b) present the refinement pattern of the sample $x = 0.5$ and the unit cell parameters depending on the Eu^{2+} concentration, respectively. The unit cell parameter increases linearly with increasing Ba^{2+} concentration following Vegard's law. The unit cell parameter of $BaTiO_3$ obtained by DFT calculations was 3.99 Å. Upon increasing the Eu^{2+} concentration it decreased to a value of 3.91 Å for $EuTiO_3$, which is in excellent agreement with experimental values.

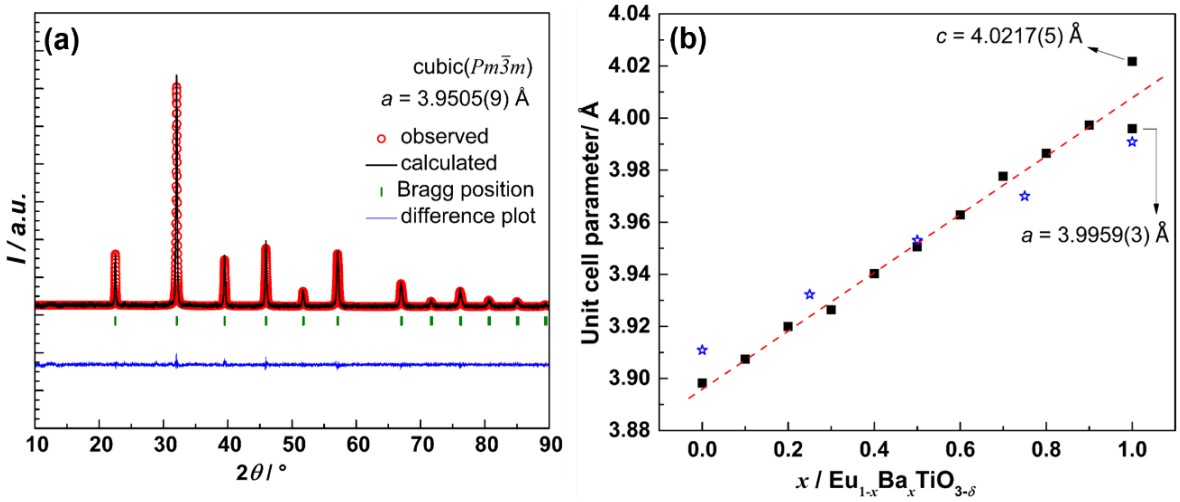

Fig. 3.2 Powder X-ray diffraction refinement pattern of sample $Eu_{0.5}Ba_{0.5}TiO_{3-\delta}$ (a) and the unit cell parameters as a function of the Ba^{2+} concentration (b), the star symbols denote the unit cell parameters calculated using DFT.

The chemical compositions of all samples are summarized in Table 3.1. The cationic ratio for all samples was in good agreement with the nominal composition. In addition, all samples showed oxygen deficiency due to the reducing atmosphere used during both the synthesis and the sintering process. There is no clear relationship between the oxygen deficiency and Ba^{2+} content. Nevertheless, in this study, the effect of oxygen vacancies on the TE properties can be neglected at high temperature ($T > 783$ K) compared to that of Eu^{2+} content, which will be discussed later in more detail.

Table 3.1 Experimental composition, refined unit cell parameter (a), experimental bulk density (d), relative density (ζ), porosity (ε) of the sintered bulk $Eu_{1-x}Ba_xTiO_{3-\delta}$ ($0 \le x \le 0.9$) samples. Estimated standard deviations (ESDs) are given in brackets.

Sample No.	Experimental composition				a / Å	d / g/cm³	ζ*/ %	ε / %
	Eu	Ba	Ti	O				
$x = 0$	0.988(9)		1.00(1)	2.98(6)	3.9048(4)	6.18	89	11
$x = 0.1$	0.900(5)	0.104(1)	1.02(1)	2.86(3)	3.9074(4)	5.92	86	14
$x = 0.2$	0.793(8)	0.205(4)	1.03(1)	2.97(3)	3.9199(6)	5.69	84	16
$x = 0.3$	0.692(8)	0.307(4)	1.01(1)	2.95(3)	3.9264(3)	6.37	97	3
$x = 0.4$	0.604(7)	0.387(3)	1.00(1)	2.95(3)	3.9402(7)	6.17	94	6
$x = 0.5$	0.499(7)	0.513(5)	1.01(1)	2.93(3)	3.9505(9)	5.97	93	7
$x = 0.6$	0.387(4)	0.604(6)	1.01(1)	2.97(3)	3.9627(8)	6.07	95	5
$x = 0.7$	0.297(3)	0.704(7)	1.00(1)	2.87(3)	3.9776(6)	5.78	91	9
$x = 0.8$	0.207(3)	0.795(8)	1.03(1)	2.92(3)	3.9865(3)	5.55	90	10
$x = 0.9$	0.100(1)	0.892(8)	1.01(1)	2.89(3)	3.9973(4)	5.27	86	14

*Theoretical densities are obtained by XRD refinement calculation.

Table 3.2 Rietveld refinement results referring to $Eu_{1-x}Ba_xTiO_{3-\delta}$ samples. Atomic positions are Ti (0, 0, 0), Ba/Eu (½, ½ ½) and O (0, ½, 0). The atomic *adp* parameters U are expressed in Å^2. Please note that Eu/Ba and Ti *adp* are isotropic because of symmetry constraints.

Sample No.	a/ Å	U				R_p	$R(F^2)$
		U(Eu/Ba)	U(Ti)	$U_{11/33}$(O)	U_{22}(O)		
$x = 0.3$	3.93198(2)	0.00647(4)	0.00488(7)	0.0092(4)	0.0037(6)	0.0400	0.0212
$x = 0.5$	3.95372(8)	0.00689(3)	0.00605(7)	0.0092(3)	0.0050(5)	0.0337	0.0244
$x = 0.7$	3.98047(3)	0.00796(8)	0.0073(1)	0.0089(6)	0.0070(10)	0.0437	0.0339

Synchrotron radiation diffraction data of the selected samples ($x = 0.3$, 0.5, 0.7) collected at ambient temperature allows some insight into the structure of $Eu_{1-x}Ba_xTiO_{3-\delta}$ compounds at different length scales. SR-PXRD data have been first analyzed through the Rietveld method. Fig. 3.3 (a) shows the fit of the $x = 0.5$ sample, while the refined structural parameters for all the solid solutions are reported in Table 3.2.

The Rietveld analysis of high-resolution PXRD data shows that all the investigated $Eu_{1-x}Ba_xTiO_{3-\delta}$ solid solution members have an undistorted cubic perovskite-type structure (space group $Pm\bar{3}m$) at $T = 300$ K, consistent with the laboratory PXRD data. The volume occupied by one formula unit of $Eu_{1-x}Ba_xTiO_{3-\delta}$ increases linearly according to the larger ionic radius of Ba^{2+} with respect to Eu^{2+}.

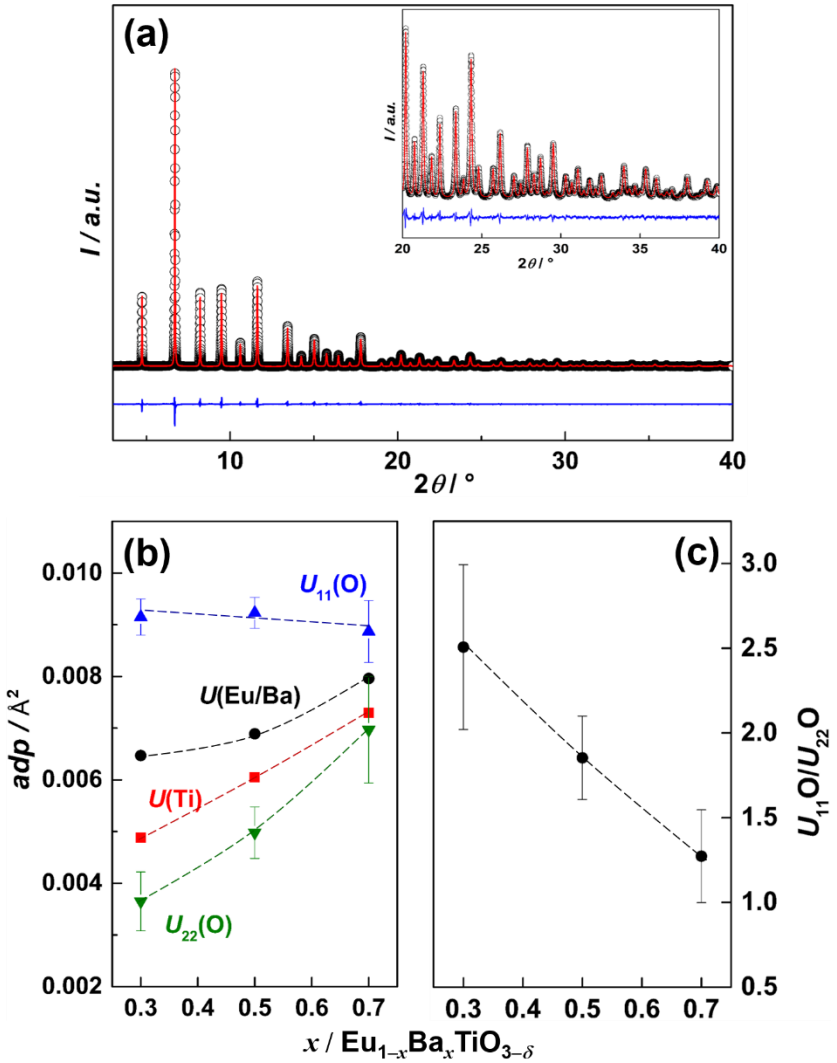

Fig. 3.3 (a) PXRD pattern of $Ba_{0.5}Eu_{0.5}TiO_{3-\delta}$. Measured (black crosses) and calculated (red line) profiles are shown as well as residuals (blue line). The inset highlights the high 2θ range. (b) U(Eu/Ba), U(Ti), U_{11}(O) and U_{22}(O) mean square displacement parameters (*adp*) represented as black circles, red squares, blue triangles up, green triangles down, respectively. (c) U_{11}(O)/U_{22}(O) ratio at 90 K.

The atomic mean square displacement parameters (*adp*) U are strongly related to the disorder status of these solid solutions [25,26]. Fig. 3.3 (b) reports the dependence of U(Eu/Ba), U(Ti), U_{11}(O), and U_{22}(O) on the Eu^{2+} concentration. In the anisotropic oxygen *adp* tensor U_{22}(O) is along the Ti–O–Ti bond and U_{11}(O) ($\equiv U_{33}$(O)) perpendicular to it. A steep decrease of the U_{11}(O)/U_{22}(O) ratio is observed as the sample becomes richer in Ba^{2+} (Fig. 3.3 (c)), because U_{22}(O) increases while U_{11}(O) remains nearly constants (Fig. 3.3 (b)). This ratio should be much larger than 1 in absence of any disorder because the potential energy surface normally rises more steeply along the Ti–O bond direction than in the direction perpendicular to it. The decreasing ratio suggests a broader distribution of the Ti–O bonds along the bonding direction, probably by imitating the off-centering of Ti^{4+} and Eu^{2+}/Ba^{2+} as known from $BaTiO_3$. The disorder picture was further investigated by a PDF analysis of the 2D data of the same sample aliquots. PDF analysis revealed a clear mismatch between the short-range structure and the long-range crystallographic phase of $Eu_{1-x}Ba_xTiO_{3-\delta}$.

$G(r)$ of any sample was not adequately reproduced by the cubic long-range structure model in the short-range region ($2.4 \leq r \leq 8$ Å, see Fig. 3.4 (a-c)). Symmetry lowering taking into account polar distortion modes as in $BaTiO_3$ [27] and non-polar modes as in $EuTiO_3$ [28], respectively, was tested. $G(r)$ fits in the range evidenced a small magnitude of structural distortion compared with other disordered perovskites [29,30]. However, a simple model based on one of the possible symmetry breaking of $Pm\bar{3}m$ was not able to reproduce the short-range order while models combing polar and non-polar modes (e.g. *Ima*2, *R*3*c*)) led to overparameterized fits. The most suitable model for the $G(r)$ of all three samples was an *Amm*2 phase (Fig. 3.4 (d-f)). This model reflects the long-range structure of pure $BaTiO_3$ at RT [31] and allows for a movement of both Ti^{4+} and Ba^{2+}/Eu^{2+} along the <110> direction of the parent cubic cell (Fig. 3.4 (d-f)), while an *I*4/*mcm* model like in $EuTiO_3$ only accounts for the rotation of the octahedral network. Additionally, the *Amm*2 model allows for the emergence of uniformly oriented electric dipoles [27].

Polar modes comprise all the symmetry-breaking atomic displacements causing ferroelectric transitions, normally cation off-centerings with respect to their coordination cage, which relate to the center (Γ point) of the Brillouin zone; non-polar modes, or zone-boundary modes (*R* point), belong, for example, the rotational modes that cause the antiferrodistortive transition in both $EuTiO_3$ and $SrTiO_3$. The Γ_4^- transformation, which is responsible for the ferroelectric transition in $BaTiO_3$ [27], can lead to the space groups *P*4*mm*, *Amm*2, or *R*3*m* depending on the direction of the order parameter, i.e. the off-centering of Ti or Ba/Eu. This means that an electric dipole could form, respectively, in the directions <100>, <110>, or <111> with respect to the parent cubic structure.

The variation of the composition clearly revealed the involvement of the TiO_6 octahedra and the Ba/EuO_{12} cuboctahedra. For $x = 0.3$ the cuboctahedron is most distorted as evidenced by the change of the Ba–O–Ba angle from 158.6° to 156.9°. Conversely, the TiO_6 octahedra becomes more regular as expressed by Baur's distortion index *D* [32], where *D* is a standard deviation of the Ti–O distance distribution, (see Fig. 3.4 (g-i)) as it was observed above from the *adp* parameters.

The agreement between data and the $Pm\bar{3}m$ model gradually improves in successive fits covering farther distances in real space ($8 \leq r \leq 40$ Å). This gives an indication about the nanometer coherence length of the disorder in $Eu_{1-x}Ba_xTiO_{3-\delta}$ (Fig. 3.4 (j-l)). As Fig. 3.4 (m-o) evidence, the disordered *Amm*2 model and the cubic model are practically equivalent in the $r > 20$ Å range. Thus, since the symmetry breaking of $Pm\bar{3}m$ symmetry is confined to the nanometer scale, it can be inferred that local distortions with different orientations coexist in the same crystallite, preserving the long-range cubic symmetry [26].

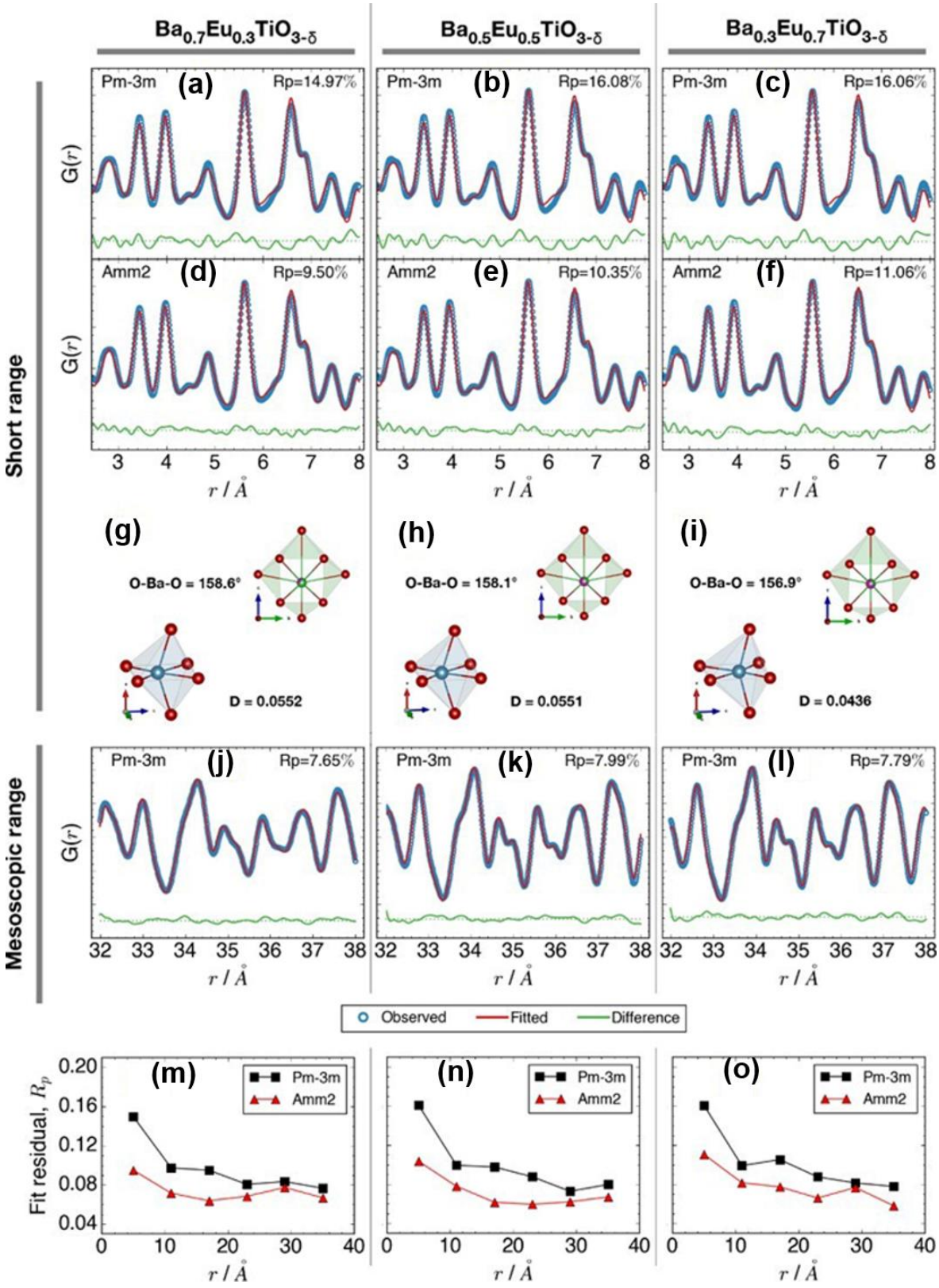

Fig. 3.4 (a)-(f) and (j)-(l) $G(r)$ functions of $Eu_{1-x}Ba_xTiO_{3-\delta}$ at different length scales and using different models. Measured (empty circles) and calculated (red line) $G(r)$ are shown as well as residuals (red line). The used space group and the residual parameter *Rp* of the refinements are written at the top of each panel. In (g)-(i) the distortions of Ti and Eu/Ba oxygen cages are depicted as sketches. *D* is the Baur's distortion index [32]. (m)-(o) report the *Rp* of fits at different *r* intervals (each 8 Å wide).

Fig. 3.5 shows SEM images of a synthesized powder sample as well as a cross-section of its corresponding sintered bulk sample for the compound $Eu_{0.5}Ba_{0.5}TiO_{3-\delta}$. As all synthesized powder samples, the illustrated sample has a homogeneous morphology and a particle size of around 40 nm (Fig. 3.5 (a) and (b)). The amorphous precursor underwent crystallization during the annealing process at 1273 K for 12 h leading to well-crystallized nanocrystals. The well-sintered bulk sample possessing high density with closed pores is clearly recognizable in Fig. 3.5(c) and (d). The bulk density and porosity are listed in Table 3.1. Assuming that the pores are spherical and homogeneously distributed in the dense bulk samples, the experimental electrical conductivity data and thermal conductivity data could be corrected with the Maxwell equation [33,34] for discussion.

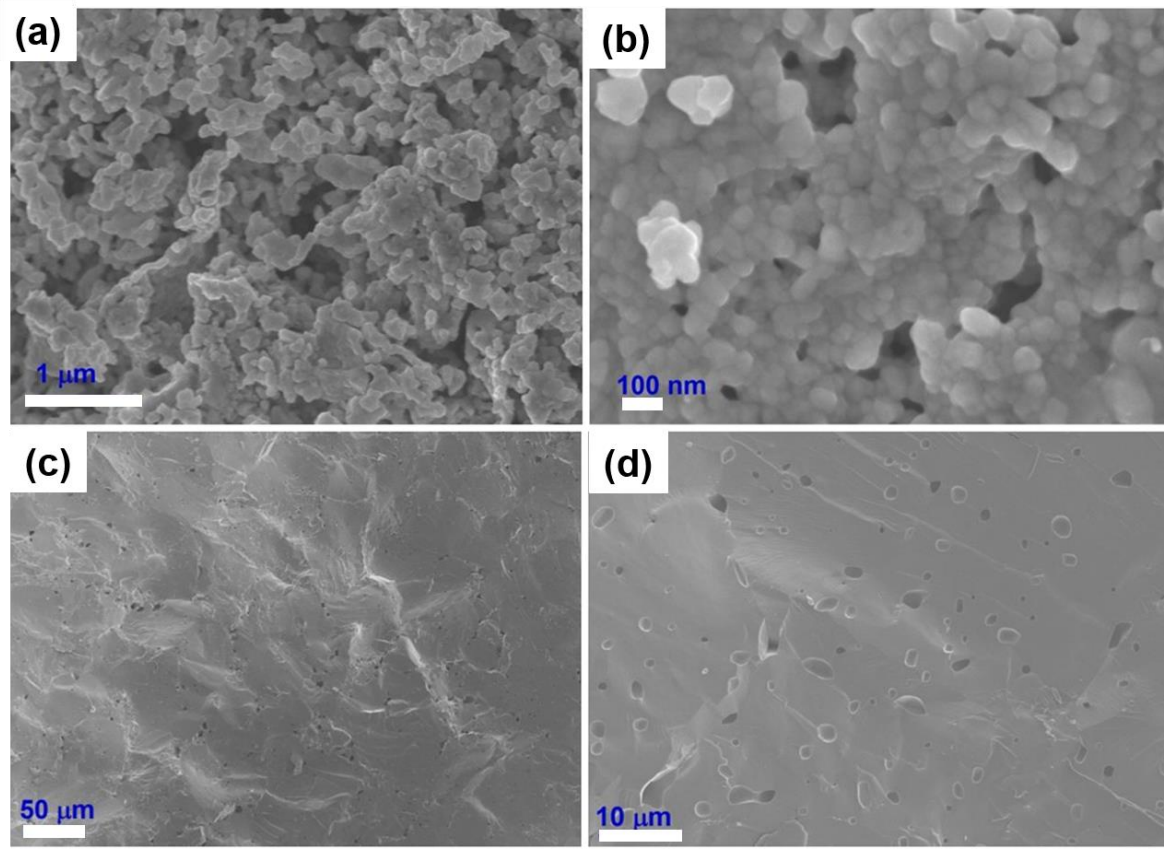

Fig. 3.5 SEM images of a synthesized powder sample (a), (b) and cross section of its corresponding well-sintered bulk sample (c), (d) for $Eu_{0.5}Ba_{0.5}TiO_{3-\delta}$.

3.3.2 Electrical transport properties

The temperature dependence of the Seebeck coefficient α of the sintered bulk samples $Eu_{1-x}Ba_xTiO_{3-\delta}$ (x = 0, 0.1, 0.2, 0.3, 0.4, 0.5, 0.6, 0.8, and 1) in the temperature range of 300 K < T < 1200 K is presented in Fig. 3.6. The α of the pristine sample $EuTiO_{3-\delta}$ is highly consistent with the reference data [35] (red dashed line with cross symbols in Fig. 3.6). After 10 % Ba^{2+} substitution, the absolute value of α significantly decreases at RT, i.e., α (x = 0.1, T = 323 K) ≈ 850 μVK^{-1}. The α of $Eu_{1-x}Ba_xTiO_{3-\delta}$ (0 < x <1) samples among each other differ not dramatically in the measured temperature range, displaying a similar temperature dependence trend with the pristine sample of

x = 0. A pure $BaTiO_3$ sample was prepared and the transport properties were evaluated under the same conditions as the substituted ones. Regarding the very large electrical resistivity of $BaTiO_3$ at room temperature, it was not possible to measure the electrical transport properties below 473 K with our ZEM measurement system. The electrical conductivity of $BaTiO_3$ was around 16 S/m at 1123 K, which is extremely lower than that of the $Eu_{1-x}Ba_xTiO_{3-\delta}$ (x < 1) samples. The sample $BaTiO_{3-\delta}$ behaves like an insulator over the entire investigated temperature range (see Fig. 3.7(a)). Hence, its σ and α are not comparable with the other $Eu_{1-x}Ba_xTiO_{3-\delta}$ (x <1) samples. The following discussion of electrical transport properties refers to the substituted samples, excluding the $BaTiO_{3-\delta}$. The values of α are negative in the entire measured temperature range, indicating that the dominant charge carriers are electrons. The α of n-type semiconductors can be calculated by the following equation [36]:

$$\alpha = \frac{-k}{e}\left(\frac{(r+2)F_{r+1}(\xi)}{(r+1)F_r(\xi)} - \xi\right) \tag{3-4}$$

where k is the Boltzmann constant, e the electron charge, ξ the chemical potential, r the scattering parameter of the relaxation time, and F_r the Fermi integral given by

$$F_r(\xi) = \int_0^\infty \frac{x^r}{1+e^{x-\xi}}dx \quad . \tag{3-5}$$

$|\alpha|$ monotonically decreases with increasing temperature due to a decrease of the Fermi integral with temperature. At low temperatures, there is no well-defined relation between Ba^{2+} substitution content and the value of α of $Eu_{1-x}Ba_xTiO_{3-\delta}$. However, at high temperatures (T > 1000 K), $|\alpha|$ measurably increases with enhanced Ba^{2+} content. In addition, the α values of $Eu_{1-x}Ba_xTiO_{3-\delta}$ are much less dependent on the temperature (T > 1000 K), suggesting that the kinetic terms of α can be neglected and the behavior of α can be described by Heikes formula [37]. $Eu_{1-x}Ba_xTiO_{3-\delta}$ compounds are considered to belong to strongly correlated electron systems [28,38,39] with a large on-site Coulomb repulsion parameter U [38,40]. Consequently, α can be estimated by the following modified Heikes formula [41]:

$$\alpha(T \to \infty) = \frac{-k}{e}\ln\frac{2(1-p)}{p} \tag{3-6}$$

where p is the charge carrier concentration per unit cell. By this means, the charge carrier concentration of $Eu_{1-x}Ba_xTiO_{3-\delta}$ can be calculated from the measured α values of $Eu_{1-x}Ba_xTiO_{3-\delta}$ at 1123 K. The results summarized in Table 3.3 show that the charge carrier concentration decreases with increasing Ba^{2+} concentration. This trend can be ascribed to the Eu 4f electrons, which will be discussed in more detail below.

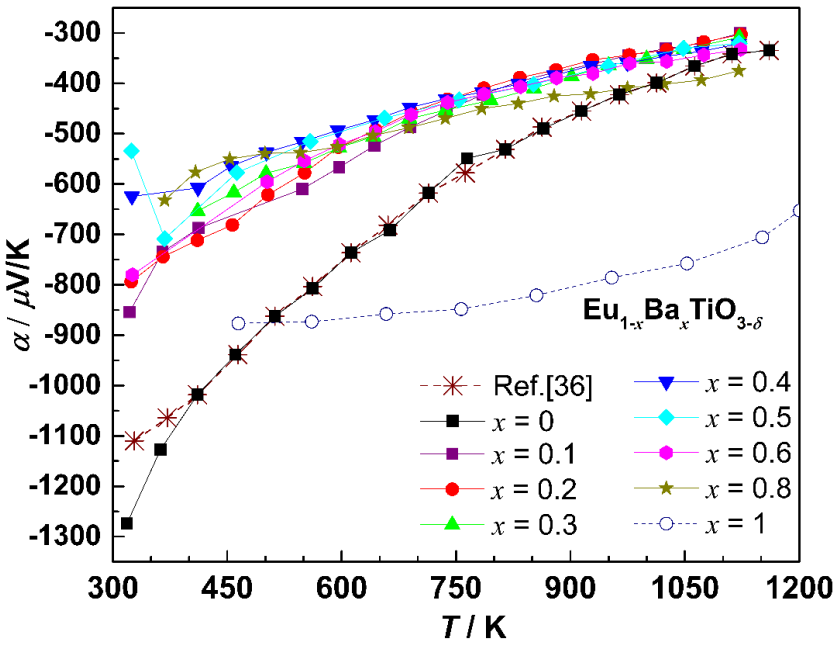

Fig. 3.6 Temperature dependence of the Seebeck coefficient α of sintered bulk samples $Eu_{1-x}Ba_xTiO_{3-\delta}$.

The electrical conductivity of the sintered $Eu_{1-x}Ba_xTiO_{3-\delta}$ samples as a function of temperature is shown in Fig. 3.7(a) and (b). The electrical conductivity increases with increasing temperature for all samples exhibiting semiconducting behavior in the whole measured temperature range, excluding $BaTiO_{3-\delta}$. With partial Ba^{2+} substitution, the electrical conductivity is considerably increased by up to a factor of 2 at 1173 K when $x \leq 0.5$ compared to the pristine sample of $x = 0$. Especially, the sample with 10 % Ba^{2+} substitution (i.e., $Eu_{0.9}Ba_{0.1}TiO_{3-\delta}$) exhibits the largest electrical conductivity at 1173 K. In addition, for the Ba^{2+} substituted samples, the electrical conductivity decreases with the increase of Ba^{2+} content at higher temperatures. This is consistent with the influence of Eu^{2+} substitution on the Seebeck coefficient at higher temperatures.

For all samples, the electrical conductivity exponentially increases between room temperature and about 470 K (see Fig. 3.7(b)), implying that electrons (main charge carriers) are excited from donor levels originating from Ti^{3+} or oxygen vacancies located below the bottom of the CB [42–44] into the conduction band in this temperature range [45,46]. At higher temperatures ($T > 783$ K), the electrical conductivity rapidly increases with increasing temperature. This can be ascribed to intrinsic excitation where the thermal energy is sufficient to excite electrons from the valence band to the conduction band.

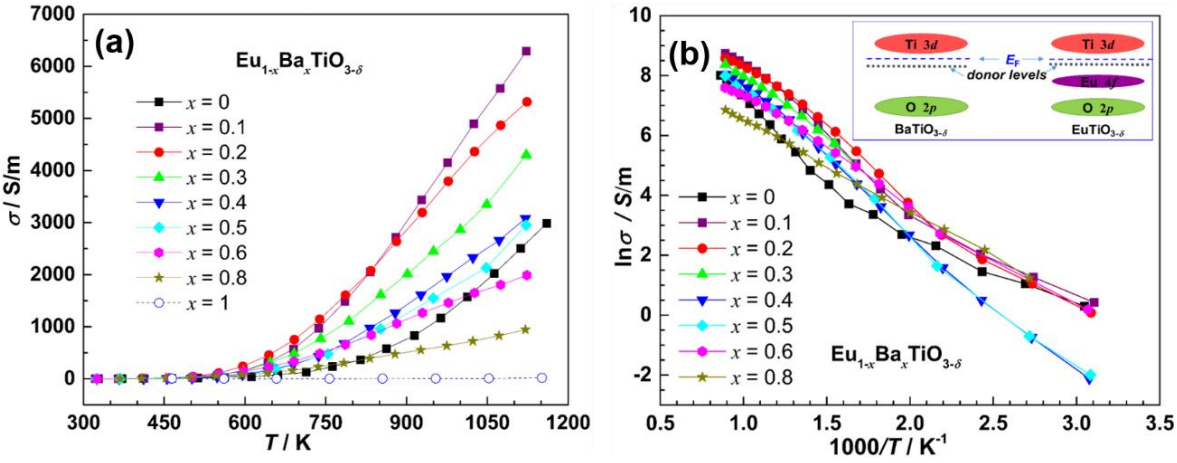

Fig. 3.7 Temperature dependence of the electrical conductivity of sintered $Eu_{1-x}Ba_xTiO_{3-\delta}$ bulk samples (a) and (b). The inset illustrates a schematic diagram of the band structures of $BaTiO_3$ and $EuTiO_3$.

The calculated total DOS of $Eu_{1-x}Ba_xTiO_{3-\delta}$ (x = 0, 0.25, 0.5, 0.75, 1) is shown in Fig. 3.8. For all samples, the conduction band mainly consists of Ti 3*d* states, while the top of the valence band consists of Eu 4*f* states instead of O 2*p* states for Eu containing samples. The results are in accordance with literature reports [47,48]. Similar as previously reported [47–50] for $EuTiO_3$ an energy gap of 0.9 eV between the filled Eu 4*f* (leading to a magnetic moment of 7μ_B) and the empty Ti 3*d* states was observed. With increasing the Ba^{2+} substitution, four obvious features can be concluded from the DOS calculations: (i) the intensity of the Eu^{2+} 4*f* DOS decreases as expected due to the dilution effect resulting from the substitution; (ii) the Eu 4*f* levels become narrower as seen from Fig. 3.8 (b); (iii) the energy gap is almost unchanged by varying the Ba^{2+} substitution level; (iv) the shapes of O 2*p* states and Ti 3*d* states are almost unchanged in the presented energy range. The results of the DOS calculations of $Eu_{1-x}Ba_xTiO_{3-\delta}$ are highly in agreement with the experimental data observed for the Seebeck coefficient and electrical conductivity measurements. This is especially obvious for two features: (i) the carrier density per unit cell of the filled Eu 4*f* is proportional to the Eu^{2+} concentration at high temperature (T > 1000 K); (ii) the almost unchanged band gap corresponds to a similar thermal activation energy as shown in Table 3.3. In principle, in the whole compositional and temperature range of this $Eu_{1-x}Ba_xTiO_{3-\delta}$ (x < 1) system electrons as charge carriers can be donated by either oxygen vacancies (not included in the DOS calculation model) or by the filled Eu^{2+} 4*f* levels. At high temperatures (T > 783 K), the electron transitions from Eu 4*f* to Ti 3*d* become dominant for conduction, which plays a central role in the improvement of the electrical conductivity [51]. Thus, it was concluded that the charge carrier concentration n became proportional to x, qualitatively consistent with the experimental results shown in Table 3.3.

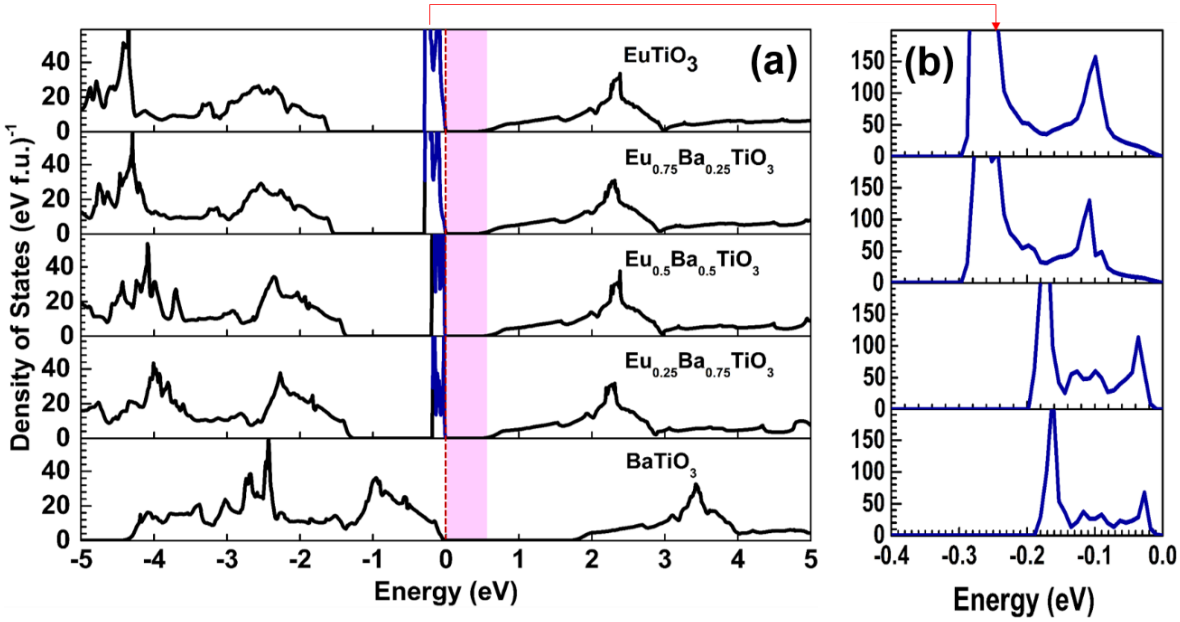

Fig. 3.8 Calculated total density of states (DOS) of $Eu_{1-x}Ba_xTiO_{3-\delta}$ (x = 0, 0.25, 0.5, 0.75, 1) (a) and the zoom in area of DOS (b). The zero level of energy is chosen as the top of the valence band. The pink area is a guide to the eye showing almost unchanged band gap.

In order to further investigate the dominant transport mechanism (thermal disorder, polaron hopping etc.) of $Eu_{1-x}Ba_xTiO_{3-\delta}$, the activation energies were quantified according to the model of Mott's adiabatic small polaron conduction [52]. $\rho(T)$ and $\alpha(T)$ curves are fitted by the formula [53]

$$\rho(T) = \rho_0 \exp\left(\frac{E_A}{k\,T}\right) \tag{3-7}$$

and

$$\alpha\,(T) = \frac{k}{e}\left(\frac{E_S}{k\,T} + r\right), \tag{3-8}$$

where E_A is the activation energy determined from the resistivity $\rho(T)$ measurement, E_S is the thermopower activation energy, ρ_0 as well as r are constants. Both the $\rho(T)$ and the $\alpha(T)$ curves were fitted in the same temperature range, and the results are illustrated in Fig. 3.9 by solid lines. When E_A is larger than E_S, thermally activated hopping with a hopping binding energy $W_p = 2(E_A - E_S)$ occurs [52,53]. The activation energies are calculated and listed in Table 3.3. The values of both E_A and E_S depend on the Eu^{2+} content, and the dependence behavior of E_A and E_S is similar. When $x \geq 0.4$, E_A is larger than E_S indicating that the dominating conduction mechanism belongs to polaron conduction. The small polaron hopping nature of $BaTiO_3$ was already clarified by Ihrig et al. [54]. Whereas, when $x < 0.4$, E_A is not larger than E_S implying the dominating conducting mechanism of $Eu_{1-x}Ba_xTiO_{3-\delta}$ system changes from polaron hopping conduction into thermally activated band conduction, which is consistent with $EuTiO_3$ [50]. PDF measurements showed that a decrease of the distortion of the TiO_6 octahedral is concomitant to the switching of the conduction regime suggesting that the local Ti environment should affect the polaron binding energy.

The carrier mobility (μ) of $Eu_{1-x}Ba_xTiO_{3-\delta}$ was calculated using the relation $\sigma = ne\mu$, where σ is the measured electrical conductivity and n is carrier concentration estimated by Heikes formula

(see equation (3-6)). The results are illustrated in Fig. 3.10 as a function of the Ba^{2+} content. The calculated μ values of as-prepared $Eu_{1-x}Ba_xTiO_{3-\delta}$ compounds are in the same order of magnitude as reference data of $BaTiO_3$ (0.1 – 0.5 $cm^2V^{-1}s^{-1}$) [54], and reveal that the carrier mobility of samples with band conduction ($x < 0.4$) was higher than that of samples with a polaron hopping mechanism ($x \geq 0.4$). The n of $BaTiO_{3-\delta}$ sample was estimated to be 8.5×10^{18} cm^{-3} at 1123 K according to Heikes formula, and the calculated carrier mobility was 0.13 $cm^2V^{-1}s^{-1}$, which is consistent with reference data [54,55].

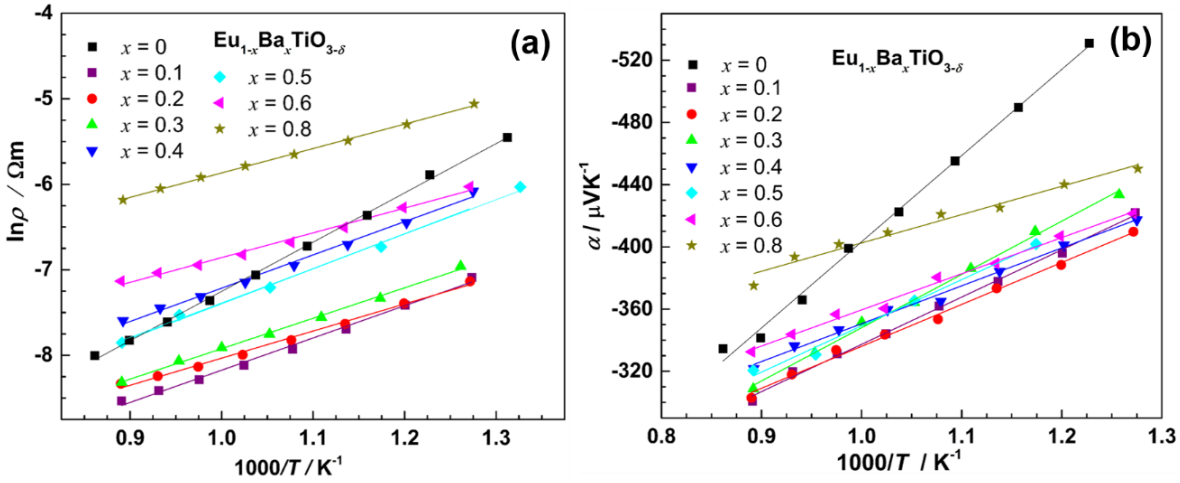

Fig. 3.9 Plot of $\ln\rho$ (a) and α (b) of $Eu_{1-x}Ba_xTiO_{3-\delta}$ samples as a function of the inverse temperature.

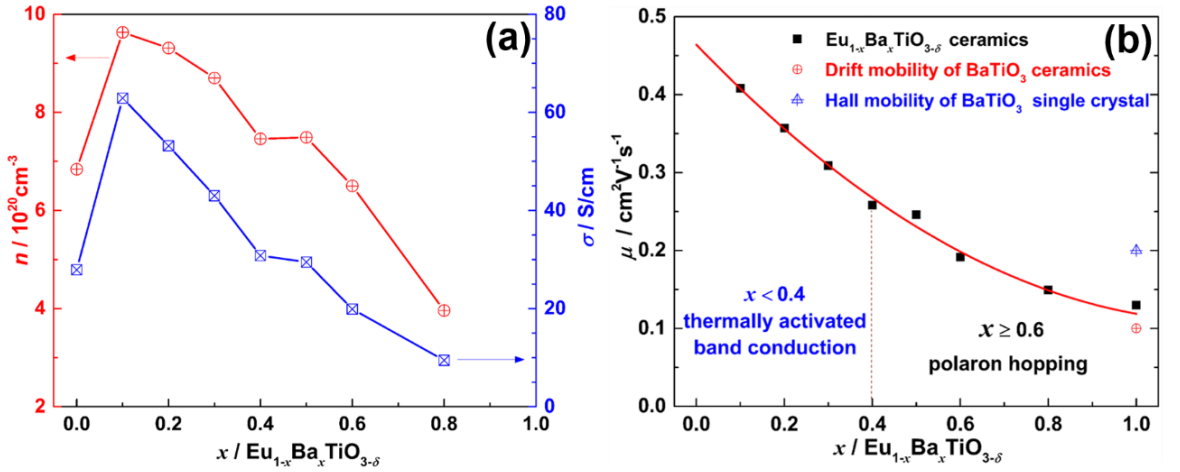

Fig. 3.10 Calculated charge carrier concentration n and measured electrical conductivity σ (a), and carrier mobility μ (b), as a function of the Ba^{2+} content x at 1123 K.

Table 3.3 Electrical conductivity σ, Seebeck coefficient α, activation energies E_A and E_S, polaron binding energy W_p, charge carrier concentration n and mobility μ of all measured $Eu_{1-x}Ba_xTiO_{3-\delta}$ samples at 1123 K.

Samples No.	σ (S/m)	E_A (eV)	α (μV/K)	E_s (eV)	W_p (eV)	n ($\times 10^{20}$ cm^3)	μ (cm^{2}V^{-1}s^{-1})
$x = 0$	2600	0.50	-338	0.55	-	6.8	0.26
$x = 0.1$	6289	0.30	-300	0.30	-	9.6	0.41
$x = 0.2$	5317	0.26	-302	0.27	-	9.3	0.35
$x = 0.3$	4300	0.29	-308	0.34	-	8.7	0.31
$x = 0.4$	3081	0.32	-321	0.24	0.16	7.5	0.26
$x = 0.5$	2948	0.33	-320	0.30	0.06	7.5	0.25
$x = 0.6$	1990	0.24	-332	0.23	0.02	6.5	0.19
$x = 0.8$	945	0.24	-375	0.18	0.12	4.0	0.15

The power factor ($PF = \alpha^2\sigma$) is primarily a measure of the electrical properties of a thermoelectric material. The PF values of $Eu_{1-x}Ba_xTiO_{3-\delta}$ are shown in Fig. 3.11. As discussed above, the Ba^{2+} substitution has a distinct influence on the electrical conductivity at high temperatures, while the variation of α among the samples is weak. Consequently, the resulting PF is mainly dependent on the variation of electrical conductivity. The PF of $Eu_{1-x}Ba_xTiO_{3-\delta}$ is enhanced when $x \leq 0.4$ and decreased when $x \geq 0.6$ compared with the pristine sample of $x = 0$. The highest PF of 0.55 mW/mK^2 is achieved for $Eu_{0.9}Ba_{0.1}TiO_{3-\delta}$ at 1070 K, which is by a factor of 2 higher compared to pristine sample $EuTiO_{3-\delta}$.

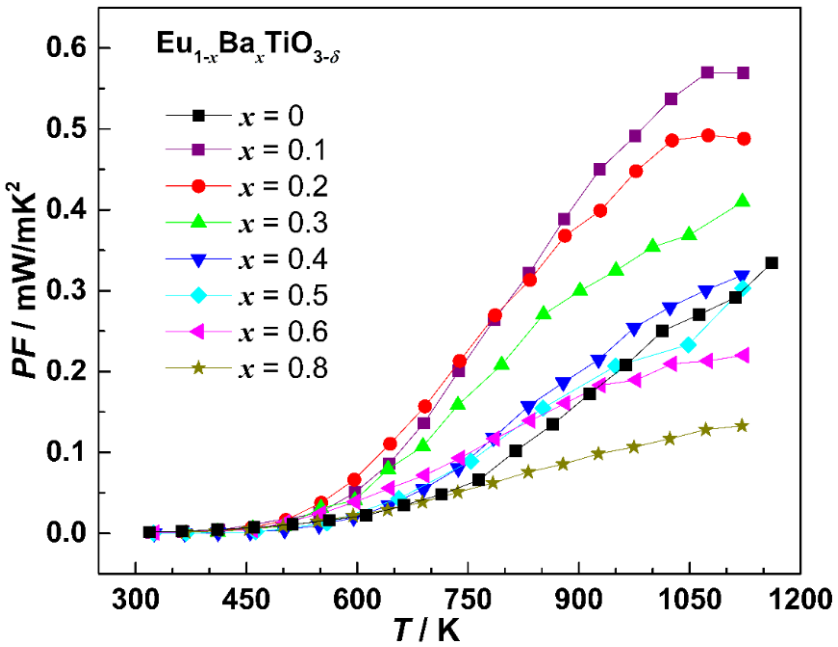

Fig. 3.11 Temperature dependence of the power factor (PF) of $Eu_{1-x}Ba_xTiO_{3-\delta}$ samples.

3.3.3 Thermal transport properties and *ZT*

The temperature dependence of the thermal conductivity (κ) of $Eu_{1-x}Ba_xTiO_{3-\delta}$ is shown in Fig. 3.12(a). At room temperature, κ generally decreases with increasing Ba^{2+} content x. The lattice thermal conductivity (κ_l) can be estimated from the equation $\kappa = \kappa_l + \kappa_e$. The electrical thermal conductivity κ_e can be derived from the Wiedemann-Franz relation, $\kappa_e = L_0\sigma T$, where L_0 is the Lorenz number. L_0 of degenerate systems is usually estimated at 2.45×10^{-8} V^2K^{-2}, although it depends on the Fermi energy, the band structure and the scattering process [56]. Since the electrical conductivity of all $Eu_{1-x}Ba_xTiO_{3-\delta}$ samples is quite low (highest value ~ 6×10^3 S/m), the calculated κ_e values account for less than 7 % of the total thermal conductivity; thus, it is reasonable to assume that $\kappa \approx \kappa_l$. In the whole measured temperature range, κ_l of all $Eu_{1-x}Ba_xTiO_{3-\delta}$ compounds approximately follows a T^{-1} dependence, indicating that the dominant phonon scattering mechanism in all $Eu_{1-x}Ba_xTiO_{3-\delta}$ compounds is the Umklapp scattering (phonon-phonon interactions). The thermal conductivity of $Eu_{1-x}Ba_xTiO_{3-\delta}$ ($x \geq 0.7$) samples possess a similar trend as $BaTiO_{3-\delta}$ sample. The transition around 390 K is due to the phase transition of tetragonal to cubic [57].

The dependence of κ_l on the Ba^{2+} content x of all $Eu_{1-x}Ba_xTiO_{3-\delta}$ compounds at 323 K and 1123 K is plotted in Fig. 3.12 (b). In a solid solution system, the lowest lattice thermal conductivity is usually associated with the highest disorder due to the mass fluctuation and point defect scattering. However, κ_l of the $Eu_{1-x}Ba_xTiO_{3-\delta}$ compounds decreased with increasing Ba^{2+} content. Similar results were previously obtained for the $BaTiO_3$–$SrTiO_3$ solid solution [58,59]. In accordance with PDF results, a possible interpretation of this finding is that Ba^{2+} substitution leads to an expansion of the Ti–O average distance, which weakens the Ti–O bond strength and consequently results in lower κ_l. In the studied system, the effect of the bond strength on the thermal conductivity appears to dominate over simultaneously occurring point defect scattering. In order to prove this theory, theoretical calculations on how the Ti–O bond length affects the lattice thermal conductivity of the $BaTiO_3$–$EuTiO_3$ solid solution should be conducted.

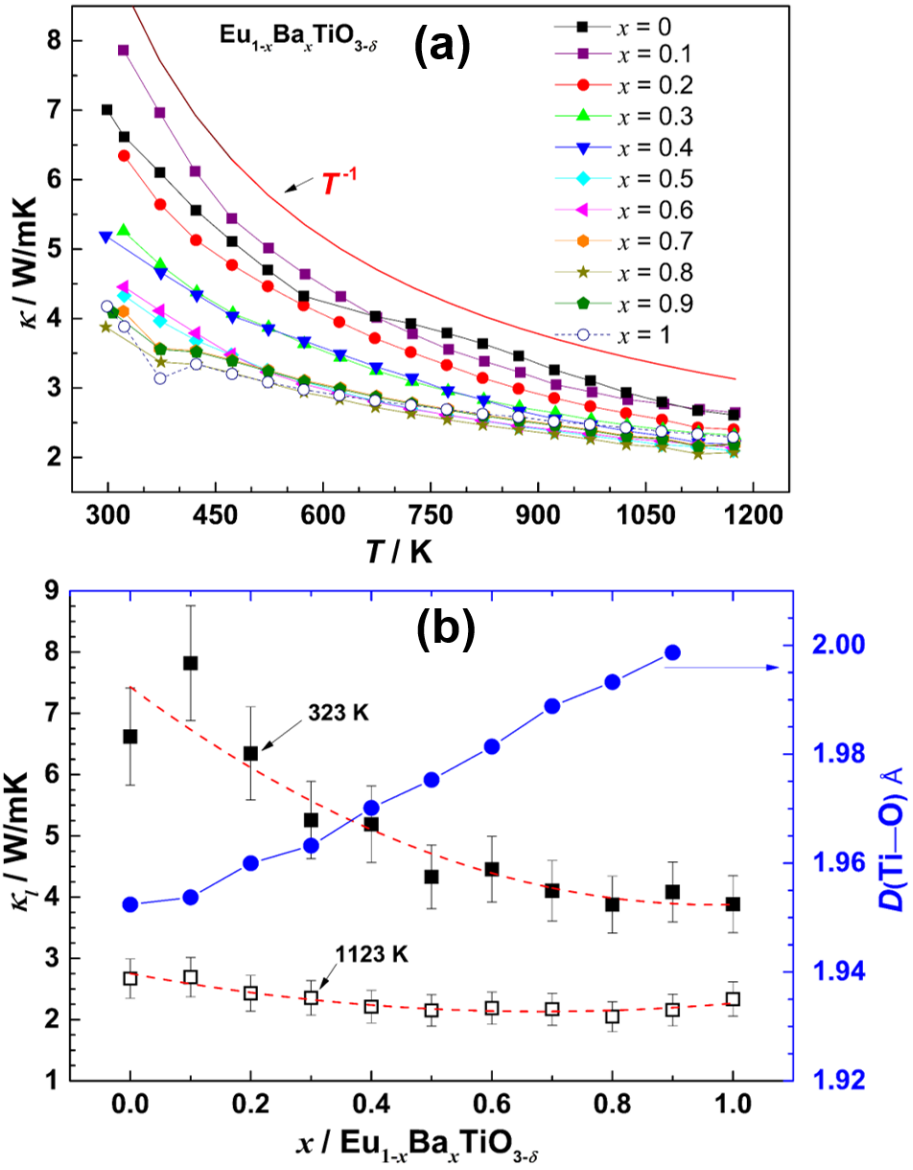

Fig. 3.12 (a) Temperature dependence of the thermal conductivity of $Eu_{1-x}Ba_xTiO_{3-\delta}$ samples; (b) compositional dependence of the lattice thermal conductivity at 323 K and 1123 K and average Ti–O distance at 323 K of $Eu_{1-x}Ba_xTiO_{3-\delta}$ samples.

The calculated *ZT* is shown in Fig. 3.13. The *ZT* of all samples monotonically increases with increasing temperature and reaches the highest value at the highest measured temperature $T = 1123$ K. Due to the enhancement of electrical conductivity as well as the resulting *PF* and the reduction of thermal conductivity, the Ba^{2+} substitution enhances the *ZT* value roughly when $x \leq 0.6$ at $T > 600$ K. From the point of view of overall Ba^{2+} substituted samples, the *ZT* value is decreasing with the increase of Ba^{2+} content. The highest *ZT* value of 0.24 is obtained at 1123 K for the $Eu_{0.9}Ba_{0.1}TiO_{3-\delta}$ sample. It is almost enhanced by 40 % compared with the pristine sample $EuTiO_{3-\delta}$, whose *ZT* value is about 0.17 at 1123 K.

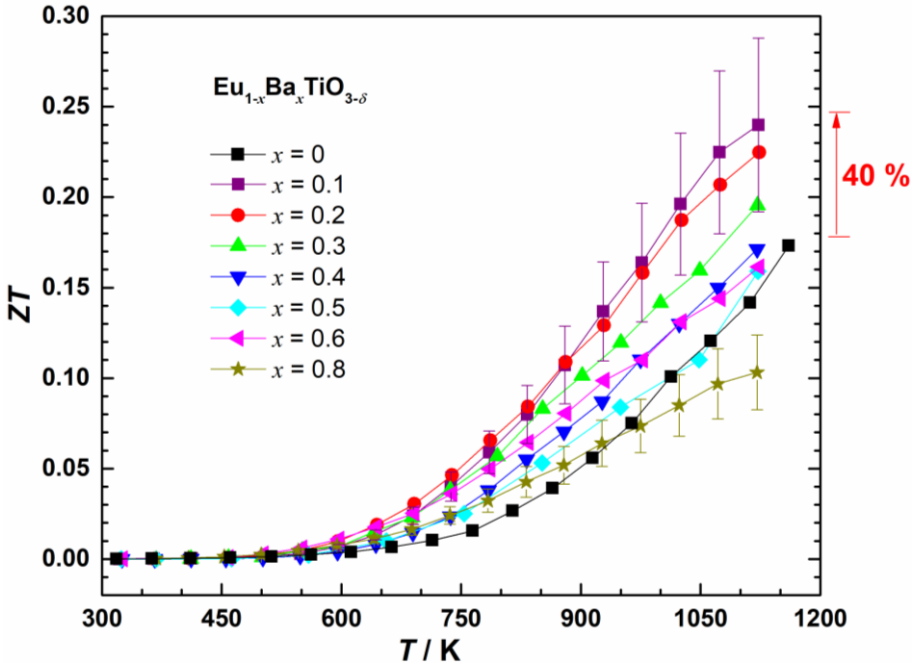

Fig. 3.13 Temperature dependence of *ZT* of $Eu_{1-x}Ba_xTiO_{3-\delta}$ samples.

3.4. Conclusions

Single phase Ba^{2+}-substituted $Eu_{1-x}Ba_xTiO_{3-\delta}$ compounds were successfully synthesized via a Pechini method followed by annealing and sintering under reducing conditions. The effects of Ba^{2+} substitution on the thermoelectric transport properties of $Eu_{1-x}Ba_xTiO_{3-\delta}$ were systematically investigated. Rietveld refinements of PXRD data revealed a cubic perovskite structure of all $Eu_{1-x}Ba_xTiO_{3-\delta}$ ($0 \leq x < 1$) synthesized samples. The unit cell parameter linearly increases with increasing Ba^{2+} content in accordance with Vegard's law. However, local polar distortions detected by PDF analysis with a coherence length of $\approx 1 - 2$ nm coexist within the cubic structure in the solid solutions. Calculations of the DOS revealed that the band gap is almost unchanged but the localized Eu^{2+} 4*f* levels are narrowing with increasing Ba^{2+} substitution. Partial Ba^{2+} substitution (i.e., if $x \leq 0.6$) increases the electrical conductivity and decreases the thermal conductivity. As a result, the *ZT* value is enhanced by the Ba^{2+} substitution in Eu^{2+}-rich compositions.

References

[1] K. Choi, M. Biegalski, Y. Li, A. Sharan, J. Schubert, R. Uecker, P. Reiche, Y. Chen, X. Pan, V. Gopalan, L. Chen, D. Schlom, C. Eom, Enhancement of ferroelectricity in strained $BaTiO_3$ thin films, *Science* 306 (2004) 1005–1009.

[2] S. Wada, K. Yako, H. Kakemoto, T. Tsurumi, T. Kiguchi, Enhanced piezoelectric properties of barium titanate single crystals with different engineered-domain sizes, *Journal of Applied Physics* 98 (2005) 14109.

[3] S. Roberts, Dielectric and piezoelectric properties of barium titanate, *Physical Review* 71 (1947) 890–895.

[4] T. McGuire, M. Shafer, R. Joenk, H. Alperin, S. Pickart, Magnetic structure of $EuTiO_3$, *Journal of Applied Physics* 37 (1966) 981–982.

[5] H. Akamatsu, Y. Kumagai, F. Oba, K. Fujita, H. Murakami, K. Tanaka, I. Tanaka, Antiferromagnetic superexchange via 3*d* states of titanium in $EuTiO_3$ as seen from hybrid Hartree-Fock density functional calculations, *Physical Review B* 83 (2011) 214421.

[6] J. Lee, L. Fang, E. Vlahos, X. Ke, Y. Jung, L. Kourkoutis, J. Kim, P. Ryan, T. Heeg, M. Roeckerath, V. Goian, M. Bernhagen, R. Uecker, P. Hammel, K. Rabe, S. Kamba, J. Schubert, J. Freeland, D. Muller, C. Fennie, P. Schiffer, V. Gopalan, E. Johnston-Halperin, D. Schlom, A strong ferroelectric ferromagnet created by means of spin-lattice coupling, *Nature* 466 (2010) 954–958.

[7] T. Katsufuji, H. Takagi, Coupling between magnetism and dielectric properties in quantum paraelectric $EuTiO_3$, *Physical Review B* 64 (2001) 54415.

[8] D. Janes, R. Bodnar, A. Taylor, Europium barium titanate—A magnetic ferroelectric compound, *Journal of Applied Physics* 49 (1978) 1452-1454.

[9] K. Rushchanskii, S. Kamba, V. Goian, P. Vanek, M. Savinov, J. Prokleska, D. Nuzhnyy, K. Knížek, F. Laufek, S. Eckel, S. Lamoreaux, A. Sushkov, M. Ležaić, N. Spaldin, A multiferroic material to search for the permanent electric dipole moment of the electron, *Nature materials* 9 (2010) 649–654.

[10] K. Rubi, P. Kumar, D. Repaka, R. Chen, J. Wang, R. Mahendiran, Giant magnetocaloric effect in magnetoelectric $Eu_{1-x}Ba_xTiO_3$, *Applied Physics Letters* 104 (2014) 32407.

[11] T. Wei, Q. Zhou, X. Yang, Q. Song, Z. Li, X. Qi, J. Liu, Competition between quantum fluctuation and ferroelectric order in $Eu_{1-x}Ba_xTiO_3$, *Applied Surface Science* 258 (2012) 4601–4606.

[12] H. Wu, Q. Jiang, W. Shen, Coupling between the magnetism and dielectric properties in $Eu_{1-x}Ba_xTiO_3$, *Physical Review B* 69 (2004) 014104.

[13] H. Rietveld, Line profiles of neutron powder-diffraction peaks for structure refinement, *Acta Crystallographica* 22 (1967) 151–152.

[14] H. Rietveld, A profile refinement method for nuclear and magnetic structures, *Journal of Applied Crystallography* 2 (1969) 65–71.

[15] J. Rodriguez-Carvajal, FullProf. 2k, version 5.30, March 2012, ILL.

[16] A. Hammersley, S. Svensson, M. Hanfland, A. Fitch, D. Hausermann, Two-dimensional detector software: from real detector to idealised image or two-theta scan, *International Journal of High Pressure Research* 14 (1996) 235–248.

[17] G. Ashiotis, A. Deschildre, Z. Nawaz, J. Wright, D. Karkoulis, F. Picca, J. Kieffer, The fast azimuthal integration Python library: pyFAI, *Journal of Applied Crystallography* 48 (2015) 510–519.
[18] A. Larson, R. von Dreele, Gsas, General Structure Analysis System. LANSCE, MS-H805, Los Alamos, New Mexico (1994).
[19] T. Egami, S. Billinge, Underneath the Bragg peaks: structural analysis of complex materials, Elsevier, 2003.
[20] P. Juhás, T. Davis, C. Farrow, S. Billinge, PDFgetX3: a rapid and highly automatable program for processing powder diffraction data into total scattering pair distribution functions, *Journal of Applied Crystallography* 46 (2013) 560–566.
[21] C. Farrow, P. Juhas, J. Liu, D. Bryndin, E. Božin, J. Bloch, T. Proffen, S. Billinge, PDFfit2 and PDFgui: computer programs for studying nanostructure in crystals, *Journal of Physics: Condensed Matter* 19 (2007) 335219.
[22] G. Kresse, D. Joubert, From ultrasoft pseudopotentials to the projector augmented-wave method, *Physical Review B* 59 (1999) 1758-1775.
[23] J. Heyd, G. Scuseria, M. Ernzerhof, Hybrid functionals based on a screened Coulomb potential, *The Journal of Chemical Physics* 118 (2003) 8207–8215.
[24] R. Shannon, Revised effective ionic radii and systematic studies of interatomic distances in halides and chalcogenides, *Acta Crystallographica Section A*: Crystal Physics, Diffraction, Theoretical and General Crystallography 32 (1976) 751–767.
[25] M. Scavini, M. Coduri, M. Allieta, M. Brunelli, C. Ferrero, Probing Complex Disorder in $Ce_{1-x}Gd_xO_{2-x/2}$ Using the Pair Distribution Function Analysis, *Chemistry of Materials* 24 (2012) 1338–1345.
[26] M. Scavini, M. Coduri, M. Allieta, P. Masala, S. Cappelli, C. Oliva, M. Brunelli, F. Orsini, C. Ferrero, Percolating hierarchical defect structures drive phase transformation in $Ce_{1-x}Gd_xO_{2-x/2}$: a total scattering study, *IUCrJ* 2 (2015) 511–522.
[27] M. Senn, D. Keen, T. Lucas, J. Hriljac, A. Goodwin, Emergence of Long-Range Order in $BaTiO_3$ from Local Symmetry-Breaking Distortions, *Physical Review Letters* 116 (2016) 207602.
[28] M. Allieta, M. Scavini, L. Spalek, V. Scagnoli, H. Walker, C. Panagopoulos, S. Saxena, T. Katsufuji, C. Mazzoli, Role of intrinsic disorder in the structural phase transition of magnetoelectric $EuTiO_3$, *Physical Review B* 85 (2012) 184107.
[29] S. Chong, R. Szczecinski, C. Bridges, M. Tucker, J. Claridge, M. Rosseinsky, Local Structure of a Pure Bi A Site Polar Perovskite Revealed by Pair Distribution Function Analysis and Reverse Monte Carlo Modeling: Correlated Off-Axis Displacements in a Rhombohedral Material, *Journal of the American Chemical Society* 134 (2012) 5836–5849.
[30] K. Datta, A. Richter, M. Göbbels, D. Keen, R. Neder, Direct mapping of microscopic polarization in ferroelectric $x(BiScO_3)-(1-x)(PbTiO_3)$ throughout its morphotropic phase boundary, *Physical Review B* 93 (2016) 64102.
[31] G. Kwei, A. Lawson, S. Billinge, S. Cheong, Structures of the ferroelectric phases of barium titanate, *The Journal of Physical Chemistry* 97 (1993) 2368–2377.
[32] W. Baur, The geometry of polyhedral distortions. Predictive relationships for the phosphate group, *Acta Crystallographica Section B*: Structural Crystallography and Crystal Chemistry 30 (1974) 1195–1215.

[33] A. Kovalevsky, S. Populoh, S. Patrício, P. Thiel, M. Ferro, D. Fagg, J. Frade, A. Weidenkaff, Design of $SrTiO_3$-based thermoelectrics by tungsten substitution, *The Journal of Physical Chemistry C* 119 (2015) 4466–4478.
[34] L. Zhang, T. Tosho, N. Okinaka, T. Akiyama, Thermoelectric properties of solution combustion synthesized Al-doped ZnO, *Materials Transactions* 49 (2008) 2868–2874.
[35] L. Sagarna, A. Shkabko, S. Populoh, L. Karvonen, A. Weidenkaff, Electronic structure and thermoelectric properties of nanostructured $EuTi_{1-x}Nb_xO_{3-\delta}$ (x = 0.00; 0.02), *Applied Physics Letters* 101 (2012) 33908.
[36] M. Yamamoto, H. Ohta, K. Koumoto, Thermoelectric phase diagram in a $CaTiO_3$-$SrTiO_3$-$BaTiO_3$ system, *Applied Physics Letters* 90 (2007) 072101-1.
[37] R. Heikes, R. Ure, Thermoelectricity: science and engineering, *Interscience Publishers*, 1961.
[38] R. Ranjan, H. Nabi, R. Pentcheva, Electronic structure and magnetism of $EuTiO_3$: a first-principles study, *Journal of Physics: Condensed Matter* 19 (2007) 406217.
[39] W. Koshibae, S. Maekawa, Effects of spin and orbital degeneracy on the thermopower of strongly correlated systems, *Physical Review Letters* 87 (2001) 236603.
[40] J. Kuneš, W. Pickett, Kondo and anti-Kondo coupling to local moments in EuB_6, *Physical Review B* 69 (2004) 165111.
[41] P. Chaikin, G. Beni, Thermopower in the correlated hopping regime, *Physical Review B* 13 (1976) 647-651.
[42] M. Miyauchi, M. Takashio, H. Tobimatsu, Photocatalytic activity of $SrTiO_3$ codoped with nitrogen and lanthanum under visible light illumination, *Langmuir* 20 (2004) 232–236.
[43] G. Lewis, C. Catlow, Defect studies of doped and undoped barium titanate using computer simulation techniques, *Journal of Physics and Chemistry of Solids* 47 (1986) 89–97.
[44] H. Eng, P. Barnes, B. Auer, P. Woodward, Investigations of the electronic structure of d^0 transition metal oxides belonging to the perovskite family, *Journal of Solid State Chemistry* 175 (2003) 94–109.
[45] W. Callister, D. Rethwisch, Materials science and engineering: an introduction, Wiley New York, 2007.
[46] B. Streetman, S. Banerjee, Solid state electronic devices, Prentice Hall New Jersey, 2000.
[47] S. Wemple, Polarization Fluctuations and the Optical-Absorption Edge in $BaTiO_3$, *Physical Review B* 2 (1970) 2679-2689.
[48] M. Cardona, Optical Properties and Band Structure of $SrTiO_3$ and $BaTiO_3$, *Physical Review* 140 (1965) A651-A655.
[49] J. Lee, X. Ke, N. Podraza, L. Kourkoutis, T. Heeg, M. Roeckerath, J. Freeland, C. Fennie, J. Schubert, D. Muller, P. Schiffer, D. Schlom, Optical band gap and magnetic properties of unstrained $EuTiO_3$ films, *Applied Physics Letters* 94 (2009) 212509.
[50] L. Sagarna, K. Rushchanskii, A. Maegli, S. Yoon, S. Populoh, A. Shkabko, S. Pokrant, M. Ležaić, R. Waser, A. Weidenkaff, Structure and thermoelectric properties of $EuTi(O, N)_{3\pm\delta}$, *Journal of Applied Physics* 114 (2013) 33701.
[51] L. Sagarna, S. Populoh, A. Shkabko, J. Eilertsen, A. Maegli, R. Hauert, M. Schrade, L. Karvonen, A. Weidenkaff, Influence of the Oxygen Content on the Electronic Transport Properties of $Sr_xEu_{1-x}TiO_{3-\delta}$, *The Journal of Physical Chemistry C* 118 (2014) 7821–7831.
[52] N. Mott, E.A. Davis, Electronic processes in non-crystalline materials, OUP Oxford, 2012.

[53] Y. Wang, Y. Sui, X. Wang, W. Su, Effects of substituting La^{3+}, Y^{3+} and Ce^{4+} for Ca^{2+} on the high temperature transport and thermoelectric properties of $CaMnO_3$, *Journal of Physics D: Applied Physics* 42 (2009) 55010.

[54] H. Ihrig, On the polaron nature of the charge transport in $BaTiO_3$, *Journal of Physics C: Solid State Physics* 9 (1976) 3469-3474.

[55] T. Kolodiazhnyi, A. Petric, M. Niewczas, C. Bridges, A. Safa-Sefat, J.E. Greedan, Thermoelectric power, Hall effect, and mobility of n-type $BaTiO_3$, *Physical Review B* 68 (2003) 85205.

[56] N. Wang, H. Chen, H. He, W. Norimatsu, M. Kusunoki, K. Koumoto, Enhanced thermoelectric performance of Nb-doped $SrTiO_3$ by nano-inclusion with low thermal conductivity, *Scientific Reports* 3 (2013) 3449.

[57] A. Mante, J. Volger, The thermal conductivity of $BaTiO_3$ in the neighbourhood of its ferroelectric transition temperatures, *Physics Letters A* 24 (1967) 139–140.

[58] H. Muta, A. Ieda, K. Kurosaki, S. Yamanaka, Thermoelectric Properties of Lanthanum-Doped Europium Titanate, *Materials Transactions* 46 (2005) 1466–1469.

[59] H. Muta, K. Kurosaki, S. Yamanaka, Thermoelectric properties of doped $BaTiO_3$–$SrTiO_3$ solid solution, *Journal of Alloys and Compounds* 368 (2004) 22–24.

Chapter 4 Thermoelectric properties of Ca^{2+} substituted $EuTiO_3$

This chapter is based on the publication:

"A squeeze on the perovskite structure improves the thermoelectric performance of Europium Calcium Titanates", Xingxing Xiao, Marc Widenmeyer, Kathrin Müller, Marco Scavini, Stefano Checchia, Carlo Castellano, Dongxia Ma, Songhak Yoon, Wenjie Xie, Ulrich Starke, Kiryl Zakharchuk, Andrei Kovalevsky, and Anke Weidenkaff, *Materials Today Physics*, 7 (2018) 96–105.

Abstract

In this chapter, a series of polycrystalline $Eu_{1-x}Ca_xTiO_{3-\delta}$ ($0 \leq x \leq 1$) samples was synthesized to investigate the interrelations between crystal structure, local structural disorder, and thermoelectric properties. The Ca^{2+} substitution is locally modifying (i.e., squeezing) the crystal structure resulting in distinct differences between the long-range and local scales, e.g., the sample with $x = 0.2$ shows a cubic structure in long-range scale, while tetragonal distortions are observed locally. Additionally, the contraction of the unit cell volume with an accompanying reduction of the overall symmetry facilitate the accommodation of smaller Eu^{3+} (instead of Eu^{2+}). The lattice imperfections and the shrinkage of band gap induced by Ca^{2+} substitution significantly improves electron concentration and simultaneously dramatically reduce thermal conductivity (i.e., as large as 50 % compared to the pristine sample) at room temperature. The average thermoelectric figure of merit ZT_m of $Eu_{0.2}Ca_{0.8}TiO_{3-\delta}$ is enhanced by almost 100 % compared to that of pristine $EuTiO_3$. This work demonstrates that controlling lattice deformation offers new ways to enhance the thermoelectric performance of titanates. Besides, the significant reduction of the Eu content helps to decrease materials costs.

4.1 Introduction

The crystal structure and thermoelectric properties of Ba^{2+} substituted $EuTiO_{3-\delta}$ based samples were comprehensively studied in Chapter 3. Due to the larger ionic radius of Ba^{2+}, as expected partial substitution of Eu^{2+} with Ba^{2+} lead to an expansion of the unit cell. The results revealed that the symmetry remains cubic until $x = 0.9$ in the $Eu_{1-x}Ba_xTiO_{3-\delta}$ system for the samples with ~ 40 nm particle size. A significant dependence of electrical conductivity on the Eu^{2+} content prevails at high temperatures and the decreasing thermal conductivity is ascribed to the longer Ti–O bonds when the

Ba^{2+} substitution is larger than 10 %. Although the band gap is almost unchanged by the Ba^{2+} substitution, the localized Eu 4*f* levels are becoming narrower acompanied with splitting.

On the contrary, Ca^{2+} has a smaller ionic radius and atomic mass ($r(Ca^{2+})$ = 1.48 Å, M_{Ca} = 40.078(4) g/mol) compared to Eu^{2+} ($r(Eu^{2+})$ = 1.58 Å, M_{Eu} = 151.964(1) g/mol), potentially enabling the introduction of more effective point defects for phonon scattering. The partial substitution of Eu^{2+} by Ca^{2+} is able to modify the lattice structure and increase overlap between orbitals, owing to the induced chemical pressure resulting from the chemical substitution with ionic radius different. Chemical pressure is a well-established concept [1–3] in solid state chemistry to mimic effects caused normally by applying external isostatic pressure permanently by a (partial) chemical substitution. In the case of $Eu_{1-x}Ca_xTiO_{3-\delta}$ unit cell compaction is induced in a controlled way by the partial substitution of Ca^{2+} for Eu^{2+}. The increase of overlap between orbitals can theoretically modify the localized Eu 4*f* levels [4]. On the other hand, however, the partial substitution of Eu^{2+} by Ca^{2+} is able to induce rotation, tilting, and/or distortion of the TiO_6 octahedra which finally results in an overall reduction of the symmetry. Eventually, the overall effect on the orbital overlap is unknown and the effect of lattice deformation on the Eu 4*f* levels becomes more intriguing. Inspired by these assumptions, isovalent Ca^{2+} substitution was designed to introduce only lattice alteration without extra electrons in the solid solutions, which makes the verification of the role of Eu 4*f* levels in the TE properties more reasonable. Herein, the polycrystalline $Eu_{1-x}Ca_xTiO_{3-\delta}$ samples with $0 \leq x \leq 1$ were synthesized by a targeted soft chemistry route to tune their crystal structure and local structural disorder, and to track corresponding effects exerted on the thermoelectric properties.

4.2 Experimental

4.2.1 Samples synthesis and preparation

$Eu_{1-x}Ca_xTiO_{3-\delta}$ solid solutions (x = 0, 0.2, 0.4, 0.6, 0.8, 0.9, 1) were synthesized using a modified Pechini method followed by annealing under reducing conditions. The details of the wet chemistry processes and the experimental techniques can be found in chapter 2. It was very difficult to densify the samples with x = 0.9 and x = 1 by conventional sintering. Even though the sintering was repeated several times with/without intermediate grinding, some macropores and cracks were always observed in the bulk samples. Consequently, the thermoelectric properties of these two samples are not discussed in this research study. A piece of the x = 1 sample with only some small cracks, which were not running throughout the bulk, was taken for a thermal diffusivity measurement. According to Ref. [5], $CaTiO_3$ is showing a maximum electrical conductivity about 30 S/m and 0.1 S/m at 1273 K under very low oxygen pressure ($p(O_2) = 8.08\times10^{-8}$ Pa) and air conditions, respectively. The almost insulating behavior of $CaTiO_3$ is not comparable with the Eu-containing samples. Therefore, the electrical transport properties and *ZT* value of pure $CaTiO_3$ are not discussed in this chapter.

4.2.2 Samples characterization

High-resolution PXRD data were collected at the ID22 beamline of ESRF in Grenoble, France. Powdered samples of $Eu_{1-x}Ca_xTiO_{3-\delta}$ (x = 0.2, 0.4, 0.6, 0.8, 0.9) were loaded into 0.7 mm diameter Kapton® capillaries and mounted parallel to the axis of the diffractometer. Data were collected at

room temperature in high-resolution setup, using an X-ray wavelength of 0.3542224(1) Å up to $2\theta = 42°$ ($Q_{max} \approx 12.5$ Å^{-1}) for a total counting time of about half an hour per pattern. The diffracted intensities were detected through nine Si (111) analyzer crystals, which spanned over 16° in 2θ. Rietveld analysis was executed adopting the GSAS suite of programs [6]. In the refinements, scale factors, unit cell parameters, atomic positional degrees of freedom, and atomic isotropic mean square displacements parameters (*adp*) were varied as well as the background and line shape parameters. In alternative refinements all the *adp* values were constrained to be the same.

As to the PDF analysis, powder samples were loaded into 0.7 mm diameter Kapton® capillaries and mounted on a goniometric head on top of a rotation stage of the ID15A beamline of ESRF at 320.7 mm distance from the detector, a Dectris Pilatus 2M CdTe. The X-ray energy was 85 keV (λ = 0.1459(2) Å). Sample-detector distance, detector tilt, beam position, and wavelength were calibrated using the diffraction pattern of CeO_2 via the library pyFAI [7]. Raw diffraction images were scaled, averaged, and subtracted by the background (air and an empty Kapton capillary) using the library FabIO [8]. The images were then radially integrated using pyFAI and corrected for the polarization of the incident X-ray beam. For each sample the PDF was calculated as the G(*r*) described in the literature [9] using the program GudrunX [10]. Maximum value of momentum transfer used for PDF calculation was Q_{max} = 25 Å^{-1}. PDF peaks were fitted graphically using Gaussian functions with the program Fityk [11] and structural models were refined against PDF curves using the program PDFfit2 [12]. Symmetry analysis of the PDF structural models was made by the software ISODISTORT [13]. Thereby, each refined structural model was decomposed into the contributions of symmetry-allowed distortions defined by irreducible representations (irreps) of the cubic perovskite symmetry.

The EXAFS measurements of the perovskite-type titanate $Eu_{0.8}Ca_{0.2}TiO_3$ were carried out in transmission geometry at the Eu *K*-edge (48519 eV), at ESRF on beamline BM23, using a double Si (511) crystal monochromator. The measurements were performed at room temperature. The polycrystalline powders were dispersed in a cellulose matrix and pressed into a pellet, adjusting the jump at the absorption edge. Five scans were collected for averaging, thus increasing the signal-to-noise-ratio and checking the reproducibility. The EXAFS data were reduced using the Demeter package standard procedures [14] and the fits of the k^2-weighted EXAFS data were carried out in *r* space using theoretical functions from the FEFF9 code [15]. High-quality *k*-space data were obtained up to 15 Å^{-1}.

The electrical resistivity and the Seebeck coefficient were measured simultaneously using a (ZEM-3, Ulvac Riko) measurement system from room temperature to 1173 K in a reducing atmosphere (5 vol.% H_2 in Ar). Experimental densities of the bulk samples were determined by the Archimedes method. The thermal diffusivity was measured using a Netzsch LFA 457 laser flash analyzer in the temperature range from 300 K to 1173 K under a flowing forming gas atmosphere (5 vol.% H_2 in Ar). The specific heat capacity was calculated by the Dulong-Petit law. The thermal conductivity was derived from the experimental density of the bulk sample, the thermal diffusivity, and the specific heat capacity using the relationship $\kappa = d \cdot \Lambda \cdot c_p$. The charge carrier concentration and charge mobility of $Eu_{1-x}Ca_xTiO_{3-\delta}$ (x = 0, 0.2, and 0.8) were measured simultaneously on a HT-Hall 1100 K (Fraunhofer, IPM) measurement system by using a 4-point probe van der Pauw method with a magnetic field of ± 0.5 T under the condition of forming gas in the temperature range of 300 – 673 K.

XPS was performed with a Kratos Axis Ultra system using monochromatized Al *Kα* X-ray radiation (1486.6 eV). A pass energy of 20 eV was used for the high-resolution spectra. The samples

were sputtered by Ar^+ ions for 20 min with an energy of 4 keV in order to remove the surface contamination layer. The XPS data were normalized by aligning the intensity at the low binding energy site and multiplying with a factor in order to have the same intensity of the main peak. This facilitates the qualitative comparison of the samples with strongly varying Eu content.

The oxygen content was analyzed by carbothermal fusion using carrier hot gas extraction technique (ELTRA, ONH-2000). Each measurement was repeated at least three times.

4.3 Calculations

DFT calculations on DOS of $Eu_{1-x}Ca_xTiO_3$ were performed using projector augmented wave (PAW) method [16,17] and generalized gradient approach functional plus Hubbard U (GGA + U) [18] as implemented in the VASP code [19,20]. The plane wave cutoff chosen for the calculations is 500 eV. A $\sqrt{2} \times \sqrt{2} \times 2$ supercell is modeled with Γ-centered $6 \times 6 \times 6$ k-point mesh. The valence electrons considered in the PAW potential are: $4f^7 5s^2 5p^6 6s^2$ for Eu atoms, $3s^2 3p^6 4s^2$ for Ca atoms, $3s^2 3p^6 3d^2 4s^2$ for Ti atoms, and $2s^2 2p^4$ for O atoms. The supercell consists of four primitive unit cells and hence allows x to take the values 0, 0.25, 0.5, 0.75, and 1. The selected value of the Eu on-site Coulomb parameter U is 6.2 eV, and the exchange parameter J is chosen to be 1.0 eV. The unit cell geometries are taken from the results of PXRD experiments.

4.4. Results and discussion

4.4.1 Crystal structure analysis

(i) Crystal structure of $EuTiO_3$ and $CaTiO_3$ parent compounds

The structure of the end members of the solid solution has been widely investigated. At room temperature, $EuTiO_3$ adopts the cubic undistorted perovskite structure (space group $Pm\bar{3}m$). In the cubic phase, the atomic sites are 1a Ti (0, 0, 0); 1b Eu/Ca (½, ½, ½); and 3d O (0, ½, 0). TiO_6 octahedra share corners with six different TiO_6 units with a 180° angle O–Ti–O, while Eu ions fill the cuboctahedral sites forming EuO_{12} units. Below ~ 235 K a cubic to tetragonal (space group $I4/mcm$) phase transition takes place [21] driven by the antiferrodistorsive tilting of TiO_6 octahedra along the c-axis ($a^0a^0c^-$ using the Glazer notation [22]). The tetragonal cell vectors a_T, b_T, and c_T are obtained starting from the perovskite ones a_p by the following axis transformations (1 1 0), (1 $\bar{1}$ 0), (0 0 2) and their moduli are $a_T = \sqrt{2}a_p$, $b_T = \sqrt{2}a_p$, and $c_T = 2a_p$. Each cell contains four ABO_3 formula units ($V_o = 4V_p$). $CaTiO_3$ takes the same undistorted perovskite structure only at very high T values. Starting from the high temperature cubic phase, $CaTiO_3$ transforms into the tetragonal $I4/mcm$ space group around 1635 K and undergoes a further phase transition around 1512 K towards an orthorhombic space group $Pbnm$ ($a_o = \sqrt{2}a_p$, $b_o = \sqrt{2}a_p$, and $c_o = 2a_p$,) and is maintaining this last structure down to room temperature [23,24].

Using the setting of Ref. [25], in the orthorhombic phase the Ca ions are in 4c (0 + x_{Ca}, 0 + y_{Ca}, ¼) site, the Ti in 4b (0, 1/2, 0) site, while two different oxygen site exists: O(1) 4c (0 + x_{O1}, ½ + y_{O1}, ¼), O(2) 8d (¼ + u, ¼ + v, 0 + w); this notation highlights the shifts of the atomic coordinates in respect to the same in the cubic phase. In $Pbnm$ the TiO_6 octahedra undergo an out-of-phase tilting with the same tilting amplitude ϕ_x (= ϕ_y) along x- and y-directions (which lie in the $\boldsymbol{a}_p$- $\boldsymbol{b}_p$-plane) and

an in-phase-tilting along the *z*-direction ϕ_z, along the $\boldsymbol{c}_p$-axis. This tilting architecture is defind as $a^-a^-c^+$, according to the Glazer tilt systems [22]. The tilting angles ϕ_x and ϕ_z are related to the *u*, *v*, *w* shifts of the equatorial O(2) atom by: $\phi_x = tan^{-1}4\sqrt{2}w$ and $\phi_z = tan^{-1}2(u+v)$.

(ii) PXRD analysis on $Eu_{1-x}Ca_xTiO_{3-\delta}$ compounds

Fig. 4.1 shows the laboratory PXRD results including the two parent samples $EuTiO_3$ and $CaTiO_3$. All synthesized samples were identified to be single phase. In order to get more detailed information of the crystal structure, high *Q*-resolution PXRD patterns were collected at RT on the samples (x = 0.2, 0.4, 0.6, 0.8, 0.9) using synchrotron radiation. The phase purity of all samples was further confirmed by high-resolution PXRD patterns. A small region ($14.6° \leq 2\theta \leq 15.2°$) of the patterns for all the above listed samples is shown in Fig. 4.2(a) and the Rietveld refinements for x = 0.4 and x = 0.8 are reported as examples in Fig. 4.2(b) and Fig. 4.2(c). The refined structural parameters are reported in Table 4.1. The Rietveld analysis revealed that the sample with x = 0.2 shows the undistorted cubic structure (space group $Pm\bar{3}m$), which is isostructural with $EuTiO_3$ at RT. When $x \geq 0.4$ the structure is found to be orthorhombic (*Pbnm*, isostructural with $CaTiO_3$ at RT [25]). Both in Sr^{2+} substituted $Ca_{1-x}Sr_xTiO_3$ solid solutions [26] and in pure $CaTiO_3$ [24] with increasing temperature, the sequence of observed phase transformations was *Pbnm* → *I*4/*mcm* → $Pm\bar{3}m$. In the case of $Eu_{1-x}Ca_xTiO_{3-\delta}$, the *I*4/*mcm* phase could either be absent or be the stable phase in a compositional range of $0.2 < x < 0.4$, which can be verified by future experiments.

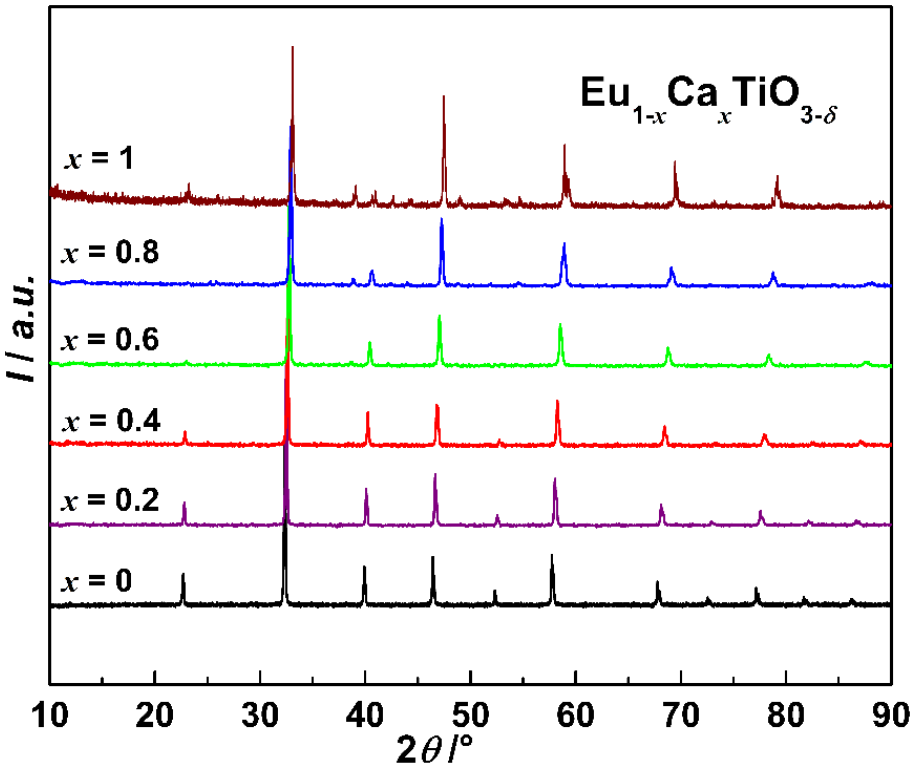

Fig. 4.1 Powder X-ray diffraction patterns of $Eu_{1-x}Ca_xTiO_{3-\delta}$ ($0 \leq x \leq 1$) samples.

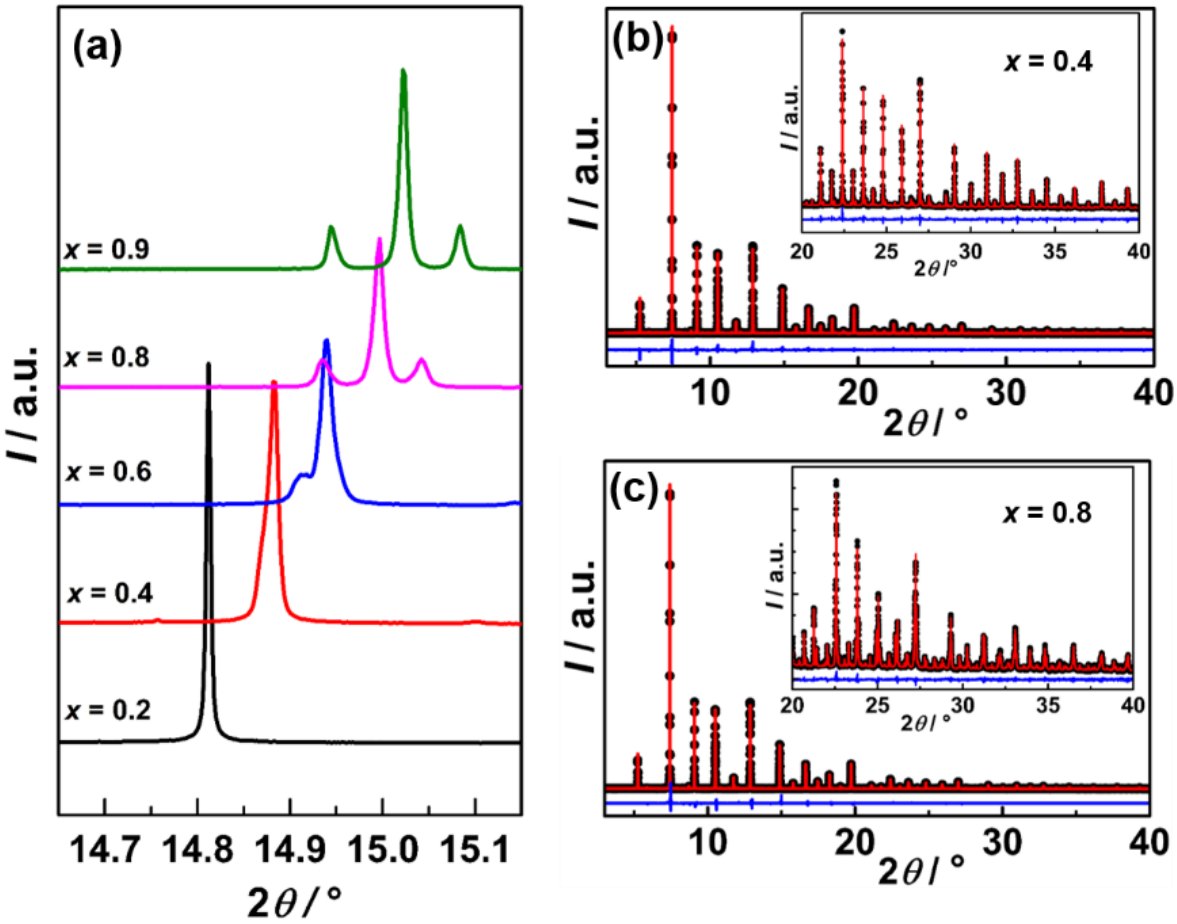

Fig. 4.2 The powder X-ray diffraction patterns for $Eu_{1-x}Ca_xTiO_{3-\delta}$ samples, showing the progressive splitting of the cubic 220 reflection (a); Rietveld refinements for the patterns of x = 0.4 (b) and x = 0.8 (c).

The unit cell parameters and volumes of all synthesized samples (plus $EuTiO_3$ [21]) are shown in Fig. 4.3(a) and (b). For a better comparison between different phases, the pseudocubic parameters a_p, b_p, c_p, and V_p are reported. All unit cell parameters and the volume decrease with increasing Ca^{2+} concentration, being an indicative of an increased chemical pressure. The trends mentioned above resemble what was previously observed for $Sr_{1-x}Ca_xTiO_3$ [26,27] and suggest that europium is mainly Eu^{2+} even in the Ca-rich solid solutions. The variation of the tilting angles ϕ as a function of the Ca^{2+} fraction x is shown in Fig. 4.3(c). In $CaTiO_3$ and related perovskites [28] the tiltings of TiO_6 octahedra along their x, y, and z axes are the order parameters of displacive structural phase transitions as a function of temperature and/or composition. In this work, the crystal structure as a function of Eu/Ca concentration instead of temperature as done in Ref. [24] was investigated, and the tilting angles ϕ_x and ϕ_z were considered as unsaturated order parameters of the structural phase transition from the cubic structure.

Table 4.1. Rietveld refinement results of synchrotron PXRD on $Eu_{1-x}Ca_xTiO_{3-\delta}$ samples at RT. Fractional atomic coordinates are dimensionless, while the *adp* values are expressed in $Å^2$. ESDs are in brackets. In the orthorhombic phase (space group *Pbnm*), the considered atomic sites are 4*a* Ti (0, ½, 0); 4*c* Eu/Ca ($x_{Ca/Eu}$, $y_{Ca/Eu}$, ¼); 4*c* O(1) (x_{O1}, y_{O1}, ¼); 8*d* O(2) (x_{O2}, y_{O2}, z_{O2}). In the cubic phase (space group $Pm\bar{3}m$) the atomic sites are 1*a* Ti (0, 0, 0); 1*b* Eu/Ca (½, ½, ½); and 3*d* O (0, ½, 0).

Sample	x = 0.20	x = 0.40	x = 0.60	x = 0.80	x = 0.90
Space group	$Pm\bar{3}m$	*Pbnm*	*Pbnm*	*Pbnm*	*Pbnm*
a/Å	3.886286(1)	5.47260(1)	5.44575(2)	5.41240(1)	5.397554(8)
b/Å	= a	5.47441(1)	5.45884(2)	5.45031(1)	5.447146(8)
c/Å	= a	7.72969(1)	7.70223(2)	7.67373(1)	7.66019(1)
V/Å³	58.695428(3)	231.57576(3)	228.96787(8)	226.36933(3)	225.21927(1)
$x_{Ca/Eu}$	-------	0.0013(2)	0.0025(2)	0.0047(1)	0.0055(1)
$y_{Ca/Eu}$	-------	0.00932(7)	0.01687(6)	0.02701(7)	0.03127(7)
$x_{O(1)}$	-------	0.5497(7)	0.5561(7)	0.5643(4)	0.5668(3)
$y_{O(1)}$	-------	0.0001(7)	-0.0045(5)	-0.0126(4)	-0.0129(3)
$x_{O(2)}$	-------	0.2638(8)	0.2743(5)	0.2839(3)	0.2867(2)
$y_{O(2)}$	-------	0.2654(7)	0.2750(4)	0.2847(3)	0.2871(2)
$z_{O(2)}$	-------	0.0250(3)	0.0305(3)	0.0344(2)	0.0358(2)
adp_{iso}(Eu/Ca)	0.00795(4)	0.00894(4)	0.00817(6)	0.00749(7)	0.00676(8)
adp_{iso}(Ti)	0.0037(1)	0.00313(8)	0.00336(8)	0.00355(9)	0.00266(8)
apd_{iso}(O(1)/O(2))	0.0182(4)	0.0122(4)	0.0108(4)	0.0098(3)	0.0074(2)
Overall *adp*	0.00774(4)	0.00730(4)	0.00635(4)	0.00589(4)	0.00490(4)
Rp	0.0853	0.0559	0.0565	0.0495	0.0639
$R(F^2)$	0.0638	0.106	0.0765	0.0798	0.0700

A monotonic increase of ϕ is observed in both *x*/*y* (ϕ_x) and *z* (ϕ_z) direction. While ϕ_z goes to zero smoothly by decreasing the Ca^{2+} concentration, some abrupt and discontinuous drop to zero can be supposed for ϕ_x (= ϕ_y). A similar trend was observed for $CaTiO_3$ by increasing temperature [24]. The degree of disorder in the solid solutions can be qualitatively derived from the analysis of the atomic mean square displacement parameters (*adp*). Fig. 4.3(d) shows the overall *adp* values obtained by refining the same *adp* value for all atoms. Contrary to expectations for a continuous solid solution (see e.g. Refs. [29,30]), the maximum *adp* value is not found in the vicinity of x = 0.5, but for x = 0.2 when the structure is cubic. With increasing Ca^{2+} concentration the *adp* values

monotonically decrease. Interestingly, even pure $EuTiO_3$ has a larger *adp* value than the orthorhombic samples ($0.4 < x < 0.9$). PDF analysis on $EuTiO_3$ revealed that locally tilted disordered zones exist even in the cubic phase, thus connecting the anomalously high *adp* values to static disorder [21].

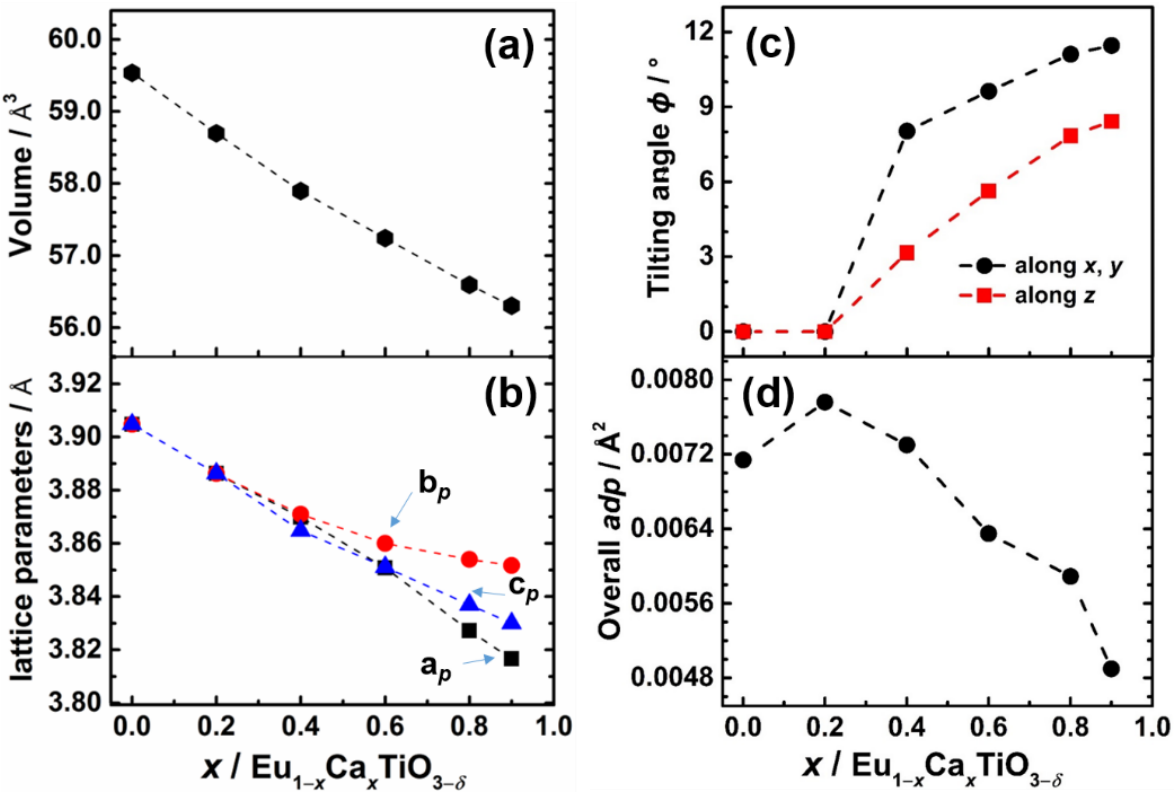

Fig. 4.3 Composition dependence of the cubic sub-cell volume (a), lattice parameters (b), tilting angles along the *x*/*y*, and *z* directions (c), and overall atomic mean square displacement parameters of $Eu_{1-x}Ca_xTiO_{3-\delta}$ using the cubic perovskite metric for sake of comparison (d). All parameters (V_p and lattice parameters a_p, b_p, c_p) refer to the underlying cubic perovskite sub-cell. The orthorhombic unit cell volume and unit cell parameters are transformed into cubic parameters according to the following relation: $a_o = \sqrt{2}a_p$, $b_o = \sqrt{2}b_p$, $c_o = 2c_p$, $V_o = 4V_p$.

In the case of the present solid solution, the *adp* values increase while the average tilting angles decrease, suggesting structural distortion at the local scale, especially in the cubic sample with $x = 0.2$. For this reason, the Eu environment in the cubic $x = 0.2$ sample was investigated by means of EXAFS at the Eu-*K* edge and PDF patterns on all the samples to reveal the discrepancy between average and local structure.

(iii) EXAFS analysis on $Eu_{0.8}Ca_{0.2}TiO_{3-\delta}$ compound

EXAFS data have been collected on the $x = 0.2$ sample due to the ambiguity between its average cubic structure and its local one. To include the first and further neighbors at the Eu *K*-edge (full fit range:1.42–3.98 Å), the results obtained from structural models spanning from structure of the $CaTiO_3$ system to space groups typical for $BaTiO_3$ [31] have been compared to check some possible polar disorder at least at the local scale in analogy to previous findings on Sr-rich $Sr_{1-x}Ca_xTiO_3$ samples [27,32].

The tested cubic model (as in the long range) is characterized by a first Eu–O shell with a crystallographic bond length R = 2.76 Å and coordination number N = 12, the Eu–Ti second shell peak (total N = 8) with R = 3.38 Å, and the Eu–Eu third shell with R = 3.90 Å and N = 6. The second tested model is related to a local tetragonal symmetry around Eu (which is almost the same for both *P*4*mm* or *I*4/*mcm* models) with two Eu–O first subshells with coordination numbers N = 8 and 4, respectively, the Eu–Ti second shell peak with N = 8 and the Eu–Eu third shell with N = 6. The results are reported in Table 4.2.

A rhombohedral *R*3*m* model with a Eu–O bimodal distribution N = 9 + 3 and an orthorhombic *Amm*2 and *Pbnm* model were also tested. They include a larger number of different Eu–O shells setting in all cases worse fit qualities with non-physical parameter values. It was not possible to try other multimodal fit models (like 4 + 4 + 4 Eu–O distances) due to the intrinsic resolution of the EXAFS technique and the need to have a minimum number of degrees of freedom to perform the fit. The *R*-factors of the cubic and the tetragonal fits, reported in Table 4.2, clearly show that a tetragonal local distortion gives the better fit. The main characteristics of the obtained parameter values are that: (i) the first Eu–O shell or the corresponding two first subshells are highly disordered (σ^2 values); (ii) the Eu-Eu shell is more disordered than the Eu–Ti one. Therefore, it can be deduced that locally a tetragonal distortion is present in the on-average-cubic x = 0.2 sample which can be also compatible with a 4 + 4 + 4 distribution of the Eu–O distances, as expected in case of octahedral tilting. On local scale it cannot be distinguished between polar or antiferrodistorsive distortion. The PDF analysis should help to achieve a deeper insight in the last two points.

Table 4.2 EXAFS fit parameters of $Eu_{0.8}Ca_{0.2}TiO_{3-\delta}$ sample: coordination number N, crystallographic bond length R, σ^2 and R-factor.

$Eu_{0.8}Ca_{0.2}TiO_{3-\delta}$	cubic model			tetragonal model			
(RT)	Eu–O	Eu–Ti	Eu–Eu	Eu–O(1)	Eu–O(2)	Eu–Ti	Eu–Eu
N	12	8	6	8	4	8	6
R(Å)	2.702(5)	3.372(5)	3.879(5)	2.749(5)	2.597(5)	3.373(5)	3.879(5)
σ^2(Å^2)	0.0325(7)	0.0070(1)	0.0112(2)	0.0267(5)	0.0267(5)	0.0071(1)	0.0112(2)
R-factor (Residual)	0.04729			0.03331			

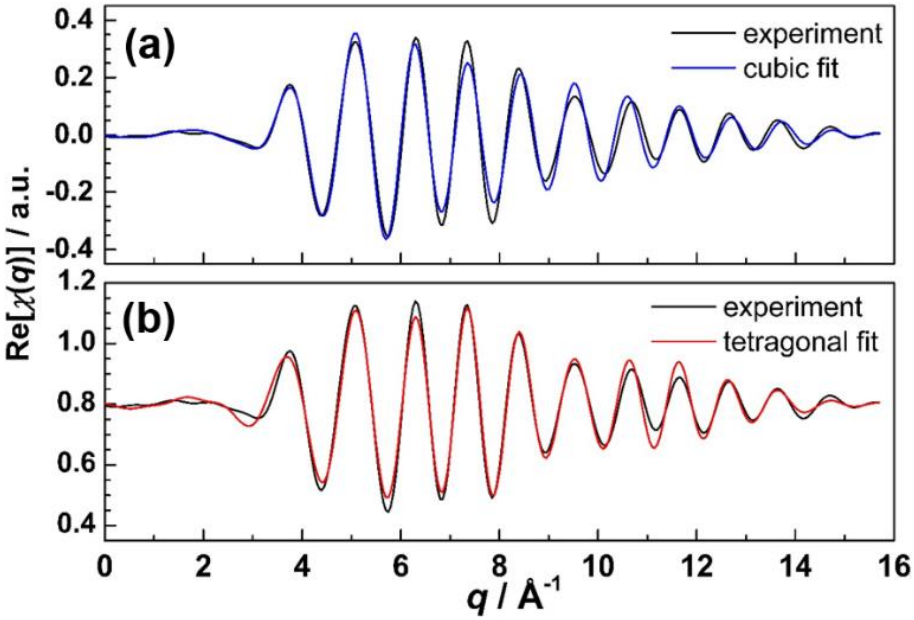

Fig. 4.4 Comparison between the back Fourier transform best-fit curves obtained from a cubic (a) and a tetragonal (b) model on the $Eu_{0.8}Ca_{0.2}TiO_{3-\delta}$ sample.

(iv) PDF analysis on $Eu_{1-x}Ca_xTiO_{3-\delta}$ compounds

The PDF, $G(r)$ curves of all the samples are presented in Fig. 4.5(a). The first and second $G(r)$ peak at around 1.95 Å and 2.75 Å represent the nearest-neighbor Ti–O and *A*–O (*A* = Ca, Eu) distances, respectively; the third $G(r)$ peak, around 3.3 Å, contains the *A*–Ti pairs. Local interatomic distances obtained by peak fits show significant differences from the bond lengths obtained by Rietveld refinements (Fig. 4.5(b–d)): i) the Ti–O distances decrease from 2.02 Å to 1.95 Å between $x = 0.2$ and $x = 0.9$; ii) in the same range of x the *A*–O distances also decrease more markedly on the local scale; iii) finally, shorter and more broadly distributed *A*–Ti distances reflect the larger orthorhombic strain and the smaller unit cell volume obtained by introducing Ca^{2+} into the solid solution. The contraction of Ti–O and *A*–O bond lengths at the local scale clearly exceeds the Vegard-like compositional dependence inferred from the long-range structures and is an indicator of the chemical pressure induced on both the *A*- and *B*-sites. Applying structural models to the $G(r)$ curve in the compositional range of $0.2 \leq x \leq 0.9$ show that the extra contribution to locally stretched bond distances originates in the nature of the short-range distortions of Eu-rich samples. All G(r) curves were successfully fitted up to $r = 8$ Å by a 2 × 2 × 2 supercell of the primitive cubic perovskite, in which atomic positions were refined within the symmetry constraints set by the *Pnma* space group. *Pnma* is an alternative setting of the orthorhombic space group of $CaTiO_3$ related to *Pbnm* by permutation of crystallographic axes, and also a subgroup of the *I4/mcm* ground-state symmetry of $EuTiO_3$, thus it represents a suitable common basis for fitting the G(r) of these solid solutions.

The symmetry-decomposition of the refined *Pnma* phases into single-irrep distortion modes is shown in Fig. 4.5(e) and indicates which distortions contribute to the short-range structure at different compositions. The Ca-rich compositions ($x \geq 0.6$) are dominated by two octahedral tilt modes (belonging to irreps R_4^+ and M_3^+) [33], by which rigid TiO_6 units rotate around one axis. These two tilt modes (depicted schematically in Fig. 4.5(f)) split the *A*–O distances in three groups of 4 and are accompanied by a scissor mode (M_4^+) that tends to create an equal number of 4 + 8 and 8 + 4 *A*–O

local bond length distributions. The composition of these modes rationalizes the split, symmetric *A*–O peak observed in $x = 0.8$ and $x = 0.9$. As x is decreased, the octahedral tilt modes are replaced by a quadrupolar distortion (M_1^+) driven by *A*–site disorder [34] and by an unconventional tilt (X_5^+), also accompanied by a scissor mode (R_5^+). Unlike rigid octahedral tilt modes, the M_1^+ quadrupolar distortion stretches all the out-of-plane *A*–O distances, forming the 4 + 8 distribution of distances observed in the $G(r)$ for $x \leq 0.6$ in accord with the EXAFS analysis on the $x = 0.2$ sample. Both M_1^+ and X_5^+ tend to form ordered short and long Ti–O distances, thus causing the Ti–O peak to be more smeared out at low-x. The longer Ti–O distances can be explained by considering that the distortion of the TiO_6 octahedra by the coupled X_5^+ and R_5^+ modes is needed to improve the *B*-site coordination sphere in absence of an octahedral tilt. In summary, PDF analysis reveals the pattern of an enhanced local distortion around *A*–cations in Eu-rich samples ($x \leq 0.4$), which stretches the Ti–O and *A*–O distances to a larger extent than observed by the reciprocal-space analysis. There might be several reasons for the trend observed above: i) the lattice instabilities of ETO [35]; ii) a gradient of the concentration of Eu^{3+} (and related Ti^{3+}), which will be explained later; iii) the different ionic radii of the involved species; iv) and the presence of Jahn-Teller-effects due to unpaired electrons of Eu^{3+} and Ti^{3+}, respectively.

While the Ca-rich compositions ($x \geq 0.6$) are dominated by two local octahedral tilt modes observed also in the average structure, the enhanced local Ti/*A*–O stretching modes revealed by PDF on lowering Ca^{2+} concentration are not reflected by symmetry breaks at larger scales; conversely, ϕ_x and ϕ_z decrease monotonically and vanish in cubic $Eu_{0.8}Ca_{0.2}TiO_{3-\delta}$, suggesting that disordered local zones merge into a more symmetric path at the average scale. This discrepancy increases the *adp* parameters found by Rietveld refinements in Eu-rich samples, leading to a peak in *adp*'s for $Eu_{0.8}Ca_{0.2}TiO_{3-\delta}$. This is a marked difference from $x = 0.5$, which would expected in a continuous solid solution where the different ionic radii determine the overall symmetry (see e.g. Refs. [29,30]).

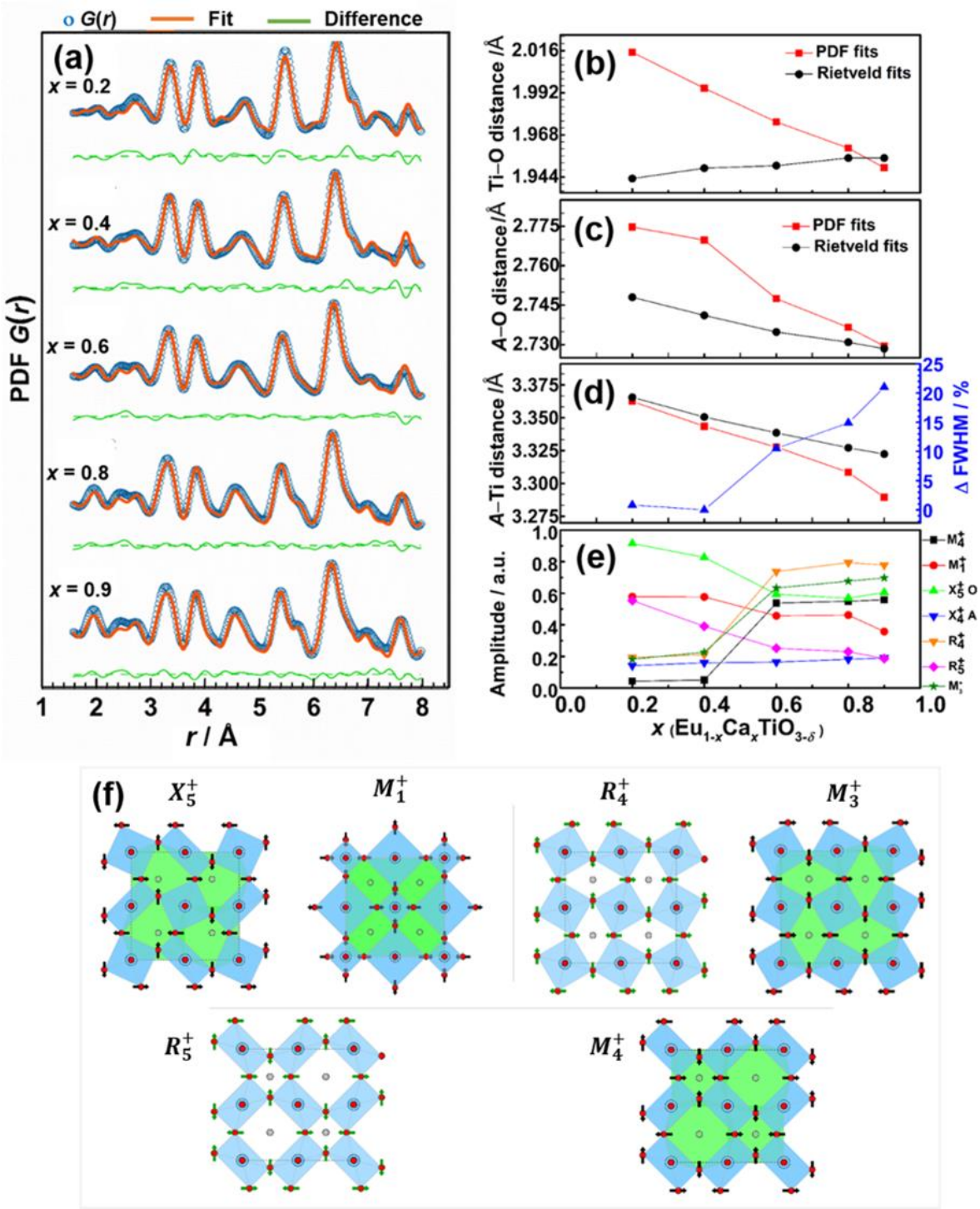

Fig. 4.5 (a) Experimental PDF fitted by structural models with *Pnma* symmetry and fit residuals with the respective mean values; (b-d) Ti–O, Ca/Eu–O, and Ca/Eu–Ti distances as inferred from the long-range models and from the respective PDF peaks; in (d) the change in full-width at half-maximum (FWHM) of the PDF peak with respect to the low-*x* minimum width is displayed; (e) normalized amplitudes of the mode intensities by comparing the undistorted perovskite structure to each refined structure obtained by PDF fits; (f) overview of the single distortions involving O atoms projected along the respective symmetry axes (red = O, blue = Ti, grey = Ca/Eu = *A*); black arrows represent in-phase displacement along the symmetry axis, green arrows out-of-phase along the symmetry axis; TiO_6 octahedra and AO_{12} cuboctahedra are highlighted in light blue and green, respectively; the cuboctahedra not highlighted in green comprise both types of *A*–O patterns visible in a single plane.

4.4.2 Electrical transport properties

The temperature dependence of the electrical conductivity of $Eu_{1-x}Ca_xTiO_{3-\delta}$ is presented in Fig. 4.6(a). The σ of all samples exponentially increases as increasing temperature. At room temperature, σ exhibits an unexpected enhancement by several orders of magnitude with increasing Ca^{2+} content, e.g., $\sigma_{(x = 0)} = 1.3\ S{\cdot}m^{-1}$ and $\sigma_{(x = 0.8)} = 4.6{\times}10^{2}\ S{\cdot}m^{-1}$ at 300 K. It is implying that the Ca^{2+} substitution causes the increase of either the charge carrier concentration n or charge mobility μ or both based on the relation $\sigma = ne\mu$, where e is the elemental electron charge. Except for $x = 0$, σ of all substituted samples converges with increasing temperature reaching similar values at the maximum measurement temperature ($T \approx 1173$ K). The Seebeck coefficient α of all samples is negative over the entire temperature range as shown in Fig. 4.6(b), indicating that the dominant charge carriers are electrons. The $x = 0$ sample reveals a giant Seebeck coefficient around room temperature, i.e. $\alpha_{(x = 0;\ 300\ K)} = -1133\ \mu V{\cdot}K^{-1}$, which is consistent with a previously reported value [36]. The temperature dependence of α corresponds to that of σ. For all samples, the absolute value of α monotonically decreases with both the increasing temperature and the Ca^{2+} content, implying a shift of the Fermi level. The α ends with a nearly temperature independent behavior at $T > 1000$ K. Consequently, the Heikes formula can be used to estimate the n [37]:

$$\alpha_{T\to\infty} = \frac{-k}{e}\ln\frac{2(1-\beta)}{\beta} \tag{4-1}$$

where β is the charge carrier concentration per unit cell. According to the value of calculated n, the μ also can be obtained. The calculated n and μ values are listed in Table 4.3.

Table 4.3. Electrical conductivity σ, Seebeck coefficient α, calculated activation energy E_a, calculated charge carrier concentration n and charge mobility μ, oxygen non-stoichiometry parameter δ, bulk density d, relative density ξ, and the calculated specific heat capacity c_p of the $Eu_{1-x}Ca_xTiO_{3-\delta}$ bulk samples.

Samples No.	$\sigma_{1150\ K}$ (S/m)	α_{1150K} (μV/K)	E_a (eV) 300 – 500 K	E_a (eV) 800 – 1150 K	$n_{1150\ K}$ ($\times10^{20}$ cm^3)	$\mu_{1150\ K}$ ($cm^2V^{-1}s^{-1}$)	δ	d (g/cm^3)	ξ* (%)	c_p (J/(g·K))
$x = 0$	2890	–330	0.21	0.50	6.84	0.26	0.02(6)	6.18	89.3	0.503
$x = 0.2$	1860	–360	0.21	0.41	5.12	0.22	0.07(5)	5.55	87.7	0.553
$x = 0.4$	2000	–360	0.16	0.30	4.91	0.25	0.02(5)	5.29	91.9	0.614
$x = 0.6$	2130	–370	0.10	0.14	4.74	0.28	0.04(5)	4.68	90.2	0.690
$x = 0.8$	2350	–340	0.05	0.07	6.41	0.23	0.03(5)	4.12	89.6	0.788
$x = 1$							0.01(5)	3.91	97.2	0.917

*Theoretical densities are obtained by XRD refinements. Estimated standard deviations are given in parentheses.

The temperature dependence of measured n and μ are shown in Fig. 4.6(c) and Fig. 4.6(d), respectively. At room temperature, n of $x = 0.8$ is enhanced by three orders of magnitude compared to that of $x = 0$ (i.e., $n_{(x = 0)} = 3.9{\times}10^{16}\ cm^{-3}$ and $n_{(x = 0.8)} = 1.6{\times}10^{19}\ cm^{-3}$). The n is presenting an

exponential increase with temperature for all samples, but the increasing rate of $x = 0$ is higher than that of $x = 0.8$ (Fig. 4.6(c)). This behavior corresponds well to the observed behavior of σ and α. It is evident from Fig. 4.6(d) that the μ of $x = 0.8$ is decreasing with increasing temperature and follows well the $T^{-1.5}$ dependence, implying that the electron scattering mechanism belongs to the nonpolar acoustical mode vibrations [4]. The μ of $x = 0$ and $x = 0.2$ shows no clear dependence below $T \sim 400$ K due to the very high resistivity and the instrumental limitation (magnetic field ± 0.5 T). At $T > 400$ K the samples $x = 0$ and $x = 0.2$ also show generally a decreasing mobility with increasing temperature. Both the calculated n and μ are in reasonable agreement with the trend of the Hall measurement data. Accordingly, the variation of σ and α is attributed to the rapid increase of n. Because the trace amounts of impurities are negligible in these $Eu_{1-x}Ca_xTiO_{3-\delta}$ samples, the generation of more itinerant electrons can be attributed to the introduction of lattice imperfections and/or the shrinkage of the band gap induced by Ca^{2+} substitution.

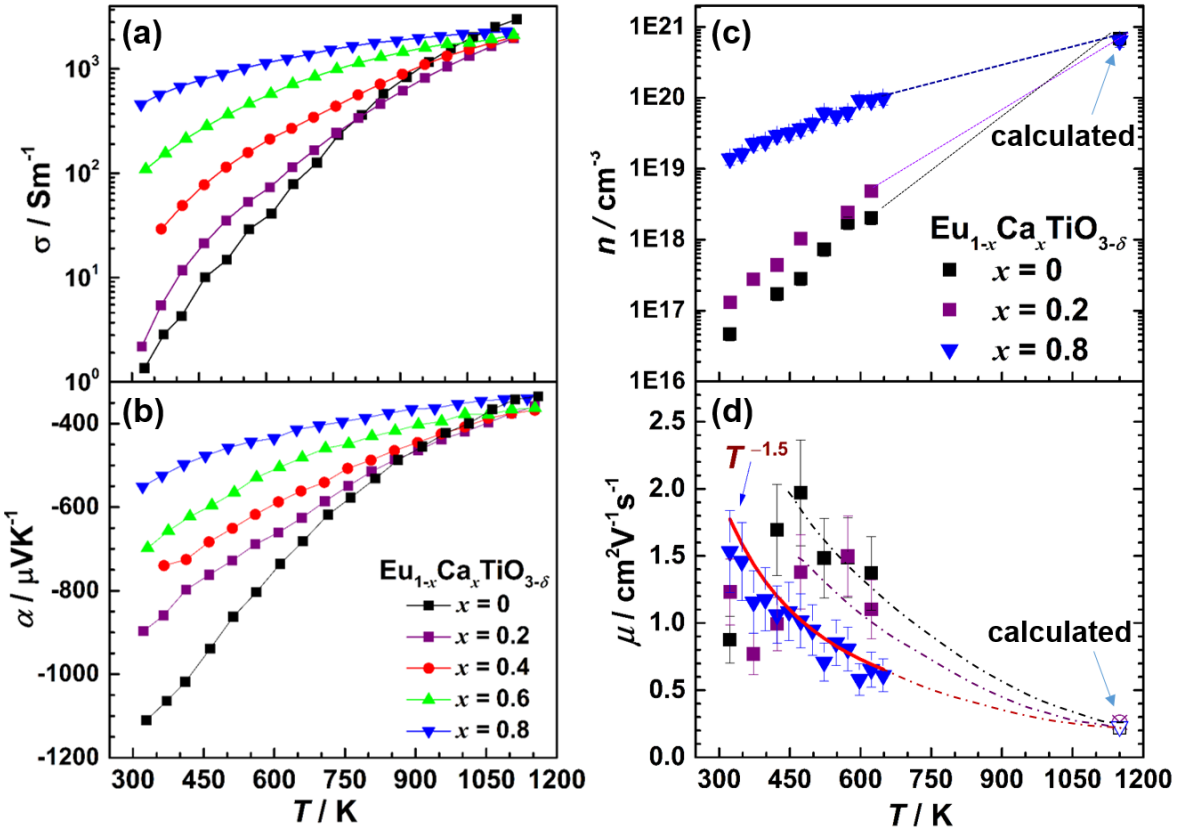

Fig. 4.6 Temperature dependence of the electrical conductivity σ (a), the Seebeck coefficient α (b), the measured charge carrier concentration n (c), and the measured charge carrier mobility μ (d) of $Eu_{1-x}Ca_xTiO_{3-\delta}$ bulk samples. The dashed curves in (c) and (d) from 650 K to 1200 K are a guide to the eye.

The predominant intrinsic point defects in most of the known reduced titanates are oxygen vacancies and the electronic defects (e.g., Eu^{3+} or Ti^{3+}/Ti^{2+}) [38–40]. The oxygen deficiency was examined and the obtained δ values are listed in Table 4.3. There is no clear trend of δ variations with the Ca^{2+} content observable likely due to the limited achievable accuracy of the analysis. This result is similar to previous studies on *A*-substituted $EuTiO_3$ (*A* = Sr, Ba), showing small deviations of δ values between the samples [41,42]. According to previous investigations, in contrast to the

known behavior in the doping regime, at large substitution levels oxygen vacancies are not the dominant factor for the transport properties anymore [5,43,44]. For example, no clear correlation between the oxygen vacancy concentration and the Ca^{2+} content was found in $La_{1-x}Ca_xTiO_{3-\delta}$, and varying the *A*-site composition only weakly influences the oxygen content even in a highly reducing atmosphere ($p(O_2) = 8\times10^{-11}$ atm) [5]. However, the electronic defect Eu^{3+} was evidently observed by XPS characterization on these samples.

4.4.3 XPS analysis on $Eu_{1-x}Ca_xTiO_{3-\delta}$ compounds

The oxidation states of each element in the samples $Eu_{1-x}Ca_xTiO_{3-\delta}$ (x = 0.2, 0.6, 0.8) were characterized by XPS with and without Ar ion sputtering. For all samples without sputtering, Ti^{4+} was found to be the only oxidation state for Ti, while Eu shows mainly Eu^{3+} together with a tiny amount of Eu^{2+}. As the surface layers were contaminated by the exposure to the ambient air environment, a large difference of the Eu oxidation behavior was observed from the surface depth profiles as reported in many references [10,11]. Therefore, it was necessary to apply Ar^+ sputtering to remove the contaminated surface layers and detect information of the clean "bulk". However, it is well known that the sputtering also has a great influence on the Ti oxidation states leading to the reduction of Ti^{4+} to Ti^{3+} and Ti^{2+} [12,13]. It was observed that the Ti 2*p* spectra varied significantly with increasing sputtering time from 5 min to 40 min, while the Eu 3*d* and 4*d* spectra as well as the O 1*s* spectra do not observably change between 20 min and 40 min. Thus, the XPS spectra were acquired after 20 min of Ar^+ sputtering. However, an analysis of the Ti 2*p* core-level spectra, in particular with regard to the monitoring of Ti^{3+} quantities, is not significant due to the strong influence of Ar^+ sputtering. For the sake of simplicity, the Eu 3*d*, Eu 4*d*, O 1*s*, and valence band were compared by means of normalized peak intensity, respectively, as shown in Fig. 4.7.

Fig. 4.7(a) shows the Eu 3*d* core-level spectra, which consist of $3d_{3/2}$ and $3d_{5/2}$ components. The two prominent peaks at binding energies of 1155 eV and 1125 eV belong to the Eu^{2+} species, which is in good agreement with Ref. [45,46]. The shape and position of the Eu^{2+} peaks of the three samples reveal a similar binding energy, while the satellite peaks A, B, and C indicated by the arrows differ. The binding energies of peaks A and C are roughly 6.5 eV and 8 eV higher than that of the Eu^{2+} $3d_{3/2}$ and $3d_{5/2}$ main peaks, respectively. In addition, the intensity of peak A is about 8 % of the Eu^{2+} $3d_{3/2}$ main peak and peak C is about 16 % of the Eu^{2+} $3d_{3/2}$ main peak, which is very similar to the reported case of some divalent Eu compounds such as EuPd and $EuAu_5$ [45]. The peaks A and C are "shake-up" peaks situated at higher binding energies originating from the Eu^{2+} of the bulk samples due to the multiplet structure of the $\underline{3d}4f^7$ (bar denotes a hole) final state configuration [45,47]. The peak B is attributed to Eu^{3+} species according to the measured binding energy [45,48]. It is evident that the relative area of these Eu^{3+} peaks increase with increasing Ca^{2+} content.

The normalized Eu 4*d* spectra almost coincide with each other among the three samples as shown in Fig. 4.7(b). The peak at about 142.7 eV belongs to Eu^{3+}, which is in agreement with the observation from the Eu 3*d* spectra. The relative area of this Eu^{3+} peak (142.7 eV) is found to be 2.4 %, 2.6 %, and 3 % for x = 0.2, 0.6, and 0.8, respectively. Both the Eu 3*d* and Eu 4*d* spectra reveal that the Ca^{2+} substituted samples are mainly composed of divalent europium with tiny amounts of trivalent europium, which is consistent with the crystal structure analysis.

The normalized O 1*s* spectra of the samples x = 0.6 and x = 0.8 nearly coincide with each other, as shown in Fig. 4.7(c). The main peak with a binding energy of 530.9 eV belongs to lattice

oxygen [49], an additional peak at higher binding energy (532.2 eV) results from surface adsorbed oxygen species [50]. Apparently, the x = 0.2 sample shows more adsorbed oxygen species than the others according to the larger peak shoulder at higher binding energy, implying that there is no significant relationship between the adsorbed oxygen species and the Eu^{3+} amount. Therefore, the Eu^{3+} species most likely originates from the intrinsic properties of the bulk samples, rather than from surface contaminations. This inference is further strengthened by investigations of the XPS valence band spectra.

Fig. 4.7(d) shows the XPS valence band spectra. The prominent peak located around 2.3 eV below the Fermi level (0 eV) is attributed to the Eu^{2+} multiplet $4f^7$ final state contribution to the valence band, which is consistent with many reported divalent Eu compounds [36,50,51]. No measurable shift of the valence-band maximum is observed within the experimental uncertainty of ± 0.1 eV. The peak D (between 4 eV and 9 eV) and the peak E (between 10 eV and 12.5 eV) show a very similar structure as previously reported for $Pb_{1-x}Eu_xTe$ [47]. Both belong to Eu^{3+} species originating from the Eu $4f^5$ final-state contributions [46,47,51]. The intensity of the peaks D and E increase with the Ca^{2+} content, showing the same variation trend with the peak B but even more pronounced. It is worth noting that an offset of the spectral tail of about 0.2 ± 0.08 eV is present in the vicinity of the Fermi level as shown in the inset of Fig. 4.7(d). The higher the Ca^{2+} content of the sample, the closer the tail is located to the Fermi level. A similar XPS spectra observation was already found in Eu^{3+}-doped $CaTiO_3$ samples [52].

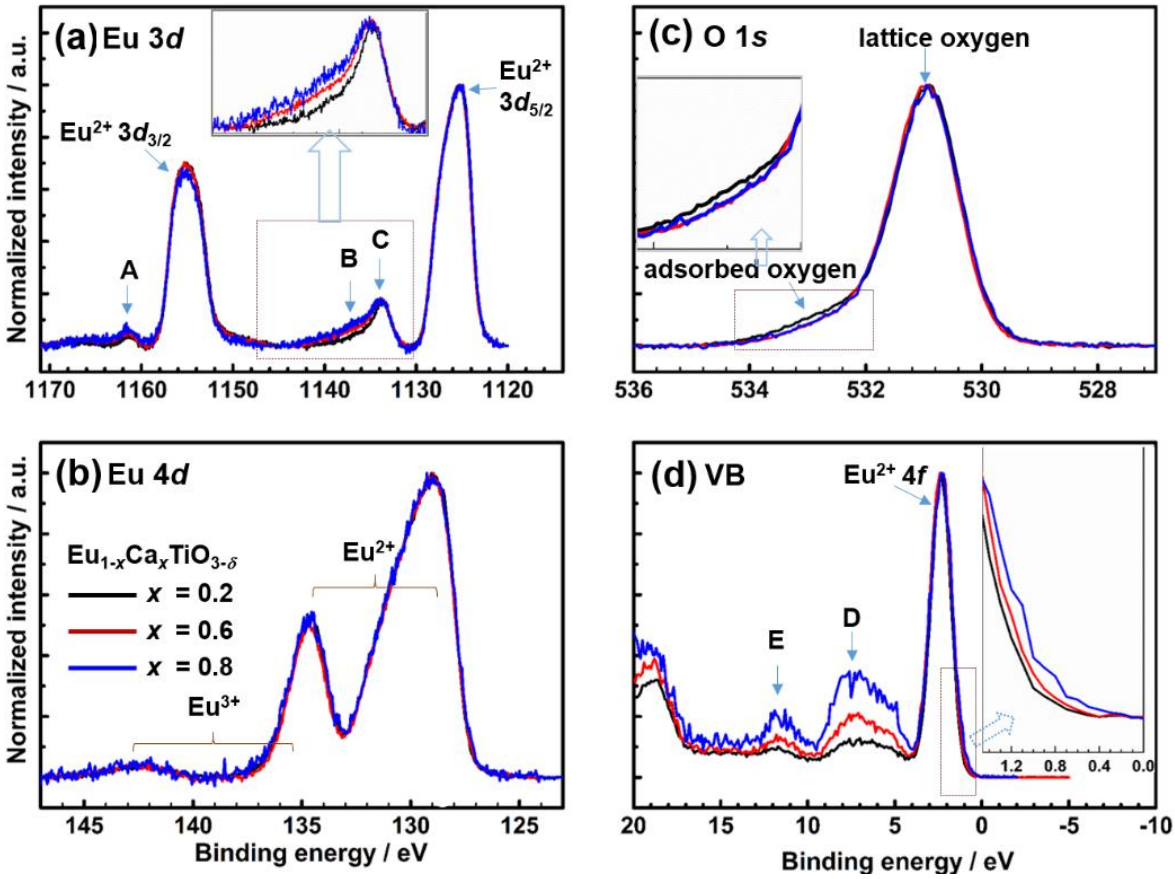

Fig. 4.7 XPS core-level spectra of Eu 3*d* (a), Eu 4*d* (b), O 1*s* (c), and valence band spectra (d) of $Eu_{1-x}Ca_xTiO_{3-\delta}$ bulk samples. The inserts of (a), (c), and (d) show the enlarged view of the corresponding area. All braces and arrows are a guide to the eye.

It is concluded from the XPS spectra analysis that (i) a small amount of Eu^{3+} is present in the Ca^{2+} substituted samples, (ii) the quantity of Eu^{3+} raises with increasing Ca^{2+} content, and (iii) the band tails [53,54] appear in Ca^{2+}-substituted samples and become broadened with increasing Ca^{2+} content. Taking into account the crystallization process of $Eu_{1-x}Ca_xTiO_{3-\delta}$, it is rational that more Eu^{3+} coexists in the Ca^{2+}-richer samples. During the synthetic process under reducing conditions the initial Eu^{3+} is considered to be reduced to Eu^{2+} and the A(II)Ti(IV)O_3 perovskite structure is formed. However, when Eu^{2+} is partly substituted by Ca^{2+}, the unit cell is shrinking accompanied by lowering the symmetry. This process offers a possibility to stabilize a tiny amount of Eu^{3+} in the perovskite-type structure because the ionic radius in 12-fold coordination of Eu^{3+} ($r(Eu^{3+})$ = 1.43 Å) is similar to that of Ca^{2+} ($r(Ca^{2+})$ = 1.48 Å), while a larger size mismatch exists between Ca^{2+} and Eu^{2+} ($r(Eu^{2+})$ = 1.59 Å). Either the presence of Eu^{3+} species or oxygen vacancies would induce the formation of Ti^{3+} for charge compensation. The relative variation of Eu^{3+} and Ti^{3+} concentration could explain the observed shorter but more broadly distributed A–Ti distances on local scale (Fig. 4.5(b)).

4.4.4 Energy Band Calculation

The activation energy E_a of the charge carrier transport was calculated according to the Arrhenius relation. The linear dependency of $\ln\rho$ against $1/T$ shows three distinguishable linear regimes for $x = 0$ at 300 K < T < 1200 K according to the change of the slope as illustrated in Fig. 4.8(a). The more Ca^{2+} incorporation, the less distinguishable are the changes of the slope, e.g., the sample $x = 0.8$ shows a nearly linear behavior of $\ln\rho$ over the entire measured temperature range. The E_a nearly proportionally decreases with raising Ca^{2+} substitution in both the high and low temperature regimes as shown in Fig. 4.8(b). However, the decline rate is different leading to smaller differences of E_a between the high and low temperatures with raising x, e.g., E_a(x = 0.8, 300 K < T < 500 K) = 0.05 eV and E_a(x = 0.8, 800 K < T < 1200 K) = 0.07 eV. The decline of E_a in the extrinsic regime (300 K < T < 500 K) indicates a change of the donor level from a deep to a shallow level.

The band gap energy E_g of the sample $x = 0$ is calculated to be 1 eV, which is well in agreement with the reported value [55]. The E_g of the substituted samples is decreasing with increasing Ca^{2+} content (see Table 4.3), e.g., E_g (x = 0.8) = 0.14 eV. This declining trend is corresponding to the result of XPS valence band spectra and the α behavior. The dramatically decrease of E_g indicates a significant modification of the electronic band structures, resulting from the changes of crystal structures and lattice defects.

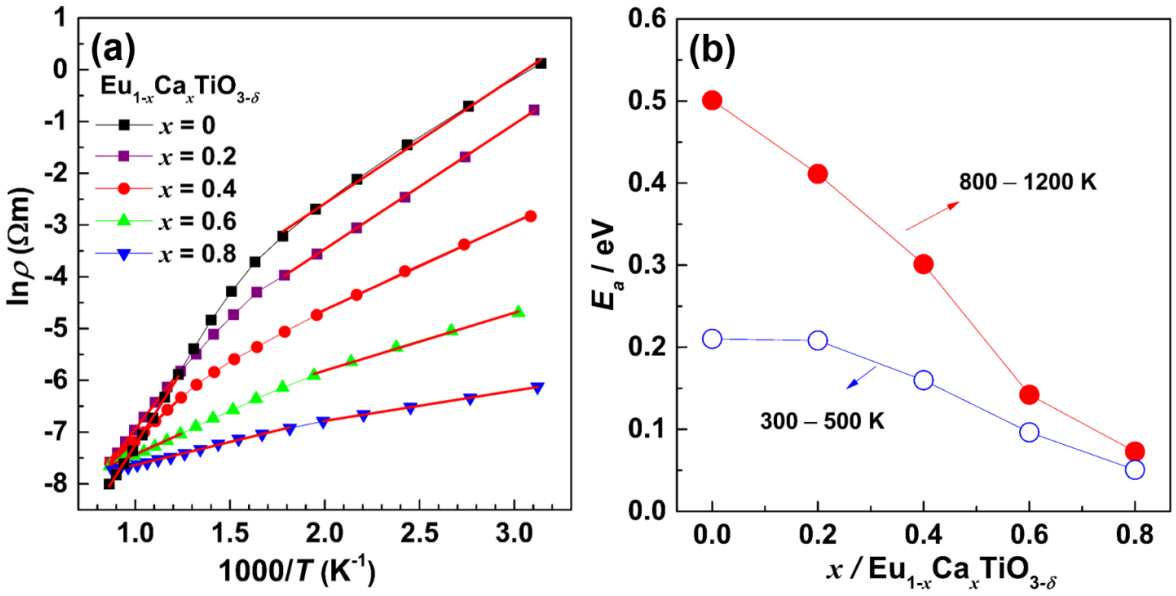

Fig. 4.8 Electrical resistivity lnρ as a function of 1000/T (a) and activation energy E_a as a function of x of $Eu_{1-x}Ca_xTiO_{3-\delta}$ bulk samples.

The calculated total DOS of $Eu_{1-x}Ca_xTiO_3$ (x = 0, 0.25, 0.5, 0.75, 1) is shown in Fig. 4.9. The bottom of the CB is mainly formed by Ti 3*d* states. For Eu containing compositions, the Eu 4*f* states are localized in between the Ti 3*d* and O 2*p* states, but closer to the Ti 3*d* states. The calculated DOS of $EuTiO_3$ is highly consistent with Ref.[56,57]. With increasing Ca^{2+} substitution, at least four obvious features of variations are observed from Fig. 4.9: (i) The DOS intensity of the Eu 4*f* is decreasing as expected, which is similar to previously reported system of $Eu_{1-x}Ba_xTiO_3$ [41]; (ii) The tails of the CB are shifting toward the Eu 4*f* states, resulting in the decreasing band gaps; (iii) The shape of the localized Eu 4*f* states is broadening accompanied by splitting, especially pronounced in the composition of $Eu_{0.25}Ca_{0.75}TiO_3$; (iv) The CB at ~ 3 eV is changing from connected ($EuTiO_3$ and $Eu_{0.75}Ca_{0.25}TiO_3$) to disconnected ($Eu_{0.5}Ca_{0.5}TiO_3$ and $Eu_{0.25}Ca_{0.75}TiO_3$) like $CaTiO_3$. The variation of DOS is in a very good agreement with the XPS valence band spectra and the calculated activation energy from the electrical resistivity, revealing that the modification of the electronic band structure is in accordance with the change of crystal symmetry and the local structure as descripted by the PDF analysis. Admittedly, the actual DOS originated from crystal field splitting can be further influenced by the presence of oxygen vacancies, Ti^{3+}, Eu^{3+}, and the lattice strain resulted from an uneven unit cell compression. Based on all the above-mentioned facts, it can be concluded that the Ca^{2+} substitution results in the shrinkage of the band gap and the increase of impurity levels. Consequently, the electrical conductivity rapidly increases with increasing Ca^{2+} content at low temperatures.

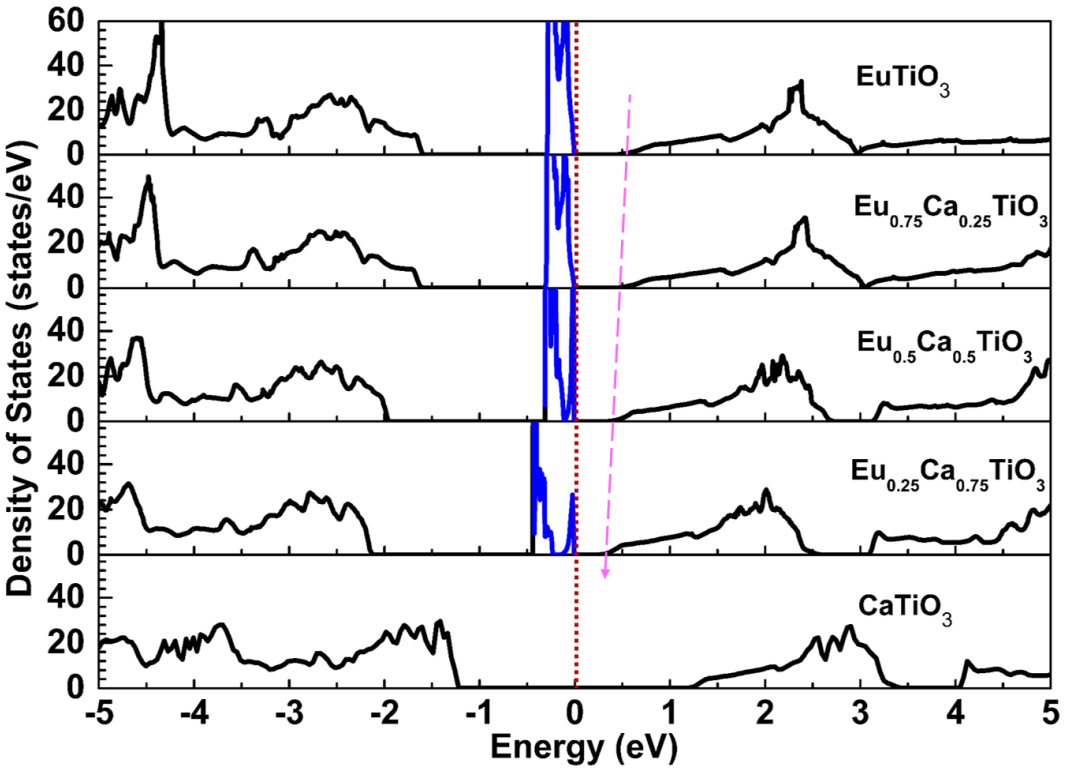

Fig. 4.9 Calculated density of states of $Eu_{1-x}Ca_xTiO_3$ (x = 0, 0.25, 0.5, 0.75, 1) compositions. The zero level of energy is chosen as the top of the valence band. The pink arrow is a guide to the eye showing the shift of the bottom of conduction band (CB).

4.4.5 Thermal transport properties

The total thermal conductivity κ consists of an electronic part κ_e and a lattice part κ_l, $\kappa = \kappa_e + \kappa_l$. Since the electrical conductivity is low in the case of $Eu_{1-x}Ca_xTiO_3$ samples, the calculated value of κ_e accounts for less than 2 % of κ. The electronic part is negligible and the lattice thermal conductivity is approximately equal to the total thermal conductivity, $\kappa \approx \kappa_l$. The density of all bulk samples shows a broad distribution in the compositional range ($0 \leq x \leq 1$) as listed in Table 4.3. For the sake of comparison, the experimentally obtained thermal conductivity data are corrected by using the Maxwell equation [20].

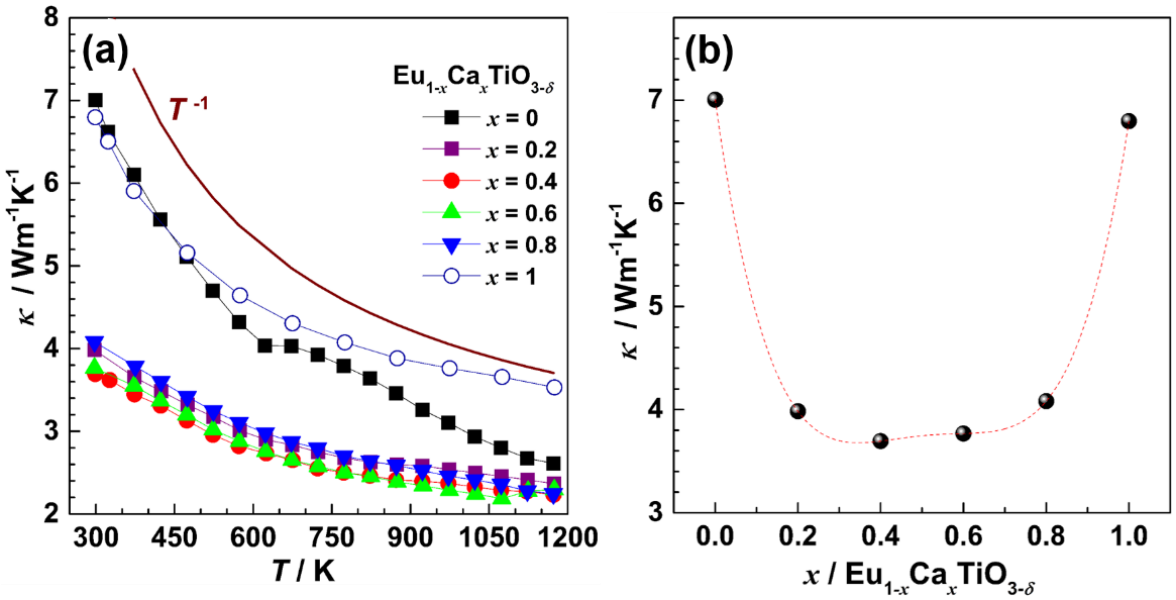

Fig. 4.10 Temperature dependence of the total thermal conductivity κ (a) of $Eu_{1-x}Ca_xTiO_{3-\delta}$ bulk samples and composition dependence of the total thermal conductivity κ at 300 K (b). The dashed lines are drawn to show the trends.

The temperature dependence of the thermal conductivity κ of $Eu_{1-x}Ca_xTiO_{3-\delta}$ is shown in Fig. 4.10(a). The κ decreases with increasing temperature approximately following the T^{-1} dependence at higher temperature, indicating that the dominant phonon scattering mechanism is the Umklapp scattering (phonon–phonon interactions). At room temperature, a significant reduction of κ is observed for all substitued samples. For example, κ of $x = 0.4$ ($\kappa \approx 3.6$ W·m^{-1}·K^{-1}) is reduced by almost 50 % compared to that of $x = 0$ ($\kappa \approx 7$ W·m^{-1}·K^{-1}). The plot of κ at room temperature as a function of the composition is presented in Fig. 4.10(b). Since the κ *vs.* composition dependence shows a striking resemblance to the often observed alloy scattering, e.g., for ZrNiSn based compounds [58], SiGe alloys [59], and $PbTe_{1-x}Se_x$ alloys [60], the huge reduction of κ is most likely attributed to the mass fluctuation due to the large difference of the atomic mass of Eu and Ca. With increasing temperature the influence of phonon scattering resulting from lattice defects (mass disorder, strain, etc.) decreases in favour of Umklapp scattering events. Consequently, the κ of all $Eu_{1-x}Ca_xTiO_{3-\delta}$ ($0.2 \leq x \leq 0.8$) samples converges to the value of the pristine sample ($x = 0$) at sufficiently high temperature, while the sample $CaTiO_3$ retaines a relatively high κ compared to the samples containing the heavy element europium.

4.4.6 Power factor and *ZT* value

The power factor ($PF = \alpha^2\sigma$) is an indicator for the electrical transport properties of thermoelectric materials. Due to the significant increase of the electrical conductivity at room temperature, the *PF* of the sample with $x = 0.8$ increases by three orders of magnitude compared with the sample with $x = 0$ as shown in Fig. 4.11, i.e. $PF_{(x = 0)} = 1.4 \times 10^{-3}$ mW·m^{-1}K^{-2} and $PF_{(x = 0.8)} = 1.38$ mW·m^{-1}K^{-2}. The *PF* values increase with the Ca^{2+} content over the entire temperature range, converging to similar

values at the maximum temperature (~1150 K). The sample with $x = 0$ exhibits a higher *PF* value at $T > 1000$ K due to the higher electrical conductivity.

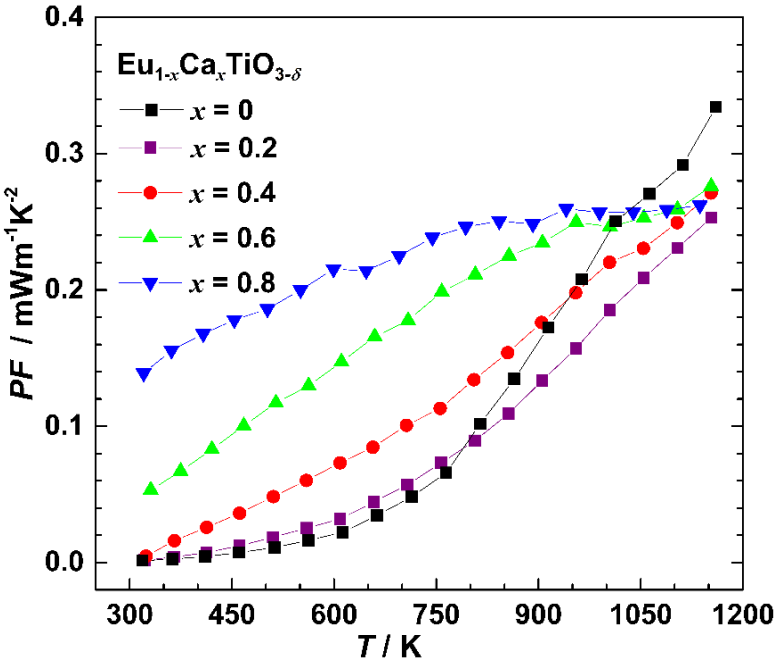

Fig. 4.11 Temperature dependence of the power factor *PF* of $Eu_{1-x}Ca_xTiO_{3-\delta}$ samples.

As a result of the reduction of κ and simultaneous the increase of power factor, the *ZT* values increase with raising Ca^{2+} content as presented in Fig. 4.12(a). The sample $x = 0.8$ exhibits the highest *ZT* value among all samples in the temperature range up to 1000 K. While at even higher temperature, the *ZT* value of $x = 0$ is markedly increased. The average *ZT* value (ZT_m) [61] decides the energy conversion efficiency of a thermoelectric device in practical applications, rather than its maximum *ZT* [62]. The ZT_m value is substantially increased by Ca^{2+} substitution as shown in Fig. 12(b). Exceedingly, the ZT_m value of $x = 0.8$ is enhanced by 100 % compared to the pristine sample. Although the highest observed *ZT* value is noticeably lower than that state of art TE materials, mainly due to the intrinsic low charge carrier mobility of oxides, partial substitution of Eu^{2+} with Ca^{2+} is more attractive for TE application perfromance compared to the pristine $EuTiO_3$.

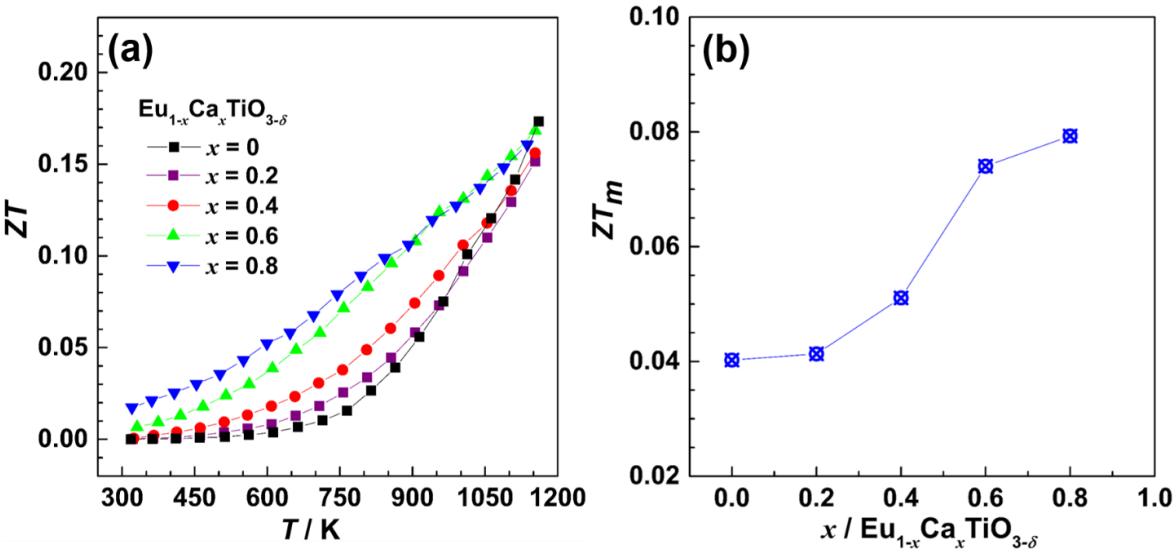

Fig. 4.12 Temperature dependence of the *ZT* value (a) and composition dependence of the average ZT_m value (b) of $Eu_{1-x}Ca_xTiO_{3-\delta}$ bulk samples.

4.5. Conclusions

Large-scale substitution of Eu^{2+} with the cheaper and environment-friendly Ca^{2+} in $EuTiO_3$ reveals a positive effect on the TE performance. Ca^{2+} substitution introduces local lattice imperfections and chemical pressure. The crystal structure modifications were detected by deviations of the local structure from the average long-range one (Rietveld refinements, PDF, EXAFS) and accompanying the accommodation of Eu^{3+} as observed from XPS. This is resulting in an alteration of the electronic band structure, which is proved by DOS calculation. At ambient temperature, Ca^{2+} substitution leads to an enhanced formation of additional point defects drastically improving the charge carrier concentration and hence affects the electrical transport properties. The influence of Ca^{2+} substitution on both electrical and thermal transport properties becomes less effective with increasing temperature in the investigated temperature range, because the source from which the carriers are generated and their scattering mechanism changes. Nevertheless, the ZT_m value of $Eu_{0.2}Ca_{0.8}TiO_{3-\delta}$ is approximately 100 % larger than that of pristine $EuTiO_3$. This work demonstrates new possibilities (e.g., controlling lattice deformation, etc.) for enhancing the TE performance of $EuTiO_3$.

References

[1] R. Morrow, J. Soliz, A. Hauser, J. Gallagher, M. Susner, M. Sumption, A. Aczel, J. Yan, F. Yang, P. Woodward, The effect of chemical pressure on the structure and properties of A_2CrOsO_6 (*A* = Sr, Ca) ferrimagnetic double perovskite, *Journal of Solid State Chemistry* 238 (2016) 46–52.

[2] A. Huon, D. Lee, A. Herklotz, Fitzsimmons, H. Lee, S. May, Effect of chemical pressure on the electronic phase transition in $Ca_{1-x}Sr_xMn_7O_{12}$ films, *APL Materials* 5 (2017) 96105.

[3] A. Kiswandhi, J. Brooks, J. Lu, J. Whalen, T. Siegrist, H. Zhou, Chemical pressure effects on structural, magnetic, and transport properties of $Mn_{1-x}Co_xV_2O_4$, *Physical Review B* 84 (2011) 205138.

[4] P. Weller, Solid state chemistry and physics, M. Dekker, 1973.

[5] V. Vashook, L. Vasylechko, M. Knapp, H. Ullmann, U. Guth, Lanthanum doped calcium titanates: synthesis, crystal structure, thermal expansion and transport properties, *Journal of Alloys and Compounds* 354 (2003) 13–23.

[6] B. Toby, EXPGUI, a graphical user interface for GSAS, *Journal of Applied Crystallography* 34 (2001) 210–213.

[7] G. Ashiotis, A. Deschildre, Z. Nawaz, J. Wright, D. Karkoulis, F. Picca, J. Kieffer, The fast azimuthal integration Python library: pyFAI, *Journal of Applied Crystallography* 48 (2015) 510–519.

[8] E. Knudsen, H. Sørensen, J. Wright, G. Goret, J. Kieffer, FabIO: easy access to two-dimensional X-ray detector images in Python, *Journal of Applied Crystallography* 46 (2013) 537–539.

[9] D. Keen, A comparison of various commonly used correlation functions for describing total scattering, *Journal of Applied Crystallography* 34 (2001) 172–177.

[10] A. Soper, GudrunN and GudrunX: programs for correcting raw neutron and X-ray diffraction data to differential scattering cross section, *Science & Technology Facilities Council*, 2011.

[11] M. Wojdyr, Fityk: a general-purpose peak fitting program, *Journal of Applied Crystallography* 43 (2010) 1126–1128.

[12] C. Farrow, P. Juhas, J. Liu, D. Bryndin, E. Božin, J. Bloch, T. Proffen, S. Billinge, PDFfit2 and PDFgui: computer programs for studying nanostructure in crystals, *Journal of Physics: Condensed Matter* 19 (2007) 335219.

[13] B. Campbell, H. Stokes, D. Tanner, D. Hatch, ISODISPLACE: a web-based tool for exploring structural distortions, *Journal of Applied Crystallography* 39 (2006) 607–614.

[14] B. Ravel, M. Newville, ATHENA, ARTEMIS, HEPHAESTUS: data analysis for X-ray absorption spectroscopy using IFEFFIT, *Journal of Synchrotron Radiation* 12 (2005) 537–541.

[15] J. Rehr, J. Kas, F. Vila, M. Prange, K. Jorissen, Parameter-free calculations of X-ray spectra with FEFF9, *Physical Chemistry Chemical Physics* 12 (2010) 5503–5513.

[16] P. Blöchl, Projector augmented-wave method, *Physical Review B* 50 (1994) 17953.

[17] G. Kresse and D. Joubert, From ultrasoft pseudopotentials to the projector augmented-wave method, *Physical Review B* 59 (1999) 1758.

[18] V. Anisimov, F. Aryasetiawan, A. Lichtenstein, First-principles calculations of the electronic structure and spectra of strongly correlated systems: the LDA+ U method, *Journal of Physics: Condensed Matter* 9 (1997) 767.

[19] G. Kresse and J. Furthmüller, Efficient iterative schemes for ab initio total-energy calculations using a plane-wave basis set, *Physical Review B* 54 (1996) 11169–11186.

[20] G. Kresse and J. Hafner, Ab initio molecular dynamics for liquid metals, *Physical Review B* 47 (1993) 558–561.
[21] M. Allieta, M. Scavini, L. Spalek, V. Scagnoli, H. Walker, C. Panagopoulos, S. Saxena, T. Katsufuji, C. Mazzoli, Role of intrinsic disorder in the structural phase transition of magnetoelectric $EuTiO_3$, *Physical Review B* 85 (2012) 184107.
[22] A. Glazer, Simple ways of determining perovskite structures, *Acta Crystallographica Section A*: *crystal physics, diffraction, theoretical and general crystallography* 31 (1975) 756–762.
[23] R. Ali, M. Yashima, Space group and crystal structure of the perovskite $CaTiO_3$ from 296 to 1720 K, *Journal of Solid State Chemistry* 178 (2005) 2867–2872.
[24] M. Yashima, R. Ali, Structural phase transition and octahedral tilting in the calcium titanate perovskite $CaTiO_3$, *Solid State Ionics* 180 (2009) 120–126.
[25] A. Beran, E. Libowitzky, T. Armbruster, A single-crystal infrared spectroscopic and X-ray-diffraction study of untwinned San Benito perovskite containing OH groups, *The Canadian Mineralogist* 34 (1996) 803–809.
[26] T. Yamanaka, N. Hirai, Y. Komatsu, Structure change of $Ca_{1-x}Sr_xTiO_3$ perovskite with composition and pressure, *American Mineralogist* 87 (2002) 1183–1189.
[27] M. Carpenter, C. Howard, K. Knight, Z. Zhang, Structural relationships and a phase diagram for $(Ca,Sr)TiO_3$ perovskites, *Journal of Physics: Condensed Matter* 18 (2006) 10725–10749.
[28] R. Ranjan, D. Pandey, N. Lalla, Novel features of $Sr_{1-x}Ca_xTiO_3$ phase diagram: evidence for competing antiferroelectric and ferroelectric interactions, *Physical Review Letters* 84 (2000) 3726–3729.
[29] M. Coduri, P. Masala, M. Allieta, I. Peral, M. Brunelli, C. Biffi, M. Scavini, Phase Transformations in the CeO_2–Sm_2O_3 System: A Multiscale Powder Diffraction Investigation, *Inorganic Chemistry* (2018) 879–891.
[30] M. Coduri, M. Scavini, M. Allieta, M. Brunelli, C. Ferrero, Defect structure of Y-doped ceria on different length scales, *Chemistry of Materials* 25 (2013) 4278–4289.
[31] G. Kwei, A. Lawson, S. Billinge, S. Cheong, Structures of the ferroelectric phases of barium titanate, *The Journal of Physical Chemistry* 97 (1993) 2368–2377.
[32] J. Bednorz, K. Müller, $Sr_{1-x}Ca_xTiO_3$: An XY Quantum Ferroelectric with Transition to Randomness, *Physical Review Letters* 52 (1984) 2289–2292.
[33] N. Benedek, C. Fennie, Why are there so few perovskite ferroelectrics? *The Journal of Physical Chemistry C* 117 (2013) 13339–13349.
[34] H. Boström, M. Senn, A. Goodwin, Recipes for improper ferroelectricity in molecular perovskites, Nature communications, 9 (2018) 2380.
[35] D. Bessas, K. Rushchanskii, M. Kachlik, S. Disch, O. Gourdon, J. Bednarcik, K. Maca, I. Sergueev, S. Kamba, M. Ležaić, R. Hermann, Lattice instabilities in bulk $EuTiO_3$, *Physical Review B* 88 (2013) 144308.
[36] L. Sagarna, A. Shkabko, S. Populoh, L. Karvonen, A. Weidenkaff, Electronic structure and thermoelectric properties of nanostructured $EuTi_{1-x}Nb_xO_{3-\delta}$ (x = 0.00; 0.02), *Applied Physics Letters* 101 (2012) 33908.
[37] P. Chaikin, G. Beni, Thermopower in the correlated hopping regime, *Physical Review B* 13 (1976) 647.
[38] A. Kovalevsky, A. Yaremchenko, S. Populoh, P. Thiel, D. Fagg, A. Weidenkaff, J. Frade, Towards a high thermoelectric performance in rare-earth substituted $SrTiO_3$: effects provided

by strongly-reducing sintering conditions, *Physical Chemistry Chemical Physics* 16 (2014) 26946–26954.

[39] A. Kovalevsky, M. Aguirre, S. Populoh, S. Patrício, N. Ferreira, S. Mikhalev, D. Fagg, A. Weidenkaff, J. Frade, Designing strontium titanate-based thermoelectrics: insight into defect chemistry mechanisms, *Journal of Materials Chemistry A* 5 (2017) 3909–3922.

[40] A. Yaremchenko, S. Populoh, S. Patrício, J. Macías, P. Thiel, D. Fagg, A. Weidenkaff, J. Frade, A. Kovalevsky, Boosting thermoelectric performance by controlled defect chemistry engineering in Ta-substituted strontium titanate, Chemistry of Materials 27 (2015) 4995–5006.

[41] X. Xiao, M. Widenmeyer, W. Xie, T. Zou, S. Yoon, M. Scavini, S. Checchia, Z. Zhong, P. Hansmann, S. Kilper, A. Kovalevsky, A. Weidenkaff, Tailoring the structure and thermoelectric properties of $BaTiO_3$ via Eu^{2+} substitution, *Physical Chemistry Chemical Physics* 19 (2017) 13469–13480.

[42] L. Sagarna, S. Populoh, A. Shkabko, J. Eilertsen, A.E. Maegli, R. Hauert, M. Schrade, L. Karvonen, A. Weidenkaff, Influence of the Oxygen Content on the Electronic Transport Properties of $Sr_xEu_{1-x}TiO_{3-\delta}$, *The Journal of Physical Chemistry C* 118 (2014) 7821–7831.

[43] K. Yoshii, M. Mizumaki, A. Nakamura, H. Abe, Structure and magnetism of $Eu_{1-x}Dy_xTiO_3$, *Journal of Solid State Chemistry* 171 (2003) 345–348.

[44] Y. Tokura, Y. Taguchi, Y. Okada, Y. Fujishima, T. Arima, K. Kumagai, Y. Iye, Filling dependence of electronic properties on the verge of metal–Mott-insulator transition in $Sr_{1-x}La_xTiO_3$, *Physical Review Letters* 70 (1993) 2126.

[45] E.-J. Cho, S.-J. Oh, S. Imada, S. Suga, T. Suzuki, T. Kasuya, Origin of the high-binding-energy structure in the 3*d* core-level spectra of divalent Eu compounds, *Physical Review B* 51 (1995) 10146–10149.

[46] B.A. Orlowski, S. Mickevičius, M. Chernyshova, I. Demchenko, A.Y. Sipatov, T. Story, V. Medicherla, W. Drube, Photoemission study of EuS layers buried in PbS, *Journal of Electron Spectroscopy and Related Phenomena* 137 (2004) 763–767.

[47] R. Denecke, L. Ley, G. Springholz, G. Bauer, Resonant photoemission studies of $Pb_{1-x}Eu_xTe$, *Physical Review B* 53 (1996) 4534–4538.

[48] E.-J. Cho, S.-J. Oh, S. Suga, T. Suzuki, T. Kasuya, Electronic structure study of Eu intermetallic compounds by photoelectron spectroscopy, *Journal of Electron Spectroscopy and Related Phenomena* 77 (1996) 173–181.

[49] R. Shvab, E. Hryha, L. Nyborg, Surface chemistry of the titanium powder studied by XPS using internal standard reference, *Powder Metallurgy* 60 (2017) 42–48.

[50] T. Kolodiazhnyi, M. Valant, J. Williams, M. Bugnet, G. Botton, N. Ohashi, Y. Sakka, Evidence of Eu^{2+} 4*f* electrons in the valence band spectra of $EuTiO_3$ and $EuZrO_3$, *Journal of Applied Physics* 112 (2012) 83719.

[51] B.A. Orlowski, S. Mickievicius, V. Osinniy, A.J. Nadolny, B. Taliashvili, P. Dziawa, T. Story, R. Medicherla, W. Drube, High-energy X-ray photoelectron spectroscopy study of MBE grown (Eu, Gd) Te layers, *Nuclear Instruments and Methods in Physics Research Section B*: *Beam Interactions with Materials and Atoms* 238 (2005) 346–352.

[52] K. Wang, B. Zhao, L. Gao, X-ray photoemission spectroscopy investigation of $CaTiO_3$: Eu for luminescence property: effect of Eu^{3+} ion, *Materials Research Bulletin* 78 (2016) 31–35.

[53] P. van Mieghem, Theory of band tails in heavily doped semiconductors, *Reviews of Modern Physics* 64 (1992) 755-793.

[54] E.H. Reihlen, M.J. Jou, D.H. Jaw, G.B. Stringfellow, Optical absorption and emission of $GaP_{1-x}Sb_x$ alloys, *Journal of Applied Physics* 68 (1990) 760–767.
[55] L. Sagarna, K.Z. Rushchanskii, A. Maegli, S. Yoon, S. Populoh, A. Shkabko, S. Pokrant, M. Ležaić, R. Waser, A. Weidenkaff, Structure and thermoelectric properties of $EuTi(O, N)_{3\pm\delta}$, *Journal of Applied Physics* 114 (2013) 33701.
[56] T. Birol, C.J. Fennie, Origin of giant spin-lattice coupling and the suppression of ferroelectricity in $EuTiO_3$ from first principles, *Physical Review B* 88 (2013) 94103.
[57] H. Akamatsu, Y. Kumagai, F. Oba, K. Fujita, H. Murakami, K. Tanaka, I. Tanaka, Antiferromagnetic superexchange via 3 d states of titanium in $EuTiO_3$ as seen from hybrid Hartree-Fock density functional calculations, *Physical Review B* 83 (2011) 214421.
[58] S. Bhattacharya, M.J. Skove, M. Russell, T.M. Tritt, Y. Xia, V. Ponnambalam, S.J. Poon, N. Thadhani, Effect of boundary scattering on the thermal conductivity of TiNiSn-based half-Heusler alloys, *Physical Review B* 77 (2008) 184203.
[59] J. Garg, N. Bonini, B. Kozinsky, N. Marzari, Role of disorder and anharmonicity in the thermal conductivity of silicon-germanium alloys: A first-principles study, *Physical Review Letters* 106 (2011) 45901.
[60] Z. Tian, J. Garg, K. Esfarjani, T. Shiga, J. Shiomi, G. Chen, Phonon conduction in PbSe, PbTe, and $PbTe_{1-x}Se_x$ from first-principles calculations, *Physical Review B* 85 (2012) 184303.
[61] H.S. Kim, W. Liu, G. Chen, C.-W. Chu, Z. Ren, Relationship between thermoelectric figure of merit and energy conversion efficiency, *Proceedings of the National Academy of Sciences* 112 (2015) 8205–8210.
[62] H.J. Wu, L.-D. Zhao, F.S. Zheng, D. Wu, Y.L. Pei, X. Tong, M.G. Kanatzidis, J.Q. He, Broad temperature plateau for thermoelectric figure of merit $ZT > 2$ in phase-separated $PbTe_{0.7}S_{0.3}$, *Nature Communications* 5 (2014) 4515.

Chapter 5 Thermoeletric properties of Mg^{2+}/ Sr^{2+} substituted $EuTiO_3$

Abstract

In this chapter, the Mg^{2+} and Sr^{2+} substituted $EuTiO_3$ samples were synthesized to study the formability of a solid solution and their TE properties. The results reveal that the ionic radius of Mg^{2+} is too small to be coordinated in AO_{12} cuboctahedra of titanates under the applied synthesis method. The formation of single-phase $Eu_{1-x}Mg_xTiO_3$ solid solution is restricted far less than 1 %. The single-phase $Eu_{1-x}Sr_xTiO_3$ solid solution is achievable in the full range of $0 \leq x \leq 1$. The partial Sr^{2+} substitution has a weak influence on unit cell parameters and the TE properties.

5.1 Introduction

In chapter 3 and 4, the Ba^{2+} / Ca^{2+} substitution can successfully form the single-phase $Eu_{1-x}Ba_xTiO_{3-\delta}$ / $Eu_{1-x}Ca_xTiO_{3-\delta}$ solid solutions in a full range of $0 \leq x \leq 1$ by using a modified Pechini method. Especially, apart from the superiority of Ca being a naturally abundant and non-toxic element, substitution with the smaller and lighter Ca^{2+} gives rise to several positive effects to improve the TE properties. The Ca^{2+}substitution introduces chemical pressure which causes lattice deformation with large lattice strain, leading to large amounts of lattice defects generation as well as electronic bandstructure variation. As a result, electrical conductivity is significantly improved. On the other hand, due to the large mass contrast at *A*-site (i.e., M_{Ca} = 40.078 g/mol, M_{Eu} = 151.964 g/mol), the mass fluctuation enhances phonon scattering and hence remarkably reduces the thermal conductivity. The essential reasons for these phenomena are closely associated with the ionic radius and the ionic mass of Ca^{2+}. Inspired by these observations, I wondered what kind of effects to the TE properties would occur if substitution is achieved by using even smaller and lighter Mg^{2+} (M_{Mg} = 24.305 g/mol).

First of all, the formability of single-phase $Eu_{1-x}Mg_xTiO_3$ solid solutions can be preliminarily evaluated according to two empirical substitution rules: (i) the difference of ionic radii between host and guest generally should be smaller than 15 %, otherwise, the solid solutions are usually hard to form and the solubility limit of the substituent is usually below 1 % [1]; (ii) perovskite compounds are favorable in a broad range of the Goldschmidt tolerance factor (*t*) [2]. Typically, a cubic perovskite ABO_3 is observed for $t \approx 1$, while smaller values ($0.7 < t < 1$) or larger values ($1 < t < 1.1$) result in distorted perovskite, combinations outside this range form non-perovskite structures [3]. The ionic radii of Eu^{2+}, Ti^{4+} and O^{2-} with the 12-, 6- and 2- fold coordination in ABO_3 crystal structure are r (Eu^{2+}, XII) = 1.58 Å (the value was extrapolated from the data given in the literature), r (Ti^{4+}, VI) = 0.745 Å, and r (O^{2-}, II) = 1.21 Å according to the literature database [4], respectively. Supposing the guest Mg^{2+} also possesses 12-fold coordination to form the perovskite structure, the ionic radius of Mg^{2+} is r (Mg^{2+}, XII) = 1.343 Å (the value was extrapolated from the data given in

the literature [4]). The difference of ionic radii between the host (Eu^{2+}) and guest (Mg^{2+}) is calculated to be 15 %, indicating that it might be difficult to form single-phase solid solutions based on the first rule. The calculated t of $Eu_{1-x}Mg_xTiO_{3-\delta}$ is to be $0.923 \leq t \leq 1.002$ in the full range of $0 \leq x \leq 1$. According to the second rule, Mg^{2+} substitution seems to be able to form a perovskite-type structure. However, in fact, $MgTiO_3$ possesses an ilmenite-type structure but not a perovskite-type structure. It is suggesting that the t range is only a prerequisite for the formation of perovskites, but not a sufficient condition. Therefore, whether single-phase $Eu_{1-x}Mg_xTiO_3$ solid solutions can be obtained as well as the solubility limit are still unknown questions. If yes, the effects aroused by Mg^{2+} substitution on thermoelectric performance could be interesting as mentioned above.

The TE properties of Sr^{2+} substituted $EuTiO_3$ had been studied and reported by Sagma et al. [5]. The reported results revealed that the Sr^{2+} substitution did not change the symmetry of crystal structure due to the very similar ionic radii of 12-fold coordination of Sr^{2+} and Eu^{2+}. The electrical transport properties were reported, excluding thermal conductivity. Therefore, for the sake of investigating completeness, the Sr^{2+} substituted samples were also synthesized and their thermoelectric properties were systematically measured and investigated in this chapter.

5.2 Experimental

Three Mg^{2+} substituted samples $Eu_{1-x}Mg_xTiO_3$ (x = 0.2, 0.4, 0.6) and four Sr^{2+} substituted samples $Eu_{1-x}Sr_xTiO_3$ (x = 0.2, 0.4, 0.6, 0.8) were synthesized using the same method as previously for Ba^{2+} and Ca^{2+} substituted samples. The notations of the samples are listed in Table 5.1. The source of Mg^{2+} and Sr^{2+} were magnesium acetate tetrahydrate (Alfa Aesar, 99.9 %) and strontium acetate hemihydrate (Alfa Aesar, ≥ 98 %), respectively. The other chemical resources were the same as previously. The details of the experimental techniques can be found in chapter 2. The samples were densified by conventional sintering at 1673 K for 10 h in a reducing atmosphere (10 vol.% H_2 in N_2). The sintered samples were cut into desired shapes for physical property measurements. A part of the sintered samples was ground to fine powder for powder XRD and chemical analysis.

Powder XRD data were collected by a Rigaku Smartlab X-ray diffractometer using Cu-$K\alpha_{1,2}$ radiation. Cu-K_β radiation was suppressed by a thin nickel foil with approximately 90 % efficiency. The diffraction patterns were recorded from 10° to 90° (2 theta) using continuous scanning at a step size of 0.01°. High-resolution powder XRD data of three samples (E8M2, E8S2, and E6S4) were collected at the ID22 beamline of ESRF in Grenoble. The samples were loaded into 0.7 mm diameter Kapton® capillaries and mounted parallel to the axis of the diffractometer. Data were collected at ambient temperature using an X-ray wavelength of 0.3542224(1) Å up to 2θ = 42° ($Q_{max} \approx 12.5$ Å^{-1}) for a total counting time of about half an hour per pattern.

The details of the experimental techniques of the measurements for the thermal diffusivity Λ, sample bulk density d, electrical resistivity ρ, and Seebeck coefficient α can be found in chapter 2. These measurements were performed under forming gas (5 vol. % H_2 in Ar). The assessment of the elemental distribution of E8M2 sample was performed by SEM (Gemini SEM 500 instrument) and EDS (Bruker Xflash 6|60 detector) studies on the polished sample.

Table 5.1 The notation, nominal composition, calculated heat capacity c_p, experimental bulk density d, theoretical density d_0, and porosity ε of the studied samples. The theoretical densities d_0 are obtained by XRD refinements excluding the sample E8M2, whose d_0 was calculated by the relation $d_{0\,(E8M2)} = 0.8d_{0\,(EuTiO3)} + 0.2\,d_{0\,(MgTiO3)}$.

Samples	Nominal compositions	c_p ($J \cdot g^{-1} \cdot K^{-1}$)	d ($g \cdot cm^{-3}$)	d_0 ($g \cdot cm^{-3}$)	ε (%)
ETO	$EuTiO_3$	0.5032	6.27	6.91	9
E8M2	$Eu_{0.8}Mg_{0.2}TiO_3$	0.5610	5.47	6.306	13.3
E8S2	$Eu_{0.8}Sr_{0.2}TiO_3$	0.5308	5.84	6.57	11.1
E6S4	$Eu_{0.6}Sr_{0.4}TiO_3$	0.5615	5.76	6.198	7
E4S6	$Eu_{0.4}Sr_{0.6}TiO_3$	0.5961	5.34	5.836	8.5
E2S8	$Eu_{0.2}Sr_{0.8}TiO_3$	0.6351	4.89	5.478	10.7

5.3 Results and discussion

5.3.1 Formability of $Eu_{1-x}Mg_xTiO_3$ solid solution

The laboratory powder X-ray diffraction patterns of $Eu_{1-x}Mg_xTiO_3$ (x = 0, 0.2, 0.4, 0.6) samples are illustrated in Fig. 5.1. It is obvious that these substituted samples have secondary phases, whose intensities increase with increasing Mg^{2+} content. The E8M2 sample was subjected to perform synchrotron radiation diffraction. The refinement results are summarized in Table 5.2 and the PXRD pattern is presented in Fig. 5.2. The results reveal that there are three phases including $EuTiO_3$, $MgTiO_3$, and $MgTi_2O_4$ in this sample according to the structure refinement [6]. The fractions of each phase component determined by XRD refinements are in good agreement with the overall by ICP–OES obtained cation contents. $MgTiO_3$ and $MgTi_2O_4$ are also the main secondary phases in samples $Eu_{1-x}Mg_xTiO_3$ with x = 0.4 and 0.6.

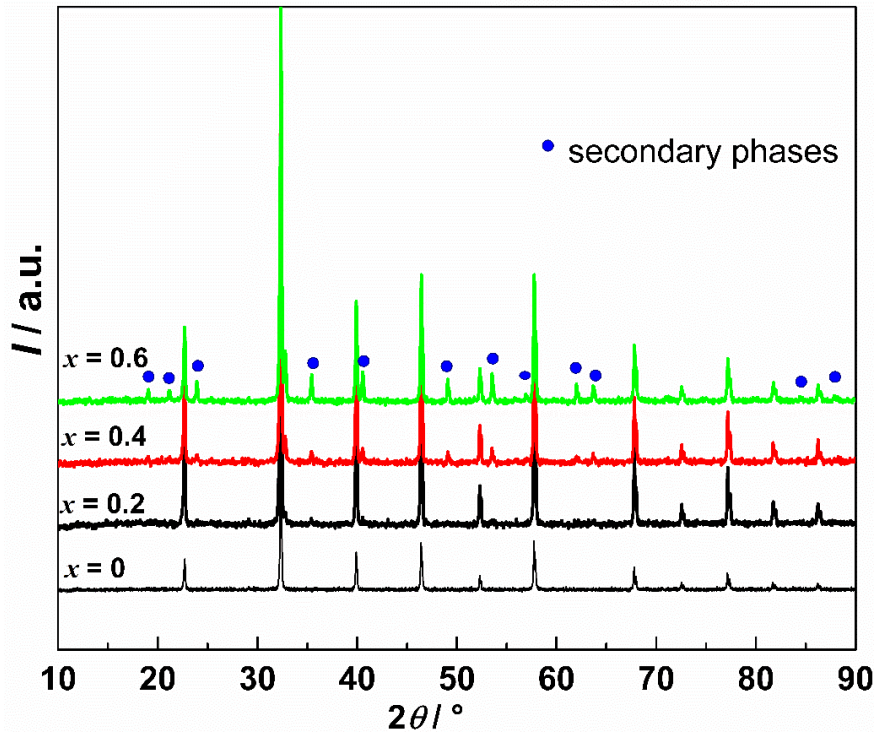

Fig. 5.1 Powder X-ray diffraction patterns of nominal chemical compositions of $Eu_{1-x}Mg_xTiO_3$ (x = 0, 0.2, 0.4, 0.6) samples.

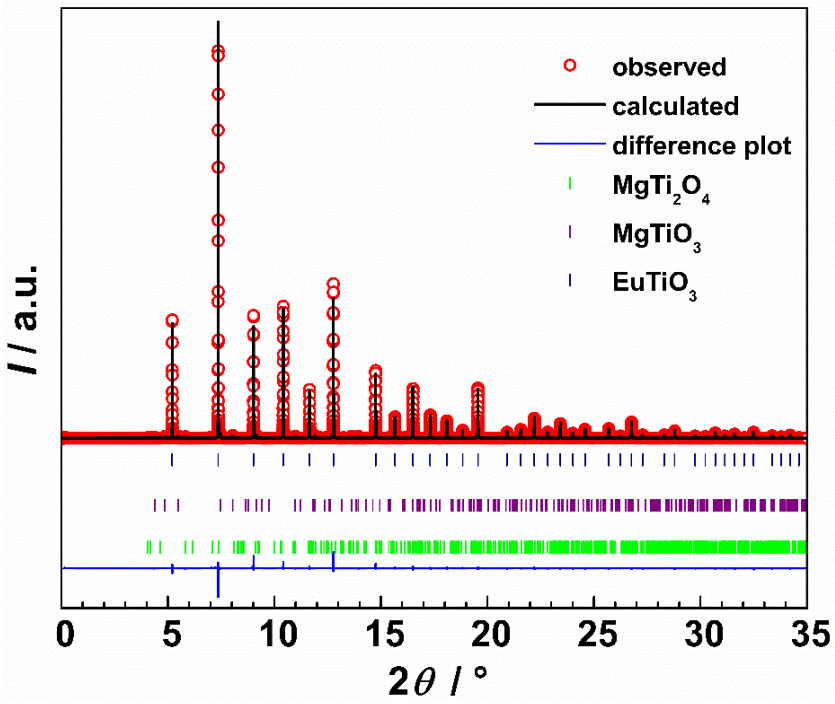

Fig. 5.2 Powder X-ray diffraction refinement pattern of the sample E8M2. X-ray wavelength λ = 0.3542224(1) Å.

Table 5.2 The chemical composition of cations probed by ICP-OES analysis and the summary of the XRD Rietveld refinements of the E8M2 sample. Estimated standard deviations are given in brackets.

Nominal chemical composition		$Eu_{0.8}Mg_{0.2}TiO_3$	
Refinement composition	$EuTiO_3$	$MgTiO_3$	$MgTi_2O_4$
Phase fraction (wt. %)	76.33(4)	17.96(8)	5.69(8)
Phase group	$Pm\bar{3}m$	$R\bar{3}H$	$Bbmm$
Crystal system	cubic	trigonal	orthorhombic
Unit cell parameter (Å)	a = 3.9023(2)	a = 5.0549(1) c = 13.9106(1)	a = 9.7504(1) b = 10.0151(8) c = 3.7394(3)
Cell volume ($Å^3$)	59.425(1)	307.824(3)	365.16(3)
Experimental chemical composition of cations	Eu: 0.79 (0.03)	Mg: 0.19 (0.01)	Ti: 0.95 (0.04)
Refinement parameter	R_p: 8.25 %	R_{wp}: 12.1 %	R_{exp}: 3.76 % χ^2: 10.3

The SEM micrograph of the polished E8M2 sample and the corresponding EDS mapping result of elemental distribution are presented in Fig. 5.3. The color clusters from the EDS mapping indicate that a phase separation takes place in the sample. Combining with the XRD refinement result, it is suggesting that the yellow area is mainly $MgTiO_3$ phase and the blue area is $MgTi_2O_4$ phase. The $MgTi_2O_4$ phase is always presented together with $MgTiO_3$ phase in the matrix. Due to the isostructural relation of $EuTiO_3$ and $SrTiO_3$ at room temperature, it is instructive to consider prior works on the investigations of (Sr, Mg)TiO_3 ceramics [7,8]. Similar secondary phases are coexistent within the $SrTiO_3$ matrix in stoichiometric and nonstoichiometric (Sr, Mg)TiO_3 ceramics. It was reported that the solubility of Mg^{2+} in the $SrTiO_3$ matrix was largely restricted to less than 20 % and 1 % in Ref. [8] and [7], respectively. The smaller Mg^{2+} cannot hold the 12-fold coordination as Sr^{2+} or Eu^{2+} in the perovskite structure. The pure $MgTiO_3$ possesses ilmenite-type structure instead of the perovskite structure, both Mg^{2+} and Ti^{4+} are octahedrally coordinated while O^{2-} is coordinated by 4 cations (i.e. 2 Mg^{2+} and 2 Ti^{4+}). The cubic perovskite has a closely packed structure and hence the possibility of interstitial solid solution formation is also very small. The difference of cell parameters between pristine ETO sample and the matrix ETO in E8M2 sample is around 0.06 %, which is neglectable considering the refinement deviations. Therefore, it is concluded that the formation of $Eu_{1-x}Mg_xTiO_3$ solid solution is restricted to far less than 1 % and nearly negligible.

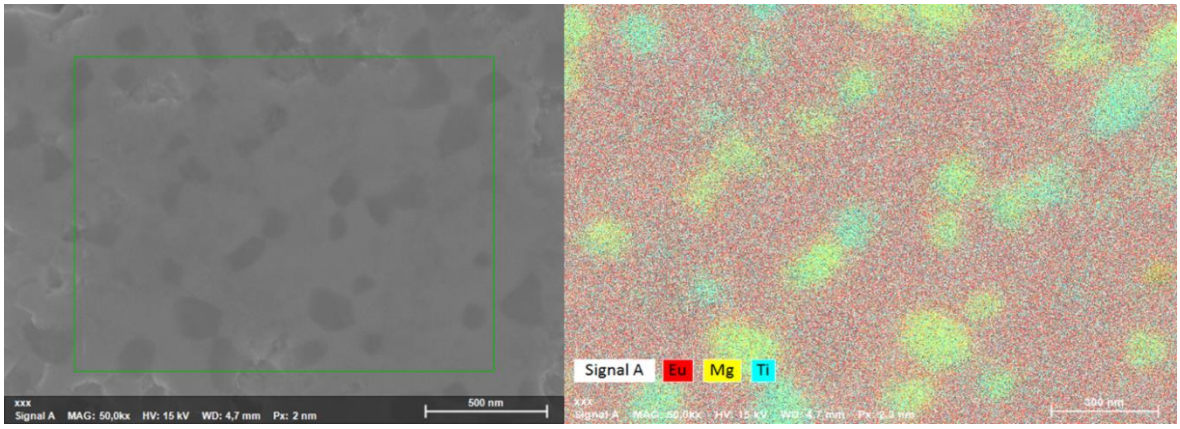

Fig. 5.3 SEM micrograph of polished E8M2 sample (left) and the responding EDS mapping result of elemental distribution (right).

5.3.2 Formability of $Eu_{1-x}Sr_xTiO_3$ solid solution

The single-phase $Eu_{1-x}Sr_xTiO_3$ solid solution was obtained in the full range of $0 \leq x \leq 1$. All Sr^{2+}-substituted samples show a cubic structure according to the laboratory powder XRD. Two samples E8S2 and E6S4 were performed synchrotron radiation diffraction and the refinement patterns are presented in Fig. 5.4. The unit cell parameters slightly increase with increasing Sr^{2+} content, which is highly consistent with Ref. [5]. The unit cell parameters of some $Eu_{1-x}A_xTiO_3$ (A = Mg^{2+}, Ca^{2+}, Sr^{2+}, Ba^{2+}) samples are illustrated in Fig 5.5. It is obvious that the Ba^{2+} / Ca^{2+} substitution significantly increases/decreases the cell parameters, while the cell parameters are slightly changed for the Sr^{2+} substitution samples compared to pristine ETO.

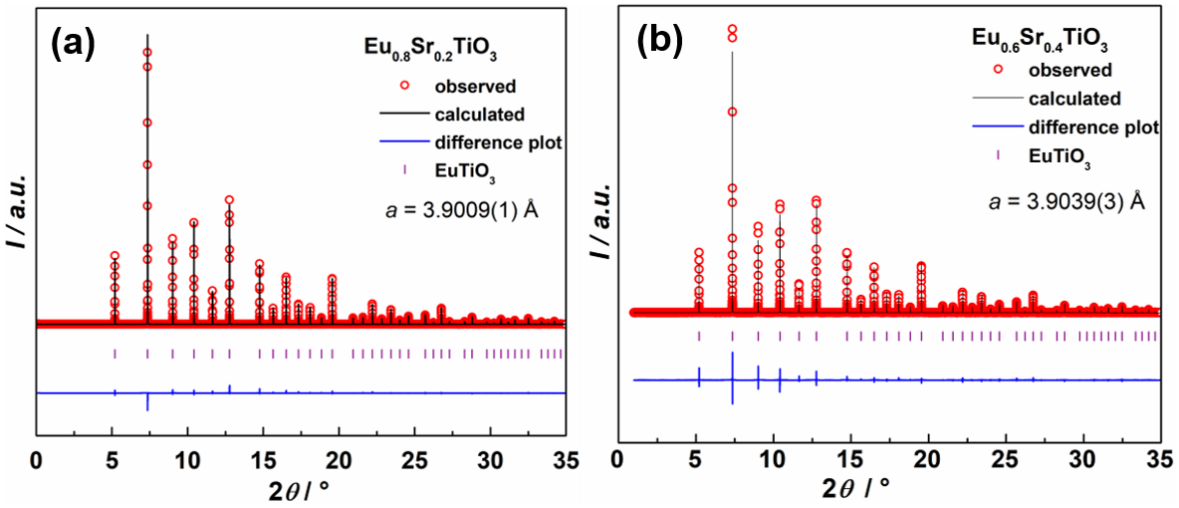

Fig. 5.4 Powder X-ray diffraction refinement pattern of E8S2 (a) and E6S4 (b) samples.

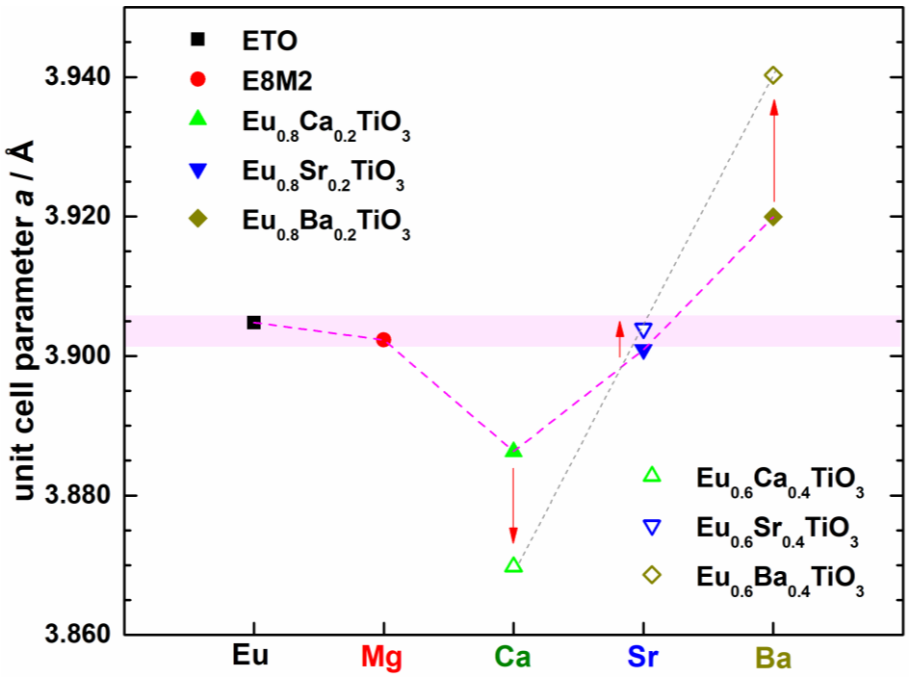

Fig. 5.5 The unit cell parameters of some $Eu_{1-x}A_xTiO_{3-\delta}$ (A = Mg^{2+}, Ca^{2+}, Sr^{2+}, Ba^{2+}) samples. The dashed lines and arrows in the figure are guides for the eye.

5.3.3 Electrical transport properties

The electrical resistivity ρ and Seebeck coefficient α of the Sr^{2+}-substituted samples and the E8M2 sample were measured as a function of temperature in the range of 300 K < T < 1200 K in the heating and cooling cycles. The obtained results are shown in Fig. 5.6, including the results of pristine ETO sample. The data obtained from the heating and the cooling cycles are almost reproducible. For the Eu-rich samples (i.e., ETO, E8S2, E6S4), the difference of the temperature dependent ρ and α are very small among the samples over a wide measured temperature range. The ρ of E8M2 is a little bit larger than other samples, which is most likely resulting from the effect of the secondary phases. The α is negative throughout the entire temperature range implying that electrons are the dominant free charge carriers. For the Sr-rich samples (i.e., E4S6 and E2S8), their α (T) valleys are found at around 550 K and their maximum $|\alpha|$ are observed about 700 μV/K. For the other samples, their $|\alpha|$ are monotonically decreasing with raising temperature when T > 350 K. The sample E6S4 shows a maximum absolute value of α at 362 K, i.e., $|\alpha|$ = 1337 μV/K. It is also the maximum $|\alpha|$ among all the studied samples in this thesis. By combining low-temperature transport properties (cf. chapter 6, Fig. 6.2), it is found that the α (T) valleys of these Eu-rich samples are below 350 K, which is much lower than 550 K. The similar α (T) performance was also observed in previous study of $Sr_xEu_{1-x}TiO_{3-\delta}$ [4], but the mechanisms behind are yet not well understood now.

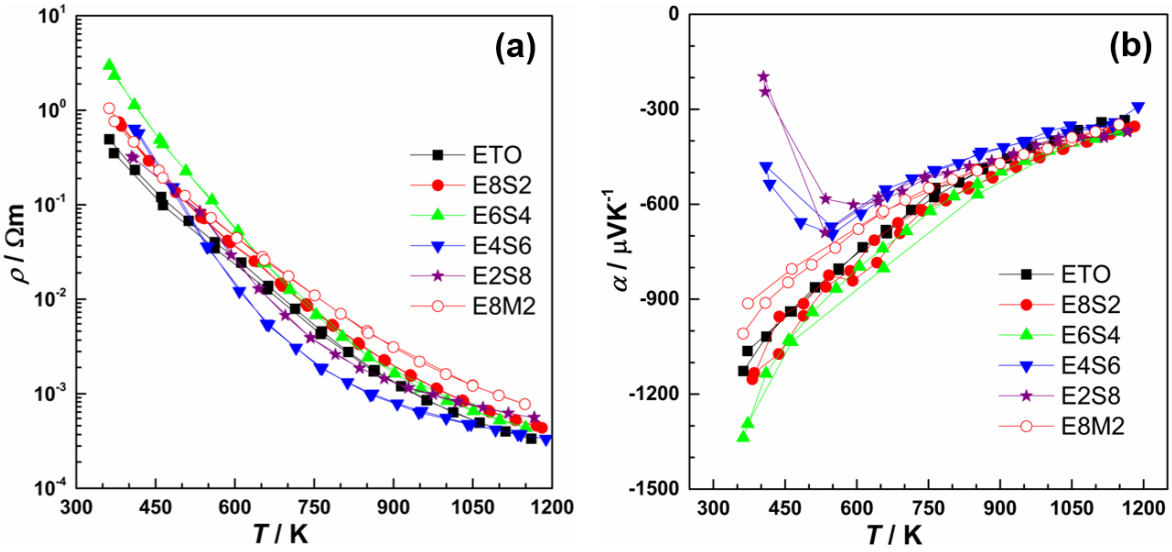

Fig. 5.6 The temperature dependence of electrical resistivity ρ (a) and Seebeck coefficient α (b) of Sr^{2+}-substituted, E8M2, and ETO samples.

5.3.4 Thermal transport properties

The temperature dependence of thermal diffusivity Λ and thermal conductivity κ of these samples are shown in Fig. 5.7. The thermal conductivity κ was calculated based on the formula, $\kappa = \Lambda c_p d$, where d is the bulk density and c_p is heat capacity. The used c_p is constant here because its value was calculated according to Dulong-Petit law. The Λ is the only temperature-dependent parameter in the formula, so the obtained κ exhibits the same temperature dependence as the measured Λ. Owing to the very high electrical resistivity as presented above, the electrical part of κ_e is negligible and the obtained κ is approximately equal to the lattice thermal conductivity κ_l. Although some secondary phases are coexistent within the E8M2 sample, the Λ of E8M2 sample is nearly identical with the pristine ETO over the entire measured temperature range. Generally, the secondary phases in a matrix generate extra grain boundary scattering which supposes to lower κ_l. The grain sizes (hundreds of nanometers, c.f., Fig. 5.3) of secondary phases are far larger than the phonon mean free path of matrix ETO (few nanometers, c.f., chapter 6), thus the extra grain boundary scattering is insignificant. Besides, the secondary phases (i.e., $MgTiO_3$ and $MgTi_2O_4$) might have high κ which compensates the influence of boundary scattering. In the end, the κ of E8M2 shows minor change compared to that of ETO. The E8S2 shows the lowest κ among the series of Sr^{2+} substituted samples. The rest Sr^{2+} substituted samples show the higher Sr^{2+} concentration the higher κ. It is mainly due to the smaller ionic mass of Sr^{2+} compared to Eu^{2+}.

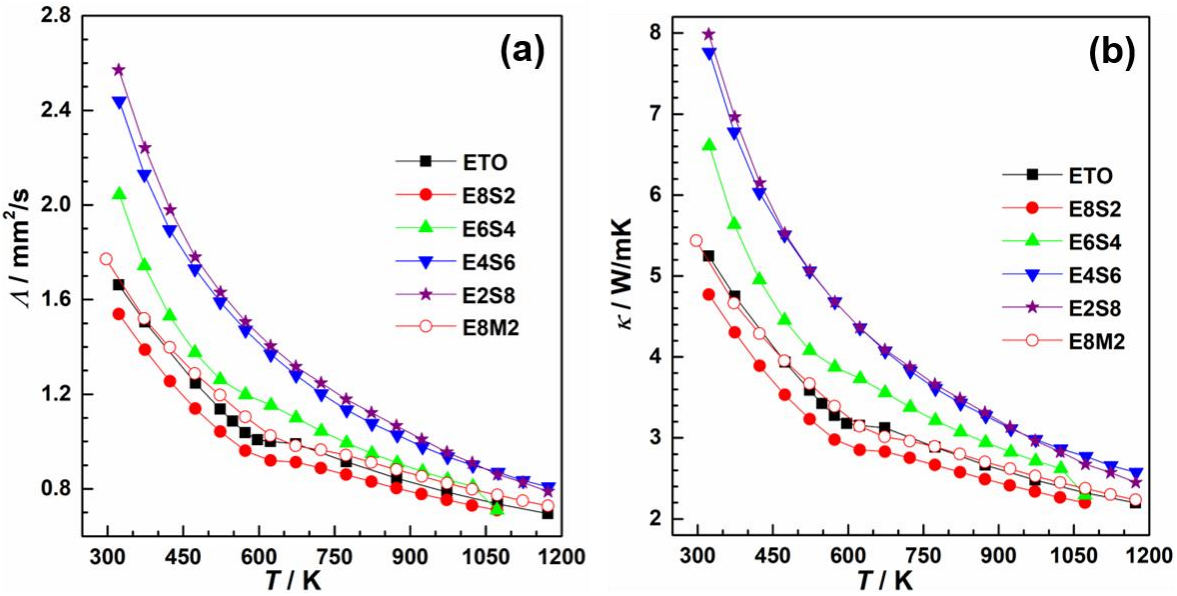

Fig. 5.7 The temperature dependence of thermal diffusivity Λ (a) and thermal conductivity κ (b) of Sr^{2+}-substituted, E8M2, and ETO samples.

5.3.5 Power factor and *ZT* value

The temperature dependence of power factor *PF* and *ZT* values of these studied samples are shown in Fig. 5.8. The E8M2 sample displays the lowest *PF* and *ZT* values among these samples, which is mainly attributed to the effect of the secondary phases. Due to the lowest electrical resistivity in the temperature range of around 600 K < *T* < 1100 K, the E4S6 sample shows the highest *PF* values in the corresponding temperature range. However, the increased *PF* of E4S6 is counteracted by the enhanced κ, which eventually results in a weak change of *ZT* compared to the ETO. Over the entire investigated temperature range, the *ZT* values of these Sr^{2+} substituted samples are approximately similar, excluding the E2S8 sample that has lower *ZT* values at higher temperatures (*T* > 950 K). Accordingly, it is concluded that partial substitution with Sr^{2+} for Eu^{2+} has a minor effect on the TE properties below 1100 K. This result is consistent with the previous studies on Sr^{2+}-substituted $EuTiO_3$-based compounds [5,9].

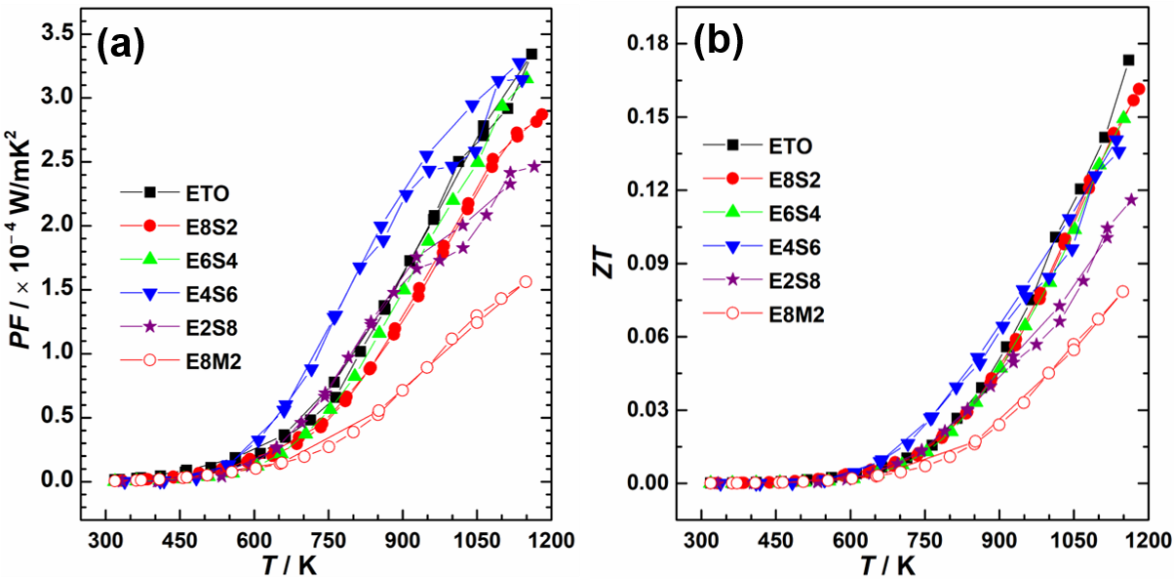

Fig. 5.8 Temperature dependence of power factor *PF* (a) and *ZT* values (b) of Sr^{2+}-substituted, E8M2, and ETO samples. Heating and cooling data were collected.

5.4 Conclusions

The ionic radius of Mg^{2+} is too small to be significantly incorporation into a perovskite structure. With the applied synthesis method, it is not possible to obtain the single-phase $EuTiO_3$-$MgTiO_3$ solid solutions. Partial substitution with Mg^{2+} for Eu^{2+} produces secondary phases which are $MgTiO_3$ with trigonal structure and $MgTi_2O_4$ with orthorhombic structure. The thermoelectric properties are weakly changed by using 20 % Mg^{2+} substitution. Owing to the identical ionic radii of Sr^{2+} and Eu^{2+} in the perovskite structure, Sr^{2+} substitution does not change the cubic crystal structure at ambient temperature. The single-phase $Eu_{1-x}Sr_xTiO_3$ solid solutions can be obtained in the full range of $0 \leq x \leq 1$. The effect of Sr^{2+} substitution on electrical resistivity and Seebeck coefficient is small, especially for the samples with $x \leq 0.4$. When $x \geq 0.6$, the substitution effect on TE properties is gradually appearing. It is mainly displayed by the enhancement of thermal conductivity and the nonmonotonic change of the Seebeck coefficient below 600 K. Overall, the effect of Sr^{2+} substitution on TE performance is small and not as remarkable as the Ba^{2+} or Ca^{2+} substitution.

References

[1] W.D. Kingery, Introduction to ceramics, *Wiley*, (1976).

[2] Z. Li, M. Yang, J.-S. Park, S.-H. Wei, J.J. Berry, K. Zhu, Stabilizing perovskite structures by tuning tolerance factor: formation of formamidinium and cesium lead iodide solid-state alloys, *Chemistry of Materials* 28 (2015) 284–292.

[3] M.R. Filip, G.E. Eperon, H.J. Snaith, F. Giustino, Steric engineering of metal-halide perovskites with tunable optical band gaps, *Nature communications* 5 (2014) 5757.

[4] R.D. Shannon, Revised effective ionic radii and systematic studies of interatomic distances in halides and chalcogenides, *Acta crystallographica section A*: *crystal physics, diffraction, theoretical and general crystallography* 32 (1976) 751–767.

[5] L. Sagarna, S. Populoh, A. Shkabko, J. Eilertsen, A.E. Maegli, R. Hauert, M. Schrade, L. Karvonen, A. Weidenkaff, Influence of the Oxygen Content on the Electronic Transport Properties of $Sr_xEu_{1-x}TiO_{3-\delta}$, *The Journal of Physical Chemistry C* 118 (2014) 7821–7831.

[6] B.A. Wechsler, R.B. von Dreele, Structure refinements of Mg_2TiO_4, $MgTiO_3$ and $MgTi_2O_5$ by time-of-flight neutron powder diffraction, *Acta Crystallographica Section B* 45 (1989) 542–549.

[7] Y. Kawada, M. Fujimoto, Phase Separation and Solid Solution in Nonstoichiometric and Stoichiometric (Sr, Mg)TiO_3 Ceramics, *Japanese Journal of Applied Physics* 29 (1990) L126-L128.

[8] T. Hirata, K. Ishioka, M. Kitajima, Vibrational spectroscopy and X-ray diffraction of perovskite compounds $Sr_{1-x}M_xTiO_3$ (M = Ca, Mg; $0 \leq x \leq 1$), *Journal of Solid State Chemistry* 124 (1996) 353–359.

[9] K. Kato, M. Yamamoto, S. Ohta, H. Muta, K. Kurosaki, S. Yamanaka, H. Iwasaki, H. Ohta, K. Koumoto, The effect of Eu substitution on thermoelectric properties of $SrTi_{0.8}Nb_{0.2}O_3$, *Journal of Applied Physics* 102 (2007) 116107.

Chapter 6 Low temperature thermoelectric properties of $Eu_{1-x}A_xTiO_{3-\delta}$ (A = Ca^{2+}, Sr^{2+}, Ba^{2+})

Abstract

The electrical resistivity (ρ), Seebeck coefficient (α), and thermal conductivity (κ) of polycrystalline $Eu_{1-x}A_xTiO_{3-\delta}$ (A = Ca^{2+}, Sr^{2+}, Ba^{2+}, $0 \le x \le 0.8$) materials were systematically investigated at low temperatures down to ~ 2 K. All samples exhibit semiconducting behavior excluding the sample $Eu_{0.2}Ca_{0.8}TiO_{3-\delta}$, which shows metal-insulator transitions at low temperatures. A lower ρ is obtained with increasing Ca^{2+} substitution. The Ca^{2+} substituted samples show the lowest ρ and the broadest temperature-independent of α at low-temperature, compared with Ba^{2+} and Sr^{2+} substituted samples. The glass-like κ of $EuTiO_{3-\delta}$ at low-temperature is powerful evidence for verifying its character of local structural disorder and lattice instability. According to the studies of heat capacity, morphologies, crystal structure, and mean free path of heat carriers, the heat conduction mechanisms are discovered involving magnonic contributions. In addition to Eu 4f hybridization and local structural disorder, the magnon-drag effect is also associated with low-temperature transport behaviors.

6.1 Introduction

$EuTiO_3$ (ETO) has three typical differences: disordered local structures, magnetic properties, and localized Eu 4f electrons, compared to the well-known perovskite-type $ATiO_3$ (A = Ca, Sr, Ba). Though ETO is recognized to be isostructural with $SrTiO_3$ on long-range scales at ambient temperature [1], the discovered local structure shows that ETO is different. It was found that the ground state of ETO consists of tilts and rotations of the oxygen octahedra instead of a simple cubic perovskite structure [2]. ETO was proposed to be an intrinsically disordered system, in which the structure itself is willing to form nanodomains in the order of ~ 20 Å and the correlation length changes dramatically over a wide temperature range [3]. The delocalization of Eu^{2+} was found to be the root origin of lattice dynamics instability [4]. Briefly, the structure of ETO might be "long-range order but local disorder". According to our previous studies, it was found that both Ba^{2+} and Ca^{2+} substitutions decrease the local structural disorder status rather than increase it. Particularly, although Ca^{2+} substitution reduces the overall symmetry, the structural order at nanometric scales is still unexpectedly increased by substitution [5]. Such an uncommon structure evolution suggests that the degree of local structural disorder of ETO is very high. Inspired by the fact that structural disorder will inevitably have a great influence on low-temperature transport properties, I was highly motivated to carry out the investigation of low-temperature TE properties of $Eu_{1-x}A_xTiO_{3-\delta}$ (A = Ca^{2+}, Sr^{2+}, Ba^{2+}, $0 \le x \le 0.8$) materials.

ETO is a magnetic material with a large spin moment of $7\mu_B$ originating from the unique electron configuration of Eu^{2+} [Xe] $4f^7$. The spin adds a new degree of freedom to materials and thus theoretically can be favorable for improving *ZT*. Unlike the electron charge, the spin is not conserved, and the net total spin of a system can be increased or decreased by spin-pumping mechanisms [6]. At finite temperatures, the thermal fluctuations of spin moments organize into spin waves or magnons [7]. Magnons are quantized spin waves, just like phonons are quantized elastic waves [8]. Similar to electrons and phonons, magnons also play an important role in energy transportation for determining some fascinating physical properties in magnetic systems [9–11]. In a non-magnetic system, charge carriers (electrons and/or holes) and lattice vibrations (phonons) are generally the main heat carriers for heat transmission through solid. Since the electrical thermal conductivity (κ_e) can be derived from the Wiedemann-Franz relation [12], the lattice thermal conductivity (κ_l) can be obtained by subtracting the κ_e from the total thermal conductivity κ, i.e., $\kappa_l = \kappa - \kappa_e$. Therefore, the measurement of κ at low temperature has been used as a powerful way to probe the lattice defects or imperfections in solids [13]. ETO is a magnetic material and the magnons will be the third type of heat carriers for heat transportation [14]. The total κ is the sum of each contribution, i.e., $\kappa = \kappa_e + \kappa_l + \kappa_m$, where κ_m is magnonic thermal conductivity [7]. The κ_m might account for a large fraction for determining the total κ in ETO, as in some magnetic systems [15–17]. For instance, in the spin-1/2 ladder system $(Sr,Ca,La)_{14}Cu_{24}O_{41}$ [18,19], the magnitude of magnonic contribution to total κ is unexpectedly large.

Since a large Seebeck coefficient (α) which was ascribed to the spin entropy was found in the system of $La_xCo_2O_4$[20], the role of spin in thermoelectric was awakened [21]. Magnons act not only as heat carriers increasing κ but also can enhance the α with a large magnitude [7]. For example, the magnon-drag effect, like phonon-drag effect [22,23], also increases the total α due to the advective transport of electrons dragged by magnons, $\alpha = \alpha_d + \alpha_g$, where α_d and α_g are electronic and magnonic Seebeck coefficient, respectively. In comparison with electrons (or holes), however, the roles of magnons in thermoelectrics are relatively less studied and not completely understood until now. Although a large spin entropy has also been detected in ETO [24], however, there are few reports on how magnons play a role in the thermoelectric properties of ETO bulk materials.

The 4*f* electrons are localized and shielded by the 5*s* and 5*p* electrons and hence not expected to contribute significantly to chemical bonding [25], but the 4*f* electrons indeed play an important role in electrical transport as evidenced before [5,26–29]. The Eu 4*f* states hybridizes with the Ti 3*d* and/or O 2*p* states [30]. The hybridization strengths are sensitive to the lattice parameters, lattice deformation, and octahedra tilting or rotation [31–33]. Some physical properties found in ETO, such as positive magnetodielectric effect [34], suppression of ferroelectricity [25], and so on [30,35,36], are related to the influence of hybridization between Eu 4*f* and Ti 3*d* or O 2*p* orbitals. Partial chemical substitutions for Eu^{2+} by cations with different ionic radii can successfully introduce unit cell variations, lattice defects, octahedra tilting or rotation, apart from the dilution effect of Eu 4*f* states. Therefore, the orbital hybridizations have to be affected and hence the electrical transport properties are anticipated to vary.

In this chapter, the low-temperature TE properties of $Eu_{1-x}A_xTiO_{3-\delta}$ ($A = Ca^{2+}$, Sr^{2+}, Ba^{2+}) solid solutions were measured down to ~ 2 K. The electrical and thermal transport mechanisms of the Ca^{2+} substituted solid solutions have been further studied and discussed. Some direct or indirect evidence was found for verifying the special local structure of ETO through the systematic study of κ of $Eu_{1-x}A_xTiO_{3-\delta}$ materials. The influences of local structural disorder and orbital hybridization on the

transport properties are discussed. The roles of magnons are uncovered through the temperature-dependent measurement of κ and α.

6.2 Experimental

The sintered bar-shaped samples were used for the low-temperature transport properties measurements, which were performed by using the thermal transport option (TTO) kit of Quantum Design and the corresponding equipment provided with their physical property measurement system (PPMS) cryostat. The data of κ, α, and electrical resistivity (ρ) were simultaneously recorded during the measurements in the temperature range of 2 K < T < 350 K by continuously changing the temperature with a sweep rate of 0.5 K/min and a temperature gradient of approximately 3 %. In order to identify possible mismatches and verify the reliability of the data obtained, measurements were carried out by a continuous heating and cooling cycle. The low-temperature c_p data were obtained on a Quantum Design® PPMS from 2 K to 350 K. The high-temperature ρ and α were measured by using a ZEM-3 instrument and the thermal diffusivity was measured by using a Netzsch LFA 457 laser flash analyzer.

For a further assessment of grain size, bulk samples were polished by using diamond pastes followed by thermal etching. The heat treatment process of thermal etching was 10 K / min from ambient temperature to 1473 K and. The heat treatment process for thermal etching was 10 K / min from ambient temperature to 1473 K and it was kept at 1473 K for 5 minutes in forming gas. After that, the furnace was cooled naturally. The micrographs of the bulk samples were performed by SEM (Gemini SEM 500 instrument) and simultaneously the element distribution information was collected by EDS (Bruker Xflash 6|60 detector). The Young's modulus E of the polished samples were tested by nanoindentation (Nanoindenter XP, Keysight). The average sound velocity v of the samples was estimated by using the relation of $v = \sqrt{\frac{E}{d}}$, where d is the density of the sample. High-resolution PXRD data at 100 K were collected by using synchrotron radiation powder diffraction at the ID22 beamline of ESRF in Grenoble. The details of experimental techniques and data analysis of XRD and pair distribution function (PDF) refinement can be found in chapter 4.

6.3 Results and discussion

6.3.1 Thermal conductivity κ

The temperature-dependent thermal conductivity $\kappa(T)$ of $Eu_{1-x}Ca_xTiO_{3-\delta}$ samples below 300 K and over the entire temperature range of 2 K < T < 1200 K were plotted as shown in Fig. 6.1 (a) and (b), respectively. Due to the large electrical resistivity in the entire temperature range of the studied $Eu_{1-x}A_xTiO_{3-\delta}$ samples, the electronic contribution κ_e to total κ is negligible. Several uncommon performances of the $\kappa(T)$ curves can be observed in these figures. There is no phononic peak at low temperature for the pristine ETO sample, whose κ increases gradually with rising temperature and shows a huge broad peak around room temperature. Such kind of $\kappa(T)$ behavior is different from typically ordinary crystalline materials, which usually show a large phononic peak at low temperatures. Similar $\kappa(T)$ appearance is also observed for the sample with x = 0.2. This sample

shows the lowest κ values between approximately 50 K and 300 K in the sample group of $Eu_{1-x}Ca_xTiO_{3-\delta}$ ($0 \leq x < 1$), but higher κ values than the pristine sample below around 50 K. These two samples exhibit a glass-like κ behavior, though they are crystalline samples. The other three substituted samples with x = 0.4, 0.6, and 0.8 exhibit crystalline behaviors, in which κ increases with T resulting in a phononic peak at around 20 K and a subsequent rapid decrease of κ with T due to the occurrence of Umklapp-scattering. The $\kappa(T)$ curves, however, do not follow the T^{-1} law as the Umklapp-scattering expected at high temperatures. On the contrary, the κ smoothly increases with rising temperature from around 60 K to 300 K, which is an unusual phenomenon in semiconductors or insulators with phonon dominated thermal conduction. The κ_l should continuously decrease with raising T when the Umklapp-scattering mechanism is activated. This phenomenon of κ increasing at intermediate temperatures and forming a broad peak at room temperature is a typical behavior caused by magnonic contributions, which is found in many magnetic systems such as $LaCoO_3$ [37], $BiFeO_3$ [38], $Eu_{0.83}Fe_4Sb_{12}$ [39], Sr-doped $La_{1.8}Eu_{0.2}CuO_4$ [40], Zn-doped La_2CuO_4 [41], (Sr, Ca, La)$_{14}Cu_{24}O_{41}$ [18]. Due to the negligible κ_e in the $Eu_{1-x}Ca_xTiO_{3-\delta}$ system, the total κ can be expressed by a simpler description $\kappa = \kappa_l + \kappa_m$. The κ is increasing rather than decreasing at intermediate temperatures, which is ascribed to the increase of κ_m. The magnitude of κ_m is large enough to change the temperature dependence of the total κ. Theoretical calculations of κ_m are in progress.

The phononic peak is generally occurring at a temperature of about $\frac{\theta_D}{10}$, where θ_D is Debye temperature [13]. The highest phononic peak is observed for the sample with x = 0.6 at 22 K, inferring that the θ_D of this sample should be at around 220 K. And it should have the largest grain size or the most integrated grains compared with the other samples. For most solid solutions, the κ_l at very low temperatures will be reduced by doping or partial substitution because of the enhancement of point defects scattering induced by the local structural distortion and random distribution of substituting atoms [37,42]. Experimentally, the unsubstituted ETO sample shows the unexpected lowest κ and the Ca^{2+} substitution increases κ below 50 K. This is an unconventional phenomenon caused by chemical substitution. The κ of all Ca^{2+} substituted samples converge towards similar values and show a weak temperature dependence above 150 K, where the heat radiation contribution is negligible because the κ (T) curves match very well between the low-temperature (by PPMS measurement system) and high-temperature (by LFA measurement system) measurements, as shown in Fig. 6.1 (b).

The plot of κ vs. T in logarithmic type can demonstrate the phonon scattering mechanisms through the dependence of $\kappa \propto T^{3-a}$ ($a \geq 0$). In ordinary crystalline solids, at sufficiently low temperatures (T << 10 K), generally, the dominant scattering mechanism is grain boundary scattering and κ follows a T^3 dependence. With increasing T, more scattering processes (e.g., point-defect scattering, phonon-electron scattering) are involved and yield a dependence of $\kappa \propto T^{3-a}$. For instance, the concurrently activated point-defect scattering and grain-boundary scattering result in a $\kappa \propto T^{2.08}$ dependence in the system of Ni-doped $CoSb_3$, and a $\kappa \propto T^1$ dependence is ascribed to the presence of dominated electron-phonon scattering by a higher concentration of Ni [43]. At high temperatures, the $\kappa \propto T^{-1}$ behavior is expected for a well-known Umklapp process (phonon-phonon scattering) mechanism [13]. In the case of $Eu_{1-x}Ca_xTiO_{3-\delta}$ samples, all the observed indexes "3−a" are much smaller than 3 at low temperatures and the index of "−1" is not observed at high temperatures. The pristine ETO sample displays $\kappa \propto T^{1.3}$ dependence at low temperatures (T < 130 K) and $\kappa \propto T^{-0.8}$ dependence at high temperatures (T > 400 K), as shown in Fig. 6.6 (b). There is an obvious anomalous

transition of κ in the vicinity of 5 K, owing to the influence of antiferromagnetic (AFM) transition. The sample with x = 0.2 has the smallest temperature dependence, $\kappa \propto T^{0.3}$ and $\kappa \propto T^{-0.3}$ at low temperatures (T < 50 K) and high temperatures (T > 400 K), respectively. For the samples with $x \geq$ 0.4, their $\kappa(T)$ curves show two humps (~ 20 K and ~ 300 K) over the entire temperature range. In the limited temperature range of below 20 K, the κ of samples with x = 0.4, 0.6, and 0.8 follow the dependence of $T^{0.6}$, $T^{0.8}$, and $T^{0.9}$, respectively. Although the T indexes (i.e., 0.3, 0.6, 0.8, 0.9) of these Ca^{2+} substituted samples are smaller than the T index (1.3) of the pristine sample, there is a tendency that the T index of the substituted samples is increasing with increasing Ca^{2+} content.

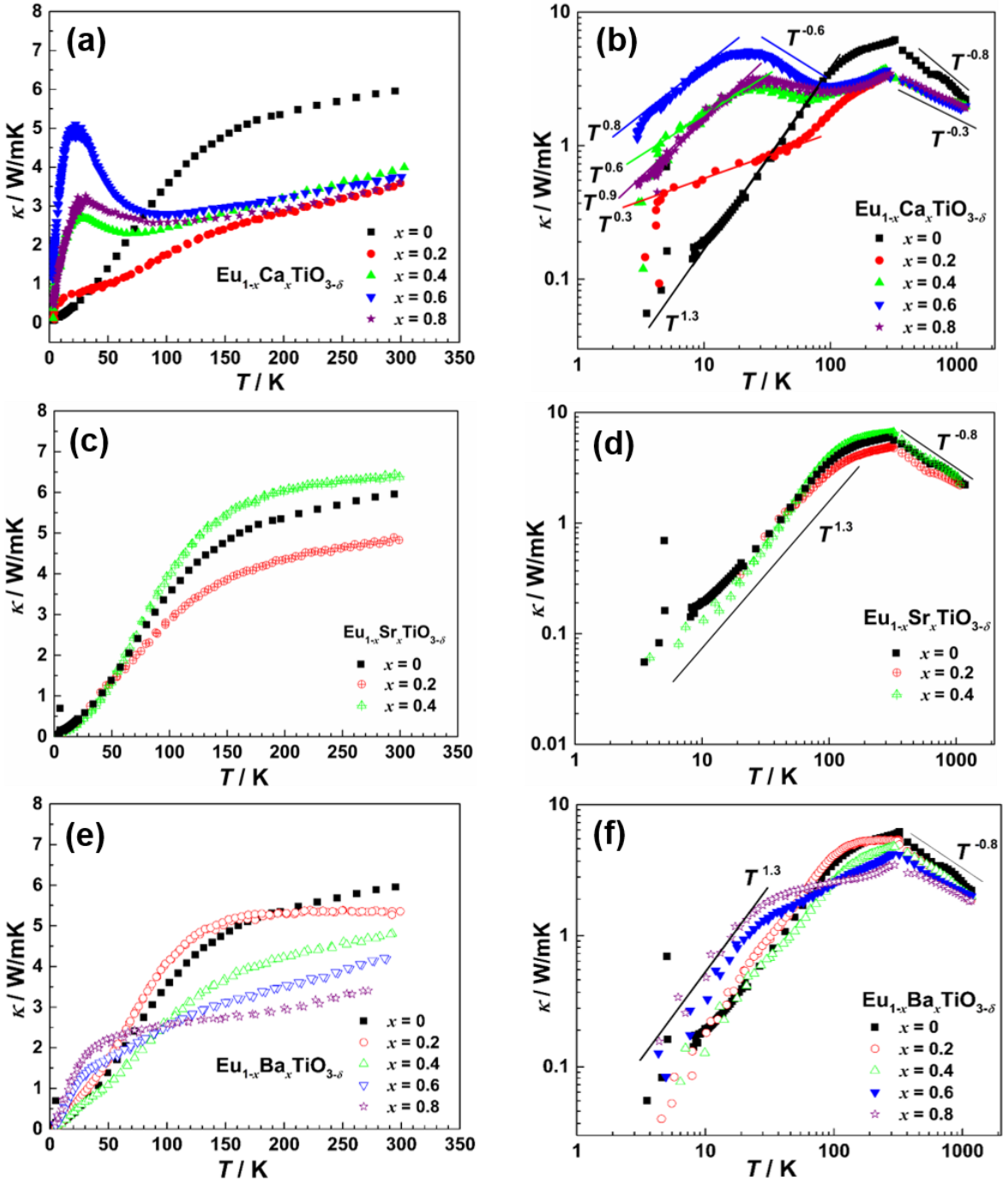

Fig. 6.1 Temperature dependence of thermal conductivity κ of $Eu_{1-x}Ca_xTiO_{3-\delta}$ samples (a) (b), $Eu_{1-x}Sr_xTiO_{3-\delta}$ samples (c) (d), and $Eu_{1-x}Ba_xTiO_{3-\delta}$ samples (e) (f).

The $\kappa(T)$ of $Eu_{1-x}Sr_xTiO_{3-\delta}$ (x = 0, 0.2, 0.4) samples and $Eu_{1-x}Ba_xTiO_{3-\delta}$ (x = 0, 0.2, 0.4, 0.6, 0.8) samples were also investigated for the sake of comparison, as shown in Fig. 6.1 (c) (d) and Fig. 6.1 (e) (f), respectively. The κ values also connect very well at the junctions between high and low temperatures. There is no phononic peak at low temperatures for these two series of samples. When $x \leq 0.4$, Ba^{2+} and Sr^{2+} substituted series samples show a similar $\kappa(T)$ dependence with the unsubstituted ETO sample, i.e, $\kappa \propto T^{1.3}$ and $\kappa \propto T^{-0.8}$ at low temperatures (T < 130 K) and high temperatures (T > 400 K), respectively. It is indicating that these samples have the same heat conduction mechanisms as the ETO sample. Some interesting phenomena are also observed in the Ba^{2+} substituted samples. The $Eu_{0.8}Ba_{0.2}TiO_{3-\delta}$ sample exhibits approximately temperature independent behavior between ~ 150 K < T < 300 K. At low temperatures, the κ is increased as the increase of Ba^{2+} content. While, an opposite trend is exhibited at higher temperatures, i.e., the higher Ba^{2+} content, the lower κ. Compared with Sr^{2+} and Ba^{2+} substituted samples, the Ca^{2+} substitution presents the most extraordinary thermal and electrical transport properties (will be presented later) at low temperatures. Thus, in what follows, the Ca^{2+} substituted samples were carried out further physical characterization for understanding the transport mechanisms behind.

Fig. 6.2 illustrates the temperature dependence of c_p of $Eu_{1-x}Ca_xTiO_{3-\delta}$ ($0 \leq x \leq 1$) samples. Interestingly, a crossover of c_p is present at around 57 K. From ~ 57 K to higher temperatures, the c_p value increases with increasing Ca^{2+} concentration, which is in reasonable agreement with the Dulong-Petit law. From ~ 57 K to lower temperatures, the c_p shows an opposite changing trend, i.e., the higher Ca^{2+} concentration, the lower values. There is a sharp endothermic peak at 4.9 K for the unsubstituted sample, which origins from the AFM ordering of $4f^7$ spins of Eu^{2+}. The observed Néel temperature T_N of the $EuTiO_{3-\delta}$ sample differs from the reported T_N (5 ~ 5.6 K) of $EuTiO_3$ [24,44–47]. The reduced T_N can be explained by defects such as Eu^{3+} and oxygen vacancies [46,48]. In this study, the $EuTiO_{3-\delta}$ sample was synthesized in a highly reducing atmosphere, resulting in generation of oxygen deficiencies and Eu^{3+} ions in the lattice as confirmed in chapter 4. Both such kind of defects can lead to a reduction in T_N as many literatures reported [45,46,48]. The Eu^{2+} ion has spin moments of $7\mu_B$ while Eu^{3+} has essentially a zero moment at low temperatures [49]. The presence of Eu^{3+} and oxygen deficiency results in unit cell parameter variation and octahedral rotation or tilting [31,46]. The alteration of crystal structure has a strong influence on the hybridization of Eu 4f and Ti 3d states and hence the AFM phase transition [31]. All of these Ca^{2+} substituted samples exhibit AFM phase transition with decreasing c_p peak intensity as increasing Ca^{2+} concentration. Additionally, the T_N of $Eu_{1-x}Ca_xTiO_{3-\delta}$ ($0 \leq x \leq 1$) gradually decreases from 4.9 K (x = 0) to 3.1 K (x = 0.6) as shown in Fig. 6.2 (b). These phenomena can be understood by the weakness of hybridization between the Eu 4f and Ti 3d or O 2p states. On the one hand, the magnetic Eu^{2+} are diluted by nonmagnetic Ca^{2+}. On the other hand, due to the smaller ionic radius, Ca^{2+} substitution results in a reduction of crystal symmetry from on average cubic to orthorhombic, thereby reducing orbital overlap. A similar observation was also obtained from the investigation of Zr and Nb doped $EuTiO_3$ [50]. $CaTiO_3$ is a nonmagnetic material and no AFM phase transition is observed at low temperatures. Therefore, the increase of c_p with increasing of Eu^{2+} concentration below 57 K is mainly ascribed to the contribution of spins entropy of the Eu^{2+} ions [24]. Additional contributions from the coupling between the magnons and phonons or magnons and electrons are also possible [51].

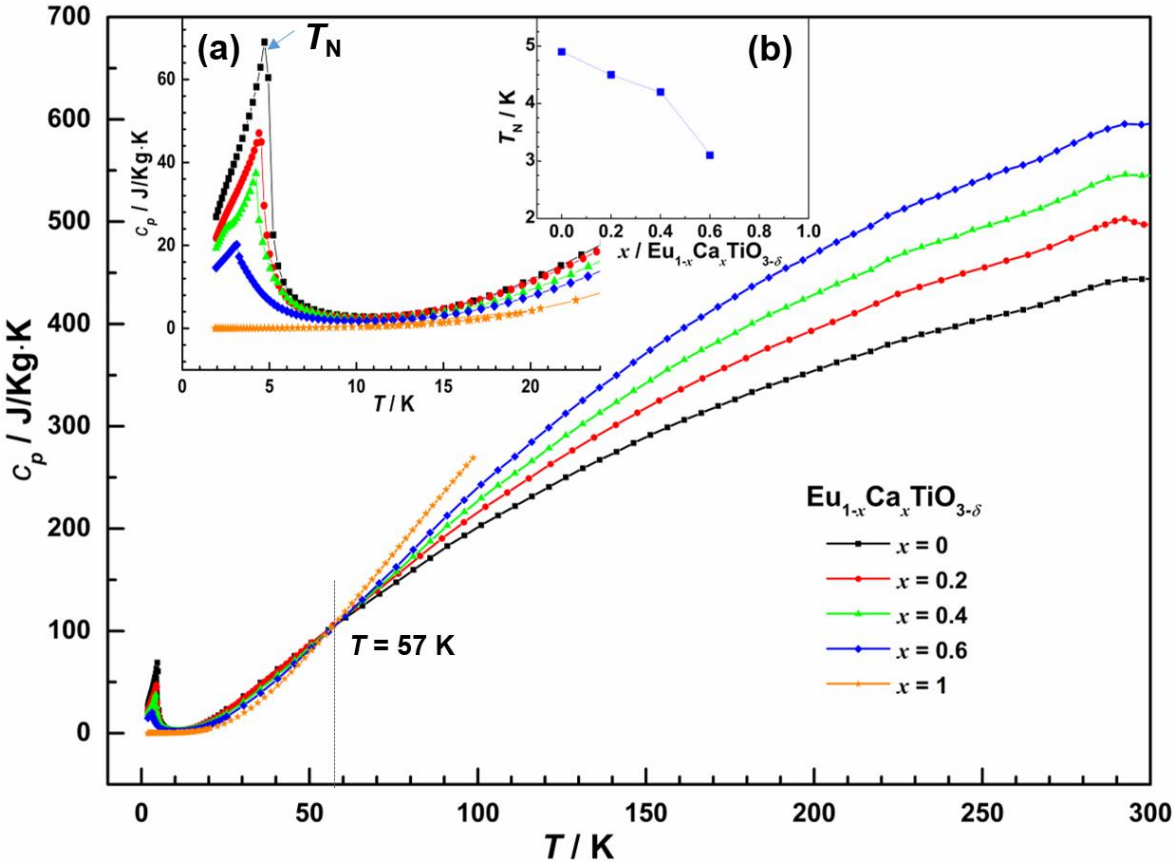

Fig. 6.2 Temperature dependent heat capacity c_p of the $Eu_{1-x}Ca_xTiO_{3-\delta}$ ($0 \le x \le 1$) samples. The inset (a) shows a zoom-in area below 20 K and inset (b) shows the T_N as function of Ca concentration. The dashed lines and arrow are guides for the eye.

Generally, the c_p is expressed solely as a sum of an electronic contribution and a lattice vibrational contribution in nonmagnetic solids, neglecting the interactions between each excitation, i.e., $c_p \approx c_{p,e} + c_{p,l} = \gamma T + \beta T^3$, where $c_{p,e}$ and $c_{p,l}$ are electronic and lattice vibrational heat capacity, γ and β are electronic and phononic specific heat coefficients, respectively. The β is related to the Debye temperature θ_D, which can be expressed by the relation of $\beta = \frac{12\pi^4 N_A k}{5\,{\theta_D}^3}$, where N_A is the Avogadro constant and k the Boltzmann constant. For these Eu^{2+} containing magnetic materials, the magnetic contribution $c_{p,m}$ should be included and thus the total c_p is the sum of the three components at low temperatures. According to previous calculations on $EuTiO_3$ [24,48], however, the magnitude of $c_{p,m}$ is considerable only below 10 K and insignificant at high temperatures compared with $c_{p,l}$. In order to determine θ_D of each sample, the c_p data between 10 K and 20 K are analyzed under the assumption of $c_p \approx \gamma T + \beta T^3$. Then the plot of c_p/T versus T^2 is obtained as shown in Fig. 6.3. Approximately linear dependence is observed in the range of 150 $K^2 < T^2 < 400$ K^2. The slopes and intercepts of these straight lines are β and γ, respectively. The calculated θ_D are listed in Table 6.1. The θ_D of the pristine $EuTiO_{3-\delta}$ is 172 K. Upon increasing Ca^{2+} substitution, the θ_D is gradually increased. The θ_D of the Ca^{2+} substituted samples with x = 0.6 is 218 K, which agrees well with the expected value of 220 K as mentioned above. The θ_D of the $CaTiO_3$ is 397 K, which is consistent with the reported value 403 K [52]. The γ is related to the

electron concentration and electron effective mass, providing a direct measure of the density of states (DOS) in the vicinity of the Fermi level [53]. The $CaTiO_3$ is an insulator and hence has the smallest value of γ. For the Eu^{2+} containing samples, the γ increases with increasing of Ca^{2+} concentration, which is corresponding to the increase of lattice defects (Eu^{3+}, Ti^{3+}, oxygen vacancy) as confirmed by XPS in chapter 4.

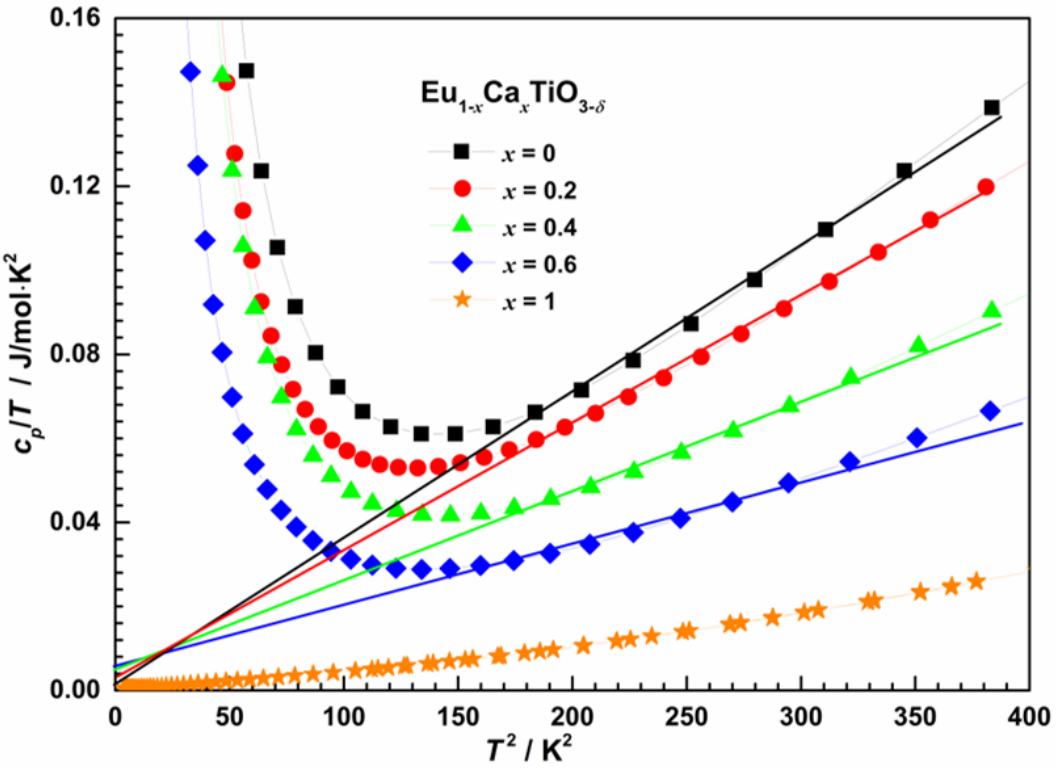

Fig. 6.3 The plot of c_p/T as a function of T^2 of the $Eu_{1-x}Ca_xTiO_{3-\delta}$ ($0 \leq x \leq 1$) samples. The solid lines are guides for the eye.

According to the simple expression for thermal conductivity $\kappa = \frac{1}{3} c_p v l$, the mean free path of heat carriers (phonons, electrons/holes, or magnons) can be calculated as $l = \frac{3k}{c_p v}$. The v was obtained from the measurement of Young's modulus at ambient temperature, and assuming that it is constant at low temperatures. Then, the temperature dependent l was calculated, as illustrated in Fig. 6.4. Over the entire temperature range, the l of the pristine ETO sample exhibits a very small value. The calculated maximum l is 6.8 nm at 12 K and the values of 1 nm < l < 1.5 nm are obtained in a large T range of 30 K < T < 300 K. The observed l can be described in two different temperature ranges (T < 30 K & T > 80 K) for all the studied $Eu_{1-x}Ca_xTiO_{3-\delta}$ samples, according to their change tendency. Below 30 K, the l increases with increasing Ca^{2+} substitution and the sample with x = 0.6 displays the highest l value of 187 nm at ~10 K. Above 80 K, the pristine ETO sample shows the highest l value with weakly temperature dependent. The l of the other three Ca^{2+} substituted samples converges to similar values with a tendency to saturate at around 150 K. A brief summary, Ca^{2+} substitution causes the mean free path of heat carriers to increase at low temperatures and decrease at high temperatures. It is understandable that the decrease of l at higher temperatures is ascribed for the enhanced point-defect scattering, owing to the mass fluctuations and strain field fluctuations

induced by *A*-site alternate ions Eu^{2+}/Ca^{2+}. The reasons for increasing *l* by Ca^{2+} substitution at low temperatures are still not yet determined. In what follows, microscopic characterizations of the samples are carried out to help for unveiling the reasons behind.

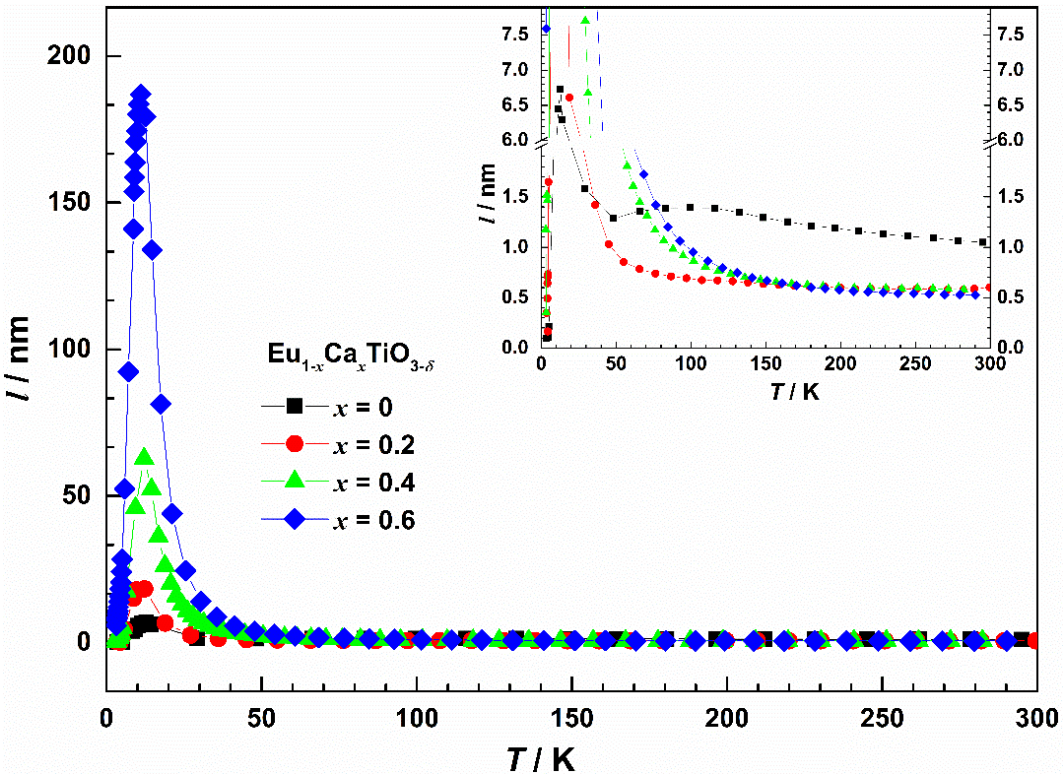

Fig. 6.4 Temperature dependent mean free path *l* of heat carries. The inset shows a magnified view below 8 nm.

Table 6.1. Some physical parameters of $Eu_{1-x}Ca_xTiO_{3-\delta}$ samples at ambient temperature: samples denotation, crystal system, average grain sizes, thermal conductivity κ, heat capacity c_p, mean free path of heat carriers *l*, average phonon velocity *v*, sample bulk density *d*, coefficients γ, and Debye temperature θ_D.

Samples	crystal system	average grain sizes (μm)	κ (W/m·K)	c_p (J/g·K)	*l* (nm)	*v* (m/s)	*d* (g/cm^3)	γ	θ_D / K
$x = 0$	cubic	~ 5	5.98	0.4443	1.05	5560	6.18	0.0015	172
$x = 0.2$	cubic	~ 6	3.56	0.4958	0.595	5700	5.55	0.0033	182
$x = 0.4$	orthorhombic	~ 10	3.98	0.5462	0.549	6480	5.29	0.0049	199
$x = 0.6$	orthorhombic	~ 20	3.78	0.5953	0.527	6950	4.68	0.0055	218
$x = 0.8$	orthorhombic	~ 30	3.65	–	–	7450	4.12	–	–
$x = 1$	orthorhombic	–	6.79	–	–	–	–	0.0003	397

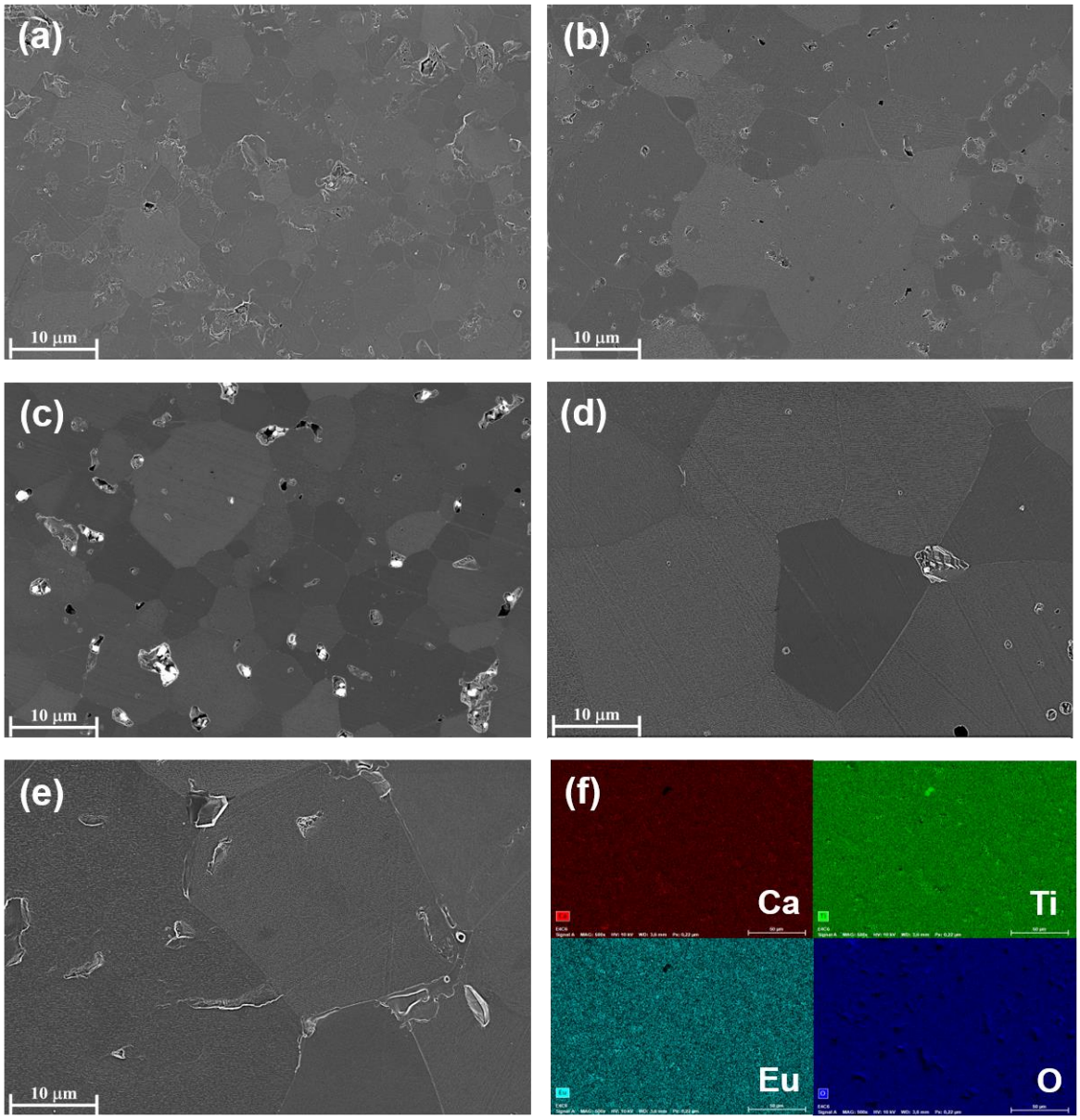

Fig. 6.5 SEM micrographs of polished and thermally etched $Eu_{1-x}Ca_xTiO_{3-\delta}$ samples of (a) x = 0, (b) x = 0.2, (c) x = 0.4, (d) x = 0.6, and (e) x = 0.8. (f) Representative EDS mapping results of individual elemental distribution in the sample with x = 0.6.

The microstructure of sintered bulk samples, such as grain size, grain morphology, and porosity, are also important factors for determining κ. Typical SEM micrographs of $Eu_{1-x}Ca_xTiO_{3-\delta}$ samples are presented in Fig. 6.5. The compositional homogeneity is verified by EDS mapping as shown in Fig. 6.5 (f). The grain boundaries are clearly shown between grains. Distinct contrast is displayed among grains, which is due to the different crystallographic orientations of grains in a polycrystalline material. The average grain size of the pristine x = 0 sample is less than 10 µm (Fig. 6.5 (a)), while that of the samples with x = 0.6 and 0.8 are much larger than 10 µm (Fig. 6.5 (d) and (e)). It is evident that the average grain size is growing with increasing Ca^{2+} concentration. In comparison with the sample of Ca^{2+}/x = 0.8, the sample with x = 0.6 has the lowest bulk porosity

with relatively homogeneous as well as completed grain size. This observation agrees well with the prediction for the largest κ peak value of the sample of Ca^{2+}/x = 0.6 below 50 K. The SEM micrographs of the Ba^{2+} and Sr^{2+} substituted samples were also characterized for the sake of comparison. Fig. 6.6 (a) and (b) present a representative image of sample $Eu_{0.6}Ba_{0.4}TiO_{3-\delta}$ and $Eu_{0.6}Sr_{0.4}TiO_{3-\delta}$, respectively. With the same substitution fraction, the Ba^{2+}-substituted samples have the largest grain size on average compared with the $Ca^{2+}$and Sr^{2+} substituted samples. The grain sizes of all the studied samples are in micro-size and far larger than *l*, suggesting that the grain boundary scattering should be very weak or negligible. This inference can be further convinced by means of the temperature dependence of κ. The $\kappa \propto T^3$ dependence at extremely low temperatures is the typical character for the grain boundary scattering. However, the *T* indexes of all the samples are far smaller than 3 even down to 2 K. A similar discovery was also found in $Sr_8Ga_{16}Ge_{30}$ compound in which the $\kappa \propto T^2$ was observed even down to *T* = 60 mK [54]. One likely interpretation was proposed that the grain boundaries are not the scattering sources for glass-like κ.

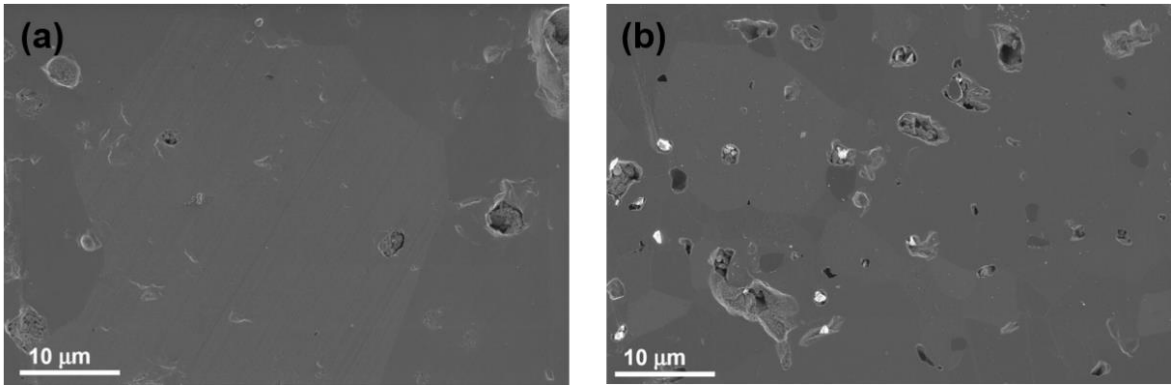

Fig. 6.6 SEM micrographs of polished and thermally etched $Eu_{0.6}Ba_{0.4}TiO_{3-\delta}$ (a) and $Eu_{0.6}Sr_{0.4}TiO_{3-\delta}$ (b) samples.

The local structural disorder has a great influence on κ [37,55,56]. All studied samples were confirmed to be single-phase by using synchrotron radiation. Fig. 6.7 shows some PXRD Rietveld analysis results at 100 K. The overall change tendency of $Eu_{1-x}Ca_xTiO_{3-\delta}$ is similar to the result obtained at 300 K (c.f., chapter 4), except for the pristine *x* = 0 sample. The pristine sample is tetragonal at 100 K on average long-range scale. The three substituted samples with $x \geq 0.4$ remain an orthorhombic crystal structure, the same as at 300 K. The sample with *x* = 0.2 still shows cubic symmetry, zero tilting angles, and maximum atomic mean square displacement parameters (*adp*) value at 100 K. In comparison with other samples, the sample with *x* = 0.2 is very interesting due to its discontinuous change of crystal symmetry as a function of Ca^{2+} substitution content.

In order to get a deep insight into the local structure, a PDF analysis of the XRD data collected at 100 K was performed. The *G*(*r*) functions of the samples with $0.2 \leq x \leq 0.8$ are shown in Fig. 6.8, together with the *G*(*r*) calculated for each sample using structural models with symmetry *Pbnm* (as in the long-range structure), *Amm*2, and $Pm\bar{3}m$. Some trends emerge clearly as the Ca^{2+} concentration is increased from *x* = 0.2 to *x* = 0.8. First, the narrow Ti–O peak (*r* ≈1.9 Å) splits into a doublet. Second, a broad singlet with high-*r* tails centered at *r* = 2.70 Å representing the *A*–O (*A* = Eu/Ca) distances morphs into the symmetric 6 + 6 distribution centered at *r* = 2.60 Å. Third, the peaks at *r* = 3.30 Å and *r* = 3.85 Å, which represent, respectively, *A*–Ti and *A*–*A* + Ti–Ti first-neighbor

interatomic distances, become broader singlets. All these features suggest a local structure transition with increasing Ca^{2+} content. At low Ca^{2+} content instead of octahedral tilts the Ti off-centering has to be considered as primary distortion. At high Ca^{2+} content the local structure can be described by orthorhombically strained tilting of rigid TiO_6 octahedra (x = 0.8) together with antiferroelectrically displaced *A* cations [57].

For both the samples with x = 0.8 and x = 0.6, the *Pbnm* orthorhombic structural models obtained from Rietveld refinements reproduce the short range (1-8 Å) $G(r)$ with good accuracy. For x = 0.4 and x = 0.2, instead, the *Pbnm* model reproduces most of the $G(r)$ features above 3 Å but is incompatible with the Ti–O and *A*–O first-neighbor distributions. A better fit for both x = 0.2 and x = 0.4 is provided by a model with *Amm*2 symmetry (*B*2*mm* using the same orthorhombic axes as for *Pbnm*). This model allows the displacement along the cubic [110] direction of both the *A* and *B* cations while TiO_6 octahedra are only allowed to distort by shifting the apical O atoms with respect to the equatorial plane. As a result, this model reproduces correctly the Ti–O and *A*–O first-neighbor peaks, giving a description of the short-range structure complementary to that provided by the *Pbnm* model. For the samples x = 0.6 and x = 0.8 the *Amm*2 model offers no improvement over the *Pbnm* model, as their short-range structure reflects increasingly the octahedral tilt-driven distortion of the long-range structure. For the sake of comparison, the cubic $Pm\bar{3}m$ model was tested against all the samples. In no case this model could describe accurately the short-range order, as it appears evident from Fig. 6.8 (i) –(l), even though the sample with x = 0.2 exhibits $Pm\bar{3}m$ symmetry from long-range Rietveld refinements.

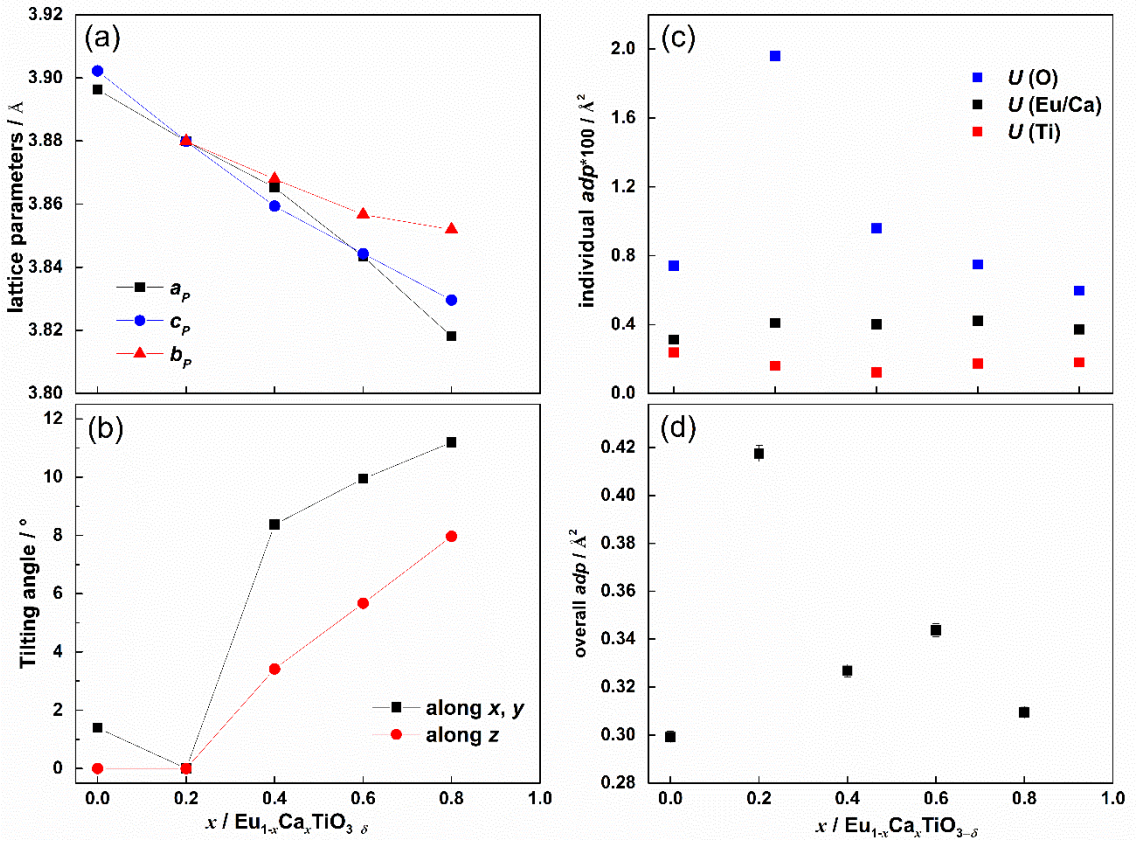

Fig. 6.7 Composition dependence of the lattice parameters (a), tilting angles along the *x*/*y*, and *z* directions (b), individual atoms overall atomic mean square displacement parameters (c), and overall atoms overall atomic mean square displacement parameters (d) of $Eu_{1-x}Ca_xTiO_{3-\delta}$ samples at 100 K.

The cubic long-range structure in the case of the x = 0.2 sample, therefore, is indicative of the frustrated order of the distortions leading to the *Pbnm* and *Amm*2 local structures. By decreasing x from 0.8 to 0.4, the volume fraction of domains with *Amm*2-like structure increases at the expense of *Pbnm*-like domains. This is apparent from i) the increase of the overall *adp* driven by O atoms, ii) the decrease in the ϕx, ϕz tilt angles. As a result of competing structural orders, O atoms are found in both rigid, tilted octahedra and in ferroelectrically distorted octahedra. Still, the volume fraction of *Pbnm*-like domains is above the percolation threshold and the long-range structures in this composition range retain a global *Pbnm* symmetry. For the sample with x = 0.2, however, *Pbnm*-like domains no longer percolate, resulting in both a cubic long-range structure characterized by high *adp* and a large contribution of *Amm*2-like coordination on the local scale. The observation of two frustrated orders in the x = 0.2 sample helps explaining its lowest κ at 100 K with respect to the other substituted samples. The competition of these two structural causes (absent in the other orthorhombic, percolating samples) explains the shortest l at 100 K (c.f. Fig. 6.4). It is concluded that the structural disorder for these samples has a larger effect on κ at low temperatures than point defects.

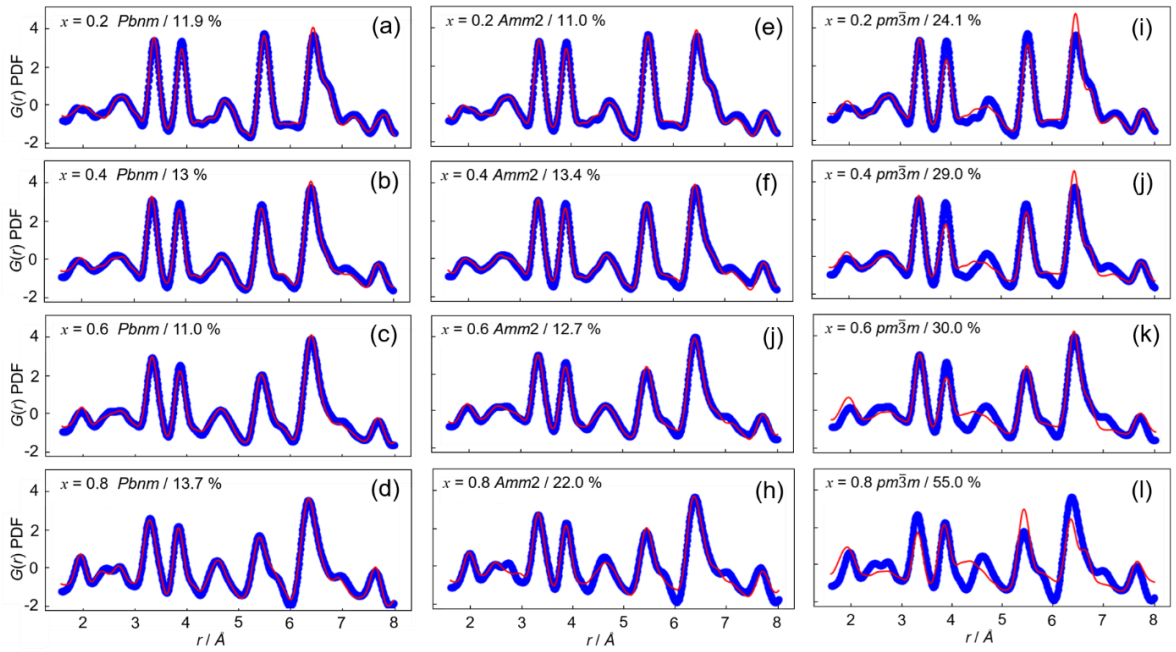

Fig. 6.8 $G(r)$ functions of the $Eu_{1-x}Ca_xTiO_{3-\delta}$ samples with x = 0.2, 0.4, 0.6, 0.8 using structural models with symmetry *Pbnm* (a-d), *Amm*2 (e-h), and *Pm*$\bar{3}$*m* (i-l).

6.3.2 Discussion of the thermal conductivity

According to the low-temperature κ studies, some uncommon behaviors are observed for these crystalline solids. First, the crystalline pristine $EuTiO_{3-\delta}$ sample does not display a phononic peak as observed in the rich-Ca^{2+} substituted samples. This can be well explained from the aspects of local structure disorder and soft-phonon modes. ETO has the feature of "long-range order but local disorder" with a very high disorder status. Based on Einstein's model, it was calculated that lattice vibrations of disordered crystals are essentially the same as those of a glass-like solid [58]. The local structure disorder is strongly related to the low κ_l at low temperatures. Besides, soft-phonon modes

play an important role in phonon transportation in ETO [59–61]. If the "soft-phonon scattering" [40] is activated, the soft phonon branches could cause a strong suppression of κ_l. Therefore, a small and glass-like κ behavior was observed in crystalline unsubstituted pristine $EuTiO_{3-\delta}$ sample. Upon Ca^{2+} substitution, the state of local lattice disorder (nanodomains, Eu^{2+} delocalization, or octahedra tilting) is broken and the ions are rearranged towards the lattice of $CaTiO_3$. $CaTiO_3$ has a much more rigid lattice than $EuTiO_3$ [62]. The heat transportation transmitted by lattice vibrations can be facilitated in the more rigid lattice, and thereby the κ_l can be enhanced. On the other hand, however, the implanted Ca^{2+} introduces more point defects which can decrease the κ_l. Eventually, Ca^{2+} substitution introduces two opposite influences counteracting each other during the phonon transmission through the lattice. The phononic peak below 50 K means that the more ordered and rigid lattice has a greater influence on κ than the point defects. This is the reason that the l is increased at low temperatures by Ca^{2+} substitution. With increasing T, in the temperature range of 60 K < T < 350 K, the dominant heat carriers become magnons which give an additive considerable contribution to the total κ, i.e., $\kappa = \kappa_l + \kappa_m$. Though the Umklapp scattering is already activated for decreasing κ_l, the sum of the final κ is governed by the large κ_m. That's why all Eu^{2+}-containing compounds display a broad increasing κ peak at intermediate temperatures. At high temperatures, the Umklapp-scattering becomes the dominant phonon scattering mechanism, then κ decreases with increasing T as expressed by $\kappa \propto T^{-n}$. In this study, all obtained n are smaller than the expected value of 1. Such similar phenomenon was also discovered in the system of ice phases which are paraelectric [63].

Substitution with Ba^{2+} or Sr^{2+} does not damage the cubic symmetry at ambient temperature, but introduces point defects. The similar $\kappa(T)$ dependence compared to the pristine sample indicates similar heat conduction and scattering mechanisms. The lattice dynamics of $SrTiO_3$ and $EuTiO_3$ have close analogies, which are manifested by the same soft phonon modes [1,47,61] and lattice instability [4,64]. Partly substitution with Sr^{2+} not only remains the same crystal structure, but also might hardly affect the primitive local structural disorder. The Ba^{2+} substitution also causes the increase of κ_l at very low temperatures, but the magnitude of the increase is very small and no obviously identified phononic peak can be observed. This phenomenon can be well understood according to the previous structural study of $Eu_{1-x}Ba_xTiO_{3-\delta}$ [29]. On the one hand, Ba^{2+} substitution decreases the local structure disorder status and forms a more ordered lattice on local scale. On the other hand, Ba^{2+} substitution enlarges bond length which is directly related to the bond strength [65]. The increased bond length gives rise to a reduction of bond strength and thereby causes a decrease of κ_l. Therefore, apart from the effect of point defects scattering, Ba^{2+} substitution also induces two opposite effects caused by the lattice variation for determining the κ_l at low temperatures. The $\kappa(T)$ behaviors of Ba^{2+}-rich samples are analogous to that of $BaTiO_3$ [66]. Because the crystal structure of $BaTiO_3$ is determined not only by the temperature but also sensitive to the grain size [67–69], the flexible crystal structures of the Ba^{2+} substituted samples could have an influence in determining the final total κ.

The phonons, electrons, and magnons are treated essentially like an ideal gas as independent heat-conducting carriers in these magnetic materials. The interactions between these carriers are ignored. As a matter of fact, the coupling of spin-lattice, spin-phonon, spin-electron, and phonon-electron, also play an important role in determining some fascinating physical properties [25,35,60,70–73]. The common phonon scattering mechanisms are phonon-boundary, phonon-point defect, and phonon-phonon Umklapp scatterings. For these $Eu_{1-x}A_xTiO_{3-\delta}$ materials, it is inadequate

to explain the $\kappa(T)$ behaviors only by these three scattering mechanisms. The influence of magnons has to be considered for understanding this unusual and complex thermal conduction process.

6.3.3 Electrical resistivity ρ

Fig. 6.9 (a) shows the plot of log ρ vs T at low temperatures (T < 350 K) for all A-site substituted samples. Because the ρ measurement was not achievable in the applied PPMS instrument when the ρ value is larger than roughly 1000 Ωm, the measured data of ρ can be obtained down to ~ 250 K for the sample Ba^{2+}/x = 0.8 and ~ 3 K for the sample Ca^{2+}/x = 0.8. From an overall observation of this plot, it is evident that the Ba^{2+} substituted samples have the largest ρ and the Ca^{2+} substituted samples have the smallest ρ among the three series samples. The ρ (T) behaviors of both Ba^{2+} and Sr^{2+} substituted samples are showing similar temperature dependency and magnitude. In addition, the deviations of ρ among these samples are insignificant. The ρ (T) behaviors of Ca^{2+}-substituted samples, by contrast, exhibit significant differences. With increasing Ca^{2+} content, the ρ values are decreased by a few orders of magnitude. The samples Ca^{2+}/x = 0.6 and x = 0.8 display the most interesting $\rho(T)$ behaviors. The ρ is decreasing with increasing temperature displaying typical semiconductor behavior for all samples, excluding the sample Ca^{2+}/x = 0.8. The slope of log ρ vs. T of the sample Ca^{2+}/x = 0.8 is in the vicinity of zero in the temperature range of ~ 180 K < T < 350 K, then a steep change appears at ~ 180 K, afterward an approximately zero slope was displayed again roughly between 50 K to 2 K. Fig. 6.9(b), (c), and (d) present the plots of log ρ vs T over the entire temperature range (~ 2 K < T < 1200 K) for Ba^{2+}, Sr^{2+}, and Ca^{2+}-substituted samples, respectively. Though the data at low T and high T were obtained by using different measurement systems, there is no mismatch of these data between the high and low T, meaning that the data are highly reliable.

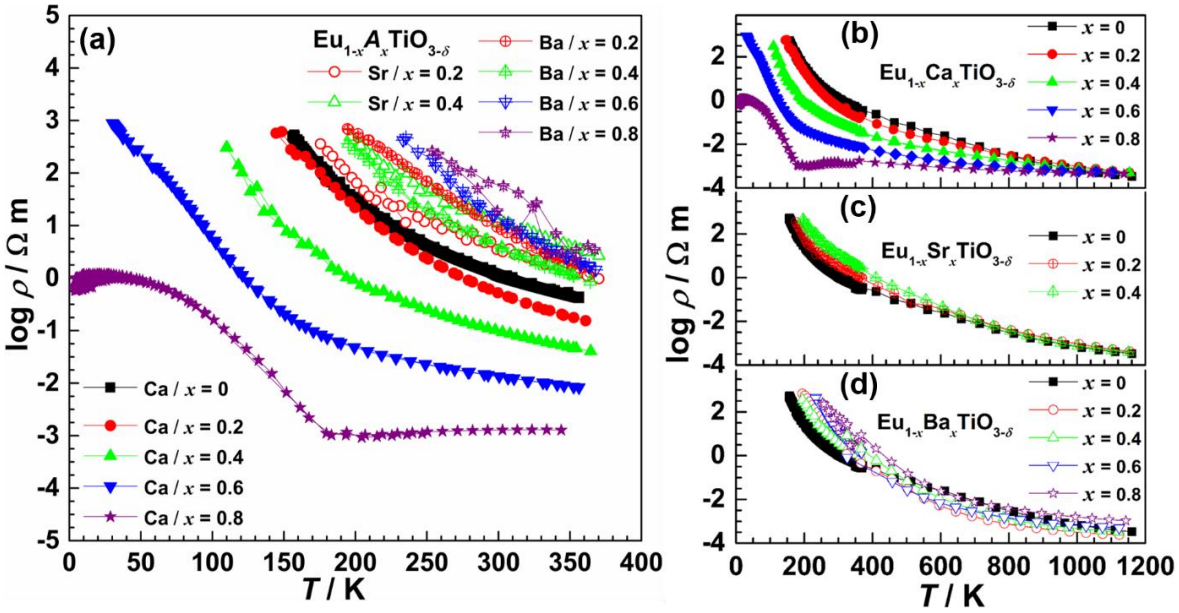

Fig. 6.9 Logarithmic plot of electrical resistivity as a function of temperature for all A-site substituted samples; (a) the low temperature range for all samples; (b), (c), and (d) the plot of full temperature range for Ba^{2+}, Sr^{2+}, and Ca^{2+}-substituted samples, respectively.

6.3.4 Seebeck coefficient α

The temperature dependences of the Seebeck coefficient (α) are illustrated in Fig. 6.10. First of all, the most striking feature is from the sample Ca^{2+}/x = 0.6, whose α is approximately temperature independent in a broad temperature range (~ 350 K < T < 75 K) and then steeply tending to zero as $T \rightarrow 0$ K, as shown in Fig. 6.10 (a). The change of α of the sample Ca^{2+}/x = 0.8 is more smoothly compared to that of the other samples. For the other two Ca^{2+}-substituted samples, their T dependences of α are similar to pristine ETO. The data of α matches very well between the high and low T as shown in Fig. 6.10 (b), meaning that the data are highly reliable. For the sake of comparison, the α of two representative samples (Sr^{2+}/x = 0.4 and Ba^{2+}/x = 0.4) are plotted in Fig. 6.10 (a). The $|\alpha|$ of these two samples monotonically decrease with decreasing T. The maximum $|\alpha|$ among these samples is observed from the sample Sr^{2+}/x = 0.4, i.e., $\alpha \approx -1200$ μV/K at 360 K. The α of Sr^{2+} and Ba^{2+}-substituted samples including the high and low T data are presented as shown in Fig. 6.10 (c) and (d), respectively. Though the data at the junction point shows small mismatch due to the very high resistivity, the changing trend of α is in well-order and acceptable. This result is consistent with the ρ (T) variation over the entire temperature range. Generally, large ρ leads to large $|\alpha|$ [74]. However, the Ba^{2+}-substituted samples do not follow this rule at low temperatures, but rather the opposite. For example, the sample Ba^{2+}/x = 0.8 shows the largest ρ and the smallest $|\alpha|$ when T < 350 K.

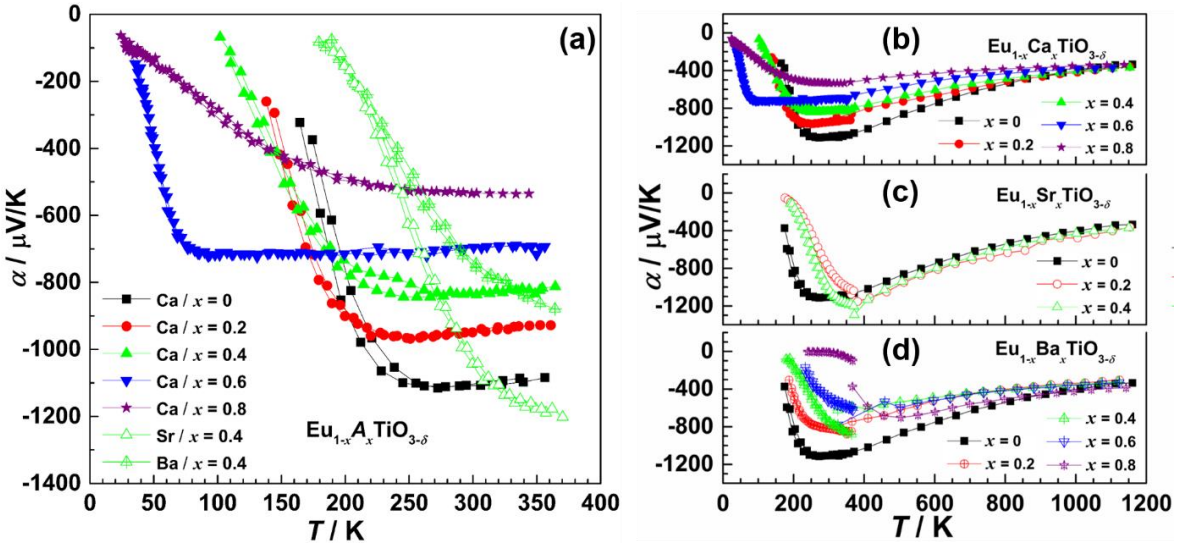

Fig. 6.10 Seebeck coefficient as a function of temperature for all *A*-site substituted samples; (a) the plot of low temperature for all Ca^{2+}-substituted, Sr^{2+}/x = 0.4 and Ba^{2+}/x = 0.4 samples; (b), (c), and (d) the plot of the entire temperature range for Ba^{2+}, Sr^{2+}, and Ca^{2+}-substituted samples, respectively.

Combining the results of ρ (T) and α (T) at low T, it is found that the isovalent substitution with Ca^{2+}, Sr^{2+}, Ba^{2+} leads to a dramatic difference in the electrical transport properties. The most extraordinary effects are observed by Ca^{2+} substitution. Therefore, further discussions will be carried out on the Ca^{2+}-substituted materials to understand the electrical transport mechanisms.

6.3.5 Discussion of the electrical transport properties

The activation energy E_a can be obtained by the plotting of lnρ vs. T^{-1} according to the Arrhenius formula. Fig. 6.11(a) shows the plot of lnρ vs. T^{-1} in the temperature range of 0 K < T < 350 K for $Eu_{1-x}Ca_xTiO_{3-\delta}$. A nearly 90° bend at around 50 K is observed for the sample Ca^{2+}/x = 0.8 and an approximately horizontal line can be fitted to these data below 50 K. Fig. 6.11(b) shows the enlarged plotting above 100 K with the calculated E_a values. The Ca^{2+}-substituted samples with $x \leq 0.4$ give rise to linear lines from the obtained data. In contrast, a linear fitting is only suitable in limited temperature ranges for the samples with x = 0.6 and x = 0.8. The slopes decrease with increasing x and consequently the obtained E_a is also decreasing when $x \leq 0.6$. Interestingly, a negative slope of lnρ vs. T^{-1} of the sample with x = 0.8 is observed and hence a negative E_a with small value (i.e., E_a = – 0.015 eV) would be obtained in the temperature range of 180 K < T < 250 K. It means that the sample shows metallic conduction behavior in this temperature range. Positive slopes of lnρ vs. T^{-1} are presented again in the temperature range of 50 K < T < 180 K, implying a semiconductor behavior. Therefore, metal-insulator transition occurs at the temperature around ~ 50 K, ~ 180 K, and ~ 250 K, respectively.

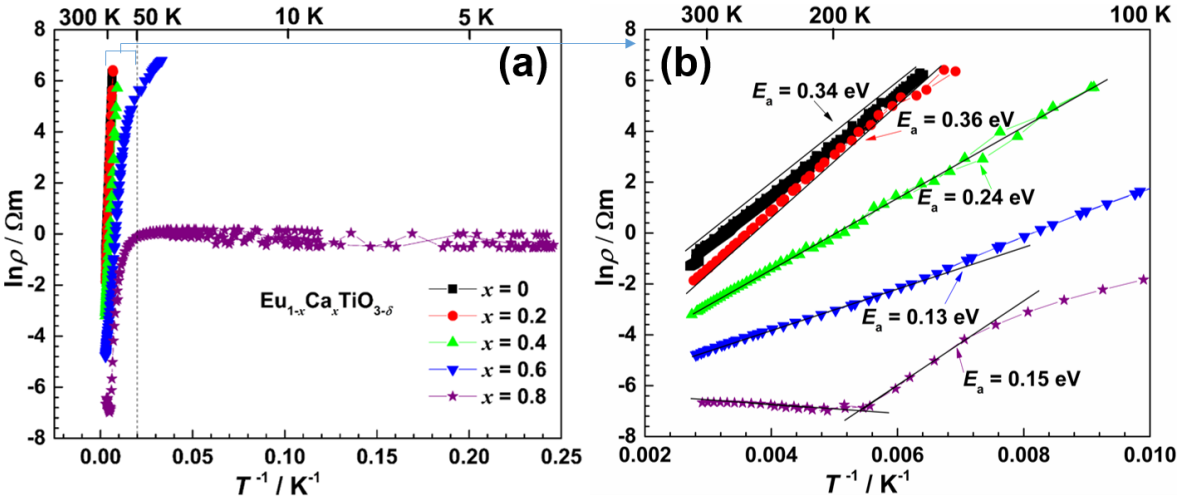

Fig. 6.11 (a) The plot of lnρ vs. T^{-1} in the temperature range of 0 K < T < 350 K and (b) 100 K < T < 350 K for $Eu_{1-x}Ca_xTiO_{3-\delta}$ samples. The dashed lines and arrows are guides for the eye.

According to the magnitude and temperature dependence of ρ and α, in addition with the very small charge carrier mobilities mentioned in chapter 4, the variable range hopping (VRH) conduction is likely the dominating charge transport mechanism at low temperatures. The type of VRH behavior is often distinguishable according to its typical temperature dependence of ρ, i.e.

$$\rho = \rho_0 \exp(T_0/T)^b \tag{6-1}$$

where ρ_0 and T_0 are material parameters and b is an index which is difficult to determine experimentally. The most often used values are ½ and ¼ for the well-known Efros–Shklovskii variable-range hopping (ES-VRH) and Mott variable-range hopping (M-VRH) [75], respectively. The ES-VRH considers the coulomb interaction between electrons. The M-VRH emphasizes the hopping path. The plots of lnρ vs. $T^{-1/4}$ are shown in Fig. 6.12(a), and the inset is the plot of

lnρ vs. $T^{-1/2}$. There is no obvious difference between b = ½ and b = ¼. Such a similar result was also found in evaporated and sputtered amorphous germanium, indistinguishable between b = ½ and b = ¼ [76]. A linear dependence is observed for the samples with x = 0 and x = 0.2 when T < 250 K, as shown in Fig. 6.12(a). With increasing x, a linear fit is only suitable in a smaller temperature range. Based on the change of the slopes, three linear dependence of T ranges (T < 60 K, 60 K < T < 180 K, and T > 180 K) are identified for the sample with x = 0.6, implying a different coefficient T_0 in the corresponding temperature range.

The VRH conduction sometimes can be clarified by combining the analysis of temperature dependence of α and ρ. In the case of M-VRH conduction [77], the α varies as $T^{1/2}$ tending to zero as $T \rightarrow 0$ K, while α tends to a finite value if the coulomb gap is taken into account [75]. The plot of α vs. $T^{1/2}$ of $Eu_{1-x}Ca_xTiO_{3-\delta}$ samples is presented in Fig. 6.12(b). A linear fit is suitable for x = 0.8 when T < 50 K. It follows approximately the law that α varies as $T^{1/2}$ tending to zero as $T \rightarrow 0$ K, suggesting that the dominating electrical transport mechanism of the sample with x = 0.8 belongs to the M-VRH in this temperature range. A linear fit is also appropriate for x = 0.6 in the temperature range of 30 K < T < 60 K. However, it seems that the α steeply goes to zero at much higher temperatures, although there are not enough measured data of $T \rightarrow 0$ available. A similar $\alpha(T)$ phenomenon is also observed for the other samples with $x \leq 0.4$. Consequently, the ES-VRH is considered as the dominated electrical transport mechanism in the samples with $x \leq 0.6$.

The low-temperature electronic transport mechanisms are very complicated, especially for the samples with x = 0.6 and 0.8. It is instructive to consider previous results on the $LaCo_{1-x}Ni_xO_3$ system [78] for understanding the transport mechanisms of $Eu_{1-x}Ca_xTiO_{3-\delta}$, due to their similar transport behaviors. The main lattice defects in $LaCo_{1-x}Ni_xO_3$ system are the electronic defects such as Co^{3+}/Co^{4+} and Ni^{2+}/Ni^{3+}. The disorder effect induced by the lattice defects dominates the metal-insulator transition in the $LaCo_{1-x}Ni_xO_3$ system, whose electrical transport mechanisms evolve from VRH to nearest-neighbor hopping, then a kind of Mott–Anderson transition, depending on the doping concentration. In the system of $Eu_{1-x}Ca_xTiO_{3-\delta}$, a large number of lattice defects (e.g. Eu^{3+}, Ti^{3+}, oxygen vacancies, etc.) are generated upon Ca^{2+} substitution (cf. chapter 4). The lattice defects form impurity levels that govern the ρ at low temperatures. The sample $Eu_{0.2}Ca_{0.8}TiO_{3-\delta}$ has the largest amount of Eu^{3+} species, the smallest distances between Eu-Eu cations, and the lowest overall lattice symmetry compared with the other studied samples. Therefore, the electronic band structure and the hybridization between orbitals of this sample could be significantly different from other samples. All combined influences result in the extraordinary $\rho(T)$ behavior.

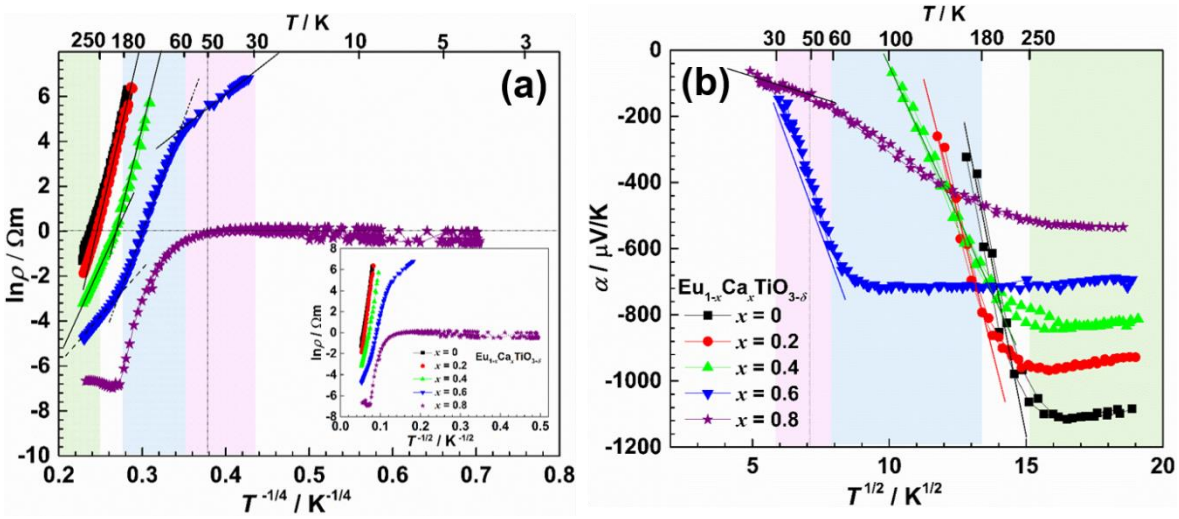

Fig. 6.12 The plot of lnρ vs. $T^{-1/4}$ (a) and α vs. $T^{1/2}$ (b) of $Eu_{1-x}Ca_xTiO_{3-\delta}$ samples. The inset in (a) is the plot of lnρ vs. $T^{-1/2}$. The dashed lines are guides for the eye.

An intriguing phenomenon of $\alpha(T)$ is that there is a "plateau" (i.e., a large constant value) in the temperature range of 250 K < T < 350 K. This "plateau" is strikingly noticeable in the sample with x = 0.6. As discussed in the section of thermal conductivity, magnons or phonons might have some contributions for enhancing α. The well-known phonon-drag effect is a kind of electron-phonon interaction and can result in a large enhancement of α at low temperatures. It is generally appreciable only at very low temperatures and negligible at room temperature [79]. The most pronounced phonon-drag contribution is typically observed around $T \approx 1/5\ \theta_D$. Considering the large $|\alpha|$ at 44 K ($1/5\ \theta_D$) of the sample with x = 0.6, the phonon-drag model is applied for verification. According to the theory of the phonon-drag for a conventional metal, α consists of two contributions, i.e., $\alpha = \alpha_d + \alpha_g = uT + wT^2 + \alpha_g$, where α_g is the phonon-drag component, u and w are the coefficients of T and T^2, respectively [80]. The linear fitting of α/T vs. T is accepted as a characteristic of a metal. Assuming this analysis model is also viable for these oxide materials, α/T vs. T was plotted as shown in Fig. 6.13. If the phonon-drag contribution to α is not negligible, the curves of α/T should have negative deviations to the straight lines due to the negative sign of α. Interestingly, the curve of the sample with x = 0.6 has a large negative deviation below ~ 220 K, while x = 0.8 has a positive deviation below ~ 180 K. The other curves can be linearly fitted above around 200 K and then steeply tend towards zero as T is decreasing. It seems that the phonon-drag effect could have some contribution to α only for the sample with x = 0.6, but does not explain the $\alpha(T)$ for the other samples.

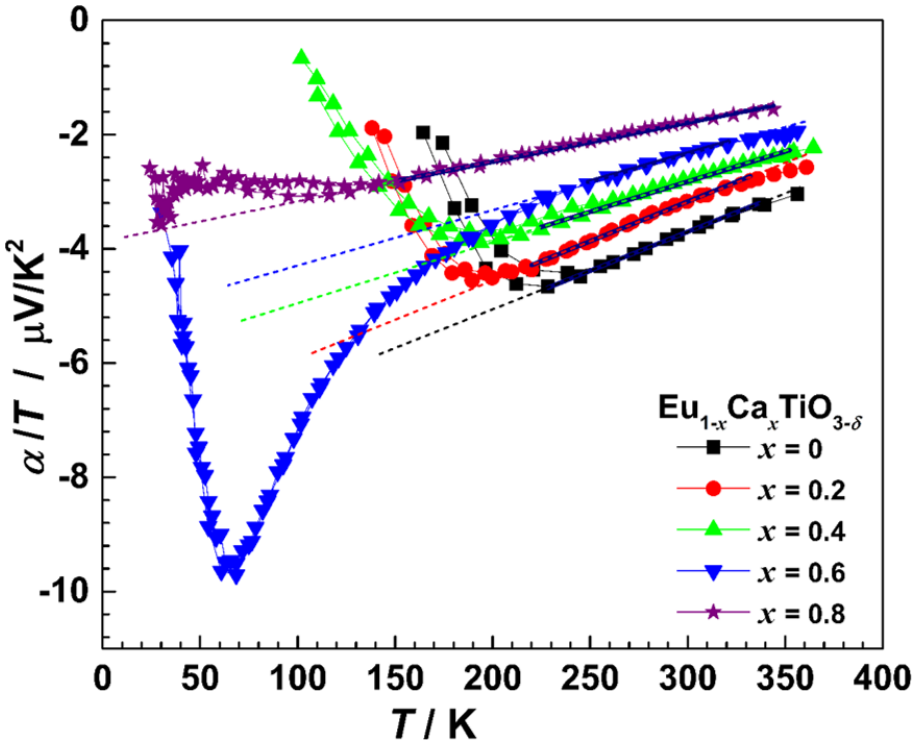

Fig. 6.13 The plot of α/T vs. T of $Eu_{1-x}Ca_xTiO_{3-\delta}$ samples. The dashed lines are guide for the eye.

Unlike the phonon-drag effect pronounced at low temperatures, the magnon-drag effect is a high-temperature phenomenon in contrast and works readily to room temperature and above [7]. The phonon-drag contribution can be suppressed in the case of porous samples due to a large concentration of defects that scatter phonons, but the magnon-drag effect will not be affected and hardly suffered from defect scattering. It was found that the magnetic κ_m with a large magnitude governs the total κ in the temperature range of ~ 50 K < T < 350 K as discussed before. Due to the similar working temperature range, the magnon-drag effect is considered to be strongly correlated with the "plateau" behavior of α. There are some different expressions for α_g based on different theories and simplified assumption models [7,11,81,82]. The theoretical calculation of α_g is not easy at the moment and it will be performed in the future for verification of this inference. Another concept relevant to explain the maximum $|\alpha|$ values of the “plateau” is the hybridization between the Eu 4*f* and Ti 3*d* or O 2*p* states [25,31]. The hybridization is sensitive to the local breaking of symmetry and the octahedral tilting [31,50,73]. The Ca^{2+} substitution decreases the distance between atoms but simultaneously reduces the symmetry and dilutes the 4*f* levels. Eventually, the 4*f* – 3*d* hybridization might decrease. The Ba^{2+} substitution increases the distance between atoms and dilutes the 4*f* levels, resulting in a decrease of 4*f* - 3*d* hybridization. It seems that the tendency of gradual decrease of the maximum $|\alpha|$ of Ca^{2+} and Ba^{2+} series substituted samples is consistent with the variation of 4*f* – 3*d* hybridization. The Sr^{2+} substitution does not obviously change the lattice, but it dilutes the 4*f* levels. The resulted 4*f* – 3*d* hybridization should also be decreased compared to the pristine ETO sample. However, the maximum $|\alpha|$ is observed in the sample of Sr^{2+}/x = 0.4 above 300 K, rather than the pristine sample. When comparing all these $\alpha(T)$ results of $Ca^{2+}/Ba^{2+}/Sr^{2+}$ substitutions, the maximum $|\alpha|$ among these samples cannot be simply explained by the 4*f* – 3*d* hybridization.

The structural disorder, structural instability, lattice defects, Eu 4*f* DOS, and strong correlation could also have influences on the electrical transport properties. There is an extensive literature on anomalous α induced by the structural disorder or lattice defects [78,83–86]. For example, an extremely small deviation of the oxygen content (i.e., $\delta < 0.002$) can result in either a large positive or a large negative α ($|\alpha| > 500$ μV/K) over a broad temperature range (100 K < T < 300 K) in a perovskite-type $LaCoO_3$ single crystal [86]. ETO possesses very complex crystal and electronic structures, as well as the unique high spin moments, all of these possibilities should keep in mind for further investigations.

6.4 Conclusions

The low temperature TE properties of $Eu_{1-x}A_xTiO_{3-\delta}$ (A = Ca^{2+}, Sr^{2+}, Ba^{2+}) solid solutions have been systematically investigated and carefully discussed. Isovalent chemical substitution with different ionic radii results in a significant difference in TE properties, indicating that the radii of the substitutes play a key role in determining transport properties. The phenomenon of glass-like thermal conductivity of ETO at very low temperatures proves the characteristics of local structure disorder and instability. Due to the smallest ionic radius of Ca^{2+} compared with the other *A*–site ions (Sr^{2+}, Ba^{2+}, Eu^{2+}), Ca^{2+}-substitution results in the most extraordinary influences on the low-temperature transport properties. The magnonic thermal conductivity is observed for all Eu^{2+} containing samples. Its contribution is most pronounced at around room temperature. The Ba^{2+} or Sr^{2+} substitution mainly affects the magnitude of thermal and electrical conductivities but does not significantly change the transport mechanisms. The magnon-drag effect, Eu 4*f* states hybridization, and local structural disorder are used together for the interpretation of electrical resistivity and Seebeck coefficient because an individual mechanism cannot explain the abnormal electronic transport phenomena of Ca^{2+}-substituted ETO.

References

[1] J.L. Bettis, M.H. Whangbo, J. Köhler, A. Bussmann-Holder, A.R. Bishop, Lattice dynamical analogies and differences between $SrTiO_3$ and $EuTiO_3$ revealed by phonon-dispersion relations and double-well potentials, *Physical Review B* 84 (2011) 184114.

[2] K.Z. Rushchanskii, N.A. Spaldin, M. Ležaić, First-principles prediction of oxygen octahedral rotations in perovskite-structure $EuTiO_3$, *Physical Review B* 85 (2012) 104109.

[3] M. Allieta, M. Scavini, L.J. Spalek, V. Scagnoli, H.C. Walker, C. Panagopoulos, S.S. Saxena, T. Katsufuji, C. Mazzoli, Role of intrinsic disorder in the structural phase transition of magnetoelectric $EuTiO_3$, *Physical Review B 85* (2012) 184107.

[4] D. Bessas, K.Z. Rushchanskii, M. Kachlik, S. Disch, O. Gourdon, J. Bednarcik, K. Maca, I. Sergueev, S. Kamba, M. Ležaić, R. P. Hermann, Lattice instabilities in bulk $EuTiO_3$, *Physical Review B 88* (2013) 144308.

[5] X. Xiao, M. Widenmeyer, K. Mueller, M. Scavini, S. Checchia, C. Castellano, D. Ma, S. Yoon. W. Xie, U. Starke, K. Zakharchuk, A. Kovalevsky, A. Weidenkaff, A squeeze on the perovskite

structure improves the thermoelectric performance of Europium Calcium Titanates, *Materials Today Physics 7* (2018) 96–105.

[6] C.W. Sandweg, Y. Kajiwara, A.V. Chumak, A.A. Serga, V.I. Vasyuchka, M.B. Jungfleisch, E. Saitoh, B. Hillebrands, Spin pumping by parametrically excited exchange magnons, *Physical Review Letters* 106 (2011) 216601.

[7] K. Vandaele, S.J. Watzman, B. Flebus, A. Prakash, Y. Zheng, S.R. Boona, J.P. Heremans, Thermal spin transport and energy conversion, *Materials Today Physics* 1 (2017) 39–49.

[8] C. Kittel, Magnons and their interactions with phonons and photons, *Journal de Physique et Le Radium*, 20 (1959) 145-147.

[9] P. Mandal, Temperature and doping dependence of the thermopower in $LaMnO_3$, *Physical Review B* 61 (2000) 14675.

[10] S. Roy, N. Khan, P. Mandal, Unconventional transport properties of the itinerant ferromagnet $EuTi_{1-x}Nb_xO_3$ (x = 0.10 – 0.20), *Physical Review B* 98 (2018) 134428.

[11] S.J. Watzman, R.A. Duine, Y. Tserkovnyak, S.R. Boona, H. Jin, A. Prakash, Y. Zheng, J.P. Heremans, Magnon-drag thermopower and Nernst coefficient in Fe, Co, and Ni, *Physical Review B* 94 (2016) 144407.

[12] N. Stojanovic, D.H.S. Maithripala, J.M. Berg, M. Holtz, Thermal conductivity in metallic nanostructures at high temperature: Electrons, phonons, and the Wiedemann-Franz law, *Physical Review B* 82 (2010) 75418.

[13] T.M. Tritt, Thermal conductivity: theory, properties, and applications, *Springer Science & Business Media*, 2005.

[14] H. Jin, O.D. Restrepo, N. Antolin, S.R. Boona, W. Windl, R.C. Myers, J.P. Heremans, Phonon-induced diamagnetic force and its effect on the lattice thermal conductivity, *Nature Materials* 14 (2015) 601.

[15] A.V. Sologubenko, S.M. Kazakov, H.R. Ott, T. Asano, Y. Ajiro, Diffusive energy transport in the S = 1 Haldane chain compound $AgVP_2S_6$, *Physical Review B* 68 (2003) 94432.

[16] A.V. Sologubenko, E. Felder, K. Gianno, H.R. Ott, A. Vietkine, A. Revcolevschi, Thermal conductivity and specific heat of the linear chain cuprate Sr_2CuO_3: Evidence for thermal transport via spinons, *Physical Review B* 62 (2000) R6108.

[17] A.V. Sologubenko, K. Gianno, H.R. Ott, A. Vietkine, A. Revcolevschi, Heat transport by lattice and spin excitations in the spin-chain compounds $SrCuO_2$ and Sr_2CuO_3, *Physical Review B* 64 (2001) 54412.

[18] C. Hess, C. Baumann, U. Ammerahl, B. Büchner, F. Heidrich-Meisner, W. Brenig, A. Revcolevschi, Magnon heat transport in $(Sr, Ca, La)_{14}Cu_{24}O_{41}$, *Physical Review B* 64 (2001) 184305.

[19] A.V. Sologubenko, K. Gianno, H.R. Ott, U. Ammerahl, A. Revcolevschi, Thermal Conductivity of the Hole-Doped Spin Ladder System $Sr_{14-x}Ca_xCu_{24}O_{41}$, *Physical Review Letters* 84 (2000) 2714.

[20] Y. Wang, N.S. Rogado, R.J. Cava, N.P. Ong, Spin entropy as the likely source of enhanced thermopower in $Na_xCo_2O_4$, *Nature* 423 (2003) 425.

[21] J. He, T.M. Tritt, Advances in thermoelectric materials research: Looking back and moving forward, *Science* 357 (2017) eaak9997.

[22] C. Ruf, H. Obloh, B. Junge, E. Gmelin, K. Ploog, G. Weimann, Phonon-drag effect in GaAs-$Al_xGa_{1-x}As$ heterostructures at very low temperatures, *Physical Review B* 37 (1988) 6377.

[23] C.M. Jaworski, J. Yang, S. Mack, D.D. Awschalom, R.C. Myers, J.P. Heremans, Spin-Seebeck effect: A phonon driven spin distribution, *Physical Review Letters* 106 (2011) 186601.
[24] A. Midya, P. Mandal, K. Rubi, R. Chen, J.-S. Wang, R. Mahendiran, G. Lorusso, M. Evangelisti, Large adiabatic temperature and magnetic entropy changes in $EuTiO_3$, *Physical Review B* 93 (2016) 94422.
[25] T. Birol, C.J. Fennie, Origin of giant spin-lattice coupling and the suppression of ferroelectricity in $EuTiO_3$ from first principles, *Physical Review B* 88 (2013) 94103.
[26] X. Chi, K. Rubi, A. Chaudhuri, L.M. Wong, X. Yu, C. Diao, A. Kumar, M.B.H. Breese, S. Wang, R. Mahendiran, A. Rusydi, Oxygen electronic screening and hybridization determining the insulator-metal transition of $Eu_{1-x}Ba_xTiO_3$, *Physical Review B* 98 (2018) 85152.
[27] L. Sagarna, A. Shkabko, S. Populoh, L. Karvonen, A. Weidenkaff, Electronic structure and thermoelectric properties of nanostructured $EuTi_{1-x}Nb_xO_{3-\delta}$ (x = 0.00; 0.02), *Applied Physics Letters* 101 (2012) 33908.
[28] L. Sagarna, S. Populoh, A. Shkabko, J. Eilertsen, A.E. Maegli, R. Hauert, M. Schrade, L. Karvonen, A. Weidenkaff, Influence of the Oxygen Content on the Electronic Transport Properties of $Sr_xEu_{1-x}TiO_{3-\delta}$, *The Journal of Physical Chemistry C* 118 (2014) 7821–7831.
[29] X. Xiao, M. Widenmeyer, W. Xie, T. Zou, S. Yoon, M. Scavini, S. Checchia, Z. Zhong, P. Hansmann, S. Kilper, A. Kovalevsky, A. Weidenkaff, Tailoring the structure and thermoelectric properties of $BaTiO_3$ via Eu^{2+} substitution, *Physical Chemistry Chemical Physics* 19 (2017) 13469–13480.
[30] H. Akamatsu, Y. Kumagai, F. Oba, K. Fujita, H. Murakami, K. Tanaka, I. Tanaka, Antiferromagnetic superexchange via 3*d* states of titanium in $EuTiO_3$ as seen from hybrid Hartree-Fock density functional calculations, *Physical Review B* 83 (2011) 214421.
[31] H. Akamatsu, Y. Kumagai, F. Oba, K. Fujita, K. Tanaka, I. Tanaka, Strong Spin-Lattice Coupling Through Oxygen Octahedral Rotation in Divalent Europium Perovskites, *Advanced Functional Materials* 23 (2013) 1864–1872.
[32] H. Akamatsu, K. Fujita, H. Hayashi, T. Kawamoto, Y. Kumagai, Y. Zong, K. Iwata, F. Oba, I. Tanaka, K. Tanaka, Crystal and electronic structure and magnetic properties of divalent europium perovskite oxides $EuMO_3$ (M = Ti, Zr, and Hf): experimental and first-principles approaches, *Inorganic Chemistry* 51 (2012) 4560–4567.
[33] T. Kolodiazhnyi, M. Valant, J.R. Williams, M. Bugnet, G.A. Botton, N. Ohashi, Y. Sakka, Evidence of Eu^{2+} 4*f* electrons in the valence band spectra of $EuTiO_3$ and $EuZrO_3$, *Journal of Applied Physics* 112 (2012) 83719.
[34] K. Rubi, R. Mahendiran, Magnetic Field Dependence of Dielectric Constant and Resistivity of $Eu_{0.98}Ba_{0.02}TiO_3$, *IEEE Transactions on Magnetics* 52 (2016) 1–4.
[35] T. Katsufuji, H. Takagi, Coupling between magnetism and dielectric properties in quantum paraelectric $EuTiO_3$, *Physical Review B* 64 (2001) 54415.
[36] Z. Guguchia, K. Caslin, R.K. Kremer, H. Keller, A. Shengelaya, A. Maisuradze, J.L. Bettis Jr, J. Kohler, A. Bussmann-Holder, M-H. Whangbo, Nonlinear pressure dependence of T_N in almost multiferroic $EuTiO_3$, *Journal of Physics: Condensed Matter 25* (2013) 376002.
[37] Y. Wang, Y. Sui, P. Ren, L. Wang, X. Wang, W. Su, H.J. Fan, Correlation between the structural distortions and thermoelectric characteristics in $La_{1-x}A_xCoO_3$ (A = Ca and Sr), *Inorganic Chemistry* 49 (2010) 3216–3223.

[38] B. Ramachandran, K.K. Wu, Y.K. Kuo, M.R. Rao, Phonon thermal transport and phonon–magnon coupling in polycrystalline $BiFeO_3$ systems, *Journal of Physics D: Applied Physics* 48 (2015) 115301.

[39] E. Bauer, S. Berger, A. Galatanu, H. Michor, C. Paul, G. Hilscher, V.H. Tran, A. Grytsiv, P. Rogl, Magnetic and thermodynamic properties of Eu-filled skutterudites, *Journal of Magnetism and Magnetic Materials* 226 (2001) 674–676.

[40] C. Hess, B. Büchner, U. Ammerahl, A. Revcolevschi, Phonon thermal conductivity in doped La_2CuO_4: Relevant scattering mechanisms, *Physical Review B* 68 (2003) 184517.

[41] C. Hess, B. Büchner, U. Ammerahl, L. Colonescu, F. Heidrich-Meisner, W. Brenig, A. Revcolevschi, Magnon Heat Transport in Doped La_2CuO_4, *Physical Review Letters* 90 (2003) 197002.

[42] V. Martelli, J.L. Jiménez, M. Continentino, E. Baggio-Saitovitch, K. Behnia, Thermal transport and phonon hydrodynamics in strontium titanate, *Physical Review Letters* 120 (2018) 125901.

[43] J. Yang, D.T. Morelli, G.P. Meisner, W. Chen, J.S. Dyck, C. Uher, Influence of electron-phonon interaction on the lattice thermal conductivity of $Co_{1-x}Ni_xSb_3$, *Physical Review B* 65 (2002) 94115.

[44] V.V. Laguta, S. Kamba, M. Maryško, B. Andrzejewski, M. Kachlík, K. Maca, J.H. Lee, D.G. Schlom, Magnetic resonance study of bulk and thin film $EuTiO_3$, *Journal of Physics: Condensed Matter* 29 (2017) 105401.

[45] K. Kugimiya, K. Fujita, K. Tanaka, K. Hirao, Preparation and magnetic properties of oxygen deficient $EuTiO_{3-\delta}$ thin films, *Journal of Magnetism and Magnetic Materials* 310 (2007) 2268–2270.

[46] V. Goian, S. Kamba, O. Pacherová, J. Drahokoupil, L. Palatinus, M. Dušek, J. Rohlíček, M. Savinov, F. Laufek, W. Schranz, A. Fuith, M. Kachlík, K. Maca, A. Shkabko, L. Sagarna, A. Weidenkaff, A.A. Belik, Antiferrodistortive phase transition in $EuTiO_3$, *Physical Review B* 86 (2012) 54112.

[47] A. Bussmann-Holder, J. Köhler, R.K. Kremer, J.M. Law, Relation between structural instabilities in $EuTiO_3$ and $SrTiO_3$, *Physical Review B* 83 (2011) 212102.

[48] A.P. Petrović, Y. Kato, S.S. Sunku, T. Ito, P. Sengupta, L. Spalek, M. Shimuta, T. Katsufuji, C.D. Batista, S.S. Saxena, C. Panagopoulos, Electric field modulation of the tetragonal domain orientation revealed in the magnetic ground state of quantum paraelectric $EuTiO_3$, *Physical Review B* 87 (2013) 64103.

[49] T.R. McGuire, M.W. Shafer, R.J. Joenk, H.A. Alperin, S.J. Pickart, Magnetic structure of $EuTiO_3$, *Journal of Applied Physics* 37 (1966) 981–982.

[50] L. Li, H. Zhou, J. Yan, D. Mandrus, V. Keppens, Research Update: Magnetic phase diagram of $EuTi_{1-x}B_xO_3$ (B = Zr, Nb), *APL materials* 2 (2014) 110701.

[51] A. Gupta, B.T. Kavakbasi, B. Dutta, B. Grabowski, M. Peterlechner, T. Hickel, S.V. Divinski, G. Wilde, J. Neugebauer, Low-temperature features in the heat capacity of unary metals and intermetallics for the example of bulk aluminum and Al_3Sc, *Physical Review B* 95 (2017) 94307

[52] B.F. Woodfield, J.L. Shapiro, R. Stevens, J. Boerio-Goates, R.L. Putnam, K.B. Helean, A. Navrotsky, Molar heat capacity and thermodynamic functions for $CaTiO_3$, *The Journal of Chemical Thermodynamics* 31 (1999) 1573–1583.

[53] W. Liu, X. Tan, K. Yin, H. Liu, X. Tang, J. Shi, Q. Zhang, C. Uher, Convergence of conduction bands as a means of enhancing thermoelectric performance of n-type $Mg_2Si_{1-x}Sn_x$ solid solutions, *Physical Review Letters* 108 (2012) 166601.

[54] J.L. Cohn, G.S. Nolas, V. Fessatidis, T.H. Metcalf, G.A. Slack, Glasslike heat conduction in high-mobility crystalline semiconductors, *Physical Review Letters* 82 (1999) 779.
[55] W.G. Zeier, Y. Pei, G. Pomrehn, T. Day, N. Heinz, C.P. Heinrich, G.J. Snyder, W. Tremel, Phonon Scattering through a Local Anisotropic Structural Disorder in the Thermoelectric Solid Solution $Cu_2Zn_{1-x}Fe_xGeSe_4$, *Journal of the American Chemical Society* 135 (2013) 726–732.
[56] J.L. Cohn, J.J. Neumeier, C.P. Popoviciu, K.J. McClellan, T. Leventouri, Local lattice distortions and thermal transport in perovskite manganites, *Physical Review B* 56 (1997) R8495.
[57] N.A. Benedek, C.J. Fennie, Why are there so few perovskite ferroelectrics?, *The Journal of Physical Chemistry C* 117 (2013) 13339–13349.
[58] D.G. Cahill, S.K. Watson, R.O. Pohl, Lower limit to the thermal conductivity of disordered crystals, *Physical Review B* 46 (1992) 6131.
[59] Q. Jiang, H. Wu, Magnetic influence on frequency of soft-phonon mode in incipient ferroelectric $EuTiO_3$, *Journal of Applied Physics* 93 (2003) 2121–2125.
[60] S. Kamba, D. Nuzhnyy, P. Vaněk, M. Savinov, K. Knížek, Z. Shen, E. Šantavá, K. Maca, M. Sadowski, J. Petzelt, Magnetodielectric effect and optic soft mode behaviour in quantum paraelectric $EuTiO_3$ ceramics, *EPL (Europhysics Letters)* 80 (2007) 27002.
[61] D.S. Ellis, H. Uchiyama, S. Tsutsui, K. Sugimoto, K. Kato, D. Ishikawa, A.Q.R. Baron, Phonon softening and dispersion in $EuTiO_3$, *Physical Review B* 86 (2012) 220301.
[62] J.A. Souza, J.P. Rino, A molecular dynamics study of structural and dynamical correlations of $CaTiO_3$, *Acta Materialia* 59 (2011) 1409–1423.
[63] R.G. Ross, P. Andersson, G. Bäckström, Effects of H and D order on the thermal conductivity of ice phases, *The Journal of Chemical Physics* 68 (1978) 3967–3972.
[64] L. Feng, T. Shiga, J. Shiomi, Phonon transport in perovskite $SrTiO_3$ from first principles, *Applied Physics Express* 8 (2015) 71501.
[65] W.G. Zeier, A. Zevalkink, Z.M. Gibbs, G. Hautier, M.G. Kanatzidis, G.J. Snyder, Thinking like a chemist: intuition in thermoelectric materials, *Angewandte Chemie International Edition* 55 (2016) 6826–6841.
[66] H.-E. Zimmer, J. Engert, P. Frach, I. Henning, E. Hegenbarth, Glasslike behaviour of polycrystalline $BaTiO_3$ at very low temperatures, *Ferroelectrics Letters Section* 6 (1986) 33–40.
[67] M. Yashima, T. Hoshina, D. Ishimura, S. Kobayashi, W. Nakamura, T. Tsurumi, S. Wada, Size effect on the crystal structure of barium titanate nanoparticles, *Journal of Applied Physics* 98 (2005) 14313.
[68] K. Uchino, E. Sadanaga, T. Hirose, Dependence of the crystal structure on particle size in barium titanate, *Journal of the American Ceramic Society* 72 (1989) 1555–1558.
[69] A.J.H. Mante, J. Volger, The thermal conductivity of $BaTiO_3$ in the neighbourhood of its ferroelectric transition temperatures, *Physics Letters A* 24 (1967) 139–140.
[70] P.G. Reuvekamp, R.K. Kremer, J. Köhler, A. Bussmann-Holder, Spin-lattice coupling induced crossover from negative to positive magnetostriction in $EuTiO_3$, *Physical Review B* 90 (2014) 94420.
[71] C.J. Fennie, K.M. Rabe, Magnetic and electric phase control in epitaxial $EuTiO_3$ from first principles, *Physical Review Letters* 97 (2006) 267602.
[72] P. Reuvekamp, K. Caslin, Z. Guguchia, H. Keller, R.K. Kremer, A. Simon, J. Köhler, A. Bussmann-Holder, Tiny cause with huge impact: polar instability through strong magneto-

electric-elastic coupling in bulk $EuTiO_3$, *Journal of Physics: Condensed Matter* 27 (2015) 262201.
[73] P. Parisiades, E. Liarokapis, J. Köhler, A. Bussmann-Holder, M. Mezouar, Pressure-temperature phase diagram of multiferroic $EuTiO_3$, *Physical Review B* 92 (2015) 64102.
[74] G.J. Snyder, E.S. Toberer, Complex thermoelectric materials, in: Materials For Sustainable Energy: A Collection of Peer-Reviewed Research and Review Articles from Nature Publishing Group, *World Scientific* (2011) 101–110.
[75] N. Mott, Conduction in non-crystalline materials, *Oxford University Press*, Walton Street, UK, (1987).
[76] M.-L. Theye, A. Gheorghiu, T. Rappeneau, A. Lewis, Transport properties of evaporated versus sputtered amorphous germanium films, *Journal de Physique* 41 (1980) 1173–1181.
[77] S. Boutiche, Variable Range Hopping Conductivity: Case of the non-constant density of states, *Solar Energy Conference*, Sharjah, UAE, (2001) 19-22
[78] T. Wu, G. Wu, X.H. Chen, Effect of disorder on transport and electronic structure in $LaCo_{1-x}Ni_xO_3$ system, *Solid State Communications* 145 (2008) 293–298.
[79] D.K.C. MacDonald, Thermoelectricity: an introduction to the principles, *Courier Corporation*, 2006.
[80] J. Fukuyado, K. Narikiyo, M. Akaki, H. Kuwahara, T. Okuda, Thermoelectric properties of the electron-doped perovskites $Sr_{1-x}Ca_xTi_{1-y}Nb_yO_3$, *Physical Review B* 85 (2012) 75112.
[81] M.E. Lucassen, C.H. Wong, R.A. Duine, Y. Tserkovnyak, Spin-transfer mechanism for magnon-drag thermopower, *Applied Physics Letters* 99 (2011) 262506.
[82] B. Flebus, R.A. Duine, Y. Tserkovnyak, Landau-Lifshitz theory of the magnon-drag thermopower, *EPL (Europhysics Letters)* 115 (2016) 57004.
[83] J. Jackle, Effect of electron-phonon interaction on the thermopower of amorphous metals, *Journal of Physics F: Metal Physics* 10 (1980) L43-L46.
[84] S.N. Guin, S. Banerjee, D. Sanyal, S.K. Pati, K. Biswas, Origin of the Order–Disorder Transition and the Associated Anomalous Change of Thermopower in $AgBiS_2$ Nanocrystals: A Combined Experimental and Theoretical Study, *Inorganic chemistry* 55 (2016) 6323–6331.
[85] N. Xiao, X. Dong, L. Song, D. Liu, Y. Tay, S. Wu, L.-J. Li, Y. Zhao, T. Yu, H. Zhang, W. Huang, H.H. Hng, P.M. Ajayan, Q. Yan, Enhanced thermopower of graphene films with oxygen plasma treatment, *ACS Nano* 5 (2011) 2749–2755.
[86] K. Berggold, M. Kriener, C. Zobel, A. Reichl, M. Reuther, R. Müller, A. Freimuth, T. Lorenz, Thermal conductivity, thermopower, and figure of merit of $La_{1-x}Sr_xCoO_3$, *Physical Review B* 72 (2005) 155116.

Chapter 7 Conclusions and outlook

7.1 Conclusions

Alkaline-earth metal cations A^{2+} (A = Mg^{2+}, Ca^{2+}, Sr^{2+}, Ba^{2+}) substituted europium titanates have been synthesized for studying their crystal structure, local structural disorder, TE properties, and the correlation between the crystal structures and TE properties. The spin effects on TE properties were also traced by means of low temperature transport properties measurements. An overview graph of the obtained results is illustrated in Fig. 7.1.

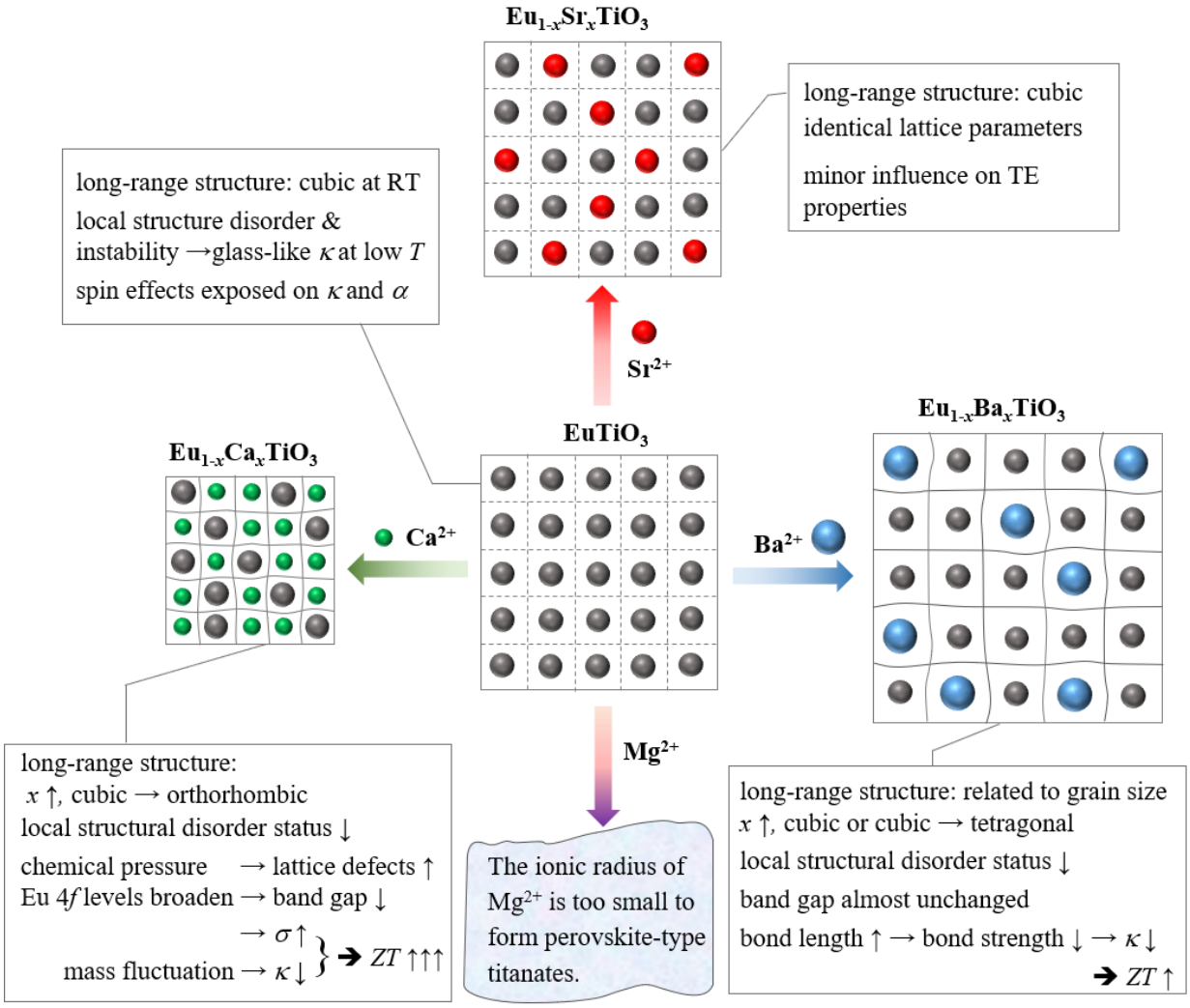

Fig. 7.1 A simplified overview diagram of the obtained results.

In this dissertation, a simple soft chemistry method was introduced to prepare an europium aqueous solution starting from Eu_2O_3 powder material. This was successfully used in a Pechini synthesis approach to form oxide precursors as mentioned in chapter 2. A subsequent parameter adjusted thermal treatment allowed to synthesize $EuTiO_3$-based materials with chemically homogeneous (nano-sized) particles. By using a conventional sintering method, highly compacted and densified bulk samples were successfully obtained for physical transport properties measurements. Applying this experimental synthesis procedure, the perovskite-type $Eu_{1-x}A_xTiO_{3-\delta}$ (A = Ba^{2+}, Sr^{2+}, Ca^{2+}) solid solutions with high purity and homogenous microstructure were successfully synthesized in the full range of $0 \leq x \leq 1$. Due to the fact that the ionic radius of Mg^{2+} is too small to be bonded in an AO_{12} cuboctahedron, it was impossible to obtain a single-phase $Eu_{1-x}Mg_xTiO_{3-\delta}$ solid solution via the same synthesis method.

Because the 12-fold coordinated Sr^{2+} and Eu^{2+} have an equal ionic radius, the obtained $Eu_{1-x}Sr_xTiO_{3-\delta}$ solid solutions maintained the crystal structure of long-range cubic symmetry. The κ of $Eu_{1-x}Sr_xTiO_{3-\delta}$ solid solutions displayed the same temperature dependence as the pristine ETO sample, indicating that Sr^{2+} substation did not change the main heat conduction mechanism. Due to analogous lattice dynamics between $SrTiO_3$ and $EuTiO_3$, combining with the observed thermal conductivity results, it was proposed that partial Sr^{2+} substitution (less than 40 %) did not change the local crystal structure but enhanced point defect formation due to the random distribution of the introduced cations. The ρ of $Eu_{1-x}Sr_xTiO_{3-\delta}$ solid solutions were only weakly changed compared to the pristine ETO sample. The behavior and magnitude of the α of $Eu_{1-x}Sr_xTiO_{3-\delta}$ were distinctly different. The sample with 40 % Sr^{2+} substitution shows the largest $|\alpha|$ at around 360 K and the smallest κ at low temperatures (T < 100 K). On an overall view, Sr^{2+} substitution causes minor influences on the thermoelectric properties.

Although the Ba^{2+} substitution led to an unit cell expansion, the crystal structures of $Eu_{1-x}Ba_xTiO_{3-\delta}$ solid solutions maintained the long-range cubic symmetry even in Ba^{2+}-rich compounds. The local structural disorder status was changing depending on the chemical compositions. The Eu/BaO_{12} cuboctahedron became more distorted in Eu^{2+}-richer samples, but the TiO_6 octahedra turned out to be more distorted in Ba^{2+}-richer samples. The local distortions with different orientations coexisted in the same crystallite preserving the long-range cubic symmetry. The extension of Ti–O bond length resulted in a decrease of the bond strength, which was closely correlated to the reduction of thermal conductivity. The substitution effect on transport properties was more pronounced at high temperatures when T > 783 K, where the ρ is proportional to Eu^{2+} content. It was concluded that the Eu 4*f* levels dominate the electrical transport properties by means of thermally activated electrons from Eu 4*f* levels to Ti 3*d* states. Due to the increase of electrical conductivity and simultaneous reduction of thermal conductivity, partial substitution with Ba^{2+} can improve the TE performance of $Eu_{1-x}Ba_xTiO_{3-\delta}$ at higher temperatures when $x \leq 0.4$.

In $Eu_{1-x}Ca_xTiO_3$ compounds, the Ca^{2+} substitution not only led to an cubic sub-cell volume contraction and symmetry breaking but also introduced lots of lattice defects resulting from the chemical pressure. On the long-range scale (average), the crystal structure was changed from cubic to orthorhombic with increasing Ca^{2+} substitution, resulting in an overall reduction of lattice symmetry. On the local scale, on the contrary, the structural distortion or disorder decreased and the concentration of lattice defects (e.g., Eu^{3+}, Ti^{3+}) increased, tending to a very complicated and different system compared to ETO. Consequently, extraordinary substitution effects were observed from Ca^{2+} substitution compared with Ba^{2+} and Sr^{2+}. For example, the sample with 80 % substitution showed

metal-insulator-transitions at low temperatures and the sample with 60 % substitution displayed an anomalous Seebeck coefficient. The Ca^{2+} substitution resulted in a significant enhancement of electrical conductivity, which was chiefly attributed to the increase of electronic defects (e.g. Eu^{3+}, Ti^{3+}, and oxygen vacancies). The atomic mass of Ca is approximately ¼ of Eu. The huge mass contrast on the *A*-site gave rise to mass-fluctuations, which has a large contribution to the reduction of thermal conductivity. Eventually, the *ZT* values were remarkably increased with increasing of Ca^{2+} content. In comparison with the Ba^{2+} substitution, the positive effect of *ZT* improvement was more pronounced at lower temperatures (T < 1000 K).

The intrinsic feature of local structural disorder of ETO (and lattice instabilities) was manifested by its glass-like κ at low temperatures. The broad peak of κ below room temperature was attributed to the contribution of magnons, which have a more pronounced effect on the κ in the temperature range of ~ 60 K < T < 300 K. The dilution of Eu^{2+} in $Eu_{1-x}A_xTiO_3$ compounds, achieved by substitution with the non-magnetic cations, does not suppress or eliminate the magnonic κ but affects its magnitude. Hence, the magnonic κ is observed in all Eu^{2+} containing samples. The resulting magnon-drag effect was responsible for the maximum $|\alpha|$ around room temperature.

In summary, the systematic isovalent chemical substitutions demonstrated the evolution of local structural disorder, the role of Eu 4*f* electrons to electrical conductivity, the magnon contributions to thermal and electronic conductions, and the interrelation among them. Owing to the intrinsic structural disorder and lattice instability of ETO, the ionic radius of the substitute played a key role in affecting the crystal structures and hence the physical properties. Both Ba^{2+} and Ca^{2+} substitutions gave rise to positive effects for developing TE performance, although the dominant transport mechanism and effective temperature region were different. The substitution by smaller Ca^{2+} results in more attractive effects. In addition, in terms of non-toxicity and natural abundance, substitution with Ca^{2+} is more favorable compared to substitution with Ba^{2+}. $Eu_{1-x}Ca_xTiO_3$ compounds can be potential thermoelectric candidates and further investigations can be carried out for improving the thermoelectric properties.

7.2 Outlook

On the basis of the results obtained above, both $Eu_{1-x}Ba_xTiO_3$ and $Eu_{1-x}Ca_xTiO_3$ solid solutions are promising alternatives to the expensive $EuTiO_3$. However, the *ZT* values of the solid solutions are still noticeably lower than that of some well-known TE materials such as Bi_2Te_3, PbTe, and half-Heusler compounds, which is mainly due to the low electrical conductivity. An effective strategy for enhancing electrical conductivity is introducing charge carriers with high mobilities. Since electrical conductivity and Seebeck coefficient are correlated via carrier concentration, improving electrical conductivity by increasing carrier mobility will bring no or less damage to the Seebeck coefficient. By doing so, the power factor could be significantly enhanced. For instance, since InSb (with mobility of 1000 mm^2V/s) nano-inclusions inject high energy electrons into TiCoSb matrix, the *ZT* value of a TiCoSb-InSb nanocomposite is much higher than that of pristine TiCoSb [1]. Due to the fact that the melting temperature of InSb is around 873 K, InSb compound is not suitable as a secondary phase in the $EuTiO_3$ system. Graphene possesses a very high melting point and even higher mobility than InSb. Some recent studies reveal that the *ZT* or *PF* values are largely enhanced via graphene doping in $SrTiO_3$-based compounds [2, 3]. Therefore, graphene could be a suitable second

compound to form a better performing nanocomposite by injecting high energy carriers into $EuTiO_3$-based materials.

References

[1] W.J. Xie, Y.G. Yan, S. Zhu, M. Zhou, S. Populoh, K. Gałązka, S.J. Poon, A. Weidenkaff, J. He, X.F. Tang, T.M. Tritt, Significant *ZT* enhancement in p-type Ti (Co, Fe) Sb–InSb nanocomposites via a synergistic high-mobility electron injection, energy-filtering and boundary-scattering approach, *Acta Materialia*, 61 (2013) 2087-2094.

[2] O. Okhay, S. Zlotnik, W. Xie, K. Orlinski, M.J.H. Gallo, G. Otero-Irurueta, A.J.S. Fernandes, D.A. Pawlak, A. Weidenkaff, A. Tkach, Thermoelectric performance of Nb-doped $SrTiO_3$ enhanced by reduced graphene oxide and Sr deficiency cooperation, *Carbon*, 143 (2019) 215-222.

[3] Y. Lin, C. Norman, D. Srivastava, F. Azough, L. Wang, M. Robbins, K. Simpson, R. Freer, I. A. Kinloch, Thermoelectric Power Generation from Lanthanum Strontium Titanium Oxide at Room Temperature through the Addition of Graphene, *ACS Applied Materials & Interfaces*, 7 (2015) 15898-15908.

Hereby I declare that this thesis titled, “Thermoelectric Properties of Alkaline Earth Metal Substituted Europium Titanates” has been independently composed by me in partial fulfillment of the requirements for the degree of Doctor of Natural Science (Dr. rer. nat.) in Materials Science from the Technical University of Darmstadt (TU Darmstadt). I certify that the work presented in this thesis is, to the best of my knowledge and belief, original and contains no material previously published or written by another person, except where due reference and permission is made.

Darmstadt
16.01.2020

Xingxing Xiao

TECHNISCHE
UNIVERSITÄT
DARMSTADT